

**THE APPLICATION OF X-RAY CRYSTALLOGRAPHY
TOWARDS THE DESIGN OF NOVEL INHIBITORS
OF MURA AND CDK2**

BY

Huijong Han

Submitted to
the Department of Medicinal Chemistry and
the Faculty of the Graduate School at

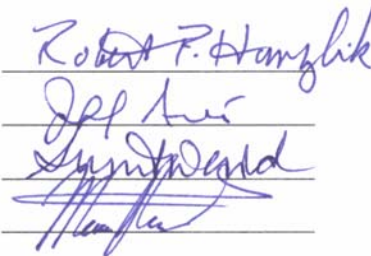
the University of Kansas

in partial fulfillment of the requirements for
the degree of Doctor of Philosophy
with a major in Medicinal Chemistry



Chairperson

Committee members



Date defended: September 26th, 2008

The Dissertation Committee for Huijong Han certifies
that this is the approved version of the following dissertation:

The Application of X-ray Crystallography
Towards the Design of Novel Inhibitors
of MurA and CDK2

Committee:



Chairperson

Date approved: September 26th, 2008

Abstract

Infectious diseases and cancers are the second and third largest causes of death worldwide. UDP-*N*-acetyl-glucosamine (UNAG) enolpyruvyl transferase (MurA) and Cyclin-dependent kinases (CDKs) are proven as antibiotic and anticancer targets, respectively.

MurA belongs to the enolpyruvyl transferase family of enzymes. MurA catalyzes the first committed step in the biosynthesis of cell wall peptidoglycan, and is the target of fosfomicin, a naturally occurring broad-spectrum antibiotic. Ever increasing resistance of bacteria to fosfomicin has placed an emphasis on the identification and characterization of novel MurA inhibitors.

Knowledge of the detailed enzymatic mechanism is essential for the discovery of potent MurA inhibitors. The studies on the mutant MurA enzymes Arg91Lys, Asp123Ala, Arg120Ala, and Cys115Asp, revealed key catalytic residues and residues important for the conformational changes in the enzymatic reaction. Several new inhibitors of MurA were identified by High-Throughput Screening (HTS), and kinetically characterized. It appears that most of these compounds bind to the open conformation of MurA, and thus the inhibitor binding site is largely solvent exposed. These results suggest that MurA inhibitors need to be designed to induce the open-closed transformation of the enzyme, like the natural substrate UNAG. Such inhibitors should be much more potent than the inhibitors discovered in this work.

CDK2 plays a critical role in the G1- to S-phase checkpoint of the cell cycle. Only a few drugs targeting CDK2 are in clinical trials, thus there is a need for the discovery of novel CDK2 inhibitors.

Six CDK2 inhibitor scaffolds were identified by HTS, and the molecular modes of action of four of them were thoroughly characterized by steady-state kinetics and crystallography. Structure-Activity Relationship (SAR) analysis of the four scaffolds gave rise to the design of analogs with excellent potency. In addition, computational studies were performed, and novel CDK2 inhibitor scaffolds were designed. The selectivities and cytotoxic properties of these inhibitors are not known yet.

Acknowledgments

I would like to express my gratitude to Dr. Ernst Schönbrunn for being an outstanding advisor and excellent professor. His constant encouragement, support, and invaluable suggestions made this work successful. I am deeply indebted to my committee members Dr. Robert P. Hanzlik, Dr. Jeffrey Aubé, Dr. Sunil David, and Dr. Mario Rivera for their time and effort in reviewing this work.

My sincere thanks go to Dr. Andreas Becker for CDK2 kinetics and taking time to introduce me to the techniques and methods of X-ray crystallography, Dr. Melanie Priestman for the invaluable previous MurA studies, Martha Healy-Fried and Dr. Todd Funke for helping me to settle down in the lab, and Katinka Bähr for the CDK2 cloning. I am grateful to Dr. Veena Vasandani for helping me MurA HTS, Dr. Rawle Francis for CDK2 HTS, and Dr. Gunda Georg and her group members, specially to Dr. Vishweshwer Katta, Dr. Sudhakar Jakkaraj, Dr. Neelam Krishnaveni, and Dr. Ramappa Chakarasali for synthesizing the CDK2 inhibitor analogs. I would like to acknowledge my colleagues, Frank Marsilio and Dr. Sanne Olesen for reviewing my thesis and providing feedback. I also would like to thank all of the faculty and students in the Department of Medicinal Chemistry for their support throughout the past five years. Special thanks go to every Dr. Schönbrunn's group member for support in the lab and everything that makes working here fun.

I am deeply and forever indebted to my parents for their love, support, and encouragement throughout my entire life. I am also very grateful to my husband, Sang-Kil, for everything he did to support me.

Funding was provided by the Goetsch family.

Table of Contents

ABSTRACT.....	3
ACKNOWLEDGMENTS	4
TABLE OF CONTENTS	5
LIST OF ABBREVIATIONS	8
LIST OF TABLES	13
LIST OF FIGURES	14
1. INTRODUCTION.....	19
1.1. MurA (UDP-<i>N</i>-acetyl-glucosamine enolpyruvyl transferase)	19
1.1.1. Reaction Mechanism of MurA.....	22
1.1.2. Structural Features of MurA	26
1.1.3. MurA Inhibition of and Resistance to Fosfomycin.....	28
1.1.4. Inhibitors of MurA	31
1.2. Cyclin-dependent kinase 2	33
1.2.1. Cell Cycle and Cyclin-Dependent Kinase (CDK)	33
1.2.2. Structural Features of CDK2	37
1.2.3. CDK Inhibitors and Their Modes of Action.....	40
2. MATERIALS AND METHODS	52
2.1. General Materials	52
2.1.1. Competent Cells.....	52
2.1.2. Chemicals.....	52
2.1.3. Solutions	52
2.1.3.1. Media	52
2.1.3.2. Antibiotics.....	53
2.1.3.3. DNA Electrophoresis	53
2.1.3.4. SDS Electrophoresis	54
2.1.3.5. FPLC Buffers.....	55
2.1.3.6. Lanzetta Reagent.....	57
2.1.3.7. Crystallization Solutions.....	57

2.2.	General Methods.....	65
2.2.1.	Preparation of Competent Cells.....	65
2.2.2.	Transformations.....	65
2.2.3.	Plasmid Preparations.....	66
2.2.4.	DNA Electrophoresis.....	66
2.2.5.	Sequencing.....	66
2.2.6.	Glycerol Stocks.....	66
2.2.7.	SDS Electrophoresis.....	66
2.2.8.	Determination of Protein Concentration.....	67
2.2.9.	PD-10.....	67
2.2.10.	Centricon.....	68
2.2.11.	Crystallization.....	68
2.2.11.1.	Hanging-Drop method.....	68
2.2.11.2.	Micro-Seeding method.....	69
2.2.12.	Data Collection.....	69
2.2.13.	Data Reduction and Structure Refinement.....	70
2.3.	<i>E. cloacae</i> and mutant MurA enzymes.....	71
2.3.1.	DNA.....	71
2.3.2.	Primers.....	71
2.3.3.	Site-directed Mutagenesis of <i>E. cloacae</i> MurA.....	71
2.3.4.	Over-expression of WT and Mutant <i>E. cloacae</i> MurA Enzymes.....	72
2.3.5.	Purification of WT and Mutant <i>E. cloacae</i> MurA Enzymes.....	72
2.3.6.	Kinetic analysis of WT and Mutant <i>E. cloacae</i> MurA Enzymes.....	74
2.3.6.1.	High-throughput Screening (HTS) of MurA.....	74
2.3.6.2.	Inhibition Study of HTS Leads.....	76
2.3.6.3.	Structure-Activity Relationships (SAR) of HTS 1 and HTS 2 on WT MurA.....	79
2.3.6.4.	Inhibition study of known inhibitors.....	80
2.3.6.5.	WT, Asp123Ala, and Arg91Lys <i>E. cloacae</i> MurA.....	81
2.3.6.6.	Arg120Ala <i>E. cloacae</i> MurA.....	84
2.3.6.7.	Cys115Asp <i>E. cloacae</i> MurA.....	85
2.3.7.	Crystallization of <i>E. cloacae</i> MurA Enzymes.....	87
2.3.7.1.	Asp123Ala and Arg91Lys MurA.....	87
2.3.7.2.	Arg120Ala MurA.....	88
2.3.7.3.	Cys115Asp MurA.....	88
2.3.7.4.	MurA with HTS2-2.....	89
2.3.7.5.	MurA with HTS1-1.....	90
2.3.8.	Further Studies with HTS2-2.....	91
2.3.8.1.	Kinetic Study of Trp71Val and Lys248Asp MurA.....	91
2.3.8.2.	MurA Oligomerization by HTS2-2.....	92
2.4.	Cyclin-Dependent Kinase 2.....	93
2.4.1.	DNA.....	93

2.4.2.	Over-expression of CDK2	93
2.4.3.	Purification of CDK2	93
2.4.4.	Crystallization of CDK2 with inhibitors.....	95
2.4.5.	Molecular docking of CDK2	95
3.	RESULTS AND DISCUSSION	97
3.1.	Structure and Mechanism of MurA.....	97
3.1.1.	The Role of Arg91 and Asp123 in <i>E. cloacae</i> MurA	97
3.1.2.	Arg120 in <i>E. cloacae</i> MurA and Enzymatic Mechanism	105
3.1.3.	The Role of Cys115 in the Enzymatic Mechanism of MurA	110
3.2.	Identification and Characterization of MurA Inhibitors.....	114
3.2.1.	Study of Known MurA Inhibitors.....	114
3.2.1.1.	Peptide Inhibitors	114
3.2.1.2.	Cnicin.....	114
3.2.2.	Identification and Characterization of Novel MurA Inhibitors	117
3.3.	Inhibitors of Cyclin-dependent Kinase 2.....	131
3.3.1.	Lead 1 and its analogs.....	134
3.3.2.	Lead 2 and its analogs.....	141
3.3.3.	Lead 3 and its analogs.....	150
3.3.4.	Lead 4 and its analogs.....	158
3.3.5.	Design of New Inhibitors and Docking Study	172
3.3.6.	Selectivity of CDK2 inhibitors	175
4.	CONCLUSION	181
	REFERENCES.....	183

List of Abbreviations

(v/v)	Volume/volume
(w/v)	Weight/volume
a	Adenine
ADP	Adenosine diphosphate
Ala	Alanine
Amp	Ampicillin
ANS	8-anilino-1-naphthalene sulphonate
Arg	Arginine
Asn	Asparagine
Asp	Aspartic acid
ATP	Adenosine triphosphate
BSA	Bovine serum albumin
c	Cytosine
CAK	CDK activating kinase
CDK2	Cyclin-dependent kinase 2
CV	Column volume
Cys	Cysteine
DMSO	Dimethylsulfoxide
DNA	Deoxyribonucleic acid
DTT	Dithiothreitol
E _a	Activation energy

<i>E. cloacae</i>	<i>Enterobacter cloacae</i>
<i>E. coli</i>	<i>Escherichia coli</i>
EDTA	Ethylene diamine tetraacetic acid
EGTA	Ethylene glycol tetraacetic acid
EP-UNAG	Enolpyruvyl UDP- <i>N</i> -acetyl-glucosamine
EPSP	5-enolpyruvyl-shikimate-3-phosphate
EPSPS	5-enolpyruvyl-shikimate-3-phosphate synthase
EtOH	Ethanol
FosA	Fosfomycin resistance protein
FPLC	Fast protein liquid chromatography
FOS	Fosfomycin
g	Guanine
Gln	Glutamate
Glu	Glutamic acid
Gly	Glycine
GOX	Glucose oxidase
GSK3 β	Glycogen synthase kinase 3 β
GST	Glutathione-S-transferase
H9	4-amino-2-(chlorodifluoromethyl)-6-methoxyquinoline-3-carbonitrile
H10	7-bromo-3,6,6-trimethyl-1-(pyridin-2-yl)-6,7-dihydro-1H-indazol-4(5H)-one
HCl	Hydrochloric acid
HEPES	N-[2-Hydroxyethyl] piperazine-N'-[2-ethanesulfonic acid]
His	Histidine

His-tag	Histidine tag containing 6 histidines
HTS1-1	2-chloro-5-(1H-pyrrol-1-yl)-benzoic acid
HTS2-2	8-nitro-3a,4,5,9b-tetrahydro-3H-cyclopenta[c]quinoline-4-carboxylic acid
HTS3-1	6,7-dihydro-6-(6-nitro-1,3-benzodioxol-5-yl)-3-(2-propenylthio)-2,4-triazino[5,6-d][3,1]benzoxazepine
HTS4-1	2-chloro-5-[5-(2-nitroethenyl)-2-furanyl]-benzoic acid
HTS6-1	(2Z,5Z)-2,5-bis((5-bromofuran-2-yl)methylene)cyclopentanone
HTS7-1	(Z)-5-imino-3-(methylthio)-6-((5-nitrofuran-2-yl)methylene)-5H-[1,2,4]thiadiazolo[4,5-a]pyrimidin-7(6H)-one
HTS8-1	(Z)-4-((5-nitrofuran-2-yl)methylene)-1-(3-(trifluoromethyl)phenyl)pyrazolidine-3,5-dione
HTS	High-throughput screening
IC	Inhibition constant
Ile	Isoleucine
IPTG	Isopropyl- β -D-thiogalactoside
Kan	Kanamycin
kDa	Kilodalton
L1	5-nitro-2-(pyridin-3-ylmethylamino)benzamide
L2	2-(4,6-diamino-1,3,5-triazin-2-yl)phenol
L3	5-tert-pentyl-4,5,6,7-tetrahydro-1H-indazole-3-carbohydrazide
L4	(2-(allylamino)-4-aminothiazol-5-yl)(phenyl)methanone
LB	Luria-Bertani
Leu	Leucine
Lys	Lysine
MAPK	Mitogen-activated protein kinase

MeOH	Methanol
MES	2-[N-Morpholino] ethanesulfonic acid
Met	Methionine
MurA	UDP- <i>N</i> -acetyl-glucosamine enolpyruvyl transferase
MurB	UDP- <i>N</i> -acetyl-enolpyruvylglucosamine reductase
MW	Molecular weight
NADPH	Nicotinamide adenosine dinucleotide phosphate
OAc	Acetate
OD	Optical density
OH	hydroxyl
PCR	Polymerase chain reaction
PEG	Polyethylene glycol
PEP	Phosphoenol pyruvate
Phe	Phenylalanine
P _i	Inorganic phosphate
PKA	Protein kinase A
PKB	Protein kinase B
Pro	Proline
P-seph	Phenyl-sepharose
Q-seph	Q-sepharose (anionic)
RNA	Ribonucleic acid
rpm	Revolutions per min
S3P	Shikimate-3-phosphate
SAR	Structure activity relationship

Ser	Serine
SDS	Sodium dodecyl sulfate
SDS-PAGE	Sodium dodecyl sulfate polyacrylamide gel electrophoresis
t	Thymine
TEMED	N,N,N',N'-Tetra-methylethylenediamine
Thr	Threonine
TI	Tetrahedral Intermediate
Tris	Tris hydroxymethyl aminomethane
Trp	Tryptophan
Tyr	Tyrosine
U/mg	μmol of product/min/mg of protein
UDP	Uridine diphosphate
UNAG	UDP- <i>N</i> -acetyl-glucosamine
UNAM	UDP- <i>N</i> -acetyl-muramic acid
UV	Ultraviolet
Val	Valine
WT	Wild type

List of Tables

Table 1:	Conserved amino acids in the loop and hinge region of MurA.....	28
Table 2:	CDK and partner cyclins	34
Table 3:	Crystallization buffers for Hampton crystallization screen #1	58
Table 4:	Crystallization buffers for Hampton crystallization screen #2	59
Table 5:	Crystallization buffers for Wizard crystallization screen #1	60
Table 6:	Crystallization buffers for Wizard crystallization screen #2	61
Table 7:	Variations of crystallization condition H1-18	62
Table 8:	Variations of crystallization condition PEG20K	63
Table 9:	Variations of crystallization condition H1-41	64
Table 10:	Activity ratio and calculated activation energy of WT and Cys115Asp MurAs	111
Table 11:	SAR table of the HTS 1 scaffold.....	124
Table 12:	SAR table of the HTS 2 scaffold.....	126
Table 13:	SAR table of the L1 scaffold (1)	138
Table 14:	SAR tables of the L1 scaffold (2).....	139
Table 15:	SAR tables of the L2 scaffold (1).....	144
Table 16:	SAR table of the L2 scaffold (2)	145
Table 17:	SAR table of the L3 scaffold (1)	153
Table 18:	SAR tables of the L3 scaffold (2).....	154
Table 19:	SAR table of the L4 scaffold (1)	161
Table 20:	SAR table of the L4 scaffold (2)	162
Table 21:	SAR table of the L4 scaffold (3)	163
Table 22:	SAR table of the L4 scaffold (4)	164
Table 23:	Compounds belonging to the L4 scaffold	165
Table 24:	Sequence alignment scores for CDKs	177
Table 25:	Sequence alignment scores for protein kinases	180

List of Figures

Figure 1: Three stages of peptidoglycan biosynthesis	20
Figure 2: The reactions catalyzed by MurA and EPSPS.....	21
Figure 3: Addition-elimination mechanism catalyzed by MurA	23
Figure 4: A stereoview of EP-UNAG bound to Cys115Ser MurA.....	24
Figure 5: Structural study with Asp305Ala MurA.....	25
(A) A stereoview of the tetrahedral intermediate bound to MurA active site.	
(B) Stereochemical course of enolpyruvyl transferase reaction.	
Figure 6: Conformational changes of MurA upon binding of UNAG	26
Figure 7: Structures of MurA at free stage, ANS binding, and UNAG binding.....	27
Figure 8: Inhibition of MurA via a covalent modification of Cys115 by fosfomycin	29
Figure 9: Structures of MurA inhibitors described in the literatures	32
Figure 10: An overview of some essential steps in cell-cycle progression.....	35
Figure 11: Overall structure of CDK2 with ATP	37
Figure 12: (A) Chemical structure of ATP.	
(B) A stereoview of ATP binding site of CDK2-ATP complex structure	38
Figure 13: Overall structures of CDK2-ATP complex and CDK2-cyclinA-ATP complex.....	39
Figure 14: Small molecule inhibitors of CDK (1).....	41
Figure 15: Small molecule inhibitors of CDK (2).....	42
Figure 16: Chemical structures of CDK inhibitors selective to CDK4 and CDK6....	43
Figure 17: A stereoview of staurosporine binding site of CDK2 complex structure	44
Figure 18: A schematic diagram of deschloroflavopiridol binding in CDK2.....	45

Figure 19: Stereoviews of indirubin-5-sulfate and oxindole(7) in the binding sites of CDK2 complex structures	47
Figure 20: Stereoviews of olomoucine and roscovitine binding sites of CDK2 complex structures	48
Figure 21: A stereoview of quinazoline inhibitor bound to CDK2.....	50
Figure 22: A stereoview of hymenialdisine bound to CDK2.....	51
Figure 23: Emission spectra of ANS study with Arg91Lys mutant MurA.....	98
Figure 24: (A) Overlap figure of overall structures of WT and Arg91Lys MurAs. (B) Overlap figure of position 91 of WT and Arg91Lys MurAs. (C) Interactions of Arg91 in the open form WT MurA. (D) Interactions of Lys91 in the open form Arg91Lys MurA	99
Figure 25: A stereoview of the loop region of the binary structure of WT MurA...	100
Figure 26: (A) Determination of K_m and V_{max} of UNAG for WT and Asp123Ala MurAs. (B) Determination of K_d of UNAG for WT and Asp123Ala MurAs	101
Figure 27: (A) Overlapped structures of WT and monomer A of Asp123Ala MurA. (B) Overlapped structures of WT and monomer B of Asp123Ala MurA.	102
Figure 28: (A) A stereoview of the loop region of the open form WT MurA structure. (B) A stereoview of UNAG binding site of the closed form WT MurA structure	104
Figure 29: Overall structure of Arg120Ala MurA complexed with UNAG and PEP	106
Figure 30: (A) A stereoview of the interactions of Arg91 in Arg120Ala MurA. (B) Stereoviews of the active sites of Arg120Ala and WT MurAs.....	107
Figure 31: The first step reaction of the proposed enzymatic mechanism of MurA based on the studies of Arg120Ala mutant.....	108

Figure 32: (A) Overlapped structures of the open form WT and Cys115Asp MurAs. (B) Differences of the loop conformation between WT and Cys115Asp MurAs	112
Figure 33: Kinetic analysis of Cys115Asp MurA.....	113
(A) K_d determination of UNAG for WT and Cys115Asp MurAs.	
(B) K_m determination of PEP for Cys115Asp MurA.	
Figure 34: (A) The co-crystal structure of cnicin with MurA and UNAG. (B) A proposed mechanism of action of cnicin in the literature. (C) A newly proposed mechanism of action of cnicin	115
Figure 35: K_i determination of cnicin on <i>E. cloacae</i> MurA.....	116
Figure 36: Representative compounds from 1 st HTS of MurA.....	118
Figure 37: K_i determination of HTS2-2	119
Figure 38: (A) Fluorescence scans from 400–600nm with excitation at 366 nm. (B) Replot of HTS2-2 ANS fluorescence data as a function of HTS2-2 concentration.....	120
Figure 39: (A) The co-crystal structure of HTS2-2 with WT <i>E. cloacae</i> MurA. (B) A stereoview of HTS2-2 binding site on MurA.....	121
Figure 40: (A) Elution profile of size exclusion column with MurA + HTS2-2 and MurA only. (B) IC_{50} determination of WT, Lys248Asp, and Trp71Val MurAs	122
Figure 41: Chemical structures and IC_{50} values of HTS hit compounds	129
Figure 42: K_i determinations of HTS7-1 and HTS8-1	130
Figure 43: Six scaffolds of CDK2 inhibitors identified by HTS.....	132
Figure 44: Stereoviews of the co-crystal structures of ADP, AlosineA, and NU6027 with CDK2	133
Figure 45: (A) A stereoview of the co-crystal structure of L1 with CDK2. (B) A schematic diagram of L1 binding in the CDK2 active site. (C) SAR strategy for the L1 scaffold	135

Figure 46: A stereoview of the co-crystal structure of L1-KVR-1-9 with CDK2	137
Figure 47: (A) A stereoview of the co-crystal structure of L2 with CDK2. (B) A schematic diagram of L2 binding in the CDK2 active site. (C) SAR strategy for the L2 scaffold	142
Figure 48: Stereoviews of the co-crystal structures of L2 analogs: L2-3 and L2-6 with CDK2	147
Figure 49: Stereoviews of the co-crystal structures of L2 analogs: L2-JWS6-52 , L2-JWS6-76 , and L2-JWS6-48 with CDK2	148
Figure 50: A stereoview of the co-crystal structure L2-8 with CDK2.....	149
Figure 51: (A) A stereoview of the co-crystal structure of L3 with CDK2. (B) A schematic diagram of L3 binding in the CDK2 active site. (C) SAR strategy for the L3 scaffold	151
Figure 52: A stereoview of both L3 enantiomers bound in the CDK2 active site.	152
Figure 53: Stereoviews of the co-crystal structures of L3 analogs: L3-3 , L3-4 , and L3-NSK-MC1-6 with CDK2	157
Figure 54: (A) A stereoview of the co-crystal structure of L4 with CDK2. (B) A schematic diagram of L4 binding in the CDK2 active site. (C) SAR strategy for the L4 scaffold	159
Figure 55: Stereoviews of the co-crystal structures of L4 analogs: L4-4 , L4-12 , and L4-14 with CDK2	167
Figure 56: Stereoviews of the co-crystal structures of L4 analogs: L4-RC1-34 and L4-RC1-35 with CDK2	168
Figure 57: Stereoviews of the co-crystal structures of L4 analogs: L4-RC1-36 , L4-RC1-37 , and L4-RC1-38 with CDK2.....	169
Figure 58: Stereoviews of the co-crystal structures of L4 analogs: L4-RC2-35 , L4-RC2-36 , and L4-RC2-37 with CDK2.....	170
Figure 59: A stereoview of the co-crystal structure of L4-RC2-38 with CDK2	171

Figure 60: (A) Orientation of inhibitors L1 and L2-6 after superposition of the respective CDK2 ligand structures.	
(B) New scaffolds with potential as inhibitors as a result of recombining the essential features and spatial orientation of both inhibitor molecules.	
(C) Designed molecules containing 2 or 3 hydrogen bond acceptors and donors	173
Figure 61: The docking results of the designed inhibitors	174
Figure 62: Sequence alignments of all 11 CDKs	176
Figure 63: Sequence alignments of several protein kinases.....	178
Figure 64: Docking results of the Lead compounds into various kinase structures.....	179

1. Introduction

1.1. MurA (UDP-*N*-acetyl-glucosamine enolpyruvyl transferase)

Since the antibiotic properties of penicillin were first discovered in 1929, many antibiotic agents have contributed to the prevention and treatment of infections caused by bacteria. Despite the success of the antibiotics in the market and clinics, infections are still the second largest cause of death and remain as a major public health problem. Antibiotic resistance is a serious public health threat and results in the return of untreatable infections on a massive scale. Thus, there is a great need for novel antibiotic agents to solve resistance problems of current antibiotics¹. One of the best known targets for antibiotic therapy is the peptidoglycan biosynthetic pathway, validated in the clinic with fosfomycin, vancomycin, and penicillins.

The peptidoglycan (murein) in a bacterial cell confers mechanical resistance to the higher internal osmotic pressure and provides the cell with structural strength. Peptidoglycan is also a structure unique to prokaryotic cells. Thus drugs targeting the biosynthesis of peptidoglycan (i.e. the Mur pathway) would be effective antibiotic agents leading to cell death, without affecting the host².

Peptidoglycan consists of glycan chains comprised of alternating *N*-acetyl-muramic acid and *N*-acetyl-glucosamine residues, and both residues are cross-linked by short peptides. This cross-linkage joining glycan chains makes peptidoglycan structures rigid and tensile². The biosynthesis of peptidoglycan is a complex process, consisting of a three-step pathway³. The first stage is the synthesis of the monomeric

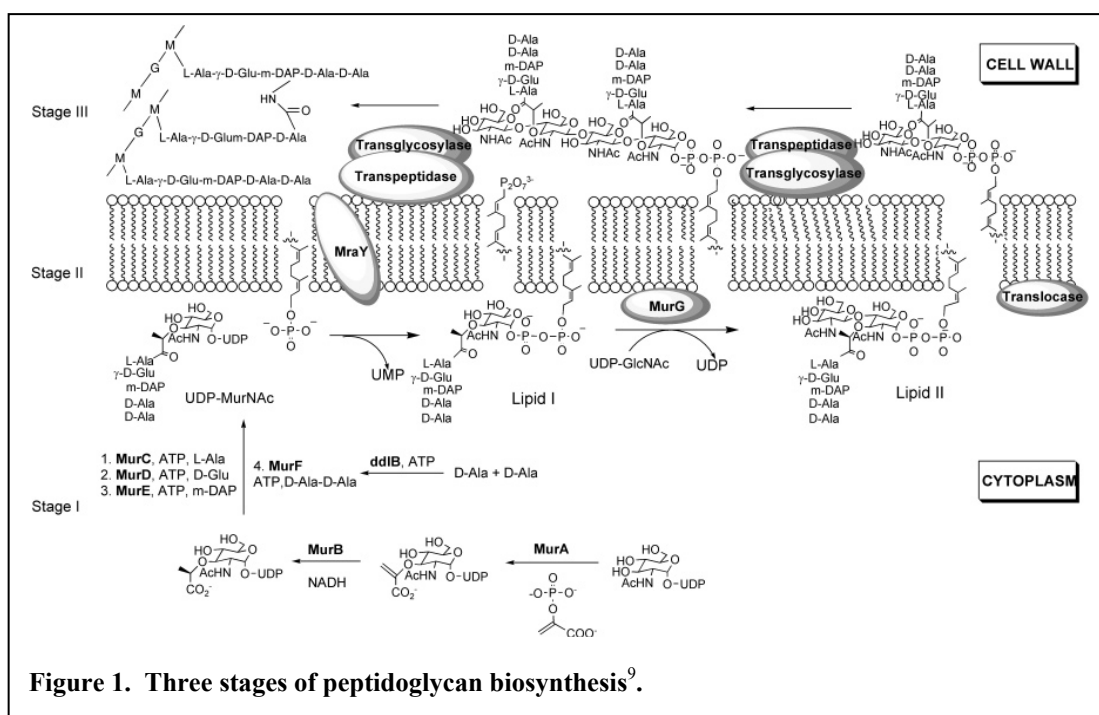
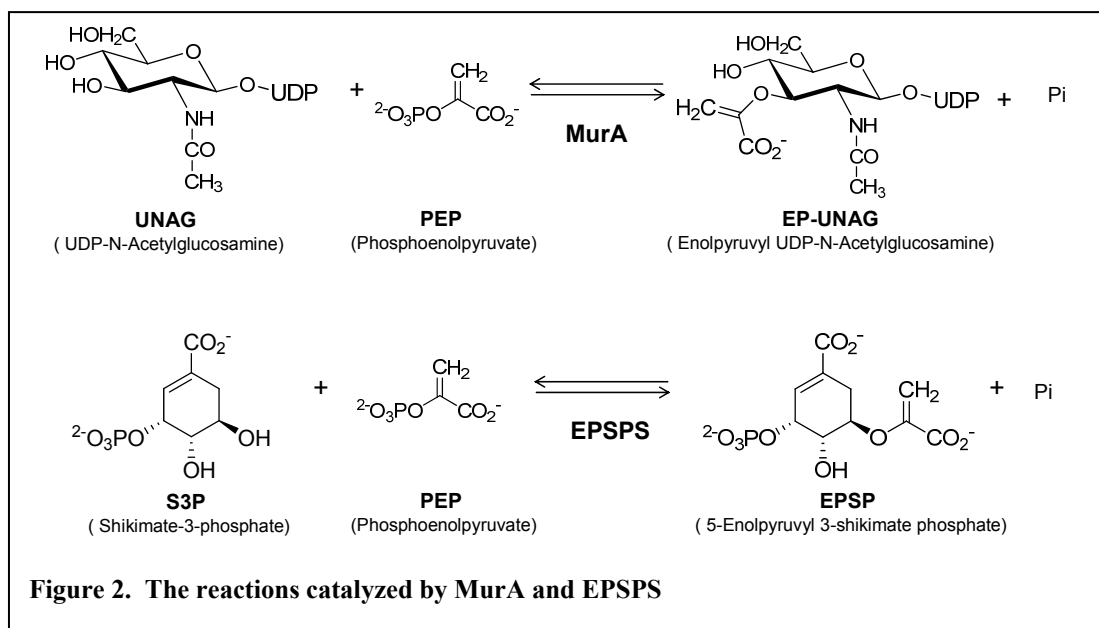


Figure 1. Three stages of peptidoglycan biosynthesis⁹.

building block, UDP-*N*-acetyl-glucosamine and UDP-*N*-acetyl-muramyl pentapeptide in the cytoplasm by the enzymes MurA-F⁴. The second stage occurs on the inner side of the membrane, with synthesis of a lipid-linked intermediate and its subsequent translocation to the external face of the cytoplasmic membrane by MraY⁵ and MurG⁶. Then, a polymerization reaction takes place in the periplasmic space catalyzed by transglycosylases⁷ and transpeptidases^{8,9} (Figure 1).

Mur enzymes are unique to bacteria and are involved in critical functions of almost all bacterial organisms¹⁰. In addition, inhibitors of Mur enzymes have potential to be bactericidal, leading to cell lysis and bacterial cell death¹¹.

The first committed step in the pathway is the transfer of an enolpyruvyl group from phosphoenol pyruvate (PEP) to UNAG producing enolpyruvyl-UDP-*N*-acetyl-glucosamine (EP-UNAG) with the release of inorganic phosphate (P_i). This step is



catalyzed by UDP-*N*-acetyl-glucosamine enolpyruvate transferase (MurA, EC 2.5.1.7.) (Figure 2)^{3, 12}. While PEP is used as a phosphoryl transferring agent in most PEP-dependent enzymatic reactions, the reaction catalyzed by MurA is unique because it involves the attack at the chemically less reactive C-2 position of PEP, leading to the cleavage of the C–O bond rather than P–O bond. MurA is inhibited by the naturally occurring antibiotic fosfomicin¹³, which is the active ingredient of the broad spectrum antibiotic Monurol[®].

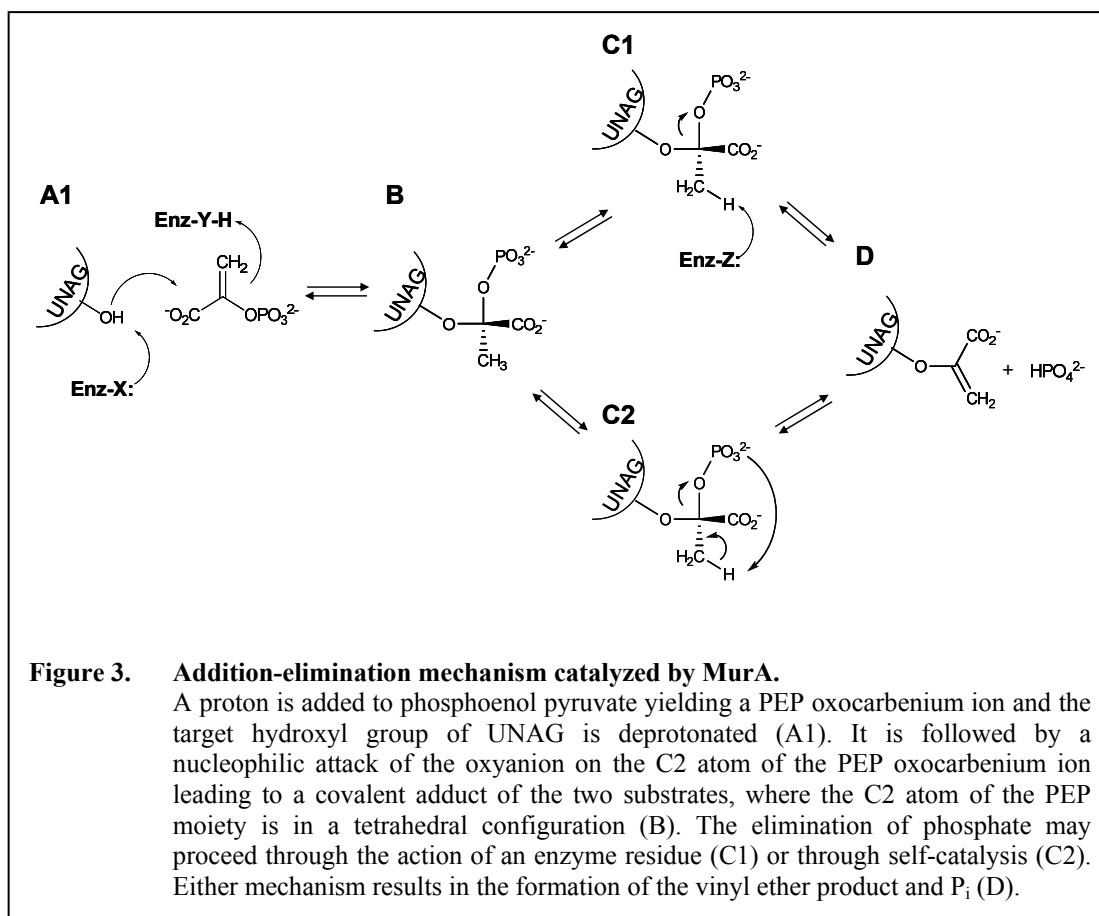
The only other enzyme known to catalyze a similar reaction is 5-enolpyruvyl-shikimate-3-phosphate synthase (EPSPS, EC 2.5.1.19) (Figure 2), which uses shikimate-3-phosphate (S3P) as its second substrate instead of UNAG. EPSPS catalyzes the sixth step in the biosynthesis of the aromatic amino acids (the shikimate pathway) in bacteria, plants, and fungi, and has been extensively studied because it is the target of glyphosate¹⁴, the active ingredient of the herbicide Roundup[®].

While Gram-negative bacteria including *E. coli* have one copy of the *murA* gene, several Gram-positive bacteria have two genes, *murA1* and *murA2*. Gene knockout experiments that removed either, but not both, of the *murA* genes showed that the organism was still viable, suggesting that the two genes encode active enzymes that can substitute for each other¹⁵. It is also known that both MurA enzymes are inhibited by fosfomycin.

1.1.1. Reaction Mechanism of MurA

The unusual reaction catalyzed by MurA has been extensively studied. Mechanistic and structural data of MurA show that the reaction follows an ordered addition-elimination mechanism, with UNAG interacting with free enzyme prior to the binding of PEP or fosfomycin. However, the detailed enzymatic mechanism of MurA has only been clearly identified recently¹⁶⁻²⁰.

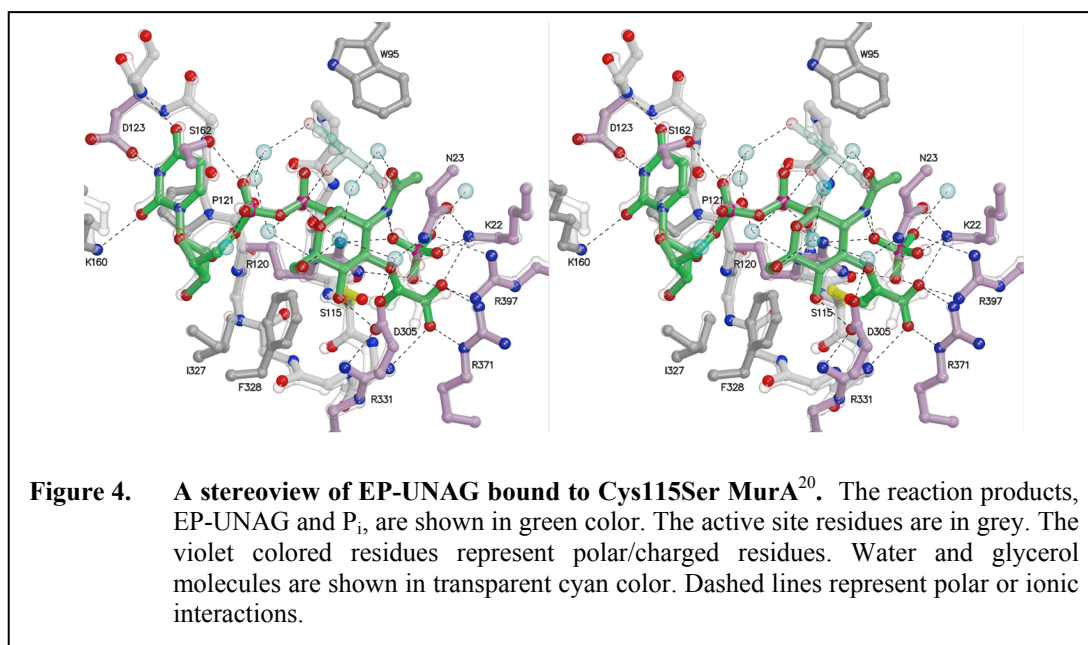
The first step of the MurA reaction is thought to proceed by protonation of PEP producing an oxocarbenium ion and deprotonation of the 3'-OH on UNAG. The oxyanion then attacks C-2 of the PEP-oxocarbenium ion, leading to a tetrahedral intermediate of both substrates (Figure 3-B). The detailed mechanism of the formation of this tetrahedral intermediate is not certain. Whether it is a concerted or a stepwise mechanism is currently under debate. The elimination step of the reaction may proceed either by the aid of a residue in the MurA active site (Figure 3-C1) or by intramolecular-catalysis (Figure 3-C2), i.e. the deprotonation of C-3 of PEP can be performed by the phosphate moiety attached to C-2 of PEP or by a basic amino acid



in the MurA active site, leading to separation of the product, EP-UNAG, and releasing of inorganic phosphate (P_i).

Some early biochemical studies of the enzymatic mechanism of MurA proposed the existence of a covalent adduct of PEP and Cys115 in the reaction^{17, 18}. Since this mechanism cannot explain the activity of Cys115Asp mutant MurA, it has been suggested that UNAG directly attacks PEP at the first step of the MurA reaction.

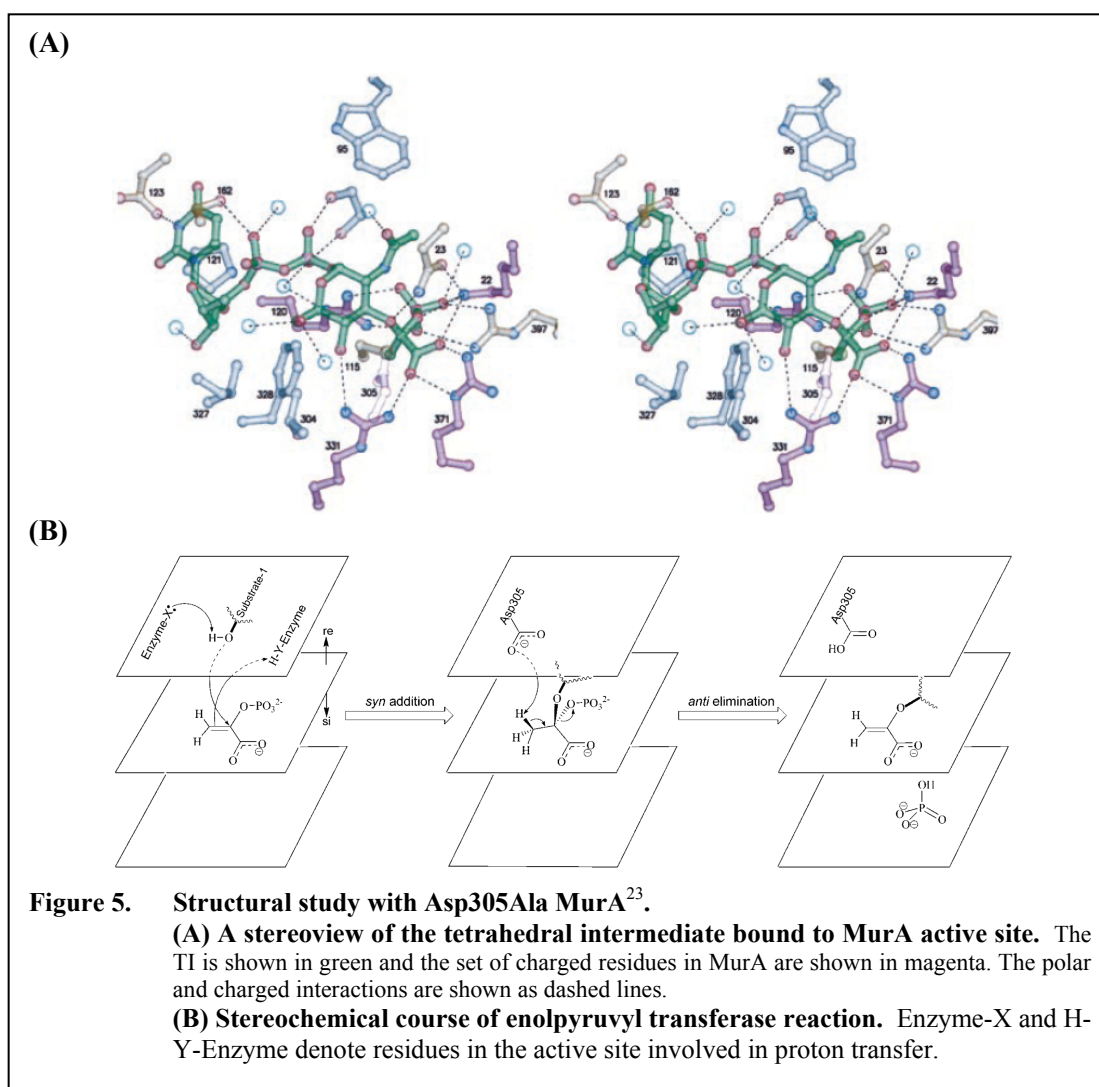
While the existence of the hemi thio-ketal intermediate of Cys115 and PEP is still debated, another role of Cys115 in the reaction catalyzed by MurA has been identified. Studies with the Cys115Ser mutant enzyme indicated that the function of



Cys115 is to support product release. Kinetic analysis of Cys115Ser mutant MurA showed a single turnover of the reaction. Structural study in the presence of the substrates depicts the product state of the enzyme with EP-UNAG and P_i (Figure 4)²⁰.

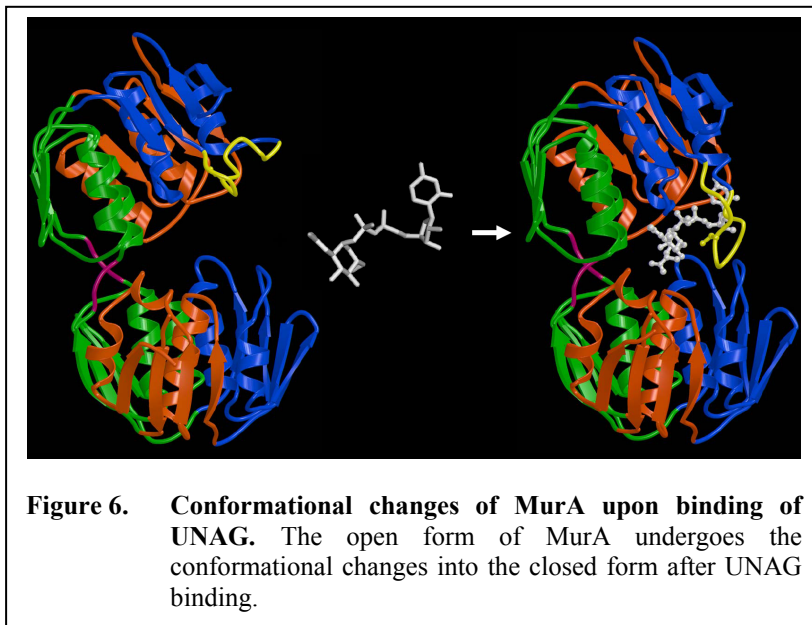
The stereochemical course of the reaction has been studied as well. Initial studies with PEP analogs had led to the conclusion that the addition of UNAG to C-2 of PEP proceeds from the *2-si* face and with the *anti* addition and the *syn* elimination steps^{19, 21, 22}. However, a structural study with Asp305Ala MurA mutant clearly demonstrated that the addition step occurs to the *2-re* face of PEP suggesting *syn* addition and *anti* elimination stereochemistry (Figure 5)²³. From the crystal structure of Asp305Ala MurA with the TI, it was shown that Asp305 is responsible for the final deprotonation reaction required for the elimination of P_i (Enz-Z of Figure 3-C1).

The identification of the residues involved in the catalysis of MurA has been enhanced by structural information given by crystallographic data. Crystallization of the MurA mutants, Cys115Ser and Asp305Ala, with products and the TI, respectively, allowed the identification of a set of charged residues, interacting with the PEP moiety of the TI or products. These charged amino acids in the active site are postulated to be critical residues in the reaction mechanism of MurA by serving as acid-base catalysts. These residues are Lys22, Arg120, Arg331, and Arg371, and



they are highly conserved through MurA enzymes from various organisms. Structural studies of mutant enzymes on these residues would provide a detailed catalytic mechanism of MurA.

1.1.2. Structural Features of MurA



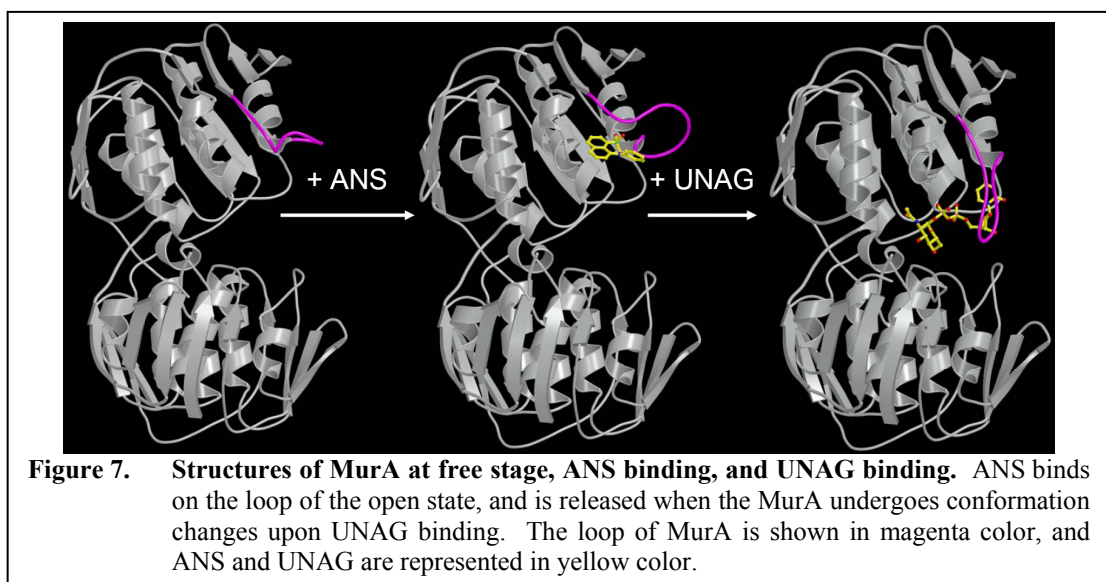
In recent years, the mechanistic understanding of the enzymatic reaction by MurA has been given a structural basis through determination of a series

of crystal structures of various forms of the enzyme^{19, 24–27}. The single polypeptide chain of MurA folds into two globular domains, each comprising an inside-out α/β barrel, built up by 6-fold repetition of a common $\beta\alpha\beta\alpha\beta\beta$ motif. This architecture is shared with EPSPS, the only other enolpyruvyl transferase, although the sequence identity between MurA and EPSPS is only ~25 %²⁸. Thus, these two enzymes share not only a unique enzymatic reaction, but also distinct structural features.

Several crystal structures of liganded and un-liganded MurA have been determined. MurA contains a highly flexible loop, which is involved in substrate and inhibitor binding. The conformation of the loop varies in these crystal structures,

depending on the presence or absence of ligands and the crystallization conditions, i.e. pH and ionic strengths. Prior to the binding of substrates, free MurA enzyme exists in an open state. Upon binding of UNAG the two domains approach each other, establishing the active site in the cleft between the two domains and generating the PEP binding site (Figure 6). One of the notable structural changes during this process is the conformation of a loop, composed of the 10 amino acid residues, Pro112–Pro121, in the top domain, N-terminal domain. The loop moves toward to the active site and closes the cleft like a lid. This ‘induced fit’ mechanism is the structural evidence of the ordered substrate binding for the MurA enzymatic reaction.

The conformational change from the open to the closed states of MurA can be monitored by the use of the extrinsic fluorophor, 8-anilino-1-naphthalene sulfonate (ANS). The co-crystal structure of MurA with ANS showed that ANS binds to the flexible loop, Pro112–Pro121, and restructures it²⁹. ANS in the open form of MurA is released by UNAG binding, thus ANS is used as a detector of the conformational



change of MurA (Figure 7). In the closed state of MurA, the loop has moved toward the cleft, and the conformation of Arg91 is changed to stabilize the closed loop conformation through hydrogen bonds to backbone carbonyl oxygen atoms of Gly113 and Arg120. Arg91 is also essential for the ANS binding to un-liganded open-form MurA, and the conformational change of this residue will dissociate ANS. Thus, Arg91 is considered as one of the critical residues in the open-closed conformational change of the loop. In addition, there are other conserved residues in the loop and the hinge regions, which may be essential for the loop conformational change (Table 1³⁰).

Table 1. Conserved amino acids in the loop and hinge region of MurA³⁰. Conservation is the result of comparing 163 MurA sequences.											
Residue	Asp49	Arg91	Pro112	Gly113	Gly114	Ile117	Gly118	Arg120	Pro121	Asp123	Asp231
Conservation	100%	100%	95.7%	100%	100%	95.7%	100%	100%	86.5%	87.1%	100%

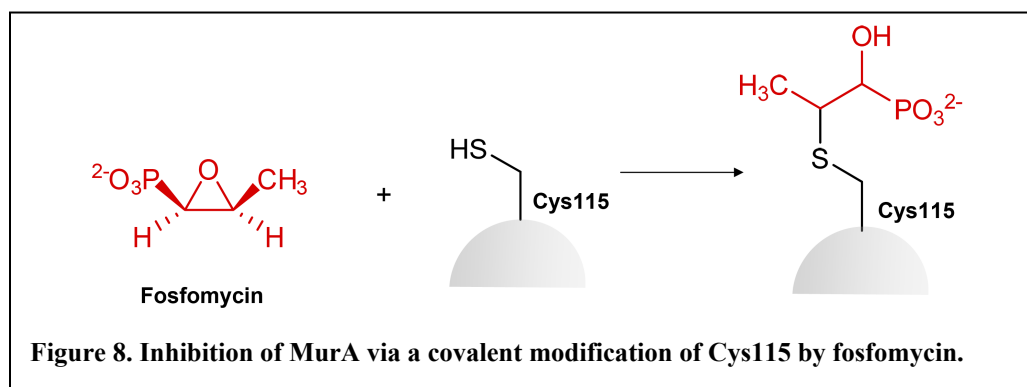
Although the large flexible loop of MurA is a unique and interesting feature, it often interferes with crystallization due to its flexible character.

1.1.3. MurA Inhibition of and Resistance to Fosfomycin

Fosfomycin ((1*R*, 2*S*)-epoxy propyl phosphonic acid³¹) is a naturally occurring antibiotic produced by certain *Streptomyces* species using PEP as a precursor. It is effective against both Gram-positive and Gram-negative bacteria. Fosfomycin is the drug for the treatment of pediatric gastrointestinal infections resulting from Shiga-like toxin-producing *E. coli* in Japan³²⁻³⁴. It is also predominantly used for the treatment of bacterial infections of the urinary tract and is clinically desirable due to its low toxicity to humans. It has been shown that fosfomycin is effective even against

bacterial infections resistant to other antibiotics, e.g. vancomycin-resistant enterococci³⁵ and quinolone-resistant *E. coli*³⁶.

The bactericidal activity of fosfomicin is exerted through inhibition of MurA. Inhibition of MurA by fosfomicin is competitive against PEP but becomes irreversible by forming a covalent bond with the active Cys115 residue of the enzyme via epoxide ring opening (Figure 8)^{26,37,38}. Fosfomicin inhibition of MurA was found to be time-dependent as well as UNAG-dependent, which suggests that the conformational change of MurA upon UNAG binding prior to fosfomicin is essential for inactivation.



Although resistance of *E. coli* to fosfomicin is rarely found in the clinic, there is a high frequency of development of fosfomicin resistance in many other pathogenic organisms causing urinary tract infections such as *Serratia marcescens*, *Klebsiella pneumoniae*, *E. cloacae*, and *Staphylococcus epidermidis*³⁹⁻⁴³. Several mechanisms of fosfomicin resistance are known: i) decreased uptake of fosfomicin^{13,44-46}, ii) inactivation of fosfomicin by a plasmid-encoded glutathione transferase⁴⁷⁻⁵², and iii)

replacement of MurA Cys115 by Asp⁵³. Detailed descriptions of these mechanisms are as follows.

i) Early instances of resistance to fosfomycin were due to chromosomal mutants resulting in decreased uptake^{44,45}. Fosfomycin is taken into cells by active transporters, L- α -glycerophosphate uptake system and glucose-6-phosphate uptake system¹³. Most chromosomally changed resistant organisms have impairments in one or both of these uptake systems, thus losing the ability to import fosfomycin into the cells⁴⁴.

ii) A decade after the first use of fosfomycin in the clinic, plasmid-mediated resistance was observed, consisting the inactivation of fosfomycin by fosfomycin resistance proteins^{39,54}. The analysis of the first enzyme (FosA) shown to inactivate fosfomycin revealed that the resistance was caused by adduct formation between fosfomycin and the sulfhydryl of glutathione, a reaction catalyzed by glutathione S-transferase^{47,48}. This reaction opens the epoxide ring to render fosfomycin inactive against MurA.

iii) Alteration of MurA Cys115 to an Asp residue has been found in *Mycobacterium* and *Chlamydiae* species, which show an innate resistance to fosfomycin^{53,55}. Studies of site-directed mutagenesis of Cys115 to Asp revealed retention of enzyme activity, but conferred resistance to fosfomycin⁵³. Since other organisms, *Actinomycetales*, *Actinomyces*, *Nocardia*, and *Streptomyces*, have Asp in place of MurA Cys115, it is expected that these organisms are also resistant to fosfomycin^{53,55}.

1.1.4. Inhibitors of MurA

As described in the previous section, fosfomycin is the most well-known inhibitor of MurA, also the only one used in the clinic. A number of novel inhibitors of MurA have been discovered through high-throughput screening (HTS) in the pharmaceutical industry. Three new inhibitors of MurA, compound 1, 2, and 3 in Figure 9, were identified with a submicromolar range of IC_{50} values ($IC_{50} = 0.2 - 0.9 \mu M$)⁵⁶. They showed UNAG-dependent and time-dependent inhibition, which suggests that these compounds may have similar modes of action as fosfomycin. However, they also showed nonspecific inhibition of DNA, RNA, and protein biosynthesis. From a whole-cell assay of peptidoglycan biosynthesis, a derivative of diarylmethane (compound 4) was identified as an inhibitor of MurA and showed the same pattern of MurA inhibition as fosfomycin⁵⁷. 4-alkyl and 4,4-bis-alkyl pyrazolidinedione derivatives (e.g. compound 5) were reported as inhibitors of MurA and MurB⁵⁸. Naphthyl tetronic acids were also identified as inhibitors targeting multiple Mur enzymes in the peptidoglycan biosynthetic pathway⁵⁹. The most potent compound (compound 6) in this group was active against both Gram-positive and Gram-negative bacteria in cell-based assays. Sesquiterpene lactones (e.g. compound 7) were shown to be irreversible inhibitors of *Pseudomonas aeruginosa* and *E. coli* MurA by alkylating Cys115⁶⁰. The sesquiterpene lactone compounds did not show inhibitory activity against Cys115Asp mutant MurA. A new series of inhibitors of MurA with 2-aminotetralone motif (compound 8) was recently discovered by screening, and a mode of action involving formation of a covalent adduct was proposed⁶¹.

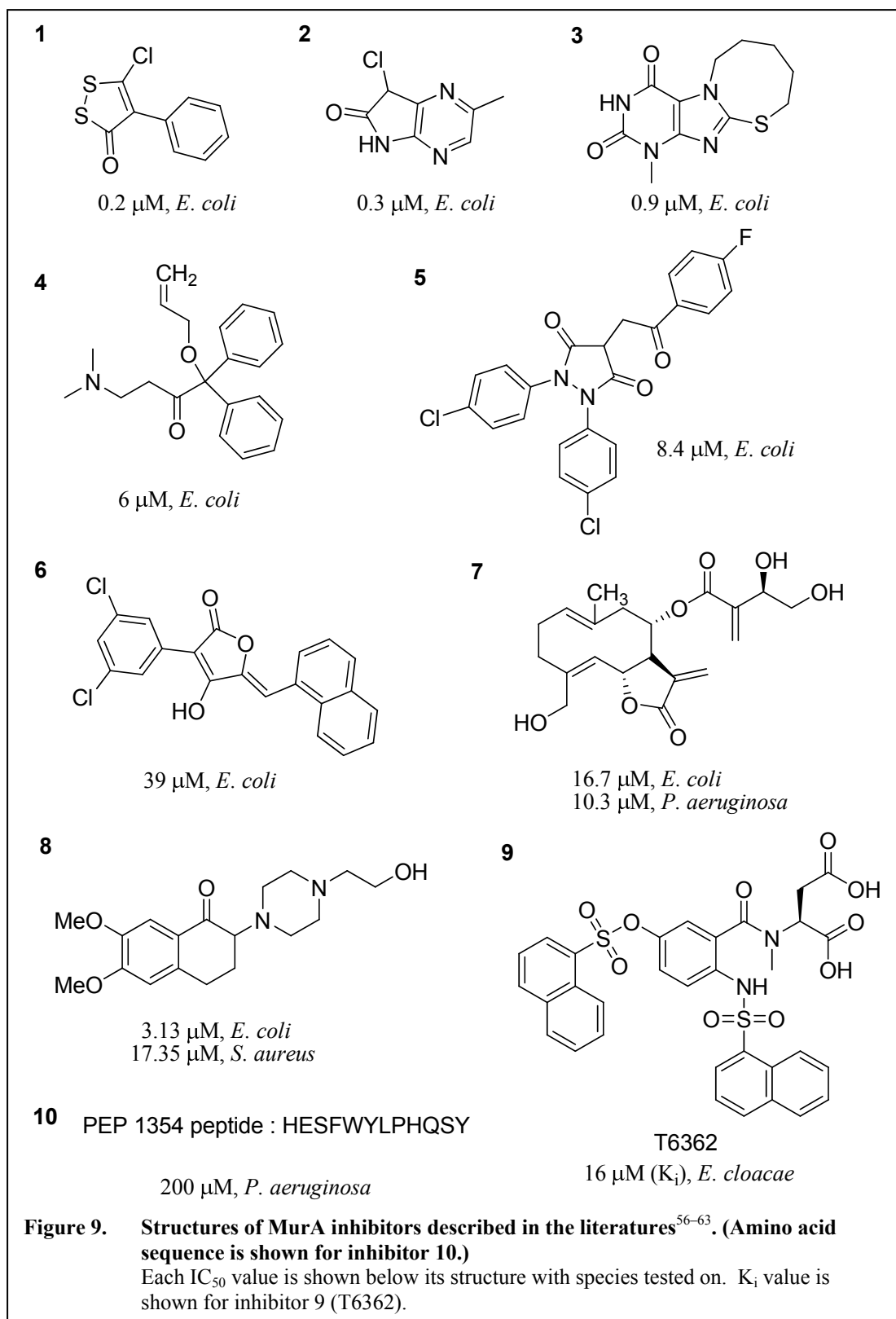


Figure 9. Structures of MurA inhibitors described in the literatures⁵⁶⁻⁶³. (Amino acid sequence is shown for inhibitor 10.) Each IC_{50} value is shown below its structure with species tested on. K_i value is shown for inhibitor 9 (T6362).

Compound 9 (T6362) discovered in Aventis was co-crystallized with MurA⁶². In the structure, the inhibitor bound on the loop in the open state of MurA. From the structural study along with kinetic analysis, it was found that the compound inhibits MurA by inhibiting the conformational change to the closed state. In addition to small molecule inhibitors, inhibitions of MurA by peptides and proteins have been discovered. A 12-mer peptide inhibitor (PEP 1354 peptide, 8 of Figure 9) of MurA was identified by phage display and showed a competitive inhibition to UNAG with an IC₅₀ value of 200 μ M for *Pseudomonas aeruginosa* MurA⁶³. A protein of RNA phage Q β (A₂) was reported to cause host cell lysis by inhibiting MurA⁶⁴. Although fosfomycin has remained the only MurA inhibitor on the market up to date, numerous efforts to find novel inhibitors of MurA, using accumulated mechanistic and structural information, are currently in progress.

1.2. Cyclin-dependent kinase 2

1.2.1. Cell Cycle and Cyclin-Dependent Kinase (CDK)

Many polypeptide chains released from a ribosome after translation often need posttranslational modification such as phosphorylation, attachment of fatty acids, or glycosylation^{65,66}. Reversible protein phosphorylation, principally on serine, threonine, or tyrosine residue, is one of the most important posttranslational modifications. The phosphorylation of a protein can change its function, leading to the gain or loss of catalytic activity, or increasing binding affinity to other proteins.

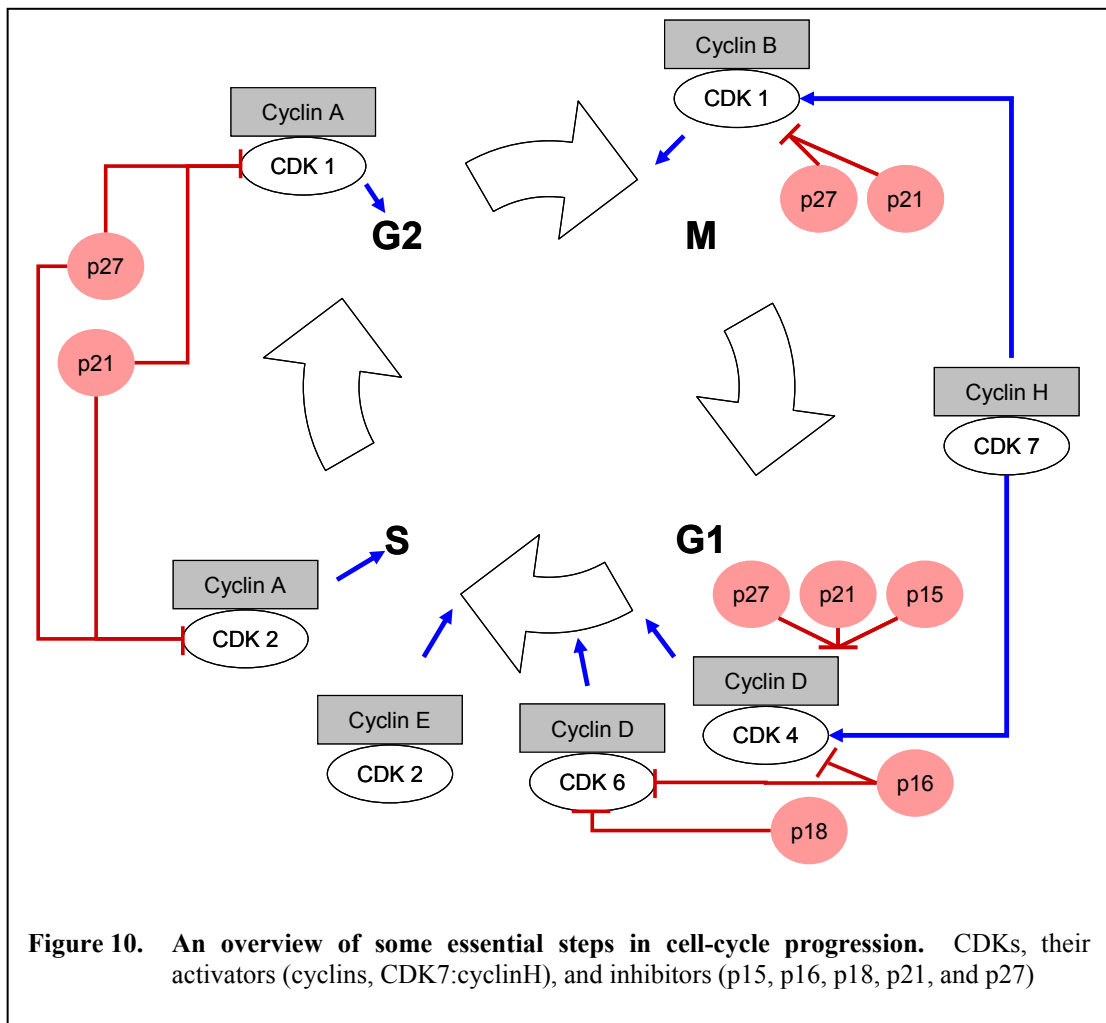
Thus, phosphorylation plays a critical role in the regulation of many cellular processes including cell cycle, growth, apoptosis, and signal transduction pathways⁶⁷. The enzymes catalyzing the phosphorylation are protein kinases. Protein kinases catalyze the transfer of a γ -phosphoryl group from ATP to the side chain hydroxyl (OH) of a serine, threonine, or tyrosine residue on a target protein. From the human genome project, genes for 518 protein kinases have been identified⁶⁸. These have been classified into 8 families based on the sequence of the catalytic domains and biological functions. The cyclin-dependent kinases (CDKs, EC 2.7.11.22), which are members of serine/threonine protein kinases, are categorized in the CMGC kinase family which is named an acronym of CDKs, mitogen-activated kinases, glycogen-synthase kinases, and CDK-like kinases.

CDKs are responsible for control of the cell cycle progression in proliferating eukaryotic cells. Currently, eleven CDKs have been identified^{69,70}. The CDK proteins have similar sizes of 30-40 kDa and share approximately 40% amino acid

Cyclin-dependent Kinase	Cyclin
CDK1	A, B
CDK2	A, E
CDK3	C
CDK4	D
CDK5	D
CDK6	D
CDK7	H
CDK8	C
CDK9	K, T
CDK11	L
unknown	F, G, I

sequence similarity. The activity of CDKs is closely associated with specific cyclins^{71,72}. The complexes of CDK and cyclin found to date are shown in Table 2. Each phase of the cell cycle is

characterized by the expression of different CDK-cyclin complexes^{70, 73}. Cyclins of the D family form complexes with CDK4 and 6 during the G1 phase⁷¹, cyclin E with CDK2 in late G1, cyclin A with CDK2 in S phase, and cyclin B with CDK1 during the transition from G2 to M phase^{74, 75}. Control of CDK activity in a cell cycle is accomplished by a number of mechanisms. CDKs are regulated by the formation of an active hetero-dimer complex with their cyclin partners. The CDKs are not catalytically active unless bound to a cyclin, resulting in a complex with basal catalytic activity. Concentrations of cyclin partners oscillate during the cell cycle and



are regulated by transcription, followed by ubiquitin-mediated degradation. Phosphorylation of the CDK at a conserved threonine residue (Thr160 in CDK2) by CDK-activating kinase (CAK, also known as CDK7) is required for full activity⁷⁶.

In addition to the positive role of cyclins and CAK on CDK activity, endogenous CDK inhibitors provide counteracting negative control⁷⁷⁻⁷⁹. There are two categories of CDK inhibitors defined by whether the inhibitor binds to CDK alone or CDK/cyclin complexes. The former category is termed the INK family, and p15, p16, p18, and p19 belong to this group of CDK inhibitors. These proteins bind to CDK and prevent formation of the complex with cyclins. CDK inhibitors in the latter category include p21, p27, and p57, and they bind to CDK/cyclin complexes (Figure 10).

Uncontrolled cell growth due to abnormal cell cycle progression is the basic feature of cancer. Thus, many of the cell cycle regulatory mechanisms have been found to be altered in cancerous tumor cells. Mutations and over-expression of cyclins, loss of the function of CDK inhibitors, and CDK substrate alterations are the hallmark of many different kinds of cancer, including lung cancer, colon cancer, breast cancer, B-cell and T-cell lymphoma, bladder cancer, and neuroblastoma⁸⁰. In particular, over-expression of cyclins D1 and E is often found in breast cancer and colon cancer^{81, 82}. Amplification and over-expression of CDK4 are also seen in various human cancers⁸³. One of the strategies for cancer treatment is to control the indiscriminate proliferation of tumor cells and arrest the cell cycle at the G1 or S phase. Inhibition of CDK activity with low molecular weight molecules could indeed

restore this cell-cycle control, and thus potentially help in combating cancer and its proliferation.

1.2.2. Structural Features of CDK2

Structural studies of CDKs have provided a detailed understanding of the activation of CDK by cyclin, ATP binding and phosphorylation. Almost 200 crystal

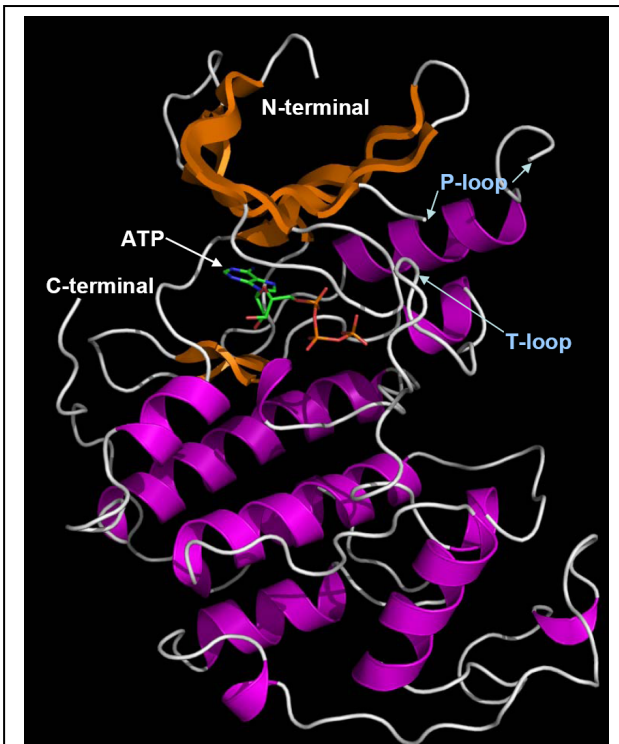
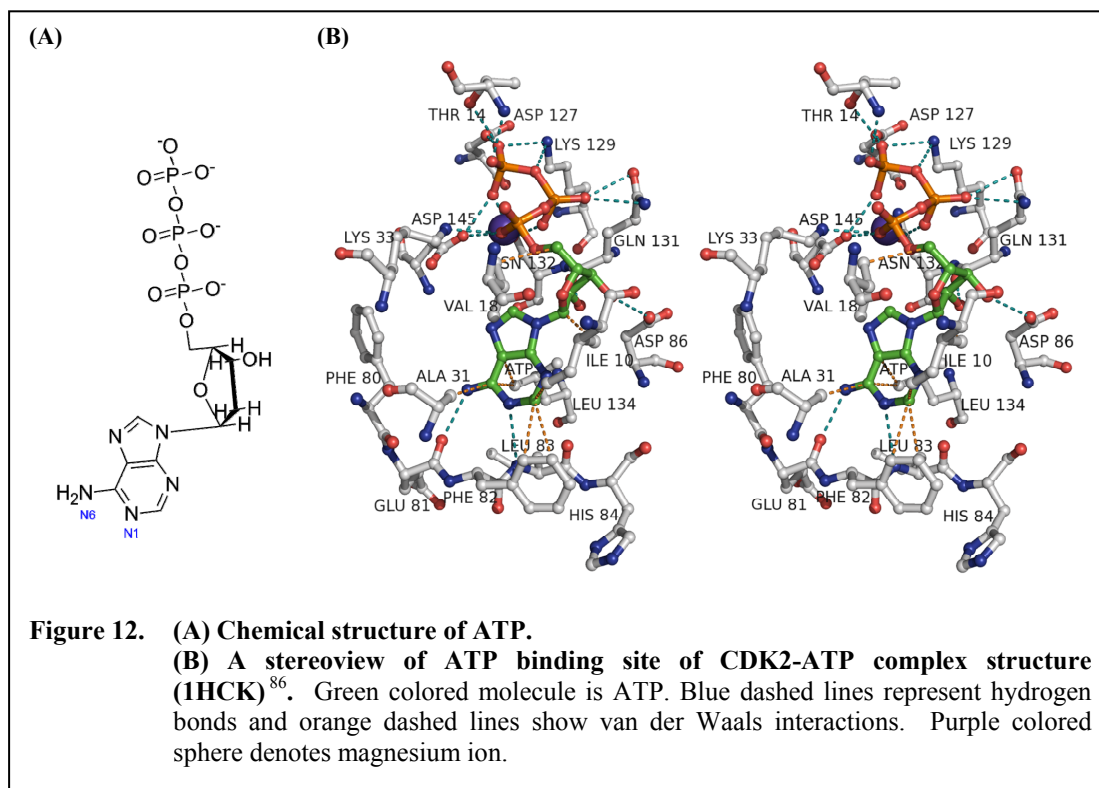


Figure 11. Overall structure of CDK2 with ATP. (PDB ID: 1HCK). The ATP binding site is located between C- and N-terminal. The P- and T-loops are flexible regions in the CDK2 structure and become rigid by the complex formation with cyclinA.

structures of CDKs have been released to date, with and without ions, cyclins, ATP, phosphorylated residues, or other ligands. Among these structural studies of CDKs, studies with CDK2 are the most abundant⁸⁴. CDK2 adopts a typical protein kinase fold. A smaller N-terminal domain consists principally of β -strands and one helix, and a larger C-terminal domain is primarily α -helical⁸⁵. The ATP binding site is

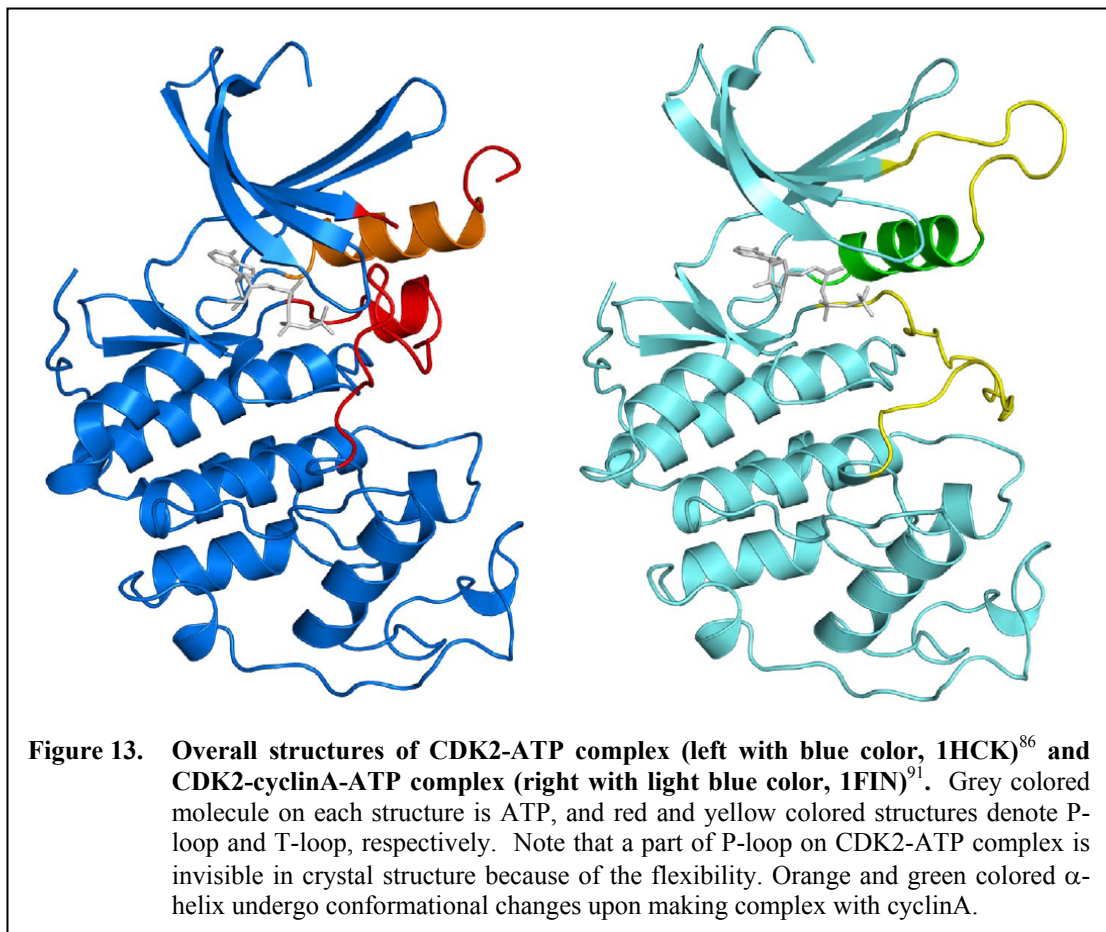
located at the interface of the two domains, and ATP binding to CDK2 induces a slight closure of the cleft (Figure 11). This ATP binding site can be divided into three regions: adenine, ribose, and phosphate binding regions, defined with reference to the chemical moieties in ATP. The adenine ring is located between Ala31 and Leu134

forming hydrophobic pockets by Ile10, Ala31, Val64, Phe80, Glu81, Phe82, Leu83, Leu134, and Ala144. In addition to the hydrophobic interactions, the N6 and N1 atoms of adenine form hydrogen bonds with the backbone carbonyl of Glu81 and the backbone NH of Leu83, respectively. The ribose ring of ATP has a hydrophobic interaction with Val18 while Asp86 and Gln131 make hydrogen bonds with its hydroxyl groups. The triphosphate component forms a hydrogen bond with Lys33 and contacts Asp145 and Asn132 by the mediation of a magnesium ion (Figure 12)⁸⁶.



In all structures of the CDK2 monomer, electron density is weakly and poorly defined in two regions, residues 36–47 corresponding to the cyclin recognition part (known as the P-loop) and residues 150–164 containing the phosphorylation site (the T-loop)^{86–89}. Binding of cyclin A to CDK2 induces significant structural changes to

CDK2, producing an optimized ATP binding site, while there is little structural change in cyclin A itself (Figure 13). This conformational change allows catalytically important residues to move into the correct positions in the active site, i.e. Glu51 and Lys33 coordinate to the α -phosphate of ATP and Asp145, Phe146, and Gly147 induce the correct conformation in the triphosphate moiety of ATP for catalytic transfer^{90,91}. Phosphorylation at Thr160 of CDK2 is required for full activity of the CDK2/cyclin A complex. The crystal structure of the CDK2 (phosphorylated Thr160)/cyclin A complex shows that the phosphorylation completes the structural changes in the active site by creating a peptide binding site. Phosphorylated Thr160



acts as an organizing center by interacting with Arg126, adjacent to the catalytic aspartate, Asp127^{89,90}.

1.2.3. CDK Inhibitors and Their Modes of Action

The development of CDK inhibitors has progressed rapidly, aided by the enlarged structural information of CDK2-ligand interactions from numerous crystal structure studies. All known CDK2 inhibitors target the ATP binding site. They compete with ATP for inhibition and interact with CDK2 in the same manner as ATP, i.e. by making hydrogen bonds with backbone of Glu81 and Leu83, and hydrophobic interactions with Ala31 and Leu134^{88,92-107}. Several classes of inhibitors based on their scaffolds have been developed and successfully modified to improve their potency as CDK2 inhibitors (Figures 14 and 15). Some of them have shown moderate selectivity.

As it will be discussed in detail in the following paragraphs, substantial efforts have led to the discovery of several different classes of CDK inhibitors with excellent potency. First-generation CDK inhibitors, UCN-01 and flavopiridol, are in late stages of clinical trials for cancer treatment, and several second-generation inhibitors such as roscovitin, E7070, and aminothiazole, are also being evaluated in clinical trials and showing promising results. However, inhibitors selective for a single CDK have yet to be identified. This could be due to the conservation of the ATP binding pocket of CDKs. CDK inhibitors can be subdivided into three main classes based on their selectivity^{108,109}: i) compounds that are not selective for any specific CDK (e.g. flavopiridol and oxindole (7)), ii) compounds that inhibit CDK1, 2, 5 (e.g.

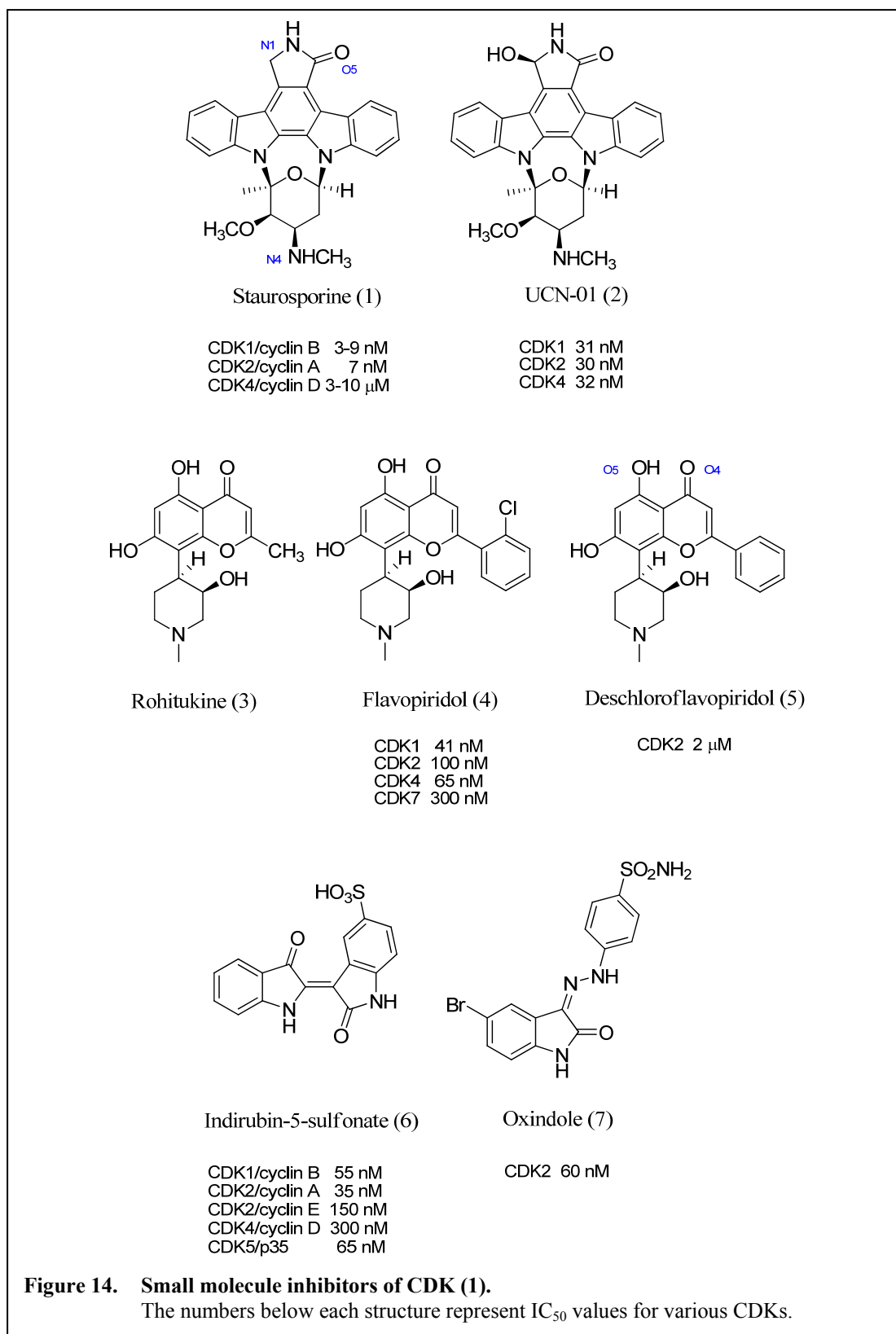


Figure 14. Small molecule inhibitors of CDK (1).
 The numbers below each structure represent IC₅₀ values for various CDKs.

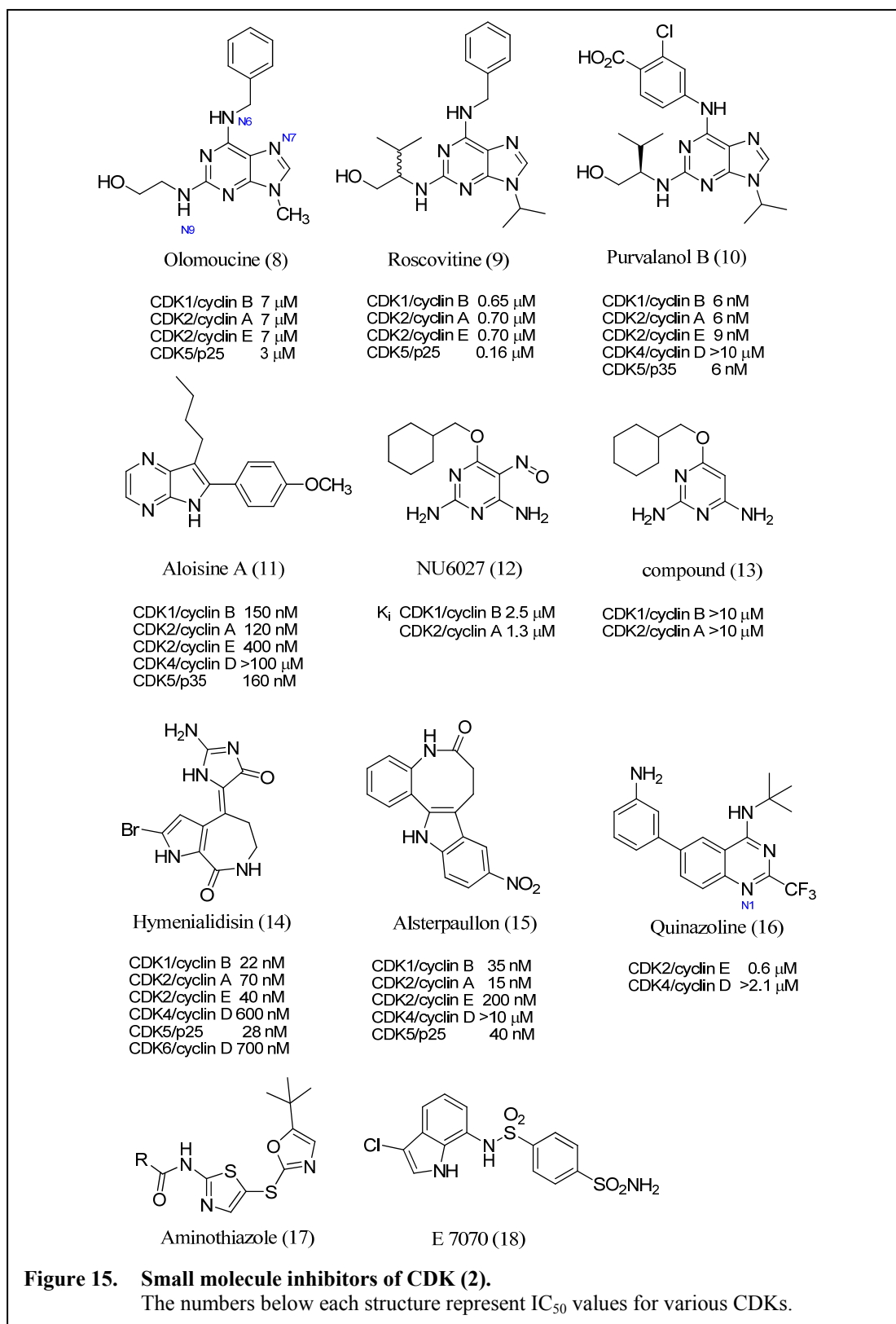
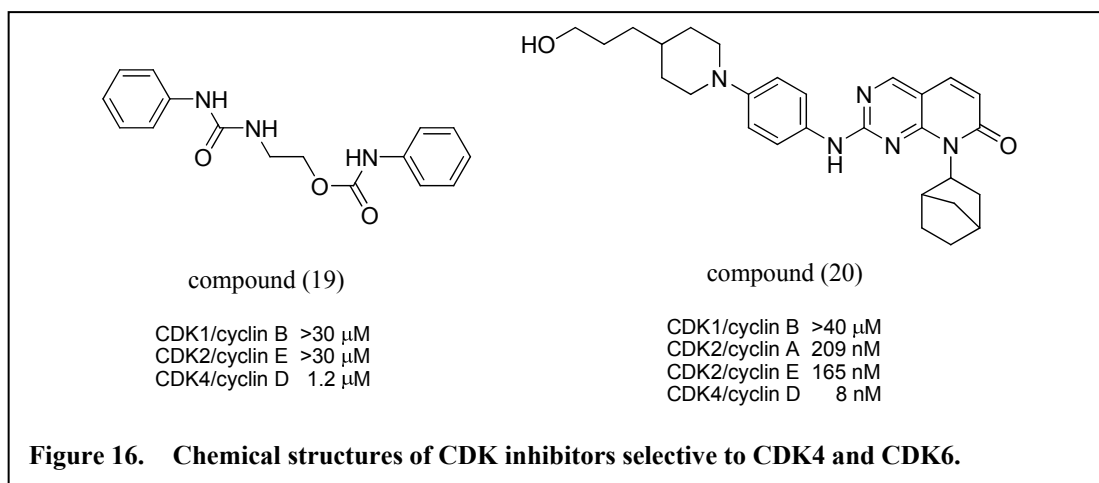


Figure 15. Small molecule inhibitors of CDK (2).
The numbers below each structure represent IC₅₀ values for various CDKs.



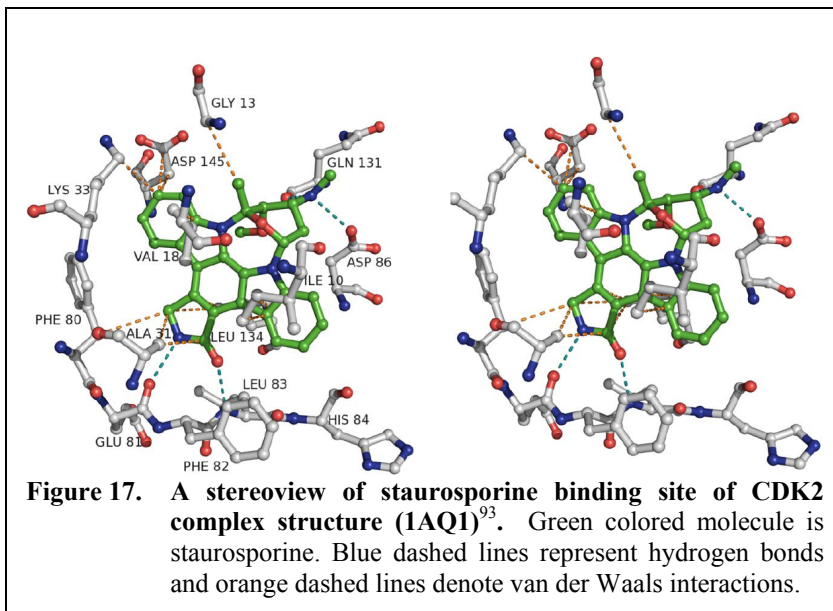
olomoucine, roscovitine, purvalanol, hymenialdisine, indirubin-5-sulfonate, and alsterpaullone), and iii) compounds that are selective for CDK4 and 6 (e.g. compounds 19 and 20 in Figure 16).

Selectivity is a key issue for CDK inhibitors because of the toxicity and inhibition of specific cancer types. The toxicities resulting from targeting specific CDKs restrict the use of inhibitors to certain cell types, for example, pituitary or pancreatic β cells for CDK4 inhibitors due to reduced proliferation of endocrine or erythroid cells, and germ cells for CDK2 inhibitors due to sterility. Inhibitors targeting specific CDKs show inhibition of certain types of tumor cells. For example, CDK4 inhibition is efficient on Her2-positive mammary gland tumors but not on MYC-induced breast carcinomas, and CDK1 inhibition by purvalanol shows cytotoxic effects in MYC-overexpressing cells but not in oncogene-type cells.

1) The first small molecule inhibitors of CDKs is Staurosporine, a metabolite from *Streptomyces sp.*, which has attracted considerable attention since it was characterized as a potent inhibitor of protein kinase C ($IC_{50} = 1$ nM)^{110, 111}. It was

later found that staurosporine is a nonspecific inhibitor of a number of protein kinases with IC_{50} values of 1 – 100 nM range. Some staurosporine derivatives are more selective protein kinase inhibitors and show anti-tumor activities in various human cancer cell lines^{112, 113}. Among them, UCN-01, also isolated from *Streptomyces*, is

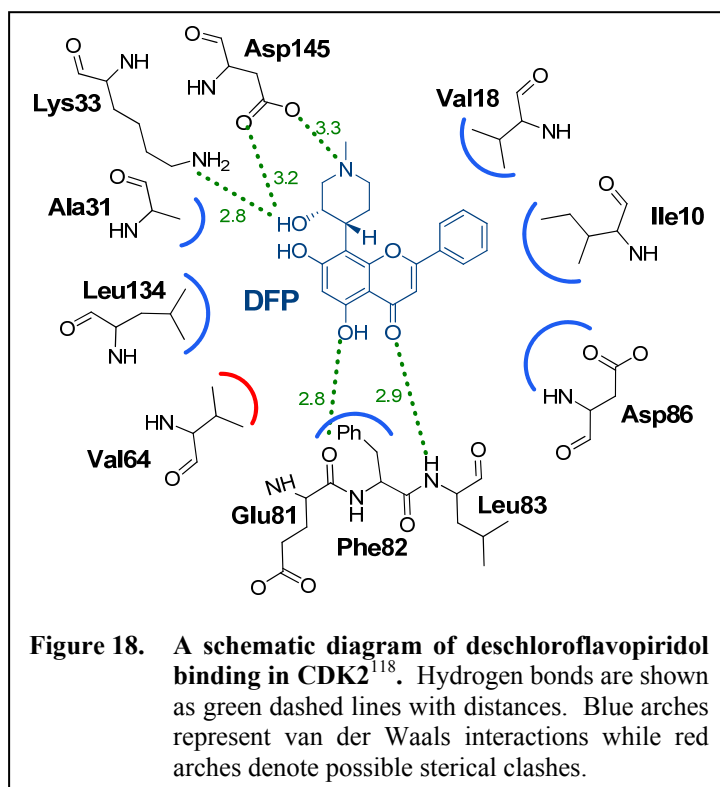
currently under-going clinical trials for cancer treatment¹¹⁴. *In vitro*, UCN-01 is effective in cell cycle regulation by inhibiting CDK2, CDK4,



and CDK6 with IC_{50} values of 30, 32, and 58 nM, respectively. In the crystal structure of the CDK2/staurosporine complex (Figure 17), staurosporine binds to the ATP binding site⁹³. The N1 atom of staurosporine makes a hydrogen bond with the backbone carbonyl of Glu81 and the O5 atom with the backbone NH of Leu83, mimicking the hydrogen bonds by ATP to CDK2. In addition, N4 of the glycosyl portion in staurosporine forms additional hydrogen bonds with the side chain oxygen of Asp86 and the backbone carbonyl of Gln131. The fused aromatic ring in staurosporine makes significant hydrophobic interactions with CDK2. The residues of CDK2 contributing to hydrophobic contacts with staurosporine include Ile10,

Gly11, Val18, Ala31, Lys33, Val64, Phe80, Phe82, Asp86, Gln131, Leu134, Ala144, and Asp145.

2) The second class of compounds extensively studied as inhibitors of CDKs are



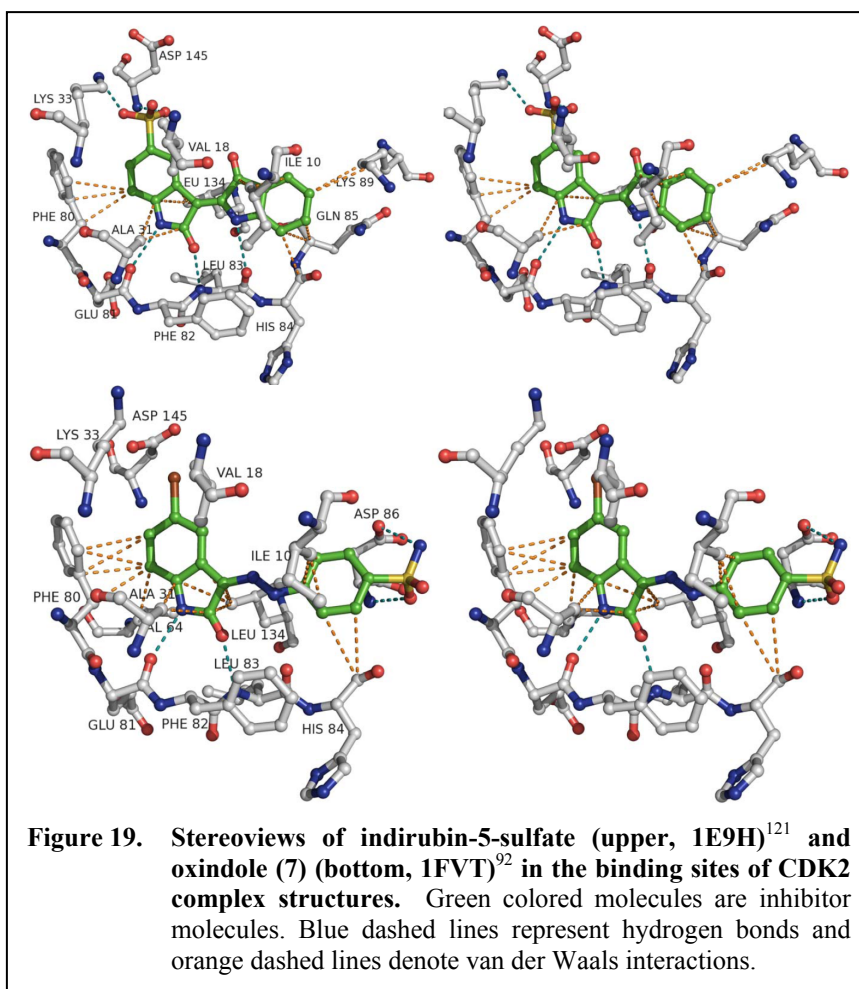
flavones. Flavopiridol and deschloroflavopiridol are synthetic flavonoid analogs of a natural alkaloid, rohitukine, extracted from the stem-bark of the plant *Dysoxylum binactariferum*. Flavopiridol is the first CDK inhibitor to enter clinical trials for cancer treatment due to its

antiproliferative properties¹¹⁵⁻¹¹⁷. Flavopiridol is active against a number of protein kinases, but it is most active against CDK/cyclin complexes with IC₅₀ values up to 100 nM. The X-ray crystal structure of CDK2/deschloroflavopiridol reveals the inhibition mode of action of deschloroflavopiridol (Figure 18)¹¹⁸. Deschloroflavopiridol binds in the ATP binding site of CDK2 with the benzopyran ring of deschloroflavopiridol occupying the same position as the adenine of ATP. The O5 hydroxyl group and O4 of deschloroflavopiridol form hydrogen bonds with the backbone carbonyl of Glu81 and the backbone NH of Leu83, respectively. The

phenyl ring of deschloroflavopiridol points toward the outside of the ATP binding site, i.e. the solvent exposed space. The piperidinyl ring occupies a part of the phosphate binding pocket of CDK2. The flavopiridol molecule has an additional chlorine atom on the phenyl ring of deschloroflavopiridol, and this difference results in an increased inhibitory potency by a factor of 10. This is probably due to the new interactions that the chloro group is able to make with Ile10, Phe82, and Leu83. This area is conserved between CDKs, but not in protein kinase A, and thus protein kinase A is not potently inhibited by flavopiridol¹¹⁹.

3) Indirubins are CDK inhibitors which belong to the oxindole class. Oxindoles have been used in traditional Chinese medicine for the treatment of chronic myelocytic leukemia¹²⁰. Indirubin analogs such as indirubin-5-sulfate have shown good inhibitory potency for CDK1, CDK2, CDK4, and CDK5 compared to other protein kinases¹⁰⁰. The crystal structures of CDK2 complexed with indirubin-5-sulfate (1E9H)¹²¹ and oxindole (7 in Figure 14, 1FVT)⁹² show that both derivatives bind to the ATP binding site in a similar fashion (Figure 19). The amide nitrogen of lactam acts as a hydrogen bond donor to the backbone carbonyl of Glu81, and the amide oxygen of lactam forms a hydrogen bond with the backbone NH of Leu83. In addition to these two hydrogen bonds, the indole NH of oxindole donates a hydrogen bond to the backbone carbonyl of Leu83. In the structures, it is shown that oxindoles make an additional interaction with Phe80, which is not seen in the ATP binding to CDK2. The sulfate group of indirubin-5-sulfate induces a conformational change of Asp145 and Phe146 to avoid possible steric hindrance. This makes CDK2 adopt a

conformation similar to the one it adopts when bound to cyclin A. Also, the sulfate group makes additional ionic interactions with Lys33 and Asp145, which may explain the increased potency of



indirubin sulfate ($IC_{50} = 35$ nM for CDK2/cyclinA), compared to the indirubin without the sulfate group ($IC_{50} = 2.2$ μ M for CDK2/cyclinA). In the crystal structure of oxindole (compound 7 in Figure 14) bound to CDK2, one of the sulfonamide oxygens accepts a hydrogen bond from the backbone NH of Asp86 and the sulfonamide NH donates a hydrogen bond to the side chain of Asp86. It is likely that these interactions of the sulfonamide contribute to the high inhibitory potency of oxindole (compound 7)¹¹⁹.

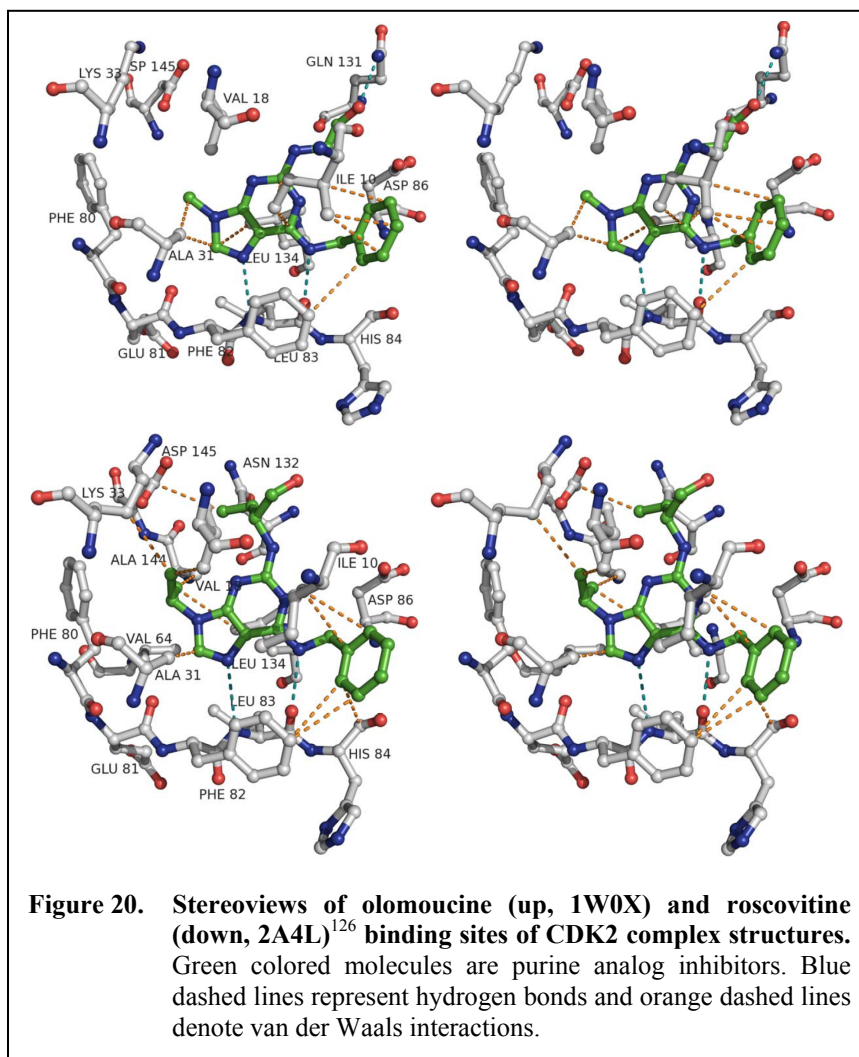
4) The CDK inhibitors of purine derivatives have been identified by screening. The compound olomoucine represents the initial purine analogous inhibitor¹²².

Olomoucine

inhibits CDK1, CDK2, and CDK5 but does not inhibit CDK4 or CDK6¹²³.

Roscovitrine is the most promising drug candidate in this group of CDK inhibitors.

Roscovitrine was identified

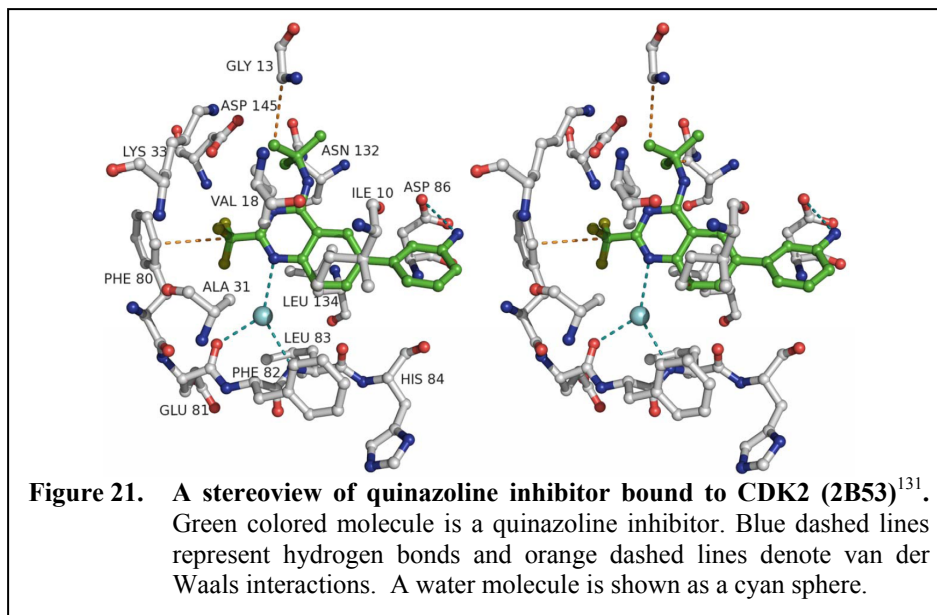


through a series of structure-activity relationship (SAR) studies, and it is currently in clinical trials^{124, 125}. In the structure of the complexes of CDK2 with olomoucine (1W0X) and roscovitrine (2A4L)¹²⁶, there are no significant differences compared to the ATP bound CDK2 structure (Figure 20). N6 of the purine ring makes a hydrogen bond with the backbone carbonyl oxygen of Leu83 and N7 with the backbone NH of

Leu83. The benzyl ring of olomoucine and roscovitine occupies space outside the ATP binding site forming hydrophobic interactions with Ile10, Phe82, and His84. The hydroxyl alkyl chain is located in the ribose binding pocket, and the alkyl group on N9 occupies the space near Lys33. Combinatorial chemistry has assisted in the discovery of CDK inhibitors with purine scaffolds that possess excellent potency^{94, 127, 128}. Purvanalol B was identified from a pool of compounds prepared by combinatorial chemistry, and it inhibits CDK2/cyclin A with a 1000-fold better potency than olomoucine ($IC_{50} = 6 \text{ nM}$)⁹⁴.

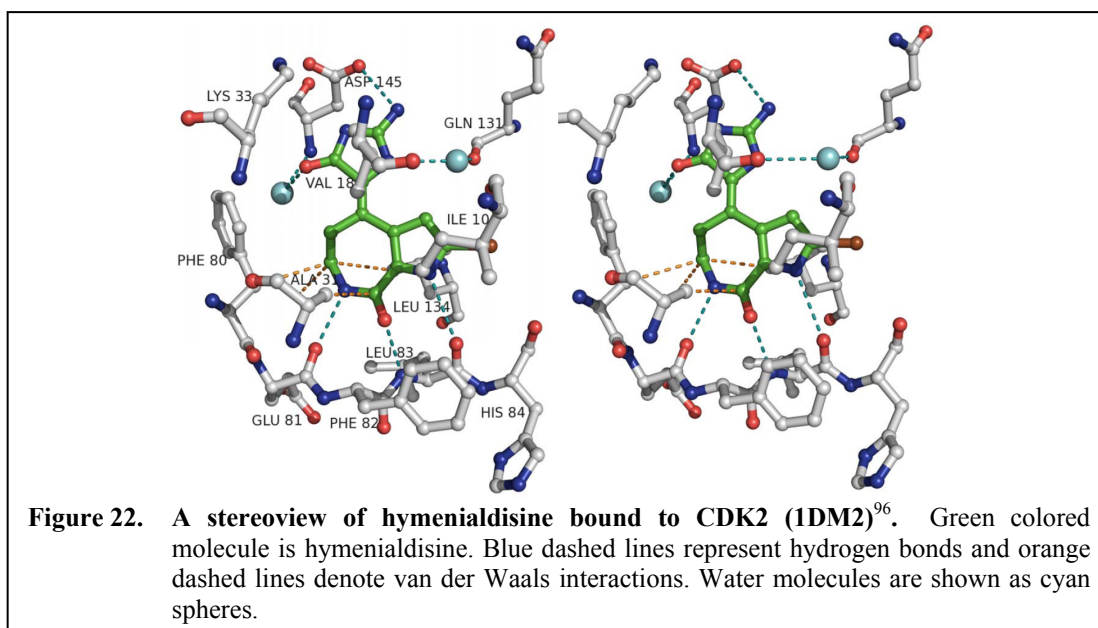
5) The pyrimidine class inhibitor, NU6027, was designed as an alternative to purine derivative inhibitors^{129, 130}. NU6027 maintains three hydrogen bonds with backbone Leu83 and Glu81. The purpose of the 5-nitroso group was to provide an intramolecular interaction with NH_2 on the 6-position, thus assisting the hydrogen atom of the NH_2 to be located on the correct position for a hydrogen bond with the backbone oxygen of Glu81. The concept of the design of NU6027 was supported by a study with compound 13 (Figure 15), which does not have the nitroso group and shows no inhibitory activity.

6) Quinazoline compounds were found through screening to be CDK inhibitors^{95, 131}. In the crystal structure of compound 16 (Figure 15) (2B53)¹³¹, the inhibitor is found in the ATP binding site of the enzyme (Figure 21). Interestingly, the hydrogen bonds between the inhibitor and the backbone of CDK2 are bridged with a water molecule, i.e. N1 of quinazoline has a hydrogen bond with a water



molecule and the water molecule forms hydrogen bonds with the backbone carbonyl oxygen of Glu81 and the backbone nitrogen of Leu83.

7) Hymenialdisine (compound 14 in Figure 15), the natural product isolated from a marine sponge, was found to have inhibitory potency against CDK1, CDK2, and CDK5, as well as glycogen synthase 3 β (GSK3 β)⁹⁶. In the crystal structure of hymenialdisine bound to CDK2 (1DM2)⁹⁶, three hydrogen bonds between the inhibitor and backbone of CDK2 were observed (Figure 22). The nitrogen atom of the pyrrole ring makes a hydrogen bond with the backbone oxygen of Leu83, and the amide of azepine have hydrogen bonds with the backbone nitrogen of Leu83 and the backbone carbonyl of Glu81. In addition, the guanidine ring makes direct hydrogen bonds to one of the side chain oxygen atoms of Asp145 and two more hydrogen bonds through water molecules to the backbone nitrogen of Asp145 and to the backbone carbonyl of Gln131.



8) The Paullone class of compounds were identified as CDK inhibitors from the analysis of the NCI compound collection^{132, 133}. The most potent inhibitor of this group is a nitro derivative, alsterpaullon, inhibiting CDK2/cyclin A with a 15 nM IC₅₀ value¹³³. Paullones show good potency for CDK1, CDK2, and CDK5, but show no inhibition against CDK4.

Although the studies of CDK were initially directed towards anticancer therapies, CDK inhibitors are currently being evaluated in multiple therapeutic areas, such as nervous systems, viral infections, cardiovascular diseases, reproduction, and protozoan diseases, and it seems likely that other therapeutic indications may yet be discovered. Thus, the discovery of novel CDK inhibitors with better selectivity would provide the next generation of CDK inhibitors that are effective on specific diseases as well as cancer.

2. Materials and Methods

2.1. General Materials

2.1.1. Competent Cells

Competent cell strains used: BL21(DE3) (Stratagene, La Jolla, CA) and DH5 α (Invitrogen, Carlsbad, CA).

2.1.2. Chemicals

A Labconco Water Pure Plus System (Kansas City, MO) was used to purify H₂O used for all research. All biochemical reagents were purchased from Sigma (St. Louis, MO) or Fisher (Springfield, NJ) unless otherwise noted.

2.1.3. Solutions

2.1.3.1. Media

All media was autoclaved and stored at 4 °C. Antibiotic stocks were added to the media prior to use.

Luria Bertani (LB):

10 g tryptone

5 g yeast extract

10 g NaCl

Fill to 1 L with H₂O

2.1.3.2. Antibiotics

Ampicillin (Amp, Fisher) at 100 mg/mL and kanamycin (Kan, Fisher) at 30 mg/mL were sterile filtered with a 0.45 µm filter and stored at -20 °C. Antibiotics were used as a 1:1000 dilution unless otherwise mentioned.

2.1.3.3. DNA Electrophoresis

A 50× concentrated stock solution of TAE was stored at room temperature and diluted before the use. The protocol for DNA gel is following: 500 mg of agarose in 50 mL of 1× TAE was heated with microwave until dissolved, 1 µL of ethidium bromide (5 mg/mL) was added to the solution and the gel was cast.

50× TAE (1L):

242 g Tris (pH 8.5)

57.1 mL glacial acetic acid

100 mL 0.5 M EDTA (pH 8.0)

Fill to 1 L with H₂O

Molecular ladder (Cambrex Bio Science, Rockland, ME) was prepared by adding 5 µL marker and 2 µL 10× Blue-juice (Invitrogen) to 3 µL H₂O. The DNA ladder corresponded to 10, 7, 5, 4, 3, 2.5, 2, 1.5, and 1 Kb markers.

2.1.3.4. SDS Electrophoresis

SDS-PAGE running buffer was prepared as a 10× concentrated solution and diluted prior to use. Coomassie stain was filtered with a Nalgene PES filter with 75 µm membrane size and stored in a bottle wrapped with aluminum foil at room temperature. 30 % Acrylamide/bisacrylamide, 10 % APS (Biorad, Hercules CA), TEMED (Biorad) and Tris buffers were stored at 4 °C. All other solutions were stored at room temperature. SDS-PAGE gels were made according to the following protocol and stored at 4 °C for up to 2 weeks.

Resolving SDS gel portion (1 gel):

4 mL 30 % acrylamide/bisacrylamide

100 µL 10% SDS

2.5 mL 1.5 M Tris (pH 8.8)

3.36 mL water

80 µL 10 % APS

10.0 µL TEMED

Stacking SDS gel portion (1 gel):

650 µL 30 % acrylamide/bisacrylamide

50 µL 10 % SDS

1.25 mL 0.5 M Tris (pH 6.8)

3.05 mL water

40 µL 10 % APS

5 µL TEMED

30 % Acrylamide/bisacrylamide (500 mL):

150 g acrylamide

4 g bisacrylamide

Fill to 500 mL with H₂O

10× SDS Running buffer (1L):

30 g Tris (pH 8.5)

144 g glycine

10 g SDS

Fill to 1 L with H₂O

Destaining solution (1L):

500 mL ethanol

100 mL acetic acid

400 mL H₂O

5× Treatment buffer:

300 mM Tris (pH 8.5)

10 % SDS

4 mL H₂O

Coomassie stain (1L):

1.25 g Coomassie brilliant blue R-250

500 mL 95 % ethanol

450 mL H₂O

50 mL 100 % acetic acid

25 % β-mercaptoethanol

50 % glycerol

282 mM HCl

0.05 % bromophenol blue

SDS low range marker (Biorad):

Protein Molecular marker was prepared by adding 50 μL concentrated marker and 100 μL 5× treatment buffer to 350 μL H₂O and heating the solution at 100 °C for 5 min. Marker was stored at -20 °C. The molecular weights in the marker corresponded to 97.4, 66.2, 45, 31, 21.5, and 14.4 kDa.

2.1.3.5. FPLC Buffers

All buffers for protein purification were filtered with a 0.45 μm filter and stored at 4 °C.

Buffer A:

50 mM Tris (pH 7.8)

1 mM DTT

1 mM EDTA

Buffer A + 0.4M NaCl:

50 mM Tris (pH 7.8)

0.4 M NaCl

1 mM DTT

1 mM EDTA

Buffer A + 1M (NH₄)₂SO₄:

50 mM Tris (pH 7.8)

1 M (NH₄)₂SO₄

1 mM DTT

1 mM EDTA

Buffer A (CDK-GST 1)

50 mM HEPES (pH 7.5)

150 mM NaCl

1 mM EGTA

10 mM MgCl₂

2 mM DTT

Buffer A (CDK-GST 1) + glutathione

50 mM HEPES (pH 7.5)

150 mM NaCl

1 mM EGTA

10 mM MgCl₂

2 mM DTT

10 mM glutathione, reduced

<u>Buffer A (CDK-GST 2)</u>	<u>Buffer A (CDK-GST 2) + glutathione</u>
50 mM HEPES (pH 7.5)	50 mM HEPES (pH 7.5)
150 mM NaCl	150 mM NaCl
1 mM EGTA	1 mM EGTA
10 mM MgCl ₂	10 mM MgCl ₂
2 mM DTT	2 mM DTT
0.01 mM ADP	0.01 mM ADP
	10 mM glutathione, reduced

2.1.3.6. Lanzetta Reagent

Lanzetta reagent was prepared by using plastic-ware to avoid phosphate contamination from glass. The following protocol was used: 5.25 g ammonium molybdate was dissolved in 41 mL of 12 M HCl and added to a solution containing 169 mg malachite green in 375 mL H₂O. This solution was stirred for 2 - 4 hrs, filtered using a Nalgene PES filter with 75 µm pore size and stored at room temperature wrapped in aluminium foil.

2.1.3.7. Crystallization Solutions

For crystallization screening, Hampton 1 and 2 (Tables 3 and 4, Hampton Research, Aliso Viejo, CA), and Wizard 1 and 2 (Tables 5 and 6, Emerald Biosciences, Cambridge, MA) screening solutions were purchased.

Table 3. Crystallization buffers for Hampton crystallization screen #1.

	Salt	Buffer	Precipitant
1	0.02 M CaCl ₂ · 2H ₂ O	0.1 M NaOAc · 3H ₂ O pH 4.6	30% v/v MPD
2	None	None	0.4 M K/Na tartrate · 2H ₂ O
3	None	None	0.4 M (NH ₄) ₂ PO ₄
4	None	0.1 M TRIS · HCl pH 8.5	2.0 M (NH ₄) ₂ SO ₄
5	0.2 M Na ₃ citrate · 2H ₂ O	0.1 M HEPES · Na pH 7.5	30% v/v MPD
6	0.2 M MgCl ₂ · 6H ₂ O	0.1 M TRIS · HCl pH 8.5	30% w/v PEG4,000
7	None	0.1 M Na cacodylate pH 6.5	1.4 M NaOAc · 3H ₂ O
8	0.2 M Na ₃ citrate · 2H ₂ O	0.1 M Na cacodylate pH 6.5	30% v/v 2-Propanol
9	0.2 M NH ₄ OAc	0.1 M Na ₃ citrate · 2H ₂ O pH 5.6	30% w/v PEG4,000
10	0.2 M NH ₄ OAc	0.1 M NaOAc · 3H ₂ O pH 4.6	30% w/v PEG4,000
11	None	0.1 M Na ₃ citrate · 2H ₂ O pH 5.6	1.0 M (NH ₄) ₂ PO ₄
12	0.2 M MgCl ₂ · 6H ₂ O	0.1 M HEPES · Na pH 7.5	30% v/v 2-Propanol
13	0.2 M Na ₃ citrate · 2H ₂ O	0.1 M TRIS · HCl pH 8.5	30% v/v PEG400
14	0.2 M CaCl ₂ · 2H ₂ O	0.1 M HEPES · Na pH 7.5	28% v/v PEG400
15	0.2 M (NH ₄) ₂ SO ₄	0.1 M Na cacodylate pH 6.5	30% w/v PEG8,000
16	None	0.1 M HEPES · Na pH 7.5	1.5 M Li ₂ SO ₄ · H ₂ O
17	0.2 M Li ₂ SO ₄ · H ₂ O	0.1 M TRIS · HCl pH 8.5	30% w/v PEG4,000
18	0.2 M Mg(OAc) ₂ · 4H ₂ O	0.1 M Na cacodylate pH 6.5	20% w/v PEG8,000
19	0.2 M NH ₄ OAc	0.1 M TRIS · HCl pH 8.5	30% v/v 2-Propanol
20	0.2 M (NH ₄) ₂ SO ₄	0.1 M NaOAc · 3H ₂ O pH 4.6	25% w/v PEG4,000
21	0.2 M Mg(OAc) ₂ · 4H ₂ O	0.1 M Na cacodylate pH 6.5	30% v/v MPD
22	0.2 M NaOAc · 3H ₂ O	0.1 M TRIS · HCl pH 8.5	30% w/v PEG4,000
23	0.2 M MgCl ₂ · 6H ₂ O	0.1 M HEPES · Na pH 7.5	30% v/v PEG400
24	0.2 M CaCl ₂ · 2H ₂ O	0.1 M NaOAc · 3H ₂ O pH 4.6	20% v/v 2-Propanol
25	None	0.1 M Imidazole pH 6.5	1.0 M NaOAc · 3H ₂ O
26	0.2 M NH ₄ OAc	0.1 M Na ₃ citrate 2H ₂ O pH 5.6	30% v/v MPD
27	0.2 M Na ₃ citrate · 2H ₂ O	0.1 M HEPES · Na pH 7.5	20% v/v 2-Propanol
28	0.2 M NaOAc · 3H ₂ O	0.1 M Na cacodylate pH 6.5	30% w/v PEG8,000
29	None	0.1 M HEPES · Na pH 7.5	0.8 M K/Na tartrate 2H ₂ O
30	0.2 M (NH ₄) ₂ SO ₄	None	30% w/v PEG8,000
31	0.2 M (NH ₄) ₂ SO ₄	None	30% w/v PEG4,000
32	None	None	2.0 M (NH ₄) ₂ SO ₄
33	None	None	4.0 M Na formate
34	None	0.1 M NaOAc · 3H ₂ O pH 4.6	2.0 M Na formate
35	None	0.1 M HEPES · Na pH 7.5	0.8 M NaH ₂ PO ₄ · H ₂ O 0.8 M KH ₂ PO ₄
36	None	0.1 M TRIS · HCl pH 8.5	8% w/v PEG8,000
37	None	0.1 M NaOAc · 3H ₂ O pH 4.6	8% w/v PEG4,000
38	None	0.1 M HEPES · Na pH 7.5	1.4 M Na ₃ citrate · 2H ₂ O
39	None	0.1 M HEPES · Na pH 7.5	2% v/v PEG400 2.0 M (NH ₄) ₂ SO ₄
40	None	0.1 M Na ₃ citrate · 2H ₂ O pH 5.6	20% v/v 2-Propanol 20% w/v PEG4,000
41	None	0.1 M HEPES · Na pH 7.5	10% v/v 2-Propanol 20% w/v PEG4,000
42	0.05 M KH ₂ PO ₄	None	20% w/v PEG8,000
43	None	None	30% w/v PEG1,500
44	None	None	0.2 M Mg formate
45	0.2 M Zn(OAc) ₂ · 2H ₂ O	0.1 M Na cacodylate pH 6.5	18% w/v PEG8,000
46	0.2 M Ca(OAc) ₂ · H ₂ O	0.1 M Na cacodylate pH 6.5	18% w/v PEG8,000
47	None	0.1 M NaOAc · 3H ₂ O pH 4.6	2.0 M (NH ₄) ₂ SO ₄
48	None	0.1 M TRIS · HCl pH 8.5	2.0 M (NH ₄) ₂ PO ₄
49	1.0 M Li ₂ SO ₄ · H ₂ O	None	2% w/v PEG8,000
50	0.5 M Li ₂ SO ₄ · H ₂ O	None	15% w/v PEG8,000

Table 4. Crystallization buffers for Hampton crystallization screen #2.

	Salt	Buffer	Precipitant
1	2.0 M NaCl	None	10% w/v PEG 6,000
2	0.5 M NaCl 0.01 M MgCl ₂ · 6(H ₂ O)	None	0.01 M CH ₃ (CH ₂) ₁₅ N(Br)(CH ₃) ₃
3	None	None	25% v/v Ethylene glycol
4	None	None	35% v/v 1,4-Dioxane
5	2.0 M (NH ₄) ₂ SO ₄	None	5% v/v 2-Propanol
6	None	None	1.0 M Imidazole pH 7.0
7	None	None	10% w/v PEG 1,000 10% w/v PEG 8,000
8	1.5 M NaCl	None	10% v/v Ethanol
9	None	0.1 M NaOAc · 3H ₂ O pH 4.6	2.0 M NaCl
10	0.2 M NaCl	0.1 M NaOAc · 3H ₂ O pH 4.6	30% v/v MPD
11	0.01 M CoCl ₂ · 6H ₂ O	0.1 M NaOAc · 3H ₂ O pH 4.6	1.0 M 1,6-Hexanediol
12	0.1 M CdCl ₂ · H ₂ O	0.1 M NaOAc · 3H ₂ O pH 4.6	30% v/v PEG 400
13	0.2 M (NH ₄) ₂ SO ₄	0.1 M NaOAc · 3H ₂ O pH 4.6	30% w/v PEG MME 2,000
14	0.2 M K Na tartrate · 4H ₂ O	0.1 M Na ₃ citrate · 2H ₂ O pH 5.6	2.0 M (NH ₄) ₂ SO ₄
15	0.5 M (NH ₄) ₂ SO ₄	0.1 M Na ₃ citrate · 2H ₂ O pH 5.6	1.0 M Li ₂ SO ₄ · H ₂ O
16	0.5 M NaCl	0.1 M Na ₃ citrate · 2H ₂ O pH 5.6	2% v/v Ethylene imine polymer
17	None	0.1 M Na ₃ citrate · 2H ₂ O pH 5.6	35% v/v tert-Butanol
18	0.01 M FeCl ₃ · 6H ₂ O	0.1 M Na ₃ citrate · 2H ₂ O pH 5.6	10% v/v Jeffamine M-600
19	None	0.1 M Na ₃ citrate · 2H ₂ O pH 5.6	2.5 M 1,6-Hexanediol
20	None	0.1 M MES · H ₂ O pH 6.5	1.6 M MgSO ₄ · 6H ₂ O
21	0.1 M NaH ₂ PO ₄ · H ₂ O 0.1 M KH ₂ PO ₄	0.1 M MES · H ₂ O pH 6.5	2.0 M NaCl
22	None	0.1 M MES · H ₂ O pH 6.5	12% w/v PEG 20,000
23	1.6 M (NH ₄) ₂ SO ₄	0.1 M MES · H ₂ O pH 6.5	10% v/v 1,4-Dioxane
24	0.05 M CsCl	0.1 M MES · H ₂ O pH 6.5	30% v/v Jeffamine M-600
25	0.01 M CoCl ₂ · 6H ₂ O	0.1 M MES · H ₂ O pH 6.5	1.8 M (NH ₄) ₂ SO ₄
26	0.2 M (NH ₄) ₂ SO ₄	0.1 M MES · H ₂ O pH 6.5	30% w/v PEG MME 5,000
27	0.01 M ZnSO ₄ · 7H ₂ O	0.1 M MES · H ₂ O pH 6.5	25% v/v PEG MME 550
28	None	None	1.6 M Na ₃ citrate · 2H ₂ O pH 6.5
29	0.5 M (NH ₄) ₂ SO ₄	0.1 M HEPES pH 7.5	30% v/v MPD
30	None	0.1 M HEPES pH 7.5	10% w/v PEG 6,000 5% v/v MPD
31	None	0.1 M HEPES pH 7.5	20% v/v Jeffamine M-600
32	0.1 M NaCl	0.1 M HEPES pH 7.5	1.6 M (NH ₄) ₂ SO ₄
33	None	0.1 M HEPES pH 7.5	2.0 M NH ₄ HCO ₂
34	0.05 M CdSO ₄ · H ₂ O	0.1 M HEPES pH 7.5	1.0 M NaOAc · 3H ₂ O
35	None	0.1 M HEPES pH 7.5	70% v/v MPD
36	None	0.1 M HEPES pH 7.5	4.3 M NaCl
37	None	0.1 M HEPES pH 7.5	10% w/v PEG 8,000 8% v/v Ethylene glycol
38	None	0.1 M HEPES pH 7.5	20% w/v PEG 10,000
39	0.2 M MgCl ₂ · 6H ₂ O	0.1 M Tris pH 8.5	3.4 M 1,6-Hexanediol
40	None	0.1 M Tris pH 8.5	25% v/v tert-Butanol
41	0.01 M NiCl ₂ · 6H ₂ O	0.1 M Tris pH 8.5	1.0 M Li ₂ SO ₄ · H ₂ O
42	1.5 M (NH ₄) ₂ SO ₄	0.1 M Tris pH 8.5	12% v/v Glycerol
43	0.2 M NH ₄ H ₂ PO ₄	0.1 M Tris pH 8.5	50% v/v MPD
44	None	0.1 M Tris pH 8.5	20% v/v Ethanol
45	0.01 M NiCl ₂ · 6H ₂ O	0.1 M Tris pH 8.5	20% w/v PEG MME 2,000
46	0.1 M NaCl	0.1 M BICINE pH 9.0	20% v/v PEG MME 550
47	None	0.1 M BICINE pH 9.0	2.0 M MgCl ₂ · 6H ₂ O
48	None	0.1 M BICINE pH 9.0	2% v/v 1,4-Dioxane 10% w/v PEG 20,000

Table 5. Crystallization buffers for Wizard crystallization screen #1.

	crystallant	buffer (0.1 M)	salt (0.2 M)
1	20% (w/v) PEG-8000	CHES pH 9.5	none
2	10% (v/v) 2-propanol	HEPES pH 7.5	NaCl
3	15% (v/v) ethanol	CHES pH 9.5	none
4	35% (v/v) 2-methyl-2,4-pentanediol	imidazole pH 8.0	MgCl ₂
5	30% (v/v) PEG-400	CAPS pH 10.5	none
6	20% (w/v) PEG-3000	citrate pH 5.5	none
7	10% (w/v) PEG-8000	MES pH 6.0	Zn(OAc) ₂
8	2.0 M (NH ₄) ₂ SO ₄	citrate pH 5.5	none
9	1.0 M (NH ₄) ₂ HPO ₄	acetate pH 4.5	none
10	20% (w/v) PEG-2000 MME	Tris pH 7.0	none
11	20% (v/v) 1,4-butanediol	MES pH 6.0	Li ₂ SO ₄
12	20% (w/v) PEG-1000	imidazole pH 8.0	Ca(OAc) ₂
13	1.26 M (NH ₄) ₂ SO ₄	cacodylate pH 6.5	none
14	1.0 M sodium citrate	cacodylate pH 6.5	none
15	10% (w/v) PEG-3000	imidazole pH 8.0	Li ₂ SO ₄
16	2.5 M NaCl	Na/K phosphate pH 6.2	none
17	30% (w/v) PEG-8000	acetate pH 4.5	Li ₂ SO ₄
18	1.0 M K/Na tartrate	imidazole pH 8.0	NaCl
19	20% (w/v) PEG-1000	Tris pH 7.0	none
20	0.4 M NaH ₂ PO ₄ /1.6 M K ₂ HPO ₄	imidazole pH 8.0	NaCl
21	20% (w/v) PEG-8000	HEPES pH 7.5	none
22	10% (v/v) 2-propanol	Tris pH 8.5	none
23	15% (v/v) ethanol	imidazole pH 8.0	MgCl ₂
24	35% (v/v) 2-methyl-2,4-pentanediol	Tris pH 7.0	NaCl
25	30% (v/v) PEG-400	Tris pH 8.5	MgCl ₂
26	10% (w/v) PEG-3000	CHES pH 9.5	none
27	1.2 M NaH ₂ PO ₄ /0.8 M K ₂ HPO ₄	CAPS pH 10.5	Li ₂ SO ₄
28	20% (w/v) PEG-3000	HEPES pH 7.5	NaCl
29	10% (w/v) PEG-8000	CHES pH 9.5	NaCl
30	1.26 M (NH ₄) ₂ SO ₄	acetate pH 4.5	NaCl
31	20% (w/v) PEG-8000	phosphate-citrate pH 4.2	NaCl
32	10% (w/v) PEG-3000	Na/K phosphate pH 6.2	none
33	2.0 M (NH ₄) ₂ SO ₄	CAPS pH 10.5	Li ₂ SO ₄
34	1.0 M (NH ₄) ₂ HPO ₄	imidazole pH 8.0	none
35	20% (v/v) 1,4-butanediol	acetate pH 4.5	none
36	1.0 M sodium citrate	imidazole pH 8.0	none
37	2.5 M NaCl	imidazole pH 8.0	none
38	1.0 M K/Na tartrate	CHES pH 9.5	Li ₂ SO ₄
39	20% (w/v) PEG-1000	phosphate-citrate pH 4.2	Li ₂ SO ₄
40	10% (v/v) 2-propanol	MES pH 6.0	Ca(OAc) ₂
41	30% (w/v) PEG-3000	CHES pH 9.5	none
42	15% (v/v) ethanol	Tris pH 7.0	none
43	35% (v/v) 2-methyl-2,4-pentanediol	Na/K phosphate pH 6.2	none
44	30% (v/v) PEG-400	acetate pH 4.5	Ca(OAc) ₂
45	20% (w/v) PEG-3000	acetate pH 4.5	none
46	10% (w/v) PEG-8000	imidazole pH 8.0	Ca(OAc) ₂
47	1.26 M (NH ₄) ₂ SO ₄	Tris pH 8.5	Li ₂ SO ₄
48	20% (w/v) PEG-1000	acetate pH 4.5	Zn(OAc) ₂

Table 6. Crystallization buffers for Wizard crystallization screen #2.

	crystallant	buffer (0.1 M)	salt (0.2 M)
1	10% (w/v) PEG-3000	acetate pH 4.5	Zn(OAc) ₂
2	35% (v/v) 2-methyl-2,4-pentanediol	MES pH 6.0	Li ₂ SO ₄
3	20% (w/v) PEG-8000	Tris pH 8.5	MgCl ₂
4	2.0 M (NH ₄) ₂ SO ₄	cacodylate pH 6.5	NaCl
5	20% (v/v) 1,4-butanediol	HEPES pH 7.5	NaCl
6	10% (v/v) 2-propanol	phosphate-citrate pH 4.2	Li ₂ SO ₄
7	30% (w/v) PEG-3000	Tris pH 7.0	NaCl
8	10% (w/v) PEG-8000	Na/K phosphate pH 6.2	NaCl
9	2.0 M (NH ₄) ₂ SO ₄	phosphate-citrate pH 4.2	none
10	1.0 M (NH ₄) ₂ HPO ₄	Tris pH 8.5	none
11	10% (v/v) 2-propanol	cacodylate pH 6.5	Zn(OAc) ₂
12	30% (v/v) PEG-400	cacodylate pH 6.5	Li ₂ SO ₄
13	15% (v/v) ethanol	citrate pH 5.5	Li ₂ SO ₄
14	20% (w/v) PEG-1000	Na/K phosphate pH 6.2	NaCl
15	1.26 M (NH ₄) ₂ SO ₄	HEPES pH 7.5	none
16	1.0 M sodium citrate	CHES pH 9.5	none
17	2.5 M NaCl	Tris pH 7.0	MgCl ₂
18	20% (w/v) PEG-3000	Tris pH 7.0	Ca(OAc) ₂
19	1.6 M NaH ₂ PO ₄ /0.4 M K ₂ HPO ₄	phosphate-citrate pH 4.2	none
20	15% (v/v) ethanol	MES pH 6.0	Zn(OAc) ₂
21	35% (v/v) 2-methyl-2,4-pentanediol	acetate pH 4.5	none
22	10% (v/v) 2-propanol	imidazole pH 8.0	none
23	15% (v/v) ethanol	HEPES pH 7.5	MgCl ₂
24	30% (w/v) PEG-8000	imidazole pH 8.0	NaCl
25	35% (v/v) 2-methyl-2,4-pentanediol	HEPES pH 7.5	NaCl
26	30% (v/v) PEG-400	CHES pH 9.5	none
27	10% (w/v) PEG-3000	cacodylate pH 6.5	MgCl ₂
28	20% (w/v) PEG-8000	MES pH 6.0	Ca(OAc) ₂
29	1.26 M (NH ₄) ₂ SO ₄	CHES pH 9.5	NaCl
30	20% (v/v) 1,4-butanediol	imidazole pH 8.0	Zn(OAc) ₂
31	1.0 M sodium citrate	Tris pH 7.0	NaCl
32	20% (w/v) PEG-1000	Tris pH 8.5	none
33	1.0 M (NH ₄) ₂ HPO ₄	citrate pH 5.5	NaCl
34	10% (w/v) PEG-8000	imidazole pH 8.0	none
35	0.8 M NaH ₂ PO ₄ /1.2 M K ₂ HPO ₄	acetate pH 4.5	none
36	10% (w/v) PEG-3000	phosphate-citrate pH 4.2	NaCl
37	1.0 M K/Na tartrate	Tris pH 7.0	Li ₂ SO ₄
38	2.5 M NaCl	acetate pH 4.5	Li ₂ SO ₄
39	20% (w/v) PEG-8000	CAPS pH 10.5	NaCl
40	20% (w/v) PEG-3000	imidazole pH 8.0	Zn(OAc) ₂
41	2.0 M (NH ₄) ₂ SO ₄	Tris pH 7.0	Li ₂ SO ₄
42	30% (v/v) PEG-400	HEPES pH 7.5	NaCl
43	10% (w/v) PEG-8000	Tris pH 7.0	MgCl ₂
44	20% (w/v) PEG-1000	cacodylate pH 6.5	MgCl ₂
45	1.26 M (NH ₄) ₂ SO ₄	MES pH 6.0	none
46	1.0 M (NH ₄) ₂ HPO ₄	imidazole pH 8.0	NaCl
47	2.5 M NaCl	imidazole pH 8.0	Zn(OAc) ₂
48	1.0 M K/Na tartrate	MES pH 6.0	none

The crystallization solutions in which crystals were present were optimized to obtain the best crystal by changing buffer pH and the concentrations of salt and precipitant (Tables 7-9). Every stock solution used to make in-house crystallization solutions was filtered with a 45 μ m membrane filter prior to mixing. The components of crystallization solutions are shown below.

Table 7. Variations of crystallization condition H1-18. Each row illustrates the variations attempted from the original condition, H1-18.

H1-18 condition	Mg(OAc) ₂	Na cacodylate	PEG8000
H1-18-1	0.1 M	0.1M, pH 6.0	20 %
H1-18-2 (original)	0.1 M	0.1M, pH 6.5	20 %
H1-18-3	0.1 M	0.1M, pH 7.0	20 %
H1-18-4	0.2 M	0.05M, pH 6.0	20 %
H1-18-5	0.2 M	0.05M, pH 6.5	20 %
H1-18-6	0.2 M	0.05M, pH 7.0	20 %
H1-18-7	0.2 M	0.2M, pH 6.0	20 %
H1-18-8	0.2 M	0.2M, pH 6.5	20 %
H1-18-9	0.2 M	0.2M, pH 7.0	20 %
H1-18-10	0.4 M	0.1M, pH 6.0	20 %
H1-18-11	0.4 M	0.1M, pH 6.5	20 %
H1-18-12	0.4 M	0.1M, pH 7.0	20 %
H1-18-13	0.1 M	0.1M, pH 6.0	15 %
H1-18-14	0.1 M	0.1M, pH 6.5	15 %
H1-18-15	0.1 M	0.1M, pH 7.0	15 %
H1-18-16	0.2 M	0.05M, pH 6.0	15 %
H1-18-17	0.2 M	0.05M, pH 6.5	15 %
H1-18-18	0.2 M	0.05M, pH 7.0	15 %
H1-18-19	0.2 M	0.2M, pH 6.0	15 %
H1-18-20	0.2 M	0.2M, pH 6.5	15 %
H1-18-21	0.2 M	0.2M, pH 7.0	15 %
H1-18-22	0.4 M	0.1M, pH 6.0	15 %
H1-18-23	0.4 M	0.1M, pH 6.5	15 %
H1-18-24	0.4 M	0.1M, pH 7.0	15 %

Table 8. Variations of crystallization condition PEG20K. Each row illustrates the variations attempted from the original condition, PEG20K.

PEG20K condition	MES	PEG 20K
PEG20K-1	25 mM	12.5 %
PEG20K-2	25 mM	10 %
PEG20K-3	25 mM	8 %
PEG20K-4	50 mM	12.5 %
PEG20K-5	50 mM	10 %
PEG20K-6	50 mM	8 %
PEG20K-7	100 mM	12.5 %
PEG20K-8	100 mM	10 %
PEG20K-9	150 mM	12.5 %
PEG20K-10	150 mM	10 %
PEG20K-11	200 mM	12.5 %
PEG20K-12	200 mM	10 %
PEG20K-13	200 mM	8 %
PEG20K-14	200 mM	6 %

Table 9. Variations of crystallization condition H1-41. Each row illustrates the variations attempted from the original condition, H1-41.

H1-41 conditions	HEPES	2-propanol	PEG4000
H1-41-1	0.1 M, pH 7.5	10 %	20 %
H1-41-2	0.1 M, pH 7.5	9 %	20 %
H1-41-3	0.1 M, pH 7.5	8 %	20 %
H1-41-4	0.1 M, pH 7.5	7 %	20 %
H1-41-5	0.1 M, pH 7.5	6 %	20 %
H1-41-6	0.1 M, pH 7.5	11 %	20 %
H1-41-7	0.1 M, pH 7.5	12 %	20 %
H1-41-8	0.1 M, pH 7.5	10 %	22 %
H1-41-9	0.05 M, pH 7.5	10 %	20 %
H1-41-10	0.15 M, pH 7.5	10 %	20 %
H1-41-11	0.1 M, pH 7.5	10 %	18 %
H1-41-12	0.1 M, pH 7.8	10 %	20 %
H1-41-13	0.1 M, pH 8.2	10 %	20 %
H1-41-14	0.1 M, pH 7.2	10 %	20 %
H1-41-15	0.1 M, pH 6.8	10 %	20 %
H1-41-16	0.1 M, pH 7.5	14 %	20 %
H1-41-17	0.1 M, pH 7.5	16 %	20 %
H1-41-18	0.1 M, pH 7.5	18 %	20 %
H1-41-19	0.1 M, pH 7.5	10 %	25 %
H1-41-20	0.1 M, pH 7.5	12 %	22 %

2.2. General Methods

2.2.1. Preparation of Competent Cells

Commercially available competent cells were used to make stocks of new CaCl₂ competent cells. Five milliliters of overnight cultures were grown in LB media with no antibiotic and transferred to 250 mL LB media. When the OD₅₅₀ reached to 0.5–0.7, the cells were harvested by centrifugation at 4 °C for 10 min at 6,000 rpm using a Beckman J2-21 centrifuge. The cell pellets were washed with 100 mL of sterile 0.1 M MgCl₂ and centrifuged at 4 °C for 10 min. The supernatant was discarded and the pellets were resuspended in 100 mL of sterile 0.1 M CaCl₂. The resuspended solution was incubated on ice for 20 min prior to centrifugation at 4 °C for 10 min. The supernatant was decanted and the cells were resuspended with 50 mL of sterile 0.1 M CaCl₂. Following the resuspension, the cells were incubated for 30 min on ice before 5 mL of sterile 50 % glycerol was added. The cells were aliquoted into 1.5 mL micro centrifuge tubes and stored at -80 °C.

2.2.2. Transformations

Competent cells were transformed by adding 50 to 250 ng of plasmid to 100 µL of cells. This mixture was incubated on ice for 30 min, then heat-shocked for 45 sec in 42 °C water bath and re-incubated on ice for 2 min. After adding 900 µL of LB broth, the mixture was incubated at 37 °C for 1 h with shaking at 250 rpm. The cells were then centrifuged for 1 min at 6,000 rpm using Eppendorf centrifuge 5417C and 950 µL of supernatant was removed. The pellet was resuspended in the remaining

solution and plated on LB agar plates, which contained the appropriate antibiotics, and incubated overnight at 37 °C.

2.2.3. Plasmid Preparations

Plasmids were isolated and purified using the Mini-Prep kit (Qiagen, Valencia, CA), according to the user's manual.

2.2.4. DNA Electrophoresis

All DNA samples were prepared by adding 2 μL of 10 \times Blue-juice to 8 μL of DNA (50–250 ng). DNA gels were performed at 120 volt for 30 min.

2.2.5. Sequencing

DNA sequences were determined with commercially available T7 primer (GE Healthcare) or in-house primers at the biotech research support facility in the University of Kansas Medical Center using a PE Biosystems Prism 377XL sequencer (Applied Biosystems, Foster City, CA).

2.2.6. Glycerol Stocks

An 800 μL aliquot of an overnight cell culture was mixed with 200 μL 50% glycerol and stored at -80 °C for future use.

2.2.7. SDS Electrophoresis

All SDS-PAGE samples were prepared by adding the appropriate amount of 5 \times loading buffer to the sample, followed by heating the sample at 100 °C for 5 min.

SDS-PAGE was performed using a mini PROTEAN[®] 3 cell (Biorad) at 150 volt for 1 hour.

2.2.8. Determination of Protein Concentration

Protein concentration was determined using the Coomassie reagent (Pierce, Rockford IL) according to the Bradford method. All protein concentrations were determined by comparison to a bovine serum albumin (BSA) standard curve at concentrations of 0.5, 1.0, 1.5 and 2.0 mg/mL.

The protein concentrations of standards and unknowns were determined as follows: 5 μ L of protein was added to 95 μ L of water and 900 μ L of Coomassie reagent and the absorbance was measured at 596 nm. The UV absorption of each unknown was fit to the BSA standard curve to determine the protein concentration. All measurements were recorded in a cuvette using a Shimadzu UV-1650PC spectrophotometer (Shimadzu, Colombia, MD).

2.2.9. PD-10

PD-10 desalting columns (GE Healthcare) were used to buffer exchange a protein. The columns were equilibrated with 25 mL of buffer prior to loading a 2.5 mL aliquot of protein onto the column. The protein was eluted with 3.5 mL of buffer according to the manual. The column was re-equilibrated with 25 mL of buffer before the re-use if more protein was to be used.

2.2.10. Centricon

Protein was concentrated in YM-30 or YM-10 devices (Millipore, Bedford, MA). Approximately 2 mL of protein solution was added to the Centricon device and centrifuged for 20 min at 7,000 rpm and 4 °C using a Thermo Fisher IEC Multi RF centrifuge. More protein was added and the centrifugation was repeated until all the protein had been added to the device, then the Centricon was inverted and centrifuged for 1 min to collect the concentrated protein at a desired volume.

2.2.11. Crystallization

For crystallization, proteins were concentrated to 150 mg/mL for MurA enzymes and to 10 mg/mL for CDK2. All proteins were crystallized using the hanging-drop vapor-diffusion method. The VDX 24 well plate (Hampton Research) and 22 mm siliconized glass coverslips (Hampton Research) were used for crystallization. Micro-seeding was performed on the droplets without crystal growth after overnight incubation at 19 °C. The plates were checked at intervals of 1, 2, and 4 days and 1, 2, and 4 weeks. After four weeks, the plates were moved to room temperature and checked monthly thereafter.

2.2.11.1. Hanging-Drop method

In the reservoir, 500 μ L of crystallization or equilibrium solution was placed. A few microliters (2 μ L unless otherwise mentioned) of protein solution was mixed with the same amount of crystallization solution on a glass coverslide. The glass slide was placed on the top of the reservoir and the plate was incubated at 19 °C.

2.2.11.2. Micro-Seeding method

Crystal seeds were prepared by crushing a harvested crystal and diluting the pieces to harvesting buffers. A micro-capillary tube was used to seed the drops, which crystal growth had not been observed. The tube was soaked in the seeding solution and placed in the center of the crystallization drop briefly. The coverslides were placed back on the reservoir and the plate was incubated at 19 °C.

2.2.12. Data Collection

The crystals with proper sizes were used for data collection, and soaked into cryo-protectant solutions briefly. A cryo-loop was used to take the crystal out from the solution and it was mounted on the goniometer to be flash-frozen in the cryo stream. The crystal was centered by adjusting the position of goniometer. Data collections were performed in two places, the University of Kansas (Lawrence, KS) and H. Lee Moffitt Cancer Center (Tampa, FL). The equipment at the University of Kansas is a Raxis IV++ imaging plate (MSC) with CuK α X-rays generated by a Rigaku rotating anode (RU300), and focused by Osmic mirror optics (MSC) with CrystalClear (Rigaku, The Woodlands, TX) software. The facility in H. Lee Moffitt Cancer Center is a Raxis HTC imaging plate with CuK α X-rays generated by a Rigaku rotating anode with Collect (Rigaku) software. General conditions for data collection were following: 0.5° frame width for 180° of phi axis rotation, 100–180 mm distance, and 2 to 10 min of exposure time.

2.2.13. Data Reduction and Structure Refinement

Collected data sets were indexed and scaled with XDS¹³⁴ or HKL-2000¹³⁵. The structures have been solved by the molecular replacement method. Molecular replacements and refinements were performed with the CNS¹³⁶ program package. Diffraction data were limited to low resolution reflections 20.0 – 4.0 Å in the cross-rotation and translation search. Refinements were performed using data for the highest resolution with no σ cut-off applied. Several rounds of minimization, simulated annealing and restrained individual B factor refinement were carried out. The resulting electron density maps (F_o-F_c , $2F_o-F_c$) were evaluated with O ¹³⁷. Solvent molecules were added to the model at chemically reasonable positions ($2.0 \text{ \AA} \leq d \leq 3.2 \text{ \AA}$) from other oxygen or nitrogen atom where the difference density was observed clearly.

Ligand molecules, if necessary, were drawn with Sybyl 7.1 (Tripos Association, St. Louis, MO) or Maestro 8.0 (Schrödinger, New York, NY) and saved as the PDB formats. The texts of the PDB files were edited to have proper atom names and hydrogen atoms were eliminated. The edited structures were run for xplo2d¹³⁸ to acquire parameter and topology files. The numbers of hydrogen atoms in topology files were fixed before use. The PDB files of ligands were called on O , moved to fit to electron densities, and the final coordinates were saved for further refinements. After the final cycle of refinements, figures were prepared with Molscript¹³⁹ or PyMol (DeLano Scientific, Palo Alto, CA).

2.3. *E. cloacae* and mutant MurA enzymes

2.3.1. DNA

E. cloacae MurA was in a pET9d derived vector, with a stop codon before the C-terminal His-tag.

2.3.2. Primers

Primers for site-directed mutagenesis were synthesized by MWG Biotech AG, and diluted to 100 pmol/ μ L with dd H₂O and stored at -20 °C.

Arg120Ala MurA #1 5'-gcc att ggc gcg **gct** cct gtt gac ctg-3'

Arg120Ala MurA #2 5'-cag gtc aac agg **agc** cgc gcc aat ggc-3'

Lys248Asp MurA #1 5'-gcc att tct ggc ggc **aac** att gtt tgc cgt aat gcg-3'

Lys248Asp MurA #2 5'-cgc att acg gca aac aat **gtt** gcc gcc aga aat ggc-3'

Trp71Val MurA #1 5'-cgt aat ggc tcc gtc **gtg** atc gat gcc agc aac-3'

Trp71Val MurA #2 5'-gtt gct ggc atc gat **cac** gac gga gcc att acg-3'

2.3.3. Site-directed Mutagenesis of *E. cloacae* MurA

Site-directed mutagenesis of WT *E. cloacae* MurA vector was performed using Quik change site-directed mutagenesis kit (Stratagene).

The mutagenesis of Asp123Ala and Arg91Lys were performed by Dr. Andreas Becker.

2.3.4. Over-expression of WT and Mutant *E. cloacae* MurA Enzymes

Large-scale over-expression was carried out using the following protocol: an overnight culture was prepared in which 50 μ L of the glycerol stock was added to 50 mL of LB-kan and incubated at 37 °C overnight. A 5 mL aliquot of the overnight culture was added to each of 6 flasks containing 500 mL of LB-kan and 1 drop of antifoam. When the optical density measured at 600 nm (OD_{600}) of the cell culture reached 0.4 – 0.8, cells were induced by adding IPTG to a final concentration of 0.5 μ M. After induction, the cells were allowed to grow at 37 °C for 4 – 6 h with shaking at 250 rpm. The cells were then harvested by centrifugation at 6,000 rpm for 10 min using a Beckman J2-21 centrifuge. The supernatant was discarded, and the cell pellets were collected and stored at -80 °C till future use.

2.3.5. Purification of WT and Mutant *E. cloacae* MurA Enzymes

MurA was purified using an ÄKTA FPLC and pre-packed columns (GE Healthcare). The cell pellets were suspended in 8–10 mL extraction buffer (50 mM Tris, 1 mM DTT, 1 mM EDTA, 0.1 M NaCl, 0.1% Triton X-100, pH 8.0) / 1 g of cells plus 1 mg lysozyme / 1 g of cells by stirring for 1 h at 4 °C. The solution was sonicated on ice for 2 \times 30 sec and centrifuged for 30 min at 14,000 rpm using a Beckman J2-21 centrifuge, and then the supernatant was collected. The combined supernatants were subjected to a 25 % $(NH_4)_2SO_4$ precipitation for 1 h. The amount of $(NH_4)_2SO_4$ added for this precipitation was calculated using the following equation:

$$\text{g (NH}_4\text{)}_2\text{SO}_4 \text{ for 1 L} = \frac{515X}{100 - 0.27X}, \quad \text{Equation 1}$$

where X is the desired percentage of $(\text{NH}_4)_2\text{SO}_4$.

After the $(\text{NH}_4)_2\text{SO}_4$ precipitation, the solution was centrifuged at 4 °C for 1 h at 18,000 rpm using a Beckman J2-21 centrifuge to remove the precipitates. The supernatant from this centrifugation was purified using the phenyl sepharose (P-seph) 26/10 column (GE healthcare), a hydrophobic interaction based column. The column was pre-equilibrated with Buffer A + 1 M $(\text{NH}_4)_2\text{SO}_4$, the supernatant was loaded onto the column and the protein was eluted from the column by decreasing the salt concentration in the mobile phase via a gradient of Buffer A + 1 M $(\text{NH}_4)_2\text{SO}_4$ to Buffer A over 10 column volumes (CV). Every third fraction was evaluated on SDS-PAGE and the results were compared with the chromatograph. Fractions containing MurA were combined, desalted, and concentrated to < 50 mL using an Amicon ultrafiltration device with a 30 kD Millipore filter (Fisher Scientific). Desalting was accomplished by adding Buffer A until the conductivity readings were below $5 \mu\text{S} / \text{cm}^2$ on a Corning Checkmate II conductivity meter (Fisher Scientific). The desalted and concentrated MurA was then loaded onto a Q-seph 26/10 column (GE healthcare) and eluted from the column by increasing the salt concentration in the mobile phase via a gradient of Buffer A to Buffer A + 0.4 M NaCl over 10 CV. Fractions analyzed on SDS-PAGE were combined, desalted, and concentrated in the same manner as for the P-seph column.

After the concentration, the fractions were aliquoted into micro centrifuge tubes and stored at -80 °C.

2.3.6. Kinetic analysis of WT and Mutant *E. cloacae* MurA Enzymes

2.3.6.1. High-throughput Screening (HTS) of MurA

High-throughput screening (HTS) with about 50,000 compounds had been performed by Dr. Melanie A. Priestman. Since then, 50,000 more compounds were purchased through the HTS facility at the University of Kansas. These newly purchased compounds included compounds selected from ChemDiv (San Diego, CA) and natural products from MicroSource (Gaylordville, CT).

The condition for MurA screening on a 384-well plate was varied a little from the previous screening. The first trial with previously used conditions did not work very well due to a low signal to noise ratio. Thus, the enzymatic reaction condition for HTS was modified. Originally, the assay was performed using 60 μ L reaction volume: 20 μ L compound, 20 μ L MurA (0.1 μ g final reaction concentration of 2.2 nM) in buffer (50 mM HEPES pH 7.0, 2 mM DTT, and 50 mM KCl), and 20 μ L of the solution containing 0.3 mM PEP and 0.3 mM UNAG in buffer (final reaction concentration of 0.1 mM for both substrates). The reaction solution was incubated at room temperature for 5 to 30 min, followed by the addition of 40 μ L of Lanzetta reagent. This condition was tested for the reproducibility. Although the reaction showed a linear correlation with time, the OD₆₅₀ of the final solution was not more than 0.2 after the reading of negative control was fixed to zero. To increase the OD

readings, higher concentrations of MurA and both substrates, UNAG and PEP, were used for this enzymatic reaction. Thus, the final condition for HTS has been changed to 60 μL reaction volume: 20 μL compound, 20 μL MurA (0.2 μg final reaction concentration of 4.4 nM) in buffer (50 mM HEPES pH 7.0, 2 mM DTT, and 50 mM KCl), and 20 μL of the solution containing 0.45 mM PEP and 0.45 mM UNAG in buffer (final concentration of 0.15 mM). At the same time, negative control reaction was set up without MurA addition. Under this condition, the linearity of the reaction by time has also been tested over 30 minutes, and the graph of optical density (OD) vs. reaction time showed a linear correlation.

The HTS assays were performed by the addition of the above solutions to a well in a 384-well plate by a Biomek FX Liquid Handling Workstation. In the 384-well plates, the compounds in 2.5 % DMSO had been plated and stored at $-20\text{ }^{\circ}\text{C}$. After thawing the compound solutions in the plates, each plate was centrifuged at 2,000 rpm for 1 min. 20 μL of MurA was then added to the wells, and the reaction started by the addition of 20 μL of PEP and UNAG mixture. The plates were centrifuged one more time after the addition of MurA and substrates, to make sure that none of the reaction components remained on the walls of the well. The reaction was allowed to proceed for 30 min before 40 μL of the Lanzetta reagent was added. The optical density was then promptly measured at 650 nm using a SpectraMax 340PC 384 Absorbance. Each plate had one column that had no compounds (positive control with no inhibition), as well as one column containing no MurA (negative control with

no reaction). The reproducibility of the screening was ensured by checking negative and positive controls on each plate.

IC₅₀ determination was carried out for the compounds that initially showed greater than 40 % inhibition of MurA. The compounds were picked up from mother plates, aliquoted to new 384 well plates. After serial dilution to vary their concentration, assays were carried out at the HTS facilities using procedure described above. Data were fit to the equation 2 to derive IC₅₀ values.

$$v = V_{\min} + \frac{V_{\max} - V_{\min}}{1 + \left(\frac{[I]}{IC_{50}}\right)^n}, \quad \text{Equation 2}$$

where v is the initial velocity, V_{\max} is the maximum velocity, V_{\min} is the minimum velocity, $[I]$ is the concentration of inhibitor and n is the hill slope.

2.3.6.2. Inhibition Study of HTS Leads

Thorough studies of HTS hits were performed by testing the activity of MurA with two different methods: determination of P₁ concentration with Lanzetta reagent and by measurement of the amount of EP-UNAG using MurA–MurB coupled assay.

HTS1-1, **HTS3-1**, and **HTS4-1** were studied by Dr. Melanie A. Priestman.

The modes of action of **HTS2-2**, **HTS7-1**, and **HTS8-1** were thoroughly determined by MurA–MurB coupled assay. The ANS fluorescence assay was performed for **HTS2-2**. K_i values of inhibitors were determined by detecting the amount of product, EP-UNAG, using MurA–MurB coupled assay. The enzyme reaction was performed in the following condition: 1 mL of 50 mM HEPES (pH 7.5),

50 mM KCl, 20 mM glucose, 20 U glucose oxidase, 1 mM PEP, 0.1 – 4 mM UNAG, 0–20 μ M inhibitor, 0.2 mM NADPH, 20 μ g MurB, and 10 μ g MurA. Before the addition of NADPH, MurB, and MurA, the absorbance of the mixture was auto-zeroed at 340 nm. The absorbance was fixed to between 1.1 and 1.2 OD by the addition of 0.2 mM NADPH. 20 μ g of MurB was then added to the reaction mixture, and the absorbance reading was performed. After about 30 seconds time course reading, the reaction was initiated by the addition of MurA. The decrease in NADPH absorbance was recorded at 340 nm, and the control reaction was conducted without MurA at each inhibitor concentration. Specific activity was calculated from the slope of the time-course curve of each reaction. The data were fit to equation 3 (the Michaelis-Menten equation):

$$v = \frac{V_{\max(\text{obs})} \times [S]}{K_{m(\text{obs})} + [S]}, \quad \text{Equation 3}$$

where v is the initial velocity, $V_{\max(\text{obs})}$ is the observed maximum velocity, $K_{m(\text{obs})}$ is the observed Michaelis constant, and $[S]$ is the substrate concentration.

The K_i values were determined by linear regression of the replot of the $K_{m(\text{obs})}$ values versus the concentration of the inhibitor and the data were fit to equation 4.

$$K_{m(\text{obs})} = \left(\frac{K_m}{K_i} \right) \times [I] + K_m. \quad \text{Equation 4}$$

Then, the K'_i values were determined by linear regression of the replot of the $1/V_{\max(\text{obs})}$ values versus the concentration of the inhibitor and the data were fit to equation 5.

$$1/V_{\max(\text{obs})} = \left(\frac{1}{K'_i \times V_{\max}} \right) \times [I] + \frac{1}{V_{\max}}, \quad \text{Equation 5}$$

where $V_{\max(\text{obs})}$ is the observed maximum velocity, K'_i is the inhibitor constant with respect to V_{\max} , V_{\max} is the true maximum velocity, and $[I]$ is the inhibitor concentration.

The dissociation constant of **HTS2-2** was measured by fluorescence experiments with ANS. Fluorescence was detected with Varian Cary Eclipse fluorescence spectrometer. The buffer used for all measurements was 50 mM sodium/potassium phosphate (pH 6.9) with 2 mM DTT with a final concentration of 125 $\mu\text{g/mL}$ MurA. Fluorescence of ANS was excited at 366 nm, and emission spectra were recorded between 400 and 600 nm. The buffer in the quartz cuvette was used for auto-zero, then 100 μM ANS was added and scanned. After the addition of MurA into the solution, the emission spectrum was read again. Various concentrations of **HTS2-2** (2.5 – 100 μM) were then mixed in the solution and the fluorescence recorded. For the data evaluation, ANS emission spectra in buffer were subtracted from the corresponding ANS/MurA or ANS/MurA/**HTS2-2** spectra, thereby giving the fluorescence intensities as a function of the UNAG concentrations. The highest points of the emission spectra were selected in between 470 and 480 nm and the intensities were read. Then, $1-F_L/F_O$ (where F_L is the intensity when a ligand is added and F_O is the intensity without the ligand) was calculated and the graph, $1-F_L/F_O$ vs. [**HTS2-2**], was fitted to the Michaelis-Menten equation to derive K_d value for **HTS2-2**.

2.3.6.3. Structure-Activity Relationships (SAR) of HTS 1 and HTS 2 on WT MurA

Compounds with **HTS 1** and **HTS 2** scaffolds were purchased from IBS (InterBioScreen, Moscow, Russia), ChemBridge, and ChemDiv to study structure-activity relationships (SAR) for WT *E. cloacae* MurA. Purchased compounds were dissolved in 100 % DMSO at 100 mM concentration. Inhibitory activity of the compounds was tested by detecting the amount of P_i produced by MurA enzyme reaction. Assays were performed in 100 μL of 50 mM HEPES, 2mM DTT, 1mM PEP, 1 mM UNAG, and 1 mM final concentration of each compound. By the addition of 22nM of WT MurA, the enzyme reactions were started. Reactions were incubated for 3 min at room temperature and stopped by the addition of 800 μL of Lanzetta reagent. After an additional 5 min for color development, 100 μL of 34 % (w/v) sodium citrate was added to stop the color change. The absorbance was then measured at 660 nm with Shimazu UV-1650PC spectrometer. A negative control reaction was performed without MurA to eliminate the auto-hydrolysis effect of PEP, and a positive control reaction was carried out without inhibitor. The inhibition activity was recorded as relative activity against the positive control. For the **HTS 2** scaffold compounds, the activity was measured daily until the inhibition was observed up to 2 weeks.

2.3.6.4. Inhibition study of known inhibitors

Peptide inhibitor, HESFWYLPHQSY, was synthesized at the University of Kansas Structural Biology Center. The activity of this peptide was tested by detecting the amount of P_i produced by MurA enzyme reaction. Assays were performed in 100 μ L of 50 mM HEPES, 2mM DTT, 1mM PEP, 1 mM UNAG, and 1 mM final concentration of the peptide. The reaction condition was the same as the reactions of HTS 1 and 2 compounds, described in the section 2.3.6.3.

The inhibition activity of cnicin was determined by MurA–MurB coupled assay. The inhibitor was incubated with MurA and with or without UNAG (0, 0.01, and 1 mM) for various times (0–10 min). In the incubation mixture, 10 μ g of MurA was used at various concentration of cnicin (0–10 mM) in a volume of 25 μ L at room temperature. The reaction mixture contained 50 mM HEPES (pH 7.5), 50 mM KCl, 20 mM glucose, 20 U glucose oxidase, 1 mM PEP, and 1, 0.99, or 0 mM UNAG in 945 μ L of total volume. Before the addition of NADPH, MurB, and the incubation mixture, the absorbance of the mixture was auto-zeroed at 340 nm. The absorbance was fixed to between 1.1 and 1.2 OD by the addition of 0.2 mM NADPH (10 μ L of 20 mM stock solution). 20 μ g of MurB (a volume of 20 μ L) was then added to the reaction mixture, and the absorbance reading was performed. After about 30 seconds time course reading, the reaction was initiated by the addition of the incubated solution (MurA + cnicin \pm UNAG). The decrease in NADPH absorbance was recorded at 340 nm. Specific activity was calculated from the slope on time-course

curve of each reaction. The graph of specific activity vs. incubation time (sec) were plotted at various inhibitor concentrations and fitted to equation 6,

$$\frac{A_t}{A_{t=0}} = F_2 + (1 - F_2)e^{-k't}, \quad \text{Equation 6}$$

where A is enzyme activity, k' is the rate constant at equilibrium, and F_1 and F_2 are the fractions of activity at zero time ($F_1=1$) and infinite time (after equilibrium has been established, F_2).

Determined k' values at various inhibition concentrations were used to determine K_i of cnicin. The graph of k' vs. [inhibitor] were plotted and fitted to the equation 7,

$$k' = k_{\text{obs}} = k_{-1} + k_1[I]. \quad \text{Equation 7}$$

The K_i value was calculated using the values of k_1 and k_{-1} fitted to the equation 8,

$$K_i = \frac{k_{-1}}{k_1} = \frac{[E][I]}{[EI*]}. \quad \text{Equation 8}$$

2.3.6.5. WT, Asp123Ala, and Arg91Lys *E. cloacae* MurA

The activity of MurA was measured using an end-point assay in 100 μ L of 50 mM HEPES (pH 7.5) and 2 mM DTT at room temperature by determining the amount of P_i produced in the reaction for primary test. The final concentrations of WT, Asp123Ala, and Arg91Lys MurA were 0.025, 0.025, and 1.7 mg/mL, respectively. Assays were performed with a final concentration of 1 mM PEP and varied concentrations of UNAG (0.010–10 mM). Every reaction was started with the addition of MurA. The reactions were allowed for 3 min prior to the addition of 800 μ L of Lanzetta reagent to stop the reactions and develop the color change by P_i .

After additional 5 min, 100 μ L of 34 % (w/v) sodium citrate was added to stop the color change. The absorbance was measured at 660 nm with Shimazu UV-1650PC spectrometer and the amount of P_i was determined in comparison with phosphate standards, and the enzyme activity was expressed as U/mg. Control reactions were used without MurA as blanks to eliminate the auto-hydrolysis effect of PEP. The approximate values of K_m and V_{max} were determined by fitting the kinetic data to the Michaelis-Menten equation (equation 3). The K_m and V_{max} values from Lanzetta assay were used to determine the range of the concentrations of substrates for MurA–MurB coupled assays.

For thorough characterizations, MurA–MurB coupled assays were performed for WT, Asp123Ala, and Arg91Lys MurA. The activities of these MurAs were tested in 950 μ L of 50 mM HEPES (pH 7.5) + 2 mM DTT + 50 mM KCl with 20 mM glucose and 20 U GOX at room temperature. The final concentration of one substrate was varied from 0.01 to 5 mM when the other was fixed to 1 mM. After the addition of PEP and UNAG, the absorbance of the mixture was auto-zeroed at 340 nm. The absorbance was fixed to between 1.1 and 1.2 OD by the addition of 0.2 mM NADPH. Then, the final concentration of 0.02 mg/mL of MurB was added to the reaction mixture, and the absorbance reading was started. After about 30 seconds time course reading, the reaction was started by the addition of MurA. The final MurA concentrations were 0.01 mg/mL for both WT and Asp123Ala MurA, and 0.68 mg/mL for Arg91Lys. The absorbance was recorded until no more NADPH consumption was detected. Specific activities of each of the reactions were

determined, based on initial slopes of each time course curve. The graph of specific activity vs. [substrate] was plotted and fitted to equation 3 to derive K_m values of each substrate.

The inhibition study by fosfomycin was performed for WT and Asp123Ala MurA using Lanzetta assay. The assay was performed in 100 μ L of 50 mM HEPES (pH 7.5) + 2 mM DTT. Concentrations of fosfomycin varied from 20 nM to 200 μ M were incubated in buffer with 0.025 mg/mL WT or Asp123Ala MurA and 1 mM UNAG at room temperature for 5 min. The reaction was initiated by the addition of 1 mM PEP to the mixture and was allowed to proceed for 3 min at room temperature before 800 μ L Lanzetta reagent was added to the solution. After 5 min of color development, 100 μ L of 34 % (w/v) sodium citrate solution was added and the absorbance was measured at 660 nm. Negative and positive controls were carried out without enzyme and without fosfomycin, respectively. IC_{50} values were derived from equation 2.

Before the ANS fluorescence assay, WT, Asp123Ala and Arg91Lys MurA enzymes in the HEPES buffer (50 mM HEPES (pH 7.5) + 2 mM DTT) were incubated with 0.5 mM UNAG for 1 hour at room temperature. The UNAG in the solution was then removed by PD-10 with 50 mM HEPES (pH 7.5) + 2 mM DTT. Each enzyme concentration was measured with Bradford assay.

Fluorescence experiments were performed using Varian Cary Eclipse fluorescence spectrometer. The buffer used for all measurements was 50 mM sodium/potassium phosphate (pH 6.9) with 2 mM DTT. The final concentration of

MurA enzymes was 125 $\mu\text{g}/\text{mL}$. Fluorescence of ANS was excited at 366 nm, and emission spectra were recorded between 400 and 600 nm. The buffer in the quartz cuvette was used for auto-zero, then 100 μM ANS was added and scanned. After the addition of MurA into the solution, the emission spectrum was scanned. Various concentrations of UNAG (5 – 500 μM) were added to the solution and the emission spectra were measured once again. For the data evaluation, ANS emission spectra in buffer were subtracted from the corresponding ANS/MurA or ANS/MurA/UNAG spectra, thereby giving the fluorescence intensities as a function of the UNAG concentrations. The highest points of the emission spectra were selected in between 470 and 480 nm and the intensities were read. Then, the $1-F_1/F_0$ was calculated and the graph, $1-F_1/F_0$ vs. [UNAG], was fitted to the Michaelis-Menten equation to derive UNAG K_d values.

2.3.6.6. Arg120Ala *E. cloacae* MurA

The activity test of Arg120Ala MurA was performed with His-tagged enzyme to eliminate the effect of genomic *E. coli* MurA. His-tagged Arg120Ala MurA was prepared by Martha L. Healy-Fried.

To determine if Arg120Ala MurA is capable of catalyzing the conversion of UNAG and PEP to EP-UNAG and P_i , but is unable to release the products (i.e. a single-turnover), urea was used to establish if the trapped products could be detected after denaturation of the enzyme•ligand complex. This was performed by incubating a reaction mixture containing 50 mM Tris (pH 8.0), 50 mM KCl, 2 mM DTT, 5 mM

UNAG, 5mM PEP, and 40 mg/mL His-tagged Arg120Ala MurA (0.9 mM), in a final volume of 400 μ L at room temperature for 5 min. To stop the reaction and denature Arg120Ala MurA, a final concentration of 6.0 M urea was added and incubated at 4 °C for 16 hr. To measure the product EP-UNAG, the coupled assays with 50 mM Tris (pH 8.0), 50 mM KCl, 2 mM DTT, 20 mM glucose, 20 U glucose oxidase, 0.20 mM NADPH, and various concentrations of the denaturation mixture (0.4–2.9 mg / 0.01–0.07 mM), were employed. An OD₃₄₀ reading was stabilized prior to the start of the reaction by the addition of 40 μ g of MurB, and the decrease in NADPH absorbance was recorded. Control experiments were conducted throughout with Arg120Ala MurA treated in the same way, but omitting PEP during the assay.

2.3.6.7. Cys115Asp *E. cloacae* MurA

MurA–MurB coupled assays were performed to determine PEP K_m for Cys115Asp MurA. The activity of Cys115Asp MurA was tested in 950 μ L of 50 mM HEPES (pH 7.5) + 2 mM DTT + 50 mM KCl with 20 mM glucose and 20 U GOX at room temperature. The final concentration of UNAG was 1 mM and PEP was varied from 1 to 500 μ M. After the addition of PEP and UNAG, the absorbance of the mixture was auto-zeroed at 340 nm. The absorbance was then fixed to between 1.1 and 1.2 OD₃₄₀ by the addition of 0.2 mM NADPH. The final concentration of 0.02 mg/mL of MurB was added to the reaction mixture, and the absorbance reading was started. After about 30 seconds time course reading, the reaction was started by the addition of Cys115Asp MurA. The final concentration of Cys115Asp MurA was

0.01 mg/mL. The reading was recorded until time course curve was observed to be flat. Specific activities of each reaction were calculated from the slope of respective time course curve. The graph of specific activity vs. [PEP] was plotted and fitted to Michaelis-Menten equation to determine PEP K_m value of Cys115Asp MurA.

Fluorescence assay with ANS was applied to determine K_d value of UNAG for Cys115Asp MurA. The buffer used for this assay was 50 mM sodium/potassium phosphate (pH 6.9) with 2 mM DTT. The final concentration of Cys115Asp MurA enzyme was 125 $\mu\text{g/mL}$. The excitation wavelength of ANS was 366 nm, and emission spectra were recorded between 400 and 600 nm. Buffer in the quartz cuvette was used for auto-zero, and 100 μM ANS was added and scanned. After the addition of MurA into the solution, the scanning was done again, then various concentrations of UNAG (5 – 1000 μM) were added to the solution and the fluorescence measured. For the data evaluation, ANS emission spectra in buffer were subtracted from the corresponding ANS/MurA or ANS/MurA/UNAG spectra, thereby giving the fluorescence intensities as a function of the UNAG concentrations. The highest points of the emission spectra were selected in between 470 and 480 nm and the intensities were read. Then, the $1-F_L/F_O$ was calculated and the graph, $1-F_L/F_O$ vs. [UNAG], was fitted to Michaelis-Menten equation to derive UNAG K_d values.

2.3.7. Crystallization of *E. cloacae* MurA Enzymes

2.3.7.1. Asp123Ala and Arg91Lys MurA

The crystallization of open forms of Asp123Ala MurA was attempted with PEG20K conditions (Table 8). Three microliters of Asp123Ala MurA (3.5 mg/mL) in HEPES buffer (50 mM HEPES (pH 7.5) + 2 mM DTT) was mixed to 3 μ L of crystallization solutions. 500 μ L of 0.5 M MES (pH 6.1) was added to the reservoir. Crystals were obtained after overnight incubation at 19 °C. Crystals from PEG20K-11 condition were harvested in 200 mM MES (pH 6.1) + 12.5 % PEG20K. The harvested crystal was soaked into the cryo-protectant solution (200 mM MES (pH 6.1) + 12.5 % PEG20K + 25 % glycerol) prior to data collection. Data collection was accomplished at the Structural Biology Center of the University of Kansas.

The open form crystal of Arg91Lys MurA was setup with PEG20K conditions. Three microliters of Arg91Lys MurA (75 mg/mL) in HEPES buffer (50 mM HEPES (pH 7.5) + 2 mM DTT) was mixed with 3 μ L of crystallization solutions. In the reservoir, 500 μ L of 0.5 M MES (pH 6.1) was added. The crystal growth was not detected after 24 hour incubation at 19 °C. Thus, microseeding method with a harvested Asp123Ala MurA crystal from the previous experiment was applied to the drops. The crystals in PEG20K-1 condition were formed after seeding and harvested on the next day. Harvesting buffer was composed with 50 mM MES (pH 6.1) and 12.5 % PEG20K. The harvested crystal was transferred to the cryo-protectant solution (50 mM MES (pH 6.1) + 12.5 % PEG20K + 25 % glycerol). After a brief

soaking, the crystal was mounted on goniometer for data collection. This crystal was measured at the Structural Biology Center of the University of Kansas.

2.3.7.2. Arg120Ala MurA

The crystallization of the closed form of Arg120Ala MurA was attempted with the variations of Hampton 1-41 condition (Table 9). Two microliters of the mixture of 84 mg/mL of Arg120Ala MurA in Tris buffer (50 mM Tris, pH 8.5, 2mM DTT, and 1 mM EDTA) with 10 mM UNAG and 10 mM PEP was added to 2 μ L of reservoir solution (H4-41-8 in Table 9). The crystal grew to a good size after the incubation for 3 days.

The harvesting conditions for this crystal could not be optimized due to the fragility of the crystal. Thus, the crystal was directly soaked into the cryo-protectant solution (20 % ethylene glycol, 0.1 M HEPES (pH 7.5), 25 % PEG4000, 1 mM UNAG, and 1 mM PEP). After the brief soaking in the cryo-protectant solution, the crystal was flash-frozen in the cryo stream. Data collection was performed at the University of Kansas Structural Biology Center.

2.3.7.3. Cys115Asp MurA

The crystallization of the open form Cys115Asp MurA was attempted with the variations of PEG20K condition (Table 8). Three microliters of 33 mg/mL of Cys115Asp MurA in phosphate buffer (50 mM Na/K phosphate (pH 6.9), 2mM DTT) was mixed with 2 μ L of crystallization solution (PEG20K-3). 500 μ L of 0.5 M MES (pH 6.1) was placed in the reservoir. Crystal growth was observed instantly, and

reached to a proper size in one hour. The crystal was soaked into the cryo protectant solution (25 mM MES (pH 6.1), 8% PEG20K, and 25 % glycerol). The crystal on a cryo-loop was then transferred to the goniometer and flash-frozen in the cryo stream. Data collection was performed at H. Lee Moffitt Cancer Center.

2.3.7.4. MurA with HTS2-2

Initial crystallization screening of MurA with **HTS2-2** was performed with Hampton 1 and 2 and Wizard 1 and 2 screens. Highly concentrated WT MurA was prepared in 50 mM HEPES (pH 7.5) + 2 mM DTT. MurA was diluted to 25 mg/mL and 50 mg/mL and prepared for crystallization by mixing with 10 mM of **HTS2-2** (from a 100 mM stock solution in DMSO). Small crystals were found in H1-18 (0.1 M Na cacodylate (pH 6.5), 0.1 M magnesium acetate, and 20 % PEG8000) condition at 50 mg/mL MurA concentration. To get an optimized crystal for the data collection, H1-18 condition was varied on pH and the concentration of buffer, salt, and precipitant as well as the concentration of MurA (Table 7). The Na cacodylate (buffer) was varied from 0.05 to 0.2 M with pH from 6.0 to 7.0, the concentration of $\text{Mg}(\text{OAc})_2$ was increased up to 0.4 M, and PEG8000 was changed from 20 % to 15 %. New drops were setup with varied H1-18 conditions at 60 mg/mL and 100 mg/mL MurA concentration. The largest crystals were formed at H1-18-15 (0.1 M Na cacodylate (pH 7.0), 0.1 M magnesium acetate, 15 % PEG8000), and harvested in the solution of 0.05 M $\text{Mg}(\text{OAc})_2$, 0.05 M Na cacodylate (pH 7.0), and 15 % PEG8000. The data collection was performed at the Structural Biology Center of the University of Kansas.

2.3.7.5. MurA with HTS1-1

HTS1-1 (1 mM of final concentration) was incubated with WT MurA (10 mg/mL in 50 mM HEPES and 2 mM DTT) at room temperature for 2 hours. Incubated solution with the inhibitor was applied to PD-10 for buffer exchange into 50 mM HEPES, 2 mM DTT for the removal of DMSO. The eluted protein solution still had orange color from **HTS1-1**, indicating that the inhibitor bound to protein even after the buffer exchange, and it was concentrated up to 65 mg/mL with a Centricon YM-30 device.

The crystallization of WT MurA with **HTS1-1** in 50 mM HEPES and 2 mM DTT was screened with Hampton 1 and 2, and Wizard 1 and 2 screening solutions. Plate shaped crystals were found in H1-41 condition (0.1 M HEPES (pH 7.5), 10 % 2-propanol, and 20 % PEG4000) after the incubation at 19 °C for a month. The crystal setup with the same protein was performed with the various H1-41 conditions (Table 9). The best crystals were detected in the H1-41-8 and H1-41-19 conditions. Since these crystals were very unstable, no harvesting condition could be identified. The crystals were transferred to cryo-protectant solutions including glycerol, ethylene glycol, MPD, PEG200, PEG400, sucrose, or xylitol. Most of the crystals dissolved in these cryo-protectant solutions, hence no harvesting conditions could be identified. Although some crystals survived in the cryo-protectant solutions for a short time, none of them diffracted well.

2.3.8. Further Studies with HTS2-2

2.3.8.1. Kinetic Study of Trp71Val and Lys248Asp MurA

Mutation and purification of Trp71Val and Lys248Asp were accomplished to investigate the effects of **HTS2-2** on WT MurA.

The K_m value of UNAG was measured in 100 μ L of 50 mM HEPES (pH 8.0) + 2 mM DTT at room temperature using the Lanzetta assay. The final concentration of both Trp71Val and Lys248Asp MurA was 220 nM. Assays were performed with a final concentration of 1 mM PEP and various concentrations of UNAG (0.025–5 mM). All assays were started with the addition of MurA. The enzyme and substrates were allowed to react for 3 min prior to the quenching of the reaction with 800 μ L of the Lanzetta reagent. After an additional 5 min, 100 μ L of 34 % (w/v) sodium citrate was added to stop the color development by inorganic phosphate. The absorbance was then measured at 660 nm and the amount of P_i was determined by comparison with phosphate standards. Enzyme activity was expressed as U/mg. Control samples without MurA were used as an auto-zero to eliminate an increase in the absorbance due to hydrolysis of P_i from PEP. The K_m values were determined by fitting the kinetic data to the Michaelis-Menten equation.

Inhibitory activities of **HTS2-2** against Trp71Val and Lys248Asp mutant MurAs were measured using the same way of UNAG K_m determination. The final concentrations of PEP and UNAG were 0.5 mM each, and the concentration of

HTS2-2 was varied from 5 to 500 μM . The IC_{50} values were determined by fitting the data to equation 2.

2.3.8.2. MurA Oligomerization by HTS2-2

Superdex 75 column (GE Healthcare) on ÄKTA FPLC was used to identify the oligomerization effect of **HTS2-2** on WT MurA. Prior to the experiment, the column was calibrated with standards. Blue Dextran 200 (GE Healthcare) was diluted to 1 mg/mL in 50 mM HEPES and 2 mM DTT, and loaded to measure the void volume of the column, then the mixture of ribonuclease A (MW: 13700), chymotrypsinogen A (MW: 25000), ovalbumin (MW: 43000), and albumin (MW: 67000) was loaded. K_{av} (gel-phase distribution coefficient, equation 9) values for each protein were calculated and K_{av} vs. log MW graph was plotted.

$$K_{av} = \frac{V_e - V_0}{V_c - V_0}, \quad \text{Equation 9}$$

where V_0 , V_e , and V_c represent void volume, elution volume, and geometric column volume, respectively.

One milliliter of WT MurA (15 mg/mL) in 50 mM HEPES + 2 mM DTT with 10 mM **HTS2-2** in DMSO was loaded to the column at flow rate of 0.5 mL/min. One CV of 50 mM HEPES + 2 mM DTT solution was eluted with the same flow rate. The molecular weight that each peak represents was calculated from the calibration curves.

2.4. Cyclin-Dependent Kinase 2

2.4.1. DNA

Recombinant GST fusion human CDK2 (GST-hCDK2) plasmid in pGEX6p1 vector was prepared by Katinka Bahr.

2.4.2. Over-expression of CDK2

The GST-hCDK2 plasmid was transformed to RIL *E. coli* competent cell and glycerol stock was prepared. An overnight culture was prepared in which 50 μ L of the glycerol stock was added to 50 mL LB with 0.1 mg/mL ampicillin (amp) and incubated at 37 °C overnight. A 5 mL aliquot of the overnight culture was added to each of 6 flasks containing 500 mL each of LB-amp and 1 drop of antifoam. When the OD₆₀₀ reached 0.4–0.6, the temperature of the incubator was lowered to 16 °C. When the temperature was stabilized, cells were induced with 0.01mM IPTG. After 24 hr culture at 16 °C, cells were centrifuged at 6,000 rpm for 10 min using a Beckman J2-21 centrifuge. The supernatant was discarded, and the cell pellets collected, combined, and frozen at -80 °C.

2.4.3. Purification of CDK2

CDK2 was purified at 4 °C using an ÄKTA FPLC (GE Healthcare). The cell pellets were resuspended with lysis buffer: 50 mM HEPES (pH 7.5), 150 mM NaCl, 1 mM EGTA, 10 mM MgCl₂, 2mM DTT, and 1 mg lysozyme/1 g of cell. After 2×30s sonications, the lysate was clarified by centrifugation. The GST-affinity

column was pre-equilibrated with Buffer A (CDK2-GST 1), the supernatant was loaded onto the column and the protein was eluted from the column by increasing the glutathione (reduced) concentration from Buffer A (CDK2-GST 1) to Buffer A (CDK2-GST 1) + glutathione (10 mM glutathione included). Fractions corresponding to the peak were run for SDS-PAGE and the results were compared with the chromatograph. Fractions containing GST-hCDK2 were combined, and GST-pre-scission protease (20:1 ratio) was added to the solution to cleave GST. During the GST cleavage reaction, the buffer was exchanged to Buffer A (CDK2-GST 2) and total volume was decreased to 150 mL. The sample was loaded to the second GST column eluting from Buffer A (CDK2-GST 2) to Buffer A (CDK2-GST 2) + glutathione to remove cleaved GST-tag and GST-pre-scission. The fractions corresponding to flow-through were run for SDS-PAGE and combined. The combined CDK2 was concentrated until the total volume was less than 15 mL. The solution was further purified with Superdex 200 column to eliminate aggregated CDK2. The size exclusion column was eluted with Buffer A (CDK2-GST 2) for 1 CV. The fractions corresponding to the peak of monomeric CDK2 ($V_e \sim 240$ mL) were run for SDS-PAGE, then combined and concentrated. The buffer of highly purified CDK2 was exchanged to 100 mM sodium/potassium phosphate (pH 6.2) with 2 mM DTT using a PD-10 column, and concentrated to about 10 mg/mL with a Centricon YM-10 device.

2.4.4. Crystallization of CDK2 with inhibitors

The co-crystals of CDK2-inhibitor were grown by vapor diffusion using the hanging drop method. Two microliters of 10 mg/mL CDK2 in phosphate buffer (100 mM Na/K phosphate (pH 6.2) + 2 mM DTT) was added to 2 μ L of reservoir solution (0.1 M HEPES (pH 7.5) and 10 % PEG3350). The final concentration of inhibitors was 1.5 mM in the drops. Crystals were formed after 1–2 days at 19 °C.

The crystals were immersed briefly in the cryo protectant solution, 50 mM HEPES (pH 7.5), 50 mM Na/K phosphate (pH 6.2), 15 % PEG3350, 0.5 mM inhibitor, and 22 % ethylene glycol, and then flash-frozen in the cryo stream. Complete diffraction data were collected at the Structural Biology Center of the University of Kansas or at H. Lee Moffitt Cancer Center. Data reduction and scaling were performed with XDS or HKL-2000. Molecular replacement and refinement were performed with the CNS program package. 1HCK (PDB ID) was used as the model structure for the molecular replacement.

2.4.5. Molecular docking of CDK2

Glide 4.5¹⁴⁰, which is a part of Maestro 8.0, was used in molecular docking studies. The PDB files of co-crystallized CDK2 structures were used for molecular docking after inhibitor molecules and alternative conformations had been removed. All water molecules were removed and hydrogen atoms were generated by the Protein Preparation Wizard. The structures of ligands were built and their ionization states, tautomers and ring conformations were varied with LigPrep in Maestro. The

receptor grid box with 8.0 Å on each side was generated at the ATP binding site of CDK2, and the constraints of the key hydrogen bonds, i.e. the carbonyl oxygen of Glu81 and Leu83 as hydrogen bond acceptors, and the backbone nitrogen of Leu83 as a hydrogen bond donor, were included in the grid file. The prepared ligands were docked into CDK2 using the prepared grid file with the extra precision (XP) mode. The default values for energy-minimization, scaling of van der Waals radii, and output settings were maintained. The outputs were saved as the Maestro-format pose viewer files (.mae). The pose viewer files were opened with the Glide Pose Viewer panel. The CDK2 structure was displayed with docked structures, and the ligand files with good contacts were saved for figures. The figures were prepared with PyMol.

3. Results and Discussion

3.1. Structure and Mechanism of MurA

MurA catalyzes the transfer of the enolpyruvyl moiety of phosphoenolpyruvate (PEP) to the 3'-OH group of UDP-N-acetyl-glucosamine (UNAG), producing enolpyruvyl-UDP-N-acetyl-glucosamine (EP-UNAG) and inorganic phosphate (P_i). In this enzymatic reaction, the C-O bond of PEP is cleaved rather than the P-O bond, which is normally favored in most chemical reactions of PEP and in other PEP-utilizing enzyme reactions. Due to this chemically unfavorable enzyme reaction by MurA, there have been many studies of the enzymatic mechanism of MurA.

The enzyme undergoes a large conformational change upon UNAG binding in the active site before PEP binds to its binding site. The structures of both conformational states, open and closed, were revealed by crystallography. This induced-fit mechanism is the structural proof to the ordered substrate binding mode assessed for the enolpyruvyl transfer reaction in which UNAG interacts with the free enzyme prior to the binding of PEP.

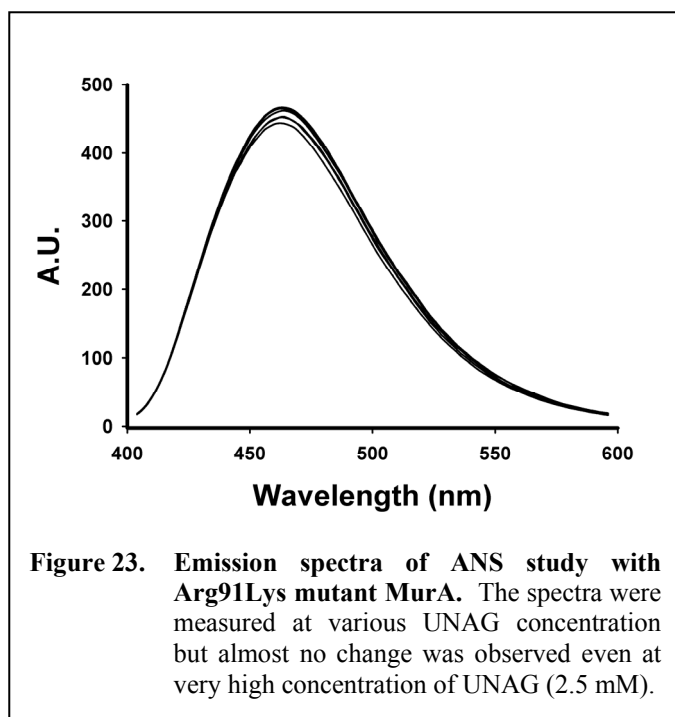
3.1.1. The Role of Arg91 and Asp123 in *E. cloacae* MurA

Site-directed mutagenesis and protein purification were performed by Dr. Andreas Becker. Kinetic analysis and crystallization were accomplished by Huijong Han. Structure refinement was done by Prof. Ernst Schönbrunn and Huijong Han.

Arg91 is located close to the loop of MurA and conserved through most species of MurA³⁰. Thus, it was thought that Arg91 is one of the crucial residues in the

regulating the loop conformational change of the MurA reaction. The structural and kinetic studies of Arg91Lys MurA were performed to evaluate the function of Arg91 in the conformational change and the enzymatic activity of MurA.

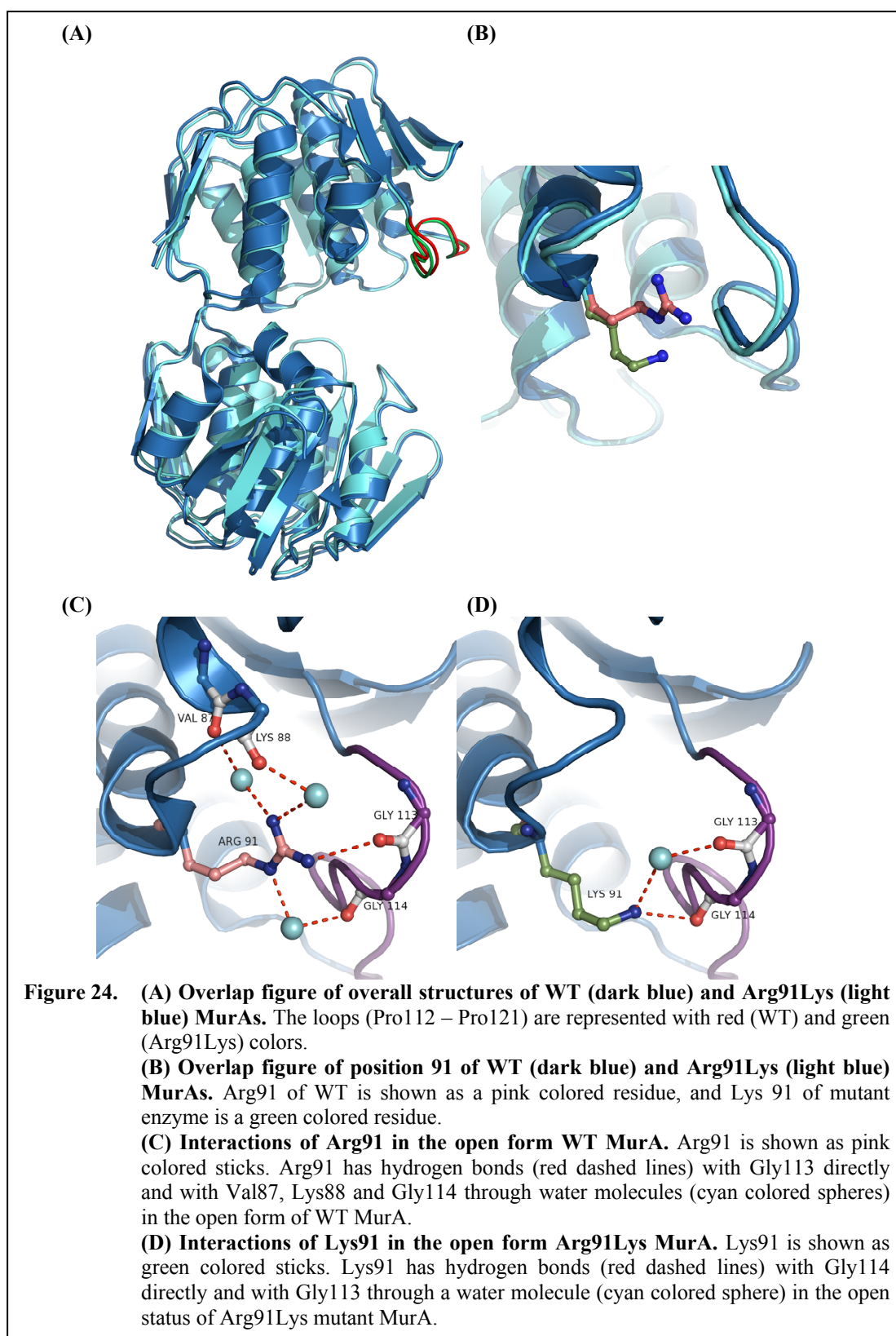
The mutation of Arg91 to Lys resulted in complete loss of the enzymatic activity (data not shown). The fluorescence study with ANS suggested that the inactivity of



this mutant is due to the loss of the conformational changes required for catalysis. Even at high concentrations of UNAG (up to 2.5 mM) almost no change in the emission spectra of ANS was observed, implying that the open form state of the mutant MurA with ANS was not affected by the

presence of UNAG (Figure 23). This infers that Arg91 is an essential residue for the open-closed conformational changes.

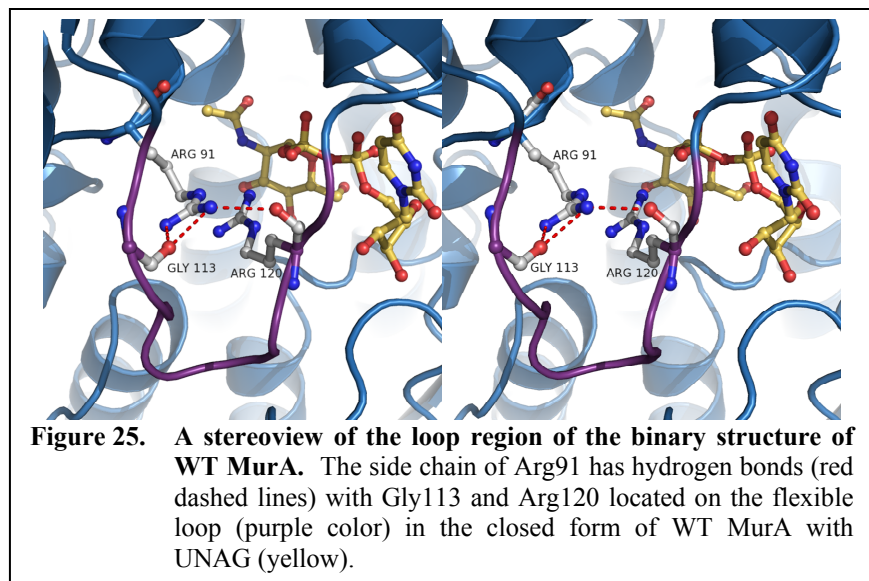
Further studies of the mutant enzyme were performed by crystallography. The un-liganded structure, the open form, of Arg91Lys *E. cloacae* MurA was solved to 2.0 Å resolution. The conformation of the mutant enzyme was the same as WT MurA including the conformation of the flexible large loop (Figure 24A). The only



difference between the mutant and WT MurA was the side chains of arginine and lysine at the 91 position (Figure 24B): The guanidinium group of Arg91 in WT MurA has hydrogen bonds with the backbone carbonyl oxygen atom of Gly113 and three water molecules, and the water molecules form hydrogen bonds with backbone carbonyls of Val87, Lys88 and Gly114 (Figure 24C). The side chain of Lys91 has hydrogen bonds with the backbone carbonyl of Gly114 and a water molecule interacting with the backbone carbonyl oxygen of Gly113 (Figure 24D). Except for the difference in the conformation and hydrogen bond interactions of side chains between Arg91 and Lys91, the backbone conformations of each structure are the same. This suggests that the mutation of Arg91 to Lys does not affect the open status of MurA.

The role of Arg91 was analyzed based on the binary structure, the closed form, of WT MurA because the closed form of the Arg91Lys mutant enzyme does not form..

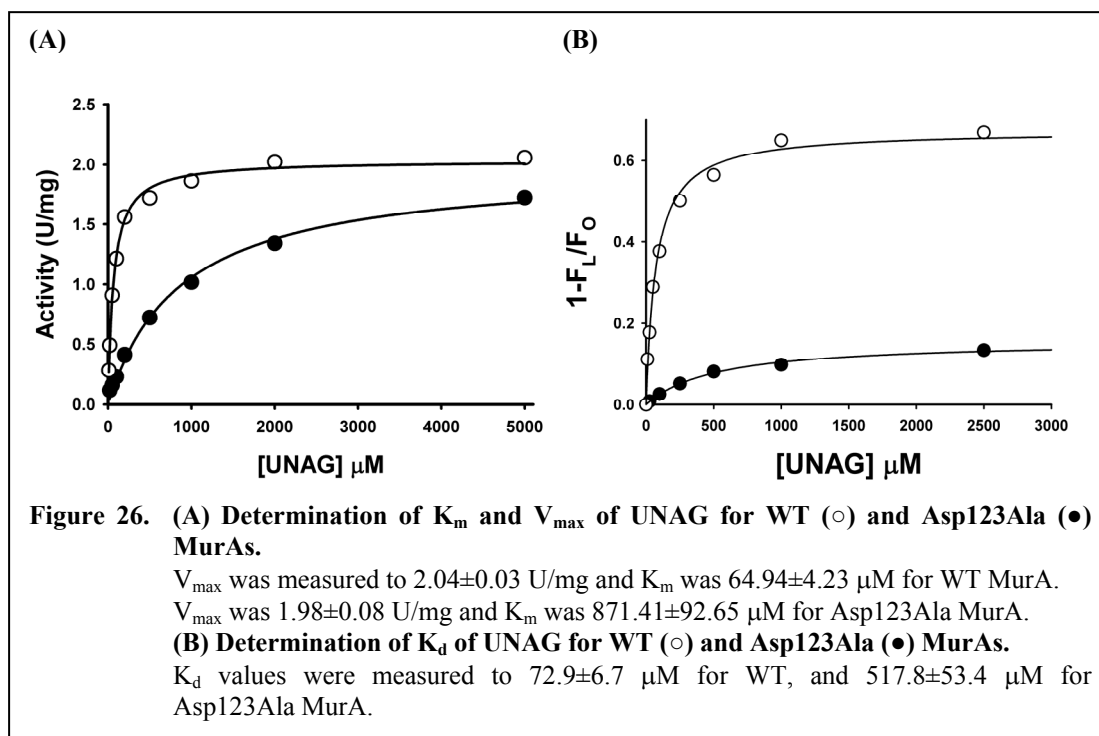
It was shown that the multiple hydrogen bond donors of the guanidinium group of arginine are required to hold the loop in the



closed status (Figure 25): The side chain of Arg91 has hydrogen bonds with the backbone carbonyl oxygen atoms of Gly113 and Arg129. Although Lys91 of the mutant enzyme has a hydrogen bond donor, one amine group is not enough to keep the hydrogen bonds with two residues as strong as a guanidinium group. Also, the side chain of Lys is shorter than of Arg and cannot reach to the acceptor residues. These hydrogen bonds are possibly key interactions at abilizing the closed form of the loop.

The location of Asp123 on MurA is close to the loop, and Asp123 is found in 87.1 % of 163 known MurA forms³⁰. The only observed variation of this residue is Gln. In order to evaluate the function of Asp123 in MurA, kinetic and structural studies of the mutant MurA, Asp123Ala, were performed.

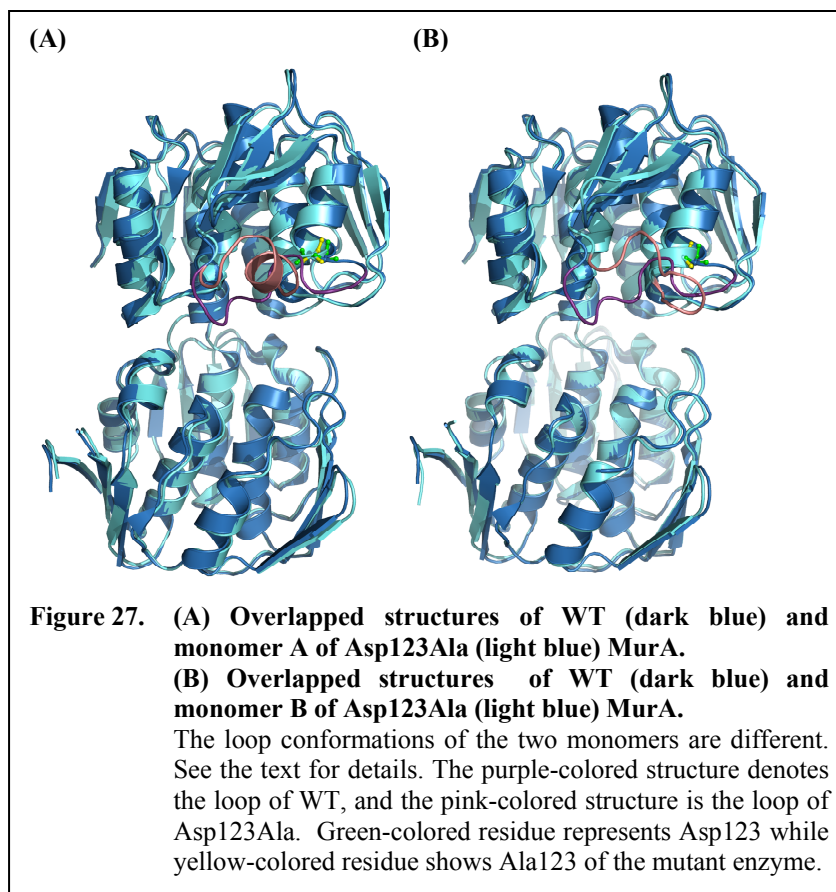
Compared to *E. cloacae* WT MurA, the Asp123Ala mutant enzyme has similar



full enzymatic activity but lower UNAG affinity, showing similar V_{\max} and higher K_m values for UNAG. The values are 1.98 U/mg of $V_{\max}(\text{UNAG})$ and 0.87 mM of $K_m(\text{UNAG})$ (Figure 26A). The ANS study of Asp123Ala mutant enzyme also indicates the binding affinity of UNAG is significantly lower than WT (Figure 26B), i.e. the derived dissociation constant (K_d) of UNAG for Asp123Ala mutant is 7 times higher than for WT. Thus, it is assumed that Asp123 is involved in the enzymatic activity by alternating the binding affinity of UNAG to MurA.

The un-liganded structure, the open status of Asp123Ala mutant MurA was solved to 2.35 Å resolution with two monomers in one unit cell. The two monomers

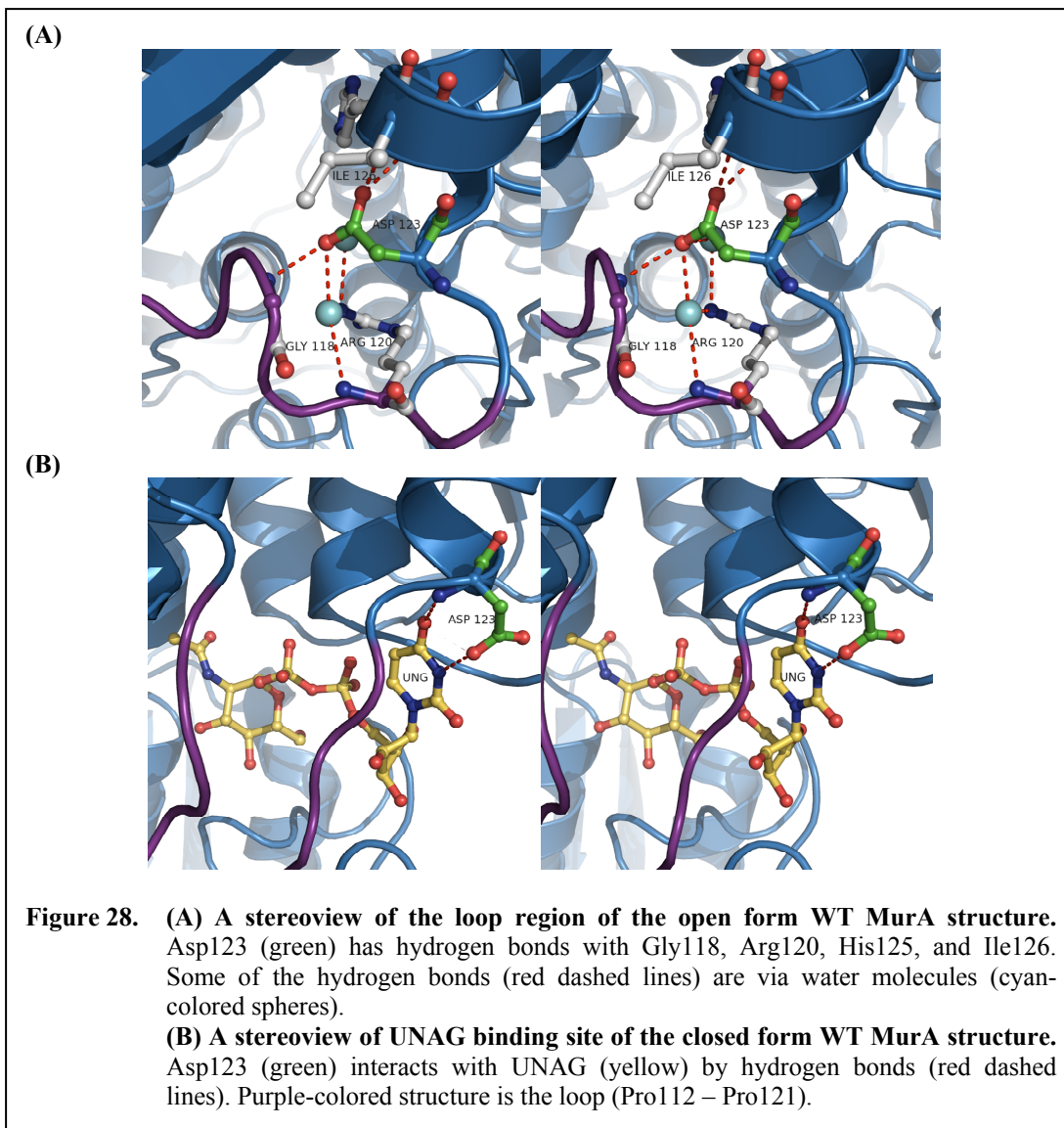
show different conformations of the loop structure, i.e. the loop structure of the monomer A adopts a partial α -helix while the loop of monomer B does not have any distinct secondary structure. The variation of the



conformation of the loop is possibly due to different crystal lattice contacts because the loop of both monomers contacts the neighboring monomeric structure. Not only are the loop conformations of these two monomers different, they also show the conformational change compared to the structure of WT (Figure 27). This difference and variation of the loop conformation is probably due to the lack of the carboxylate group on Ala123, which acts as a hydrogen bond acceptor.

In the open form structure of WT MurA, Asp123 has several hydrogen bonds, which may define the conformation of the loop, i.e. the carboxylate has hydrogen bonds with the backbone nitrogen atoms of Gly118, His125, and Ile126 as well as hydrogen bonds with water molecules bridging the side chain and backbone atoms of Arg120 (Figure 28A). In particular, hydrogen bonds of Asp123 with Gly118 and Arg120 are likely to induce more rigidity in the loop. The mutation of Asp123 to alanine eliminates these hydrogen bonds, thus allowing the loop to move to a new position.

The weak binding affinity of UNAG to Asp123Ala mutant MurA is explained by the interaction of Asp123 with UNAG in WT MurA (Figure 28B). In the binary structure of WT MurA, a couple of hydrogen bonds between Asp123 and UNAG were observed. The carboxylate of Asp123 has a hydrogen bond with N3 of the uracil moiety of UNAG, and the backbone nitrogen of Asp123 interacts with O4 of the uracil through a hydrogen bond. However, Ala123 in the mutant enzyme cannot maintain the hydrogen bond with N3 of the uracil due to the lack of a hydrogen bond acceptor.



As expected from the structures of the open and closed forms of WT MurA, Arg91 is involved in the open-closed conformational changes, and the Asp123 residue affects the binding affinity for UNAG, confirmed by kinetic and structural studies. Specifically, Arg91 showed a very strong effect on the loop conformational change resulting in loss of enzymatic activity. Based on this, it was concluded that Arg91 is an essential residue for the open-closed transition of MurA. Although

Asp123 is not a critical residue for the enzymatic activity, it affects the UNAG binding on MurA: It was observed that the loss of the hydrogen bonds of Asp123 with UNAG in the closed form lowered the UNAG affinity to the enzyme. Mutation studies of other highly conserved residues (Table 1) on the loop such as Pro112, Gly113, Gly114, Ala116, Ile117, Gly118, and Pro121 would help to further understand the induced-fit mechanism of MurA.

3.1.2. Arg120 in *E. cloacae* MurA and Enzymatic Mechanism

Site-directed mutagenesis, protein purification, and kinetic analysis of his-tagged Arg120Ala MurA were performed by Martha L. Healy-Fried. Protein purification, crystallization and structure refinement of native Arg120Ala MurA were done by Huijong Han.

The active site of WT *E. cloacae* MurA contains several charged residues: Lys22, Arg91, Arg120, Arg331, Arg371, and Arg397, which are thought to be involved in proton transfers during the enzyme reaction of MurA²³. Thus, mutational studies of these residues could potentially provide details of the enzymatic mechanism of MurA.

Mutagenesis of Arg120 in *E. cloacae* MurA to an alanine residue results in an inactive enzyme (data not shown). The inactivity of Arg120Ala mutant MurA was also proved by the co-crystal structure of Arg120Ala MurA with UNAG and PEP, solved to 1.90 Å resolution (Figure 29). Both substrates were bound in the active site in a closed conformation of the mutant MurA. The active site of the mutant enzyme has more space available because of the smaller amino acid alanine compared to arginine. This creates a conformational change of the loop in addition to a stretching

of the side chain of Arg91 into the active site. As described in section 3.1.1, Arg91 in WT MurA is involved in the open-closed conformational changes by keeping the loop position in the closed form through several hydrogen bonds with the backbone carbonyl oxygen atoms of Gly113 and Arg120 (Figure 25). It is observed that Arg91 is still involved in maintaining the loop conformation in the closed

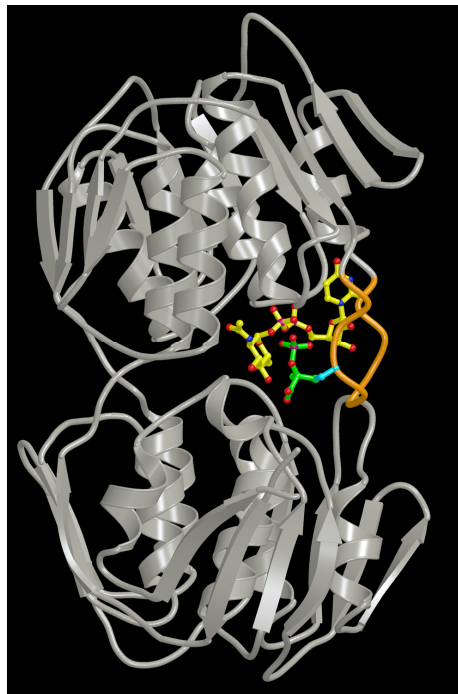
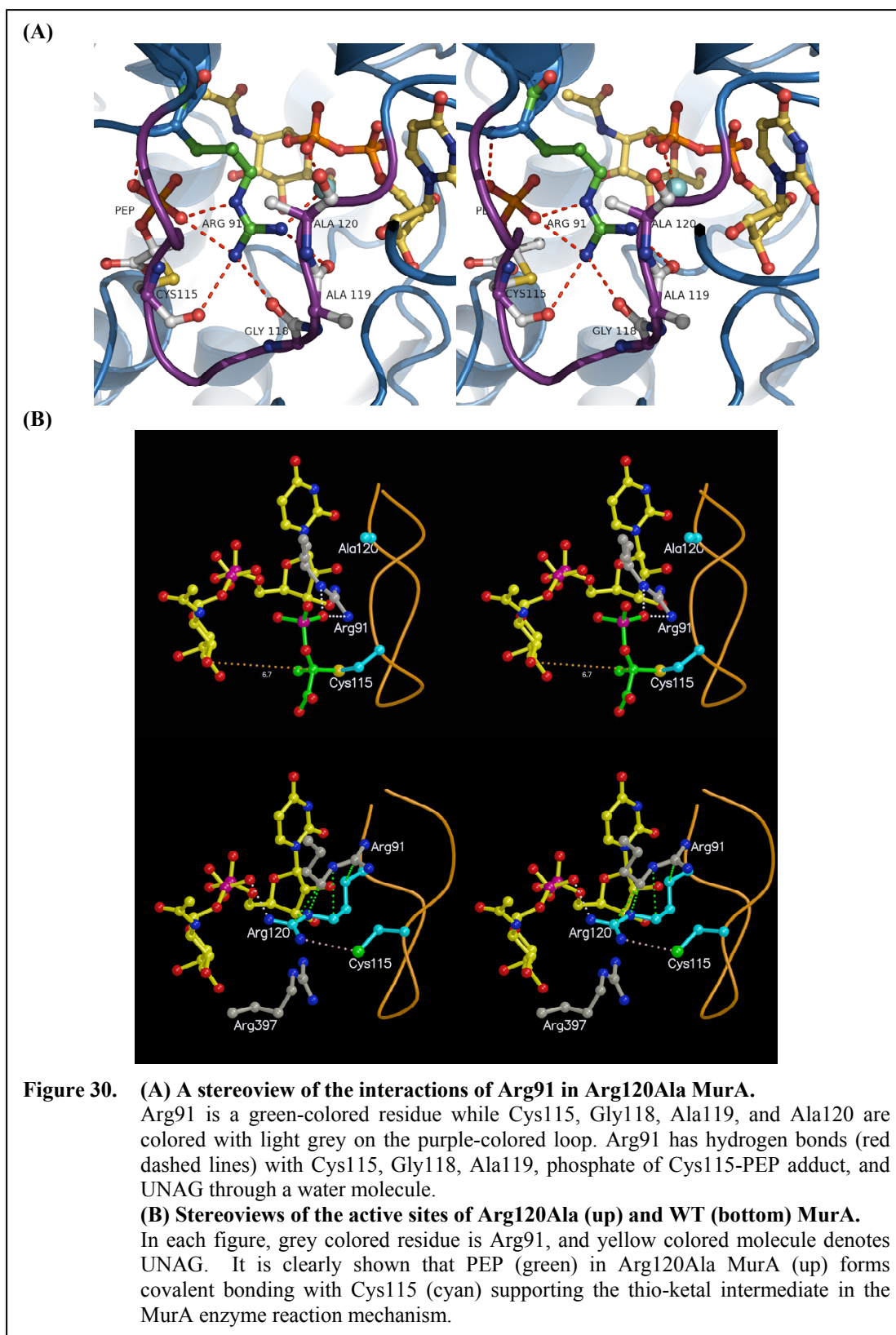
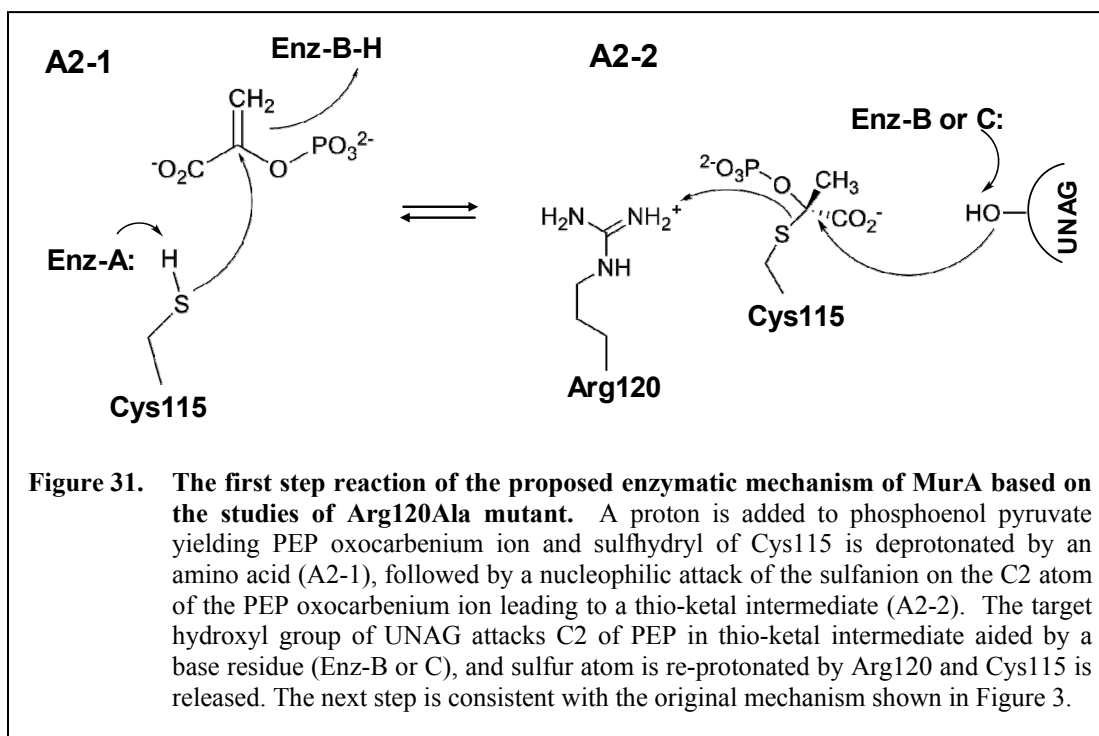


Figure 29. Overall structure of Arg120Ala MurA complexed with UNAG and PEP. Orange color represents the loop region, cyan-colored residue is Cys115, yellow colored molecule denotes UNAG, and green colored molecule is PEP.

form of Arg120Ala mutant MurA. However, the interactions of Arg91 have changed, i.e. the guanidinium group of Arg91 now forms hydrogen bonds with the backbone carbonyls of Cys115, Gly118, and Ala119 instead of Gly113 and Arg120, due to the positional change of the side chain of Arg91 in the mutant enzyme (Figure 30A). It was also found that Arg91 establishes hydrogen bonds with the phosphate group of PEP covalently bound to Cys115. The Arg120 residue forms a couple of hydrogen bonds with UNAG in the binary structure of MurA, while it is the side chain of Arg91 interacting with the UNAG molecule through a bridging water molecule in Arg120Ala MurA. In WT MurA, the side chains of Arg91 and Arg120 interacts each





other via hydrophobic interactions. The disruption of this hydrophobic interaction in the mutant enzyme induces the conformational change of the side chain of Arg91, thus Arg91 undertakes the functions of Arg120 seen in WT, i.e. filling the space of Arg120 and interacting with UNAG.

The most interesting feature of the structure of Arg120Ala MurA is the covalent bonding between PEP and Cys115 (Figure 30B). Although earlier studies had suggested the existence of a hemi thio-ketal intermediate between PEP and Cys115 during the MurA enzyme reaction, it has been visualized for the first time in this study. These findings indicate that the enzymatic mechanism may occur via the formation of the thio-ketal tetrahedral intermediate (Figure 31). In this mechanism, the stronger nucleophile, i.e. the thiol group of Cys115, in comparison to the 3'-OH of UNAG, attacks the C-2 of PEP and the PEP-Cys115 hemi thio-ketal intermediate is

formed. The 3'-OH of UNAG then attacks the reaction center, C-2 of the PEP-Cys115 tetrahedral intermediate, and Cys115 is released. In this reaction step, the sulfur atom of Cys115 needs to receive a proton because the pK_a value of a thiol group is around 8.7. The proton required in this step can be supplied from the positively charged guanidinium group of the Arg120 residue. From the binary structure of WT *E. cloacae* MurA, the distance between the sulfur atom of Cys115 and NH1 of Arg120 is 3.6 Å. Considering that the van der Waals radius of a sulfur atom is 1.85 Å compared to 1.4 and 1.45 Å of oxygen and nitrogen, respectively, and also arginine being a flexible residue, 3.6 Å is within the distance range that the proton transfer can occur between Arg120 and Cys115.

In this proposed mechanism, one of the roles of Cys115 in WT MurA is the formation of the first tetrahedral intermediate (PEP-Cys115), and the benefit of this mechanism is lowering the activation energy (E_a). In general, a thiol group is a better nucleophile than a hydroxyl group, and the PEP-Cys115 tetrahedral intermediate is less sterically hindered because the $C\beta$ of cysteine is a secondary carbon while the 3'-OH of UNAG is attached to the tertiary carbon. Thus, MurA can lower the activation energy by the formation of a thio-ketal intermediate at the first step of the mechanism, thereby accelerating the reaction.

The thio-ketal intermediate was stabilized and hence observed in the co-crystal structure of Arg120Ala mutant MurA with UNAG and PEP. We suggest that this trapped thio-ketal intermediate is due to the lack of a proton source, the guanidinium group of Arg120. To further confirm this proposed mechanism, the retaining of

enzymatic activity of Cys115Asp MurA, which does not have a thiol functional group in the active site, is explained in the next section (3.1.3). The study of the double mutant Cys115Asp/Arg120Ala of MurA is also currently underway in Prof. Schönbrunn's laboratory.

3.1.3. The Role of Cys115 in the Enzymatic Mechanism of MurA

Cys115 is the most studied residue in MurA to date, because the mutation of Cys115 to an Asp residue is known as one of the fosfomycin resistance mechanisms. This mutation has been found in some pathogenic species, such as *Mycobacterium tuberculosis* and *Chlamydia*. Previously, several studies with Cys115Asp *E. cloacae* MurA have been performed in Prof. Schönbrunn's research group. The IC₅₀ value of fosfomycin for the Cys115Asp mutant enzyme was measured to be 2.5 mM while it is less than 1 μM for WT¹⁴¹.

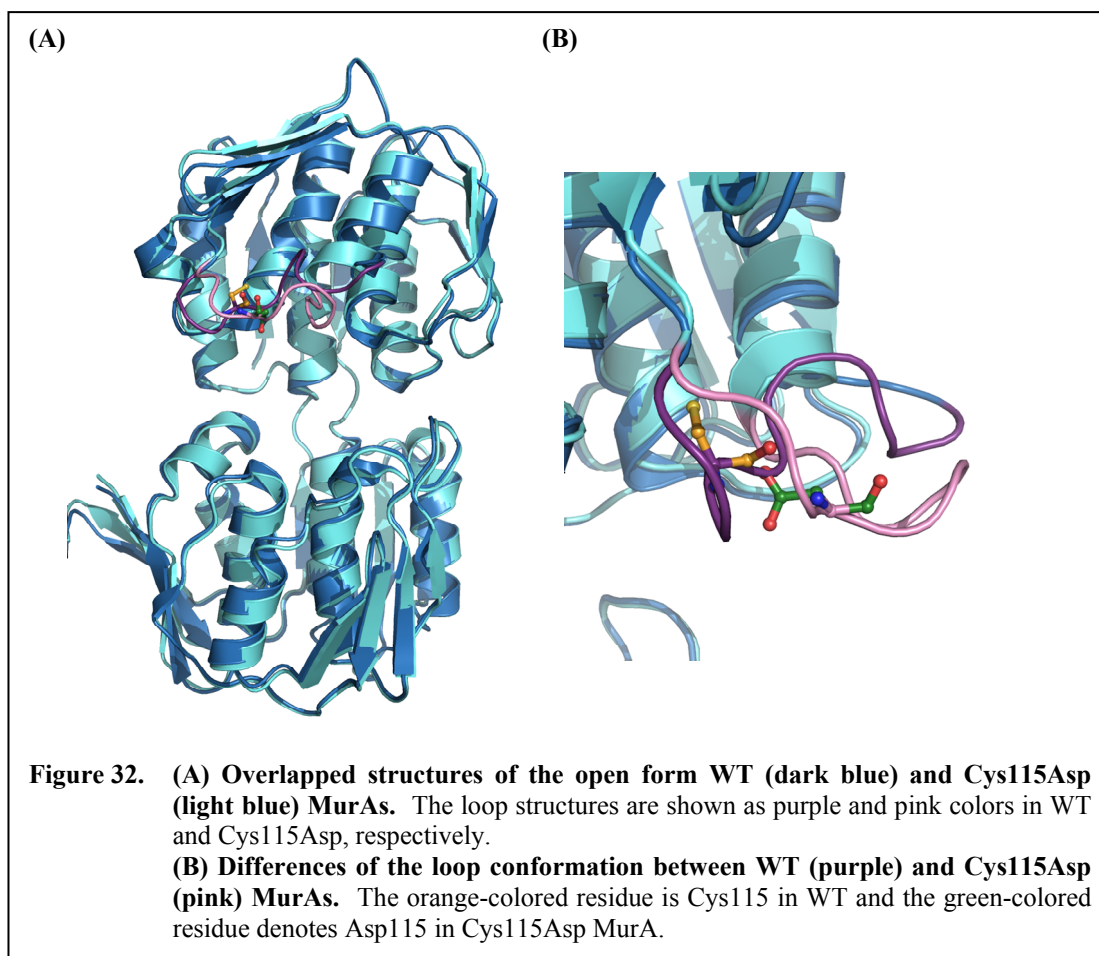
Since the complex structure of Arg120Ala MurA with UNAG and PEP showed the evidence of the thio-ketal tetrahedral intermediate, the mechanistic role of the Cys115 residue has received more attention. Although the new mechanism can lower the activation energy of the enzyme reaction, the same mechanism is not likely to happen in Cys115Asp MurA because the carboxylate in the Asp residue is much weaker nucleophile compared to the Cys residue. Therefore, the enzymatic mechanism of Cys115Asp MurA cannot include the thio-ketal intermediate, but the 3'-OH of UNAG directly attacks PEP creating a PEP-UNAG tetrahedral intermediate. It is considered that the activation energy of Cys115Asp MurA is higher than WT as a result of the direct attack of the 3'-OH of UNAG. To test this hypothesis, the

Activity Ratio	25 °C/5 °C	25 °C/15 °C	15 °C/5 °C
WT	3.6	1.5	2.4
Cys115Asp	9.1	2.0	4.6
E_a (Kcal/mol)	25 °C/5 °C	25 °C/15 °C	15 °C/5 °C
WT	11.0	7.2	14.4
Cys115Asp	18.7	12.0	25.1

activities of both WT and Cys115Asp MurAs were measured at 5, 15, and 25 °C, and the activity ratios at different temperatures were calculated to derive

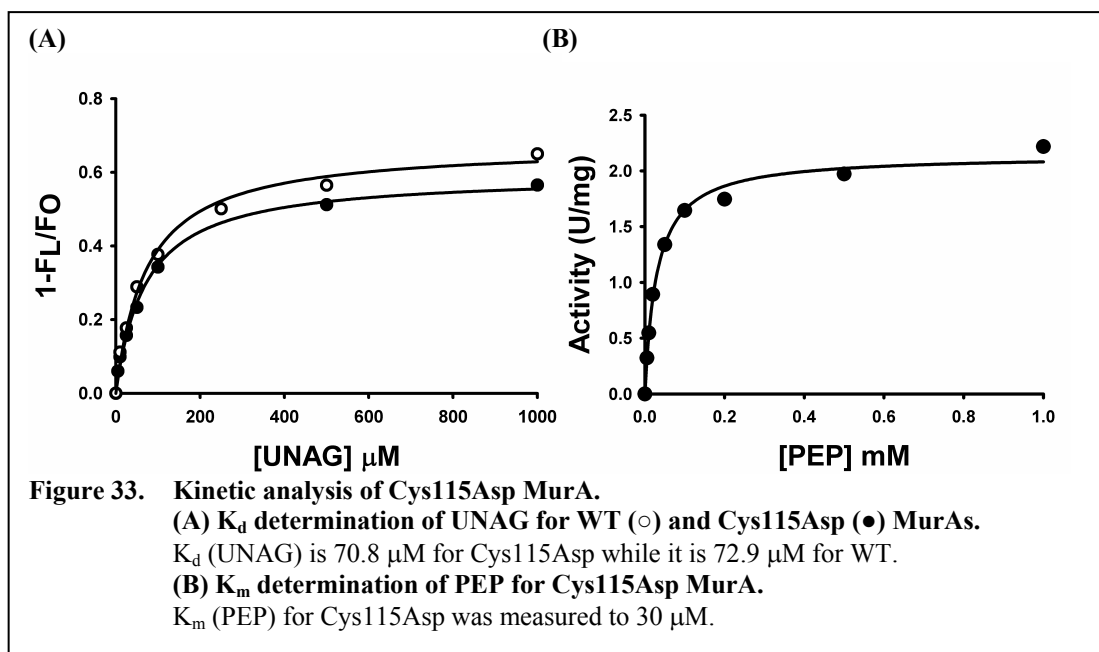
activation energy values (Table 10). Although the values of E_a differ at various temperatures in one enzyme, the data clearly demonstrate that the activation energy of Cys115Asp MurA is higher than WT.

Cys115 in *E. cloacae* MurA is located in a flexible loop that undergoes a large conformational change upon UNAG binding. Thus it was thought that the mutation of Cys115 to other amino acid residues would affect the conformation of the loop. The un-liganded structure of Cys115Asp MurA was solved to 1.95 Å resolution (Figure 32). Although this crystal was formed under the same conditions as the WT crystal, it had a different crystal lattice. The loop conformation of the open form of Cys115Asp MurA is different from WT, however this does not affect UNAG binding. From a previous kinetic study by Dr. Melanie Priestman¹⁴¹, the K_m value of UNAG for the mutant enzyme is similar to WT at pH 6, and the values are even lower than WT at pH 7 and 8, implying that UNAG binds to the mutant enzyme with better affinity at physiological pH. This was also confirmed by the determination of the dissociation constant (K_d) of UNAG (Figure 33A). The K_d value of UNAG for



Cys115Asp is 70.8 μM , and 72.9 μM for WT, indicating that the Cys115 mutation does not influence UNAG binding.

However, the mutation of Cys115 to Asp alters the binding of PEP. For WT MurA, the K_m value of PEP is too low to measure (less than 0.1 μM), whereas it was measured for Cys115Asp MurA to be 30 μM (Figure 33B). Although Cys115Asp MurA needs a higher concentration of PEP to obtain the full velocity of the enzyme reaction (V_{max}), it is still in the range of the physiological concentration of PEP, 0.2 mM ¹⁴². Thus, MurA in those species that have aspartate instead of cysteine at the



115 position is still as active as the other species that contain cysteine, but they are not inhibited by fosfomycin.

The ideal molecular mode of action of MurA inhibitor is binding in the UNAG binding site and preventing the conformational changes. This mechanistic-based inhibitor would also inhibit Cys115Asp mutant MurA, which is resistant to fosfomycin. To design this kind of inhibitor, the detailed information of enzymatic mechanism of MurA is required. Thus, the mechanistic studies of MurA described in this thesis will be used as critical information to design the inhibitors deriving the open-closed conformational changes.

3.2. Identification and Characterization of MurA Inhibitors

Although MurA is a proven antibiotic drug target, very few inhibitors have been identified. To date, fosfomycin, the active ingredient of Monurol[®], is the only marketed drug targeting MurA. Several resistant mechanisms against fosfomycin were revealed, thus, there is a need for the discovery of new inhibitors of MurA.

3.2.1. Study of Known MurA Inhibitors

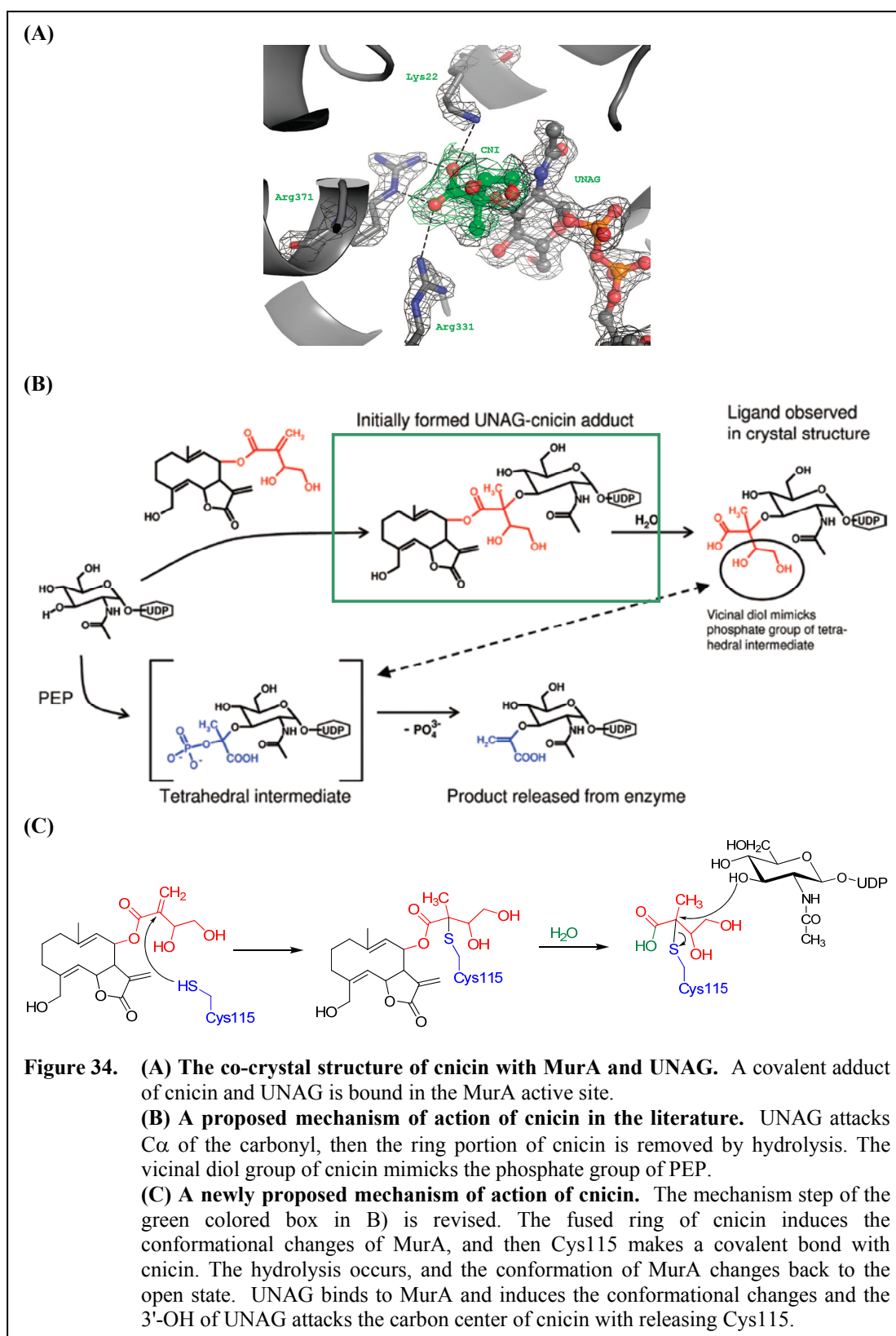
3.2.1.1. Peptide Inhibitors

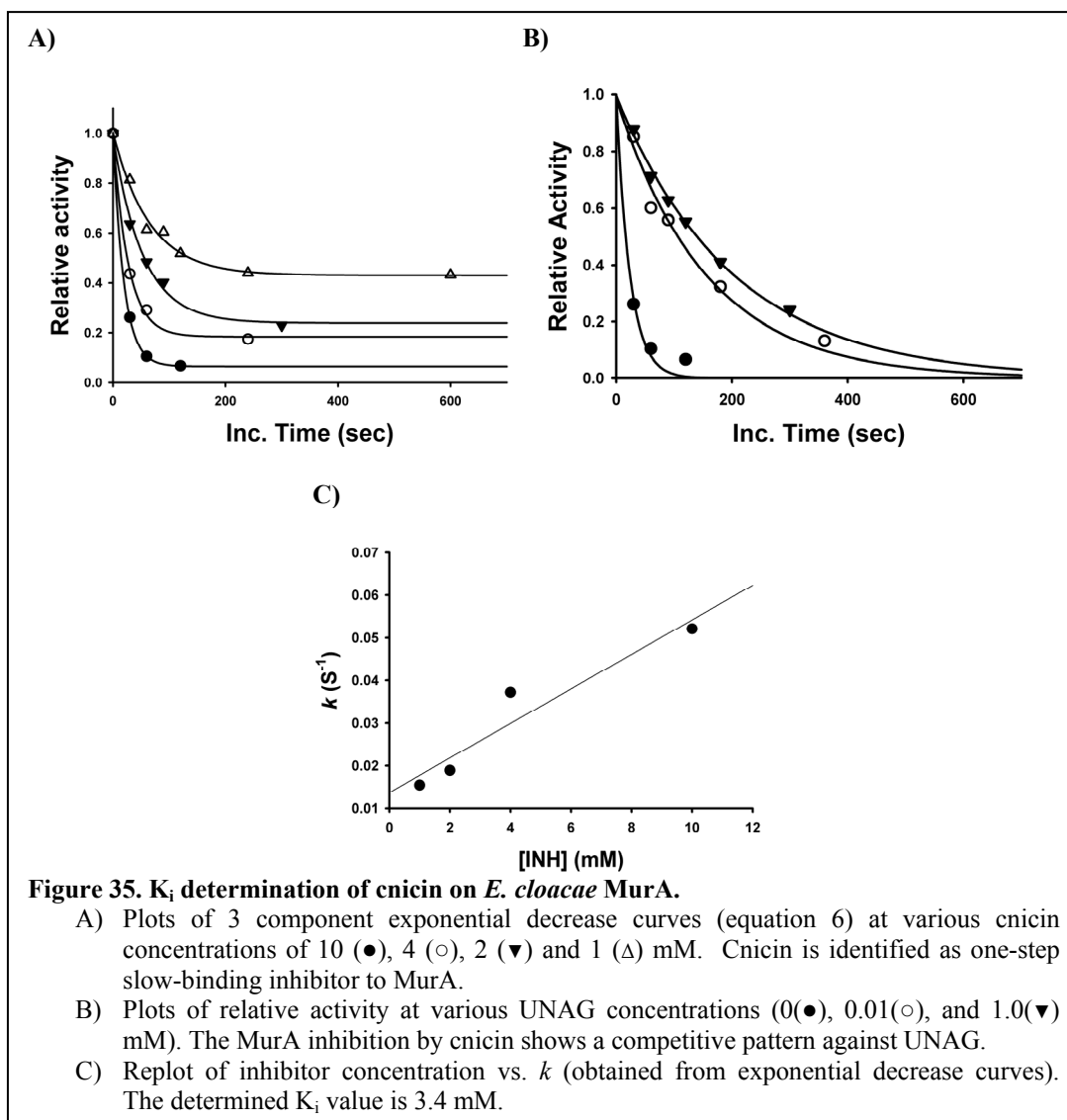
Kinetic evaluations of known inhibitors from the literatures have been performed. The peptide inhibitor, HESFWYLPQSY, identified from phage display libraries⁶³ was synthesized at the University of Kansas. No inhibitory activity of the peptide on WT *E. cloacae* MurA was found at 1 mM concentration even though the peptide was reported to inhibit *Pseudomonas aeruginosa* MurA with an IC₅₀ value of 200 μM.

Notably, a protein of viral origin, A2 maturation factor (420 amino acids), was recently reported as a potent MurA inhibitor, inducing bacterial lysis⁶⁴. The A2 maturation factor was cloned and the studies to produce the protein in a large-scale are currently underway in Prof. Schönbrunn's laboratory.

3.2.1.2. Cnicin

A natural product, cnicin was recently reported as an irreversible inhibitor by preliminary kinetic studies⁶⁰ and the co-crystal structure with *E. coli* MurA was solved by the same research group¹⁴³ (Figure 34A). Cnicin is a sesquiterpene lactone,





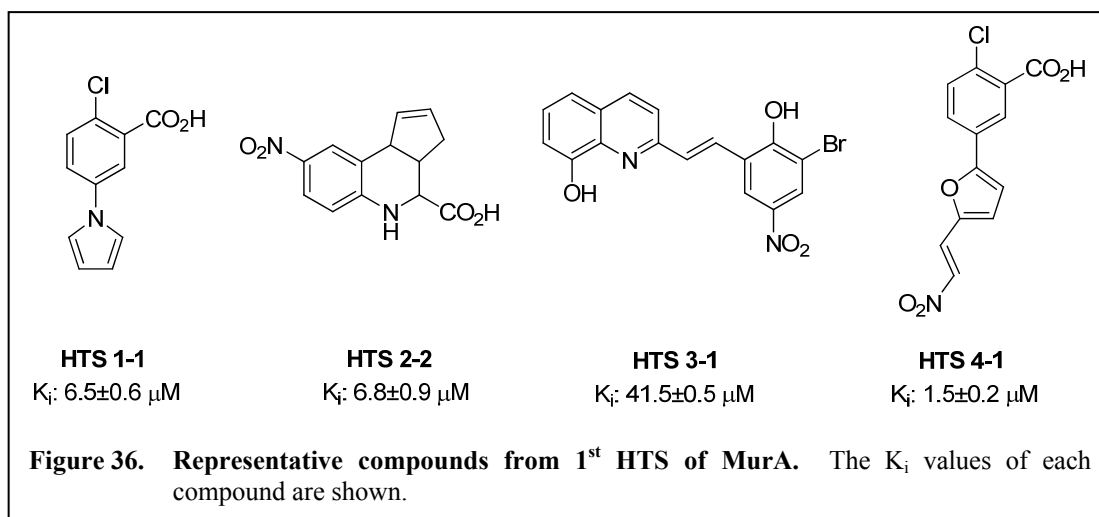
and its α,β -unsaturated carbonyl group is thought to be electrophilic. The solved structure revealed the formation of a covalent adduct between cnicin and UNAG. It shows that cnicin acts as a non-covalent suicide inhibitor (Figure 34B).

We purchased cnicin and tested its inhibitory potential on *E. cloacae* MurA. The measured inhibitory potency was much lower (K_i value of 3.4 mM) than the reported value (IC_{50} value of ~ 10 μ M). The mode of action found in our kinetic study of

cnicin indicated a one-step slow-binding inhibition (Figure 35A). In addition, the inhibition of cnicin was competitive to UNAG (Figure 35B), contrary to the mode of action reported in the literature. Although Cys115Asp mutant MurA is reportedly not inhibited by cnicin, the authors proposed the molecular mode of action of cnicin did not involve Cys115 (Figure 34B). However, based on our preliminary studies and findings that Cys115 covalently attaches to PEP, we propose a different mode of action of cnicin (Figure 34C): First, cnicin binds to the UNAG binding site of MurA and induces the conformational changes. In the closed form, Cys115 make a covalent bond with cnicin, and then the hydrolysis of cnicin occurs, releasing the fused ring system. Once the conformation of MurA goes back to the open state, UNAG binds to its binding site and induces the conformational changes again. The 3'-OH group of UNAG then attacks the Cys115-cnicin adduct and replaces Cys115, producing the UNAG-cnicin complex, found in the structure. This newly proposed mechanism seems more rational because it includes the role of Cys115, and the mechanism of action proposed in the literature indicates that cnicin is a non-specific group-specific inhibitor. To provide further confirmation, thorough kinetic and structural studies are currently ongoing.

3.2.2. Identification and Characterization of Novel MurA Inhibitors

From a previous high-throughput screening (HTS) campaign with 50,000 compounds from ChemBridge, four new chemical scaffolds of MurA inhibitors were identified¹⁴¹. Representative compounds from each scaffold were studied thoroughly (Figure 36). Initial kinetic studies indicated that freshly dissolved **HTS 2** compounds



in DMSO did not display inhibitory potential to MurA, while the ‘aged’ (incubated in DMSO or MeOH at room temperature) solutions showed inhibition. Color changes of DMSO and MeOH solutions, from light to dark, were detected as well. These results imply that there is an unidentified reaction of **HTS 2** compounds in DMSO or MeOH, and the product of this reaction is the active component as the MurA inhibitor. Black-colored solid precipitated out from **HTS2-2** solution in MeOH with time. Although the product was identified as the active ingredient, the attempt to identify the chemical structure of this compound by NMR and mass spectra was not successful (data not shown).

Inhibition kinetics were performed with **HTS2-2** to understand its molecular mode of action on MurA. **HTS2-2** was identified as a mixed inhibitor with respect to UNAG (Figure 37). The K_i for **HTS2-2**, with respect to alteration of the affinity for UNAG, is 6.8 μM, whereas the K_i' with respect to changes in maximal velocity of MurA, is 42 μM. The dissociation constant of **HTS2-2** was measured by the ANS

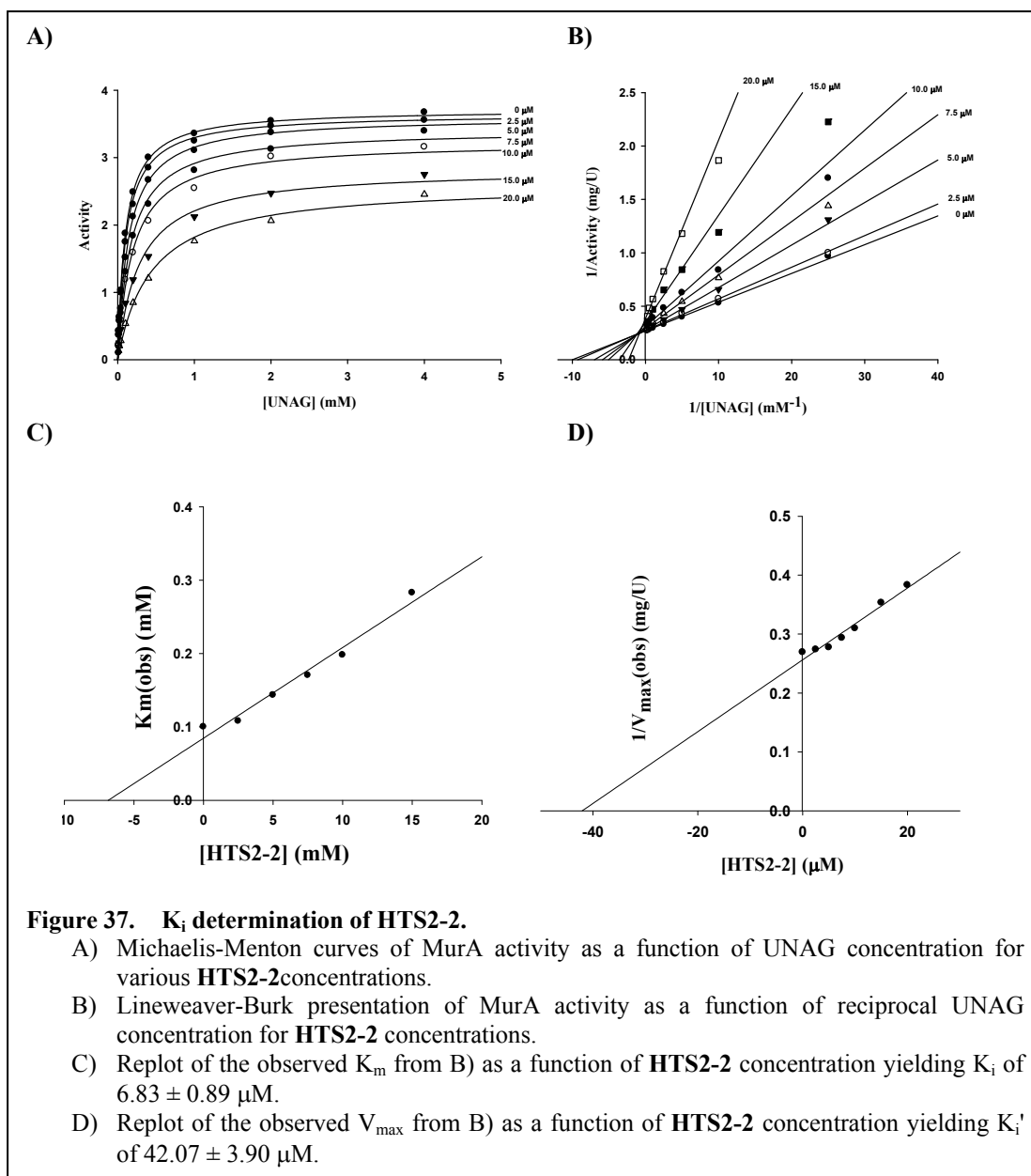
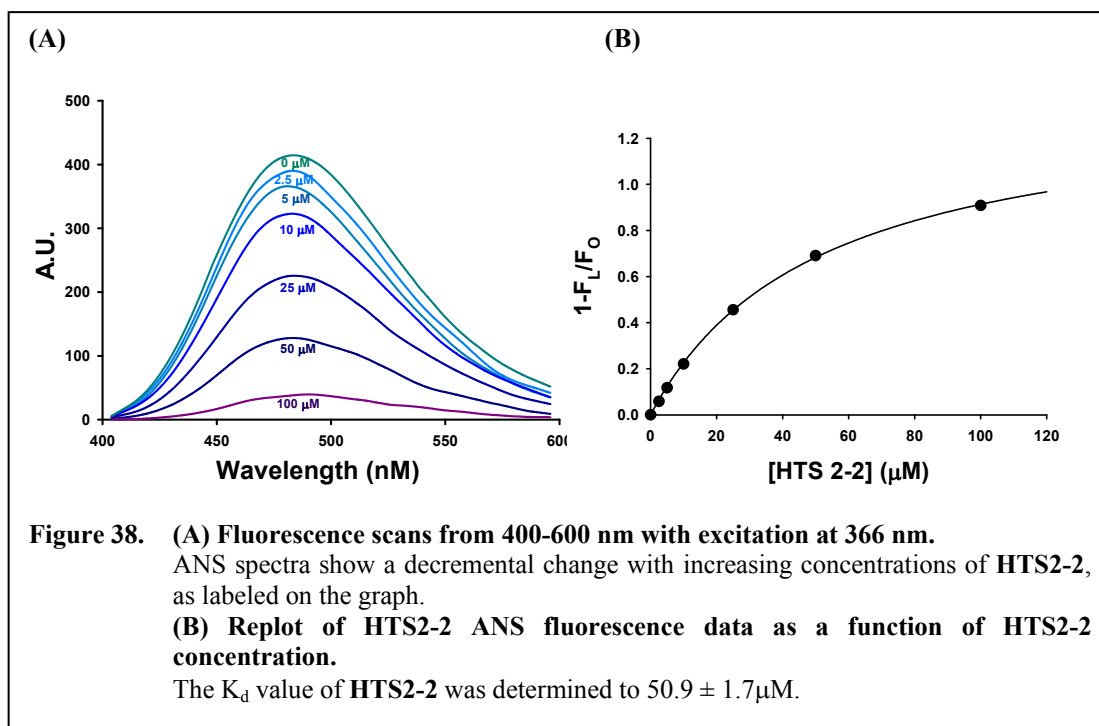


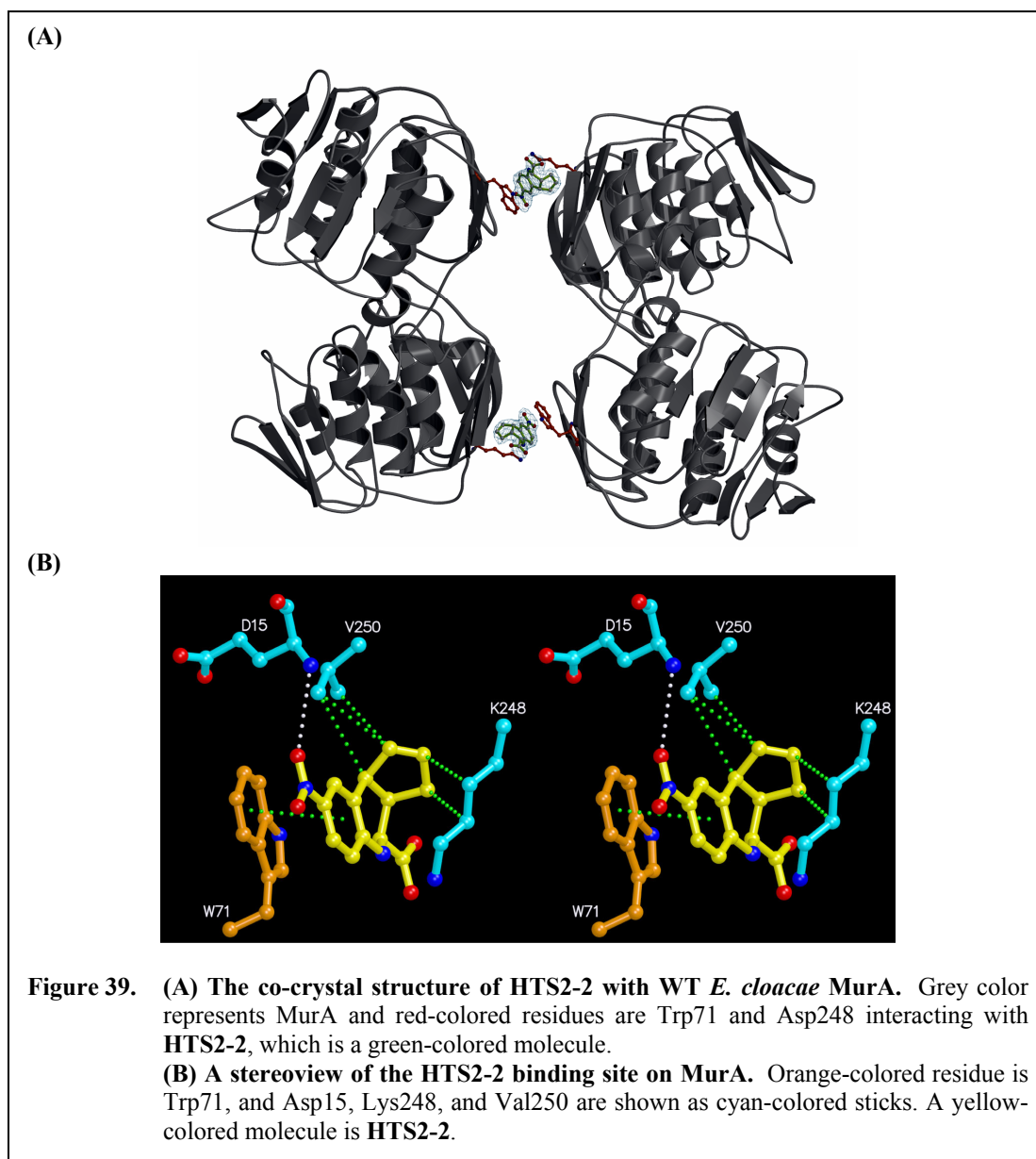
Figure 37. K_i determination of HTS2-2.

- A) Michaelis-Menten curves of MurA activity as a function of UNAG concentration for various HTS2-2 concentrations.
- B) Lineweaver-Burk presentation of MurA activity as a function of reciprocal UNAG concentration for HTS2-2 concentrations.
- C) Replot of the observed K_m from B) as a function of HTS2-2 concentration yielding K_i of $6.83 \pm 0.89 \mu\text{M}$.
- D) Replot of the observed V_{max} from B) as a function of HTS2-2 concentration yielding K_i' of $42.07 \pm 3.90 \mu\text{M}$.



fluorescence assay, and the K_d value for **HTS2-2** is $51 \mu\text{M}$ (Figure 38) indicating that this inhibitor binds in the loop region of MurA. These results of the kinetic and fluorescence studies suggest that **HTS2-2** binds in the vicinity of the UNAG binding site, but cannot cause the conformational change from the open to the closed state. Therefore, we propose that **HTS2-2** inhibits MurA in a similar way to T6362, the Aventis inhibitor (compound 9 in Figure 9), i.e. bind in the loop region of the open state MurA and inhibit the conformational changes.

Intense efforts were made to obtain co-crystal structures of MurA with the HTS inhibitors. **HTS2-2** was co-crystallized with MurA, and the structure was refined to 2.3 \AA resolution. Although clear electron density of **HTS2-2** was visible in the solved structure, the binding site was opposite to the active site of MurA (Figure 39A). A close look of the binding site demonstrates that the binding of

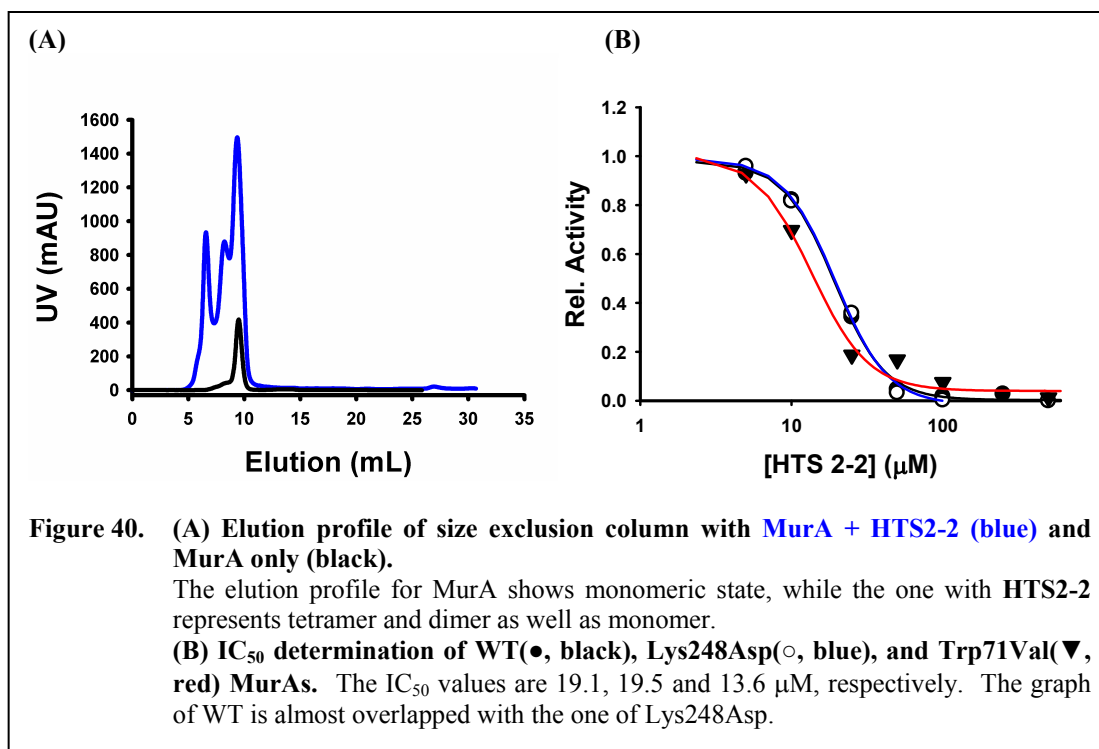


HTS2-2 with MurA is mostly from hydrophobic interactions (Figure 39B), i.e. cyclopentene ring of HTS2-2 interacts with Lys248 and Val250, and the aromatic ring is in a range of a π - π stacking interaction with Trp71. Only the nitro group of HTS2-2 has a hydrogen bond with the backbone nitrogen of Asp15. The structural

data do not corroborate with the inhibition kinetics, the latter suggesting that **HTS2-2** binds to the loop containing Cys115 in the open form of MurA.

Because of the unexpected binding of **HTS2-2** observed in the crystal structure, further studies with **HTS2-2** were performed. A mixed solution of MurA containing **HTS2-2** was subjected to a size exclusion chromatography to investigate possible oligomerization of MurA induced by the inhibition.. The elution profile of the mixture of MurA with **HTS2-2** is consistent with mixture of monomer, dimer and tetramer, whereas un-liganded MurA under the same experimental condition is clearly monomeric. These results confirmed that **HTS2-2** indeed induces oligomerization of MurA (Figure 40A).

The hydrophobic interactions of **HTS2-2** with Trp71 and Lys248 were eliminated by mutations to Val and Asp, respectively. Val and Asp were chosen because they



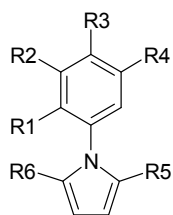
are found in the equivalent position in other MurAs. The enzymatic activities of these mutant enzymes were similar to WT, and the inhibitions by **HTS2-2** were also retained (Figure 40B). If the dimerization of MurA by **HTS2-2**, found in the co-crystal structure, is the inhibitory mechanism, **HTS2-2** should be ineffective against these mutant enzymes. Thus, the inhibitory activity of **HTS2-2** against Trp71Val and Lys248Asp MurA infers that the co-crystal structure is an artifact of crystallization, and the MurA dimerization via hydrophobic interactions with Trp71 and Lys248 is not the inhibitory mechanism by **HTS2-2**. Crystallization trials of these mutant enzymes with **HTS2-2** using the same condition as with WT enzyme failed to produce crystals, suggesting that **HTS2-2** promotes crystallization of only the WT enzyme in this particular crystal lattice. In other words, **HTS2-2** can be considered as a mere crystallization additive under this condition.

Co-crystallization of **HTS1-1** with WT MurA was attempted and crystals were formed in the presence of *iso*-propanol (H1-41 conditions in Table 9). The crystals are not X-ray graded yet, and refining the crystallization conditions is currently underway.

To study structure-activity relationships (SAR) of scaffolds **HTS 1** and **2**, 35 and 51 analogs of each scaffold were tested with WT *E. cloacae* MurA (Tables 11 and 12). For the **HTS 1** scaffold, the carboxylic acid functional group at the R2 position was essential as well as a chloride or hydroxyl group at R3 for inhibitory activity. When the pyrrole ring was changed to a pyrrolidine ring or succinimide, the inhibitory activity was significantly decreased while the variation of the 5-membered

ring to maleimide retained the inhibitory activity. For the **HTS 2** scaffold, the carboxylic acid group at the R1 or R2 position was essential for their inhibitory activity. Notably, when R2 was a carboxylic acid, aromaticity was required at the R1 position. Freshly made solutions of **HTS 2** compounds in DMSO were not active on MurA. However, the compounds became active after the incubation at room temperature, although the incubation time varied for different compounds. Thus, the activity of the compounds in this scaffold was measured until they showed inhibition, up to two weeks. As shown on the Table 12, most compounds inhibited MurA after the incubation. Thus, the SAR evaluation of the **HTS 2** scaffold was not possible although it was clear that the carboxylic acid group is required at the R1 or R2 position. It is probably due to the fact that unknown reaction of the compounds occurs in the solution and the product is the active component. Thereafter, it is proposed that the unknown reaction depends on the existence of the carboxylic acid group at the R1 or R2 position.

Table 11. SAR table of the HTS 1 scaffold.



ID	R1	R2	R3	R4	R5	R6	Remaining activity at 500 μM (%)	IC ₅₀ (μM)
H1-1	H	CO ₂ H	Cl	H	H	H		27.2 \pm 2.7
H1-2	H	CO ₂ H	OH	H	H	H	10	~190
H1-3	H	CO ₂ H	OH	H	Me	Me	14	82.6 \pm 2.1
H1-4	H	CO ₂ H	Cl	H	Ph	Me	129	

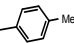
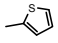
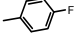
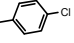
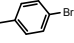
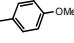
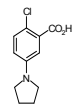
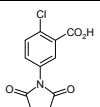
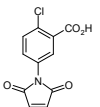
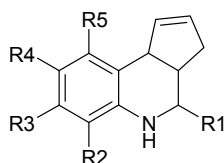
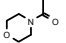
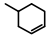
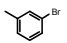
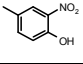
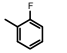
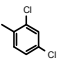
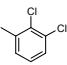
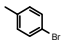
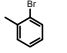
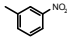
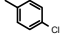
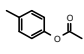
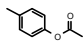
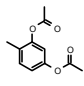
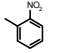
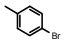
H1-5	H	CO ₂ H	Cl	H	Me	Me	100	
H1-6	Cl	CO ₂ H	H	H	H	H	102	
H1-7	H	CO ₂ H	H	H	Ph	Me	147	
H1-8	H	CO ₂ H	H	H	Me	Me	106	
H1-9	H	CO ₂ H	H	CO ₂ H	Me	Me	95	
H1-10	Me	CO ₂ H	H	H	Me	Me	110	
H1-11	H	CO ₂ H	CO ₂ H	H	Me	Me	95	
H1-12	H	CO ₂ H	H	H	Ph	CH ₂ CH ₂ CO ₂ H	129	
H1-13	H	CO ₂ H	H	H		CH ₂ CH ₂ CO ₂ H	158	
H1-14	H	CO ₂ H	H	H		CH ₂ CH ₂ CO ₂ H	139	
H1-15	H	CO ₂ H	H	H		CH ₂ CH ₂ CO ₂ H	137	
H1-16	H	CO ₂ H	H	H		CH ₂ CH ₂ CO ₂ H	171	
H1-17	H	CO ₂ H	H	H		CH ₂ CH ₂ CO ₂ H	169	
H1-18	H	CO ₂ H	H	H		CH ₂ CH ₂ CO ₂ H	140	
H1-19	Me	H	H	CO ₂ H	H	H	100	
H1-20	OH	H	H	CO ₂ H	Me	Me	97	
H1-21	Me	H	H	CO ₂ H	Me	Me	91	
H1-22	Cl	H	H	CO ₂ H	Me	Me	93	
H1-23	H	CO ₂ Me	Cl	H	H	H	104	
H1-24	H	NO ₂	Cl	H	H	H	116	
H1-25	H	CONMe ₂	Cl	H	H	H	101	
H1-26	H	CH ₂ CO ₂ H	H	H	H	H	106	
H1-27	H	Cl	CO ₂ H	H	H	H	107	
H1-28	H	Cl	CO ₂ H	H	Me	Me	108	
H1-29	H	OH	CO ₂ H	H	H	H	101	
H1-30	NO ₂	H	CO ₂ H	H	H	H	70	
H1-31	OH	H	CO ₂ H	H	H	H	103	
H1-32	H	H	OH	H	H	H	93	
H1-33							56	
H1-34							97	
H1-35							13	30.1 ± 1.7

Table 12. SAR table of the HTS 2 scaffold.



ID	R1	R2	R3	R4	R5	Remaining activity at 500 μ M (%)	IC ₅₀ (μ M)
H2-1	CO ₂ H	OH	H	Cl	NO ₂	5	
H2-2	CO ₂ H	H	Me	H	Me	7	
H2-3	CO ₂ H	H	H	NO ₂	H	8	46.8 \pm 2.0
H2-4	CO ₂ H	H	H	Br	H	8	28.9 \pm 1.9
H2-5	CO ₂ H	CF ₃	H	H	H	8	39.7 \pm 2.0
H2-6	CO ₂ H	I	H	Me	H	8	41.8 \pm 0.4
H2-7	CO ₂ H	H	H	COO(CH ₂) ₃ CH ₃	H	9	
H2-8	CO ₂ H	CONH ₂	H	H	H	9	
H2-9	CO ₂ H	H	H		H	11	
H2-10	CO ₂ H	Me	Cl	H	H	12	
H2-11	CO ₂ H	CO ₂ H	H	H	H	12	13.5 \pm 0.4
H2-12	CO ₂ H	H	H	SO ₂ NH ₂	H	14	
H2-13	CO ₂ H	H	H	acetyl	H	14	
H2-14	CO ₂ H	OMe	H	H	H	15	
H2-15	CO ₂ H	H	H	CO ₂ H	H	15	8.5 \pm 0.7
H2-16	CO ₂ H	H	H	CO ₂ Et	H	17	58.0 \pm 4.0
H2-17	CO ₂ H	H	H	COOCH ₂ CH(CH ₃) ₂	H	16	
H2-18	CO ₂ H	H	H	Me	H	19	
H2-19	CO ₂ H	OH	H	H	H	21	
H2-20	CO ₂ H		H	H	H	24	
H2-21	CO ₂ H	H	H		H	24	
H2-22	CO ₂ H	CF ₃	H	H	Cl	28	
H2-23	CO ₂ H	Me	H	I	H	32	
H2-24	CO ₂ H	H	H		H	40	
H2-25	CO ₂ H	H	H		H	44	
H2-26	CO ₂ H	H	H		H	44	

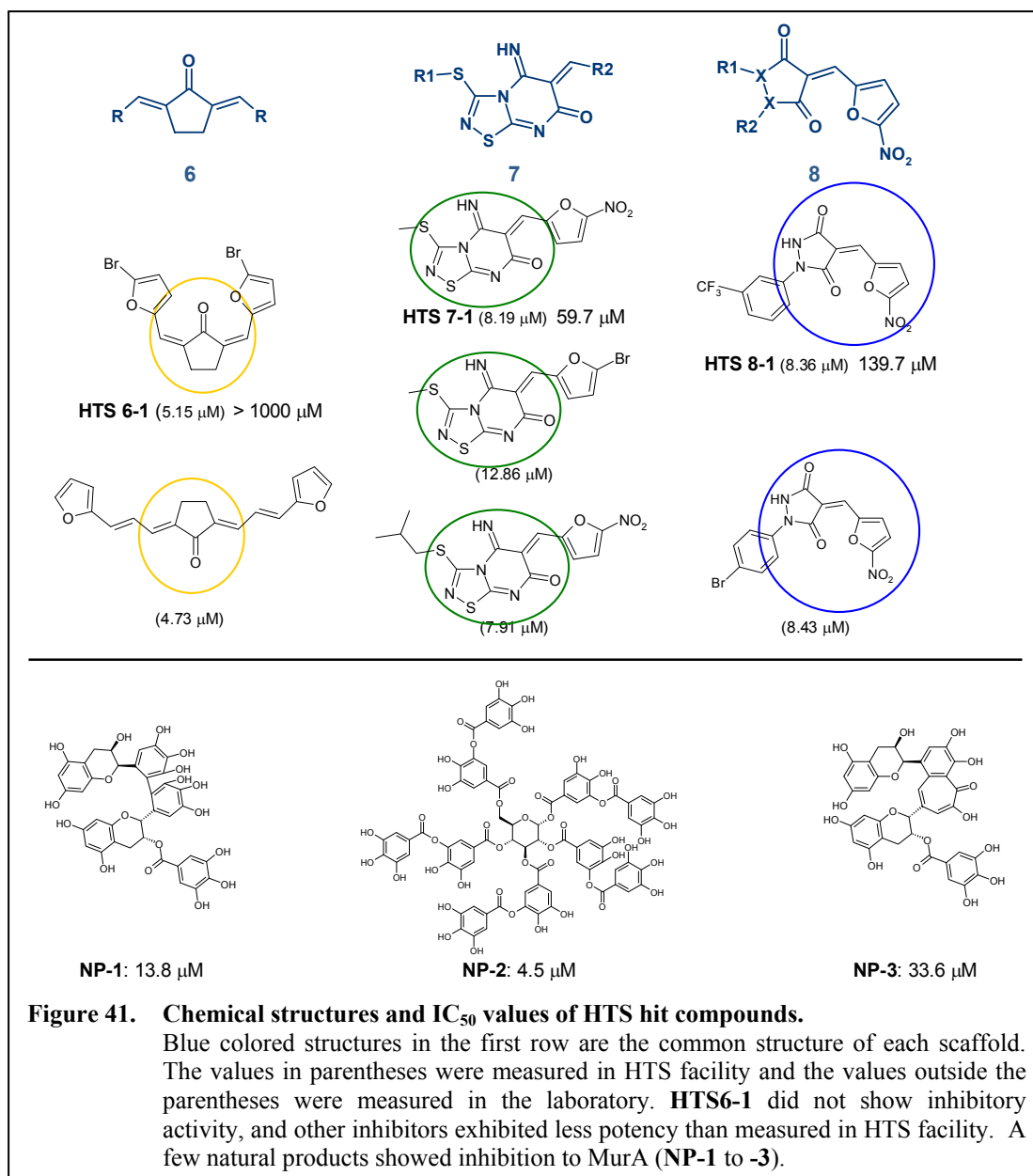
H2-27		CO ₂ H	H	H	H	66	
H2-28		CO ₂ H	CO ₂ H	H	H	NO ₂	78
H2-29		CO ₂ H	Me	H	NO ₂	H	90
H2-30		CO ₂ Et	H	H	NO ₂	H	90
H2-31		CO ₂ Et	Me	CO ₂ H	H	H	112
H2-32		H	CO ₂ H	H	H	NO ₂	102
H2-33		propyl	CO ₂ H	H	H	NO ₂	117
H2-34		CO ₂ H	H	H		NO ₂	106
H2-35	Ph	CO ₂ H	H	H		NO ₂	47
H2-36		CO ₂ H	H	H		H	16
H2-37		CO ₂ H	H	H		H	16
H2-38		CO ₂ H	H	H		H	17
H2-39		CO ₂ H	H	H		H	20
H2-40		CO ₂ H	H	H		H	22
H2-41		CO ₂ H	H	H		H	25
H2-42		CO ₂ H	H	H		H	25
H2-43		CO ₂ H	H	H		H	26
H2-44		CO ₂ H	H	H		NO ₂	28
H2-45		CO ₂ H	H	H		H	52
H2-46		CO ₂ H	H	H		NO ₂	54
H2-47		CO ₂ H	H	H		H	109
H2-48		CO ₂ H	H	H		H	120
H2-49		H	H	SO ₂ NH ₂		H	95

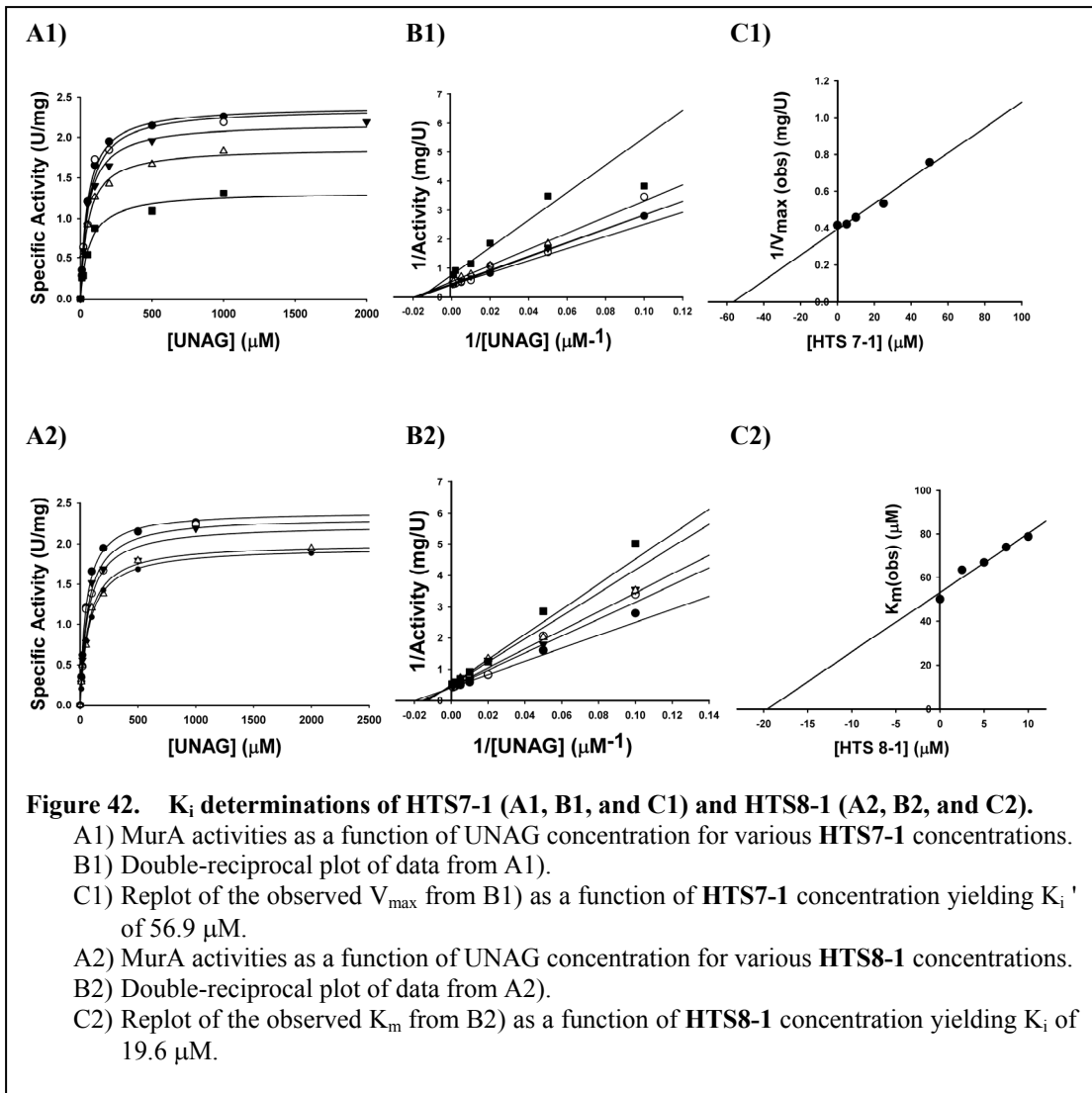
H2-50			H	H	H	98
H2-51		CO ₂ Me	H	H	H	105

In addition to the previous high-throughput screening of 50,000 compounds, 50,000 more compounds from ChemDiv and MicroSource were screened. The IC₅₀ values were determined for the compounds showing less than 40 % remaining activity against WT *E. cloacae* MurA. As a result, 49 new compounds were found with IC₅₀ values in a range of 5 μM to 50 μM. 11 compounds belong to scaffolds **HTS 2, 3, 4,** or **5**, and the others were categorized into 3 new scaffolds and natural products (**NP**). (Figure 41) Representative compounds of each group (**HTS6-1, HTS7-1, HTS8-1,** and **NP-1, -2, and -3**) were purchased and tested to confirm their inhibitory activity. Inhibitory activity of **HTS6-1** was not observed while the other compounds also showed less inhibitory potency compared to the values from HTS under the same condition. None of the compound showed time-dependent inhibition characteristics.

To understand the modes of action on MurA, inhibition kinetics of **HTS7-1** and **HTS8-1** were conducted. **HTS7-1** showed non-competitive inhibition regarding UNAG. The K_i' was determined to 56.9 μM (Figure 42A1-C1). **HTS8-1** is a mixed inhibitor with respect to UNAG. The K_i for **HTS8-1**, regarding alteration of the affinity for UNAG, is 19.6 μM, whereas the K_i', with respect to changes in maximal velocity of MurA, is 40.1 μM (Figure 42A2-C2). The efforts to obtain co-crystal structures of **HTS7-1** or **HTS8-1** with MurA have not succeeded to date.

The verifications of the HTS hits were not successful with commercially obtained compounds. One possible explanation for this is that the compounds in the HTS library did undergo chemical modifications, e.g. oxidation, radical reactions. We conclude that the best strategy for now is to repeat the HTS campaign with newer and possibly more diverse compound libraries.



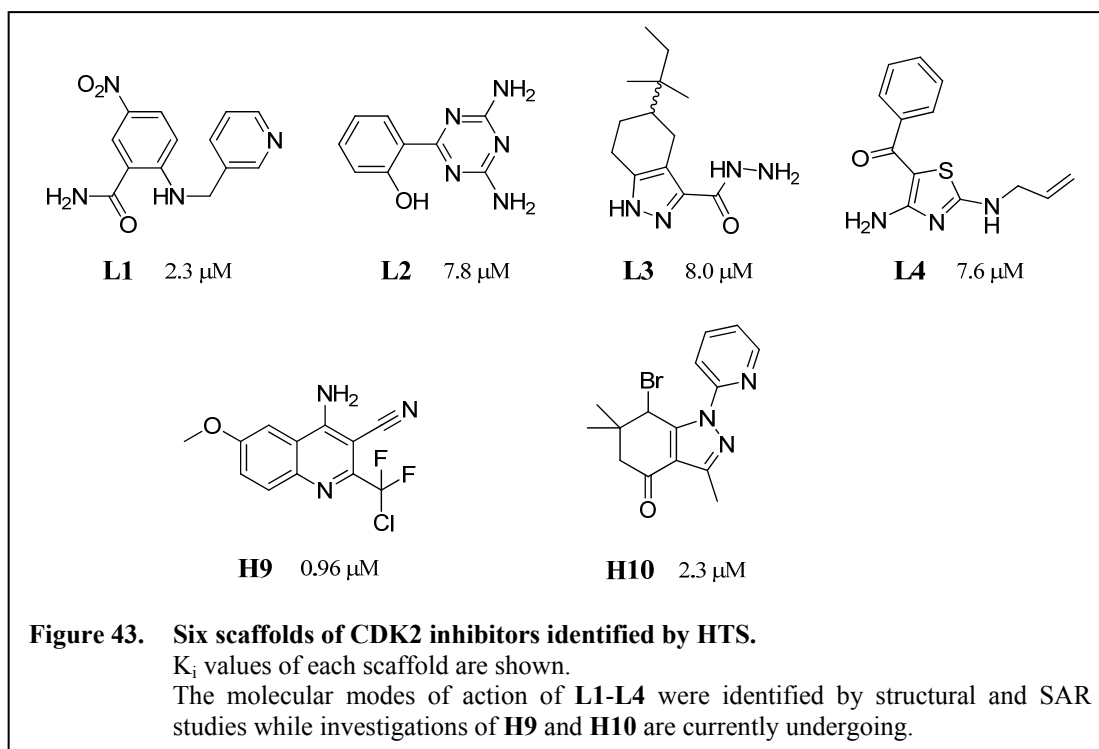


3.3. Inhibitors of Cyclin-dependent Kinase 2

High-throughput screening (HTS) was performed by Dr. Rawle Francis in the HTS facility of the University of Kansas, and kinetic analysis of CDK2 was performed by Dr. Andreas Becker. The synthesized analogs were provided by the laboratory of Dr. Gunda Georg at the University of Minnesota.

Cyclin-dependent kinases (CDKs) are key enzymes in the regulation of the cell cycle, and abnormal over-expression of CDKs is often observed in human cancer cells. Thus, intense efforts to discover anti-cancer drugs that inhibit CDKs have been made for the last two decades. Although a number of small molecule CDK inhibitors have been identified, assisted by expanded structural information about CDK2, they frequently lack adequate potency and/or specificity. It is clear that improved selectivity will be required for the next generation of CDK inhibitors.

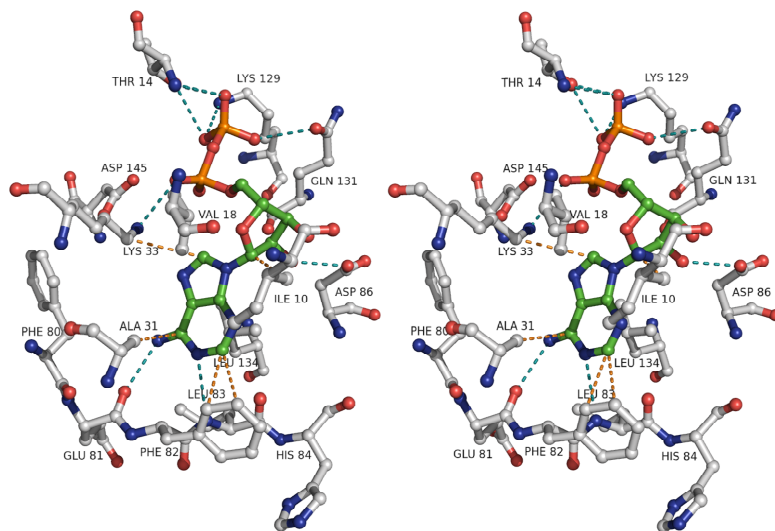
HTS was conducted with about 100,000 compounds resulting in the identification of 62 compounds demonstrating more than 60 % inhibition of CDK2 at 8.3 $\mu\text{g/mL}$ concentration. These hits were categorized into six different scaffolds and the representatives of each scaffold are shown in Figure 43 with their K_i values. Four of the representative compounds were co-crystallized with CDK2 and they were all seen to occupy the ATP binding pocket of CDK2. The co-crystallized compounds were named Lead 1 (**L1**) to Lead 4 (**L4**). More compounds with scaffolds **L1** – **L4** were purchased or synthesized, and inhibitory potencies were measured for structure



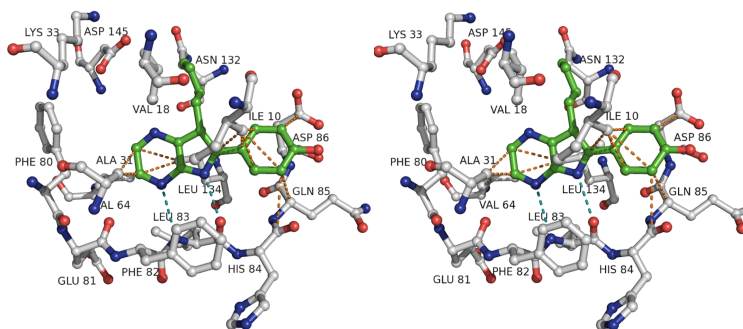
activity relationship (SAR) studies. The detailed molecular modes of action of several analogs were analyzed by crystallographic studies.

Prior to the study with the lead compounds, efforts to understand the ATP binding site of CDK were performed with the co-crystal structure of ADP on CDK2 (Figure 44). The interactions of ADP with CDK2 were almost the same as with the ATP binding although the electron density of the β -phosphate group of ADP was too weak to refine its conformation of the phosphate group. In addition, the co-crystal structures of CDK2 with two known inhibitors, aloisine A and NU6027 (chemical structures are shown in Figure 15), were solved to 1.75 and 1.85 Å resolution, respectively. Aloisine A bound to the ATP binding site has two hydrogen bonds with the backbone carbonyl oxygen and nitrogen atoms of Leu83. The phenyl ring

ADP



Aloisine A



NU6027

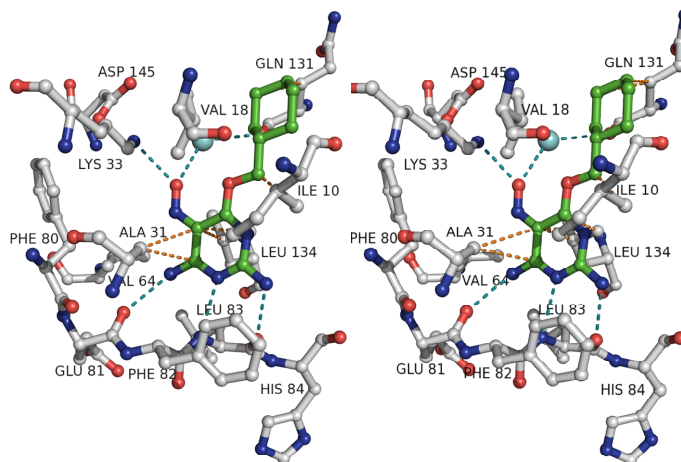


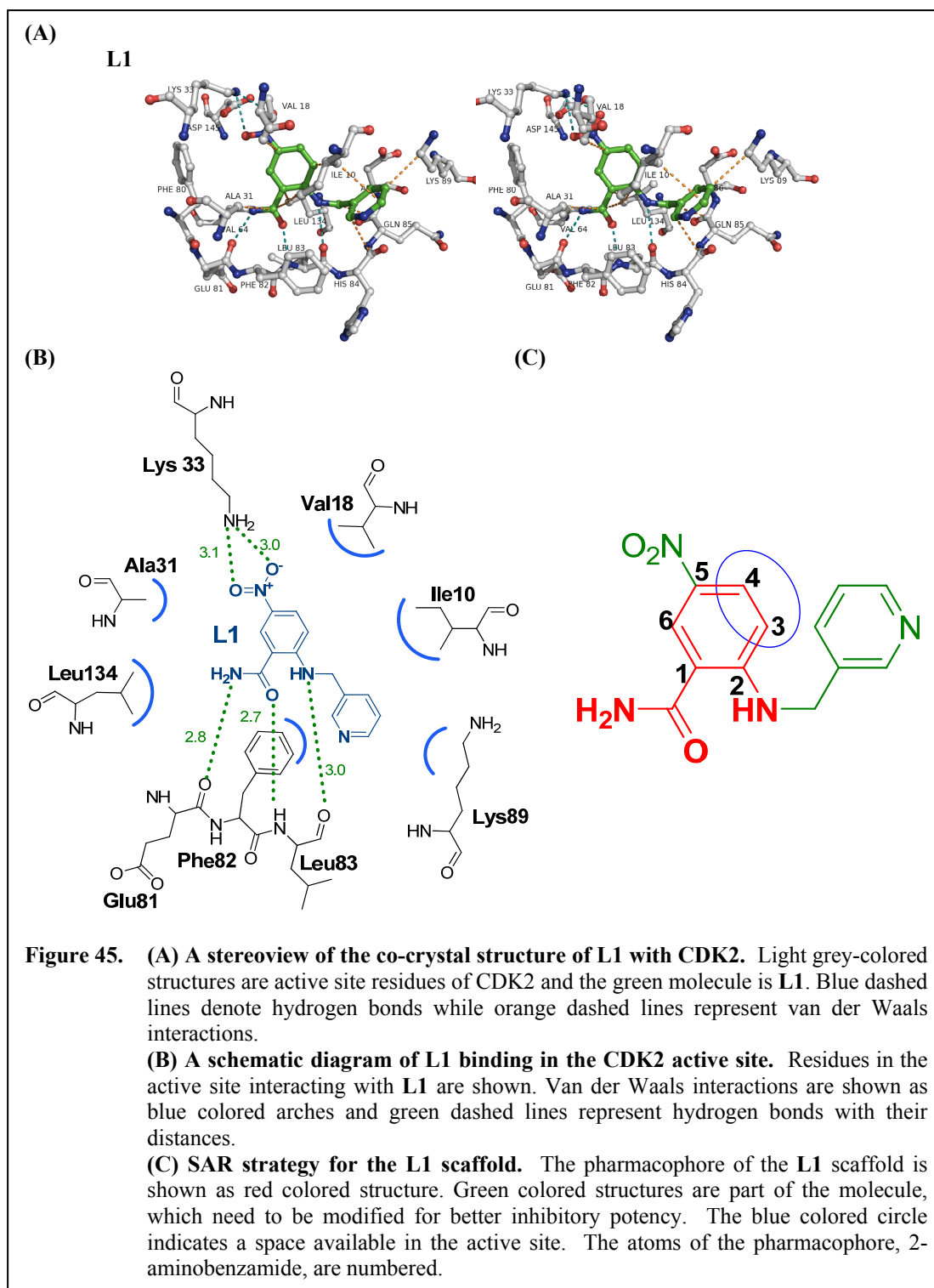
Figure 44. Stereoviews of the co-crystal structures of ADP, aloisine A, and NU6027 with CDK2. Light grey-colored structures are active site residues of CDK2 and green molecules are ligand structures. A water molecule is shown as a cyan-colored sphere. Blue dashed lines denote hydrogen bonds while orange dashed lines represent van der Waals interactions.

maintains hydrophobic forces with Ile10 and Gln85. NU6027 forms three hydrogen bonds between the pyrimidine ring and the backbone atoms of Glu81 and Leu83. The 5-nitroso group of NU6027 has hydrogen bonds with the backbone nitrogen of Asp145 and a water molecule, which interacts with the backbone carbonyl of Gln131.

From these preliminary structural studies, it was confirmed that the hydrogen bonds with the backbone atoms of Glu81 and Leu83 are probably important for the binding because they are present in every ligand bound CDK2 structures including ADP, aloisine A and NU6027. In addition to these hydrogen bonds, the hydrophobic interactions with Ala31 and Leu134 were consistently observed in the structures.

3.3.1. Lead 1 and its analogs

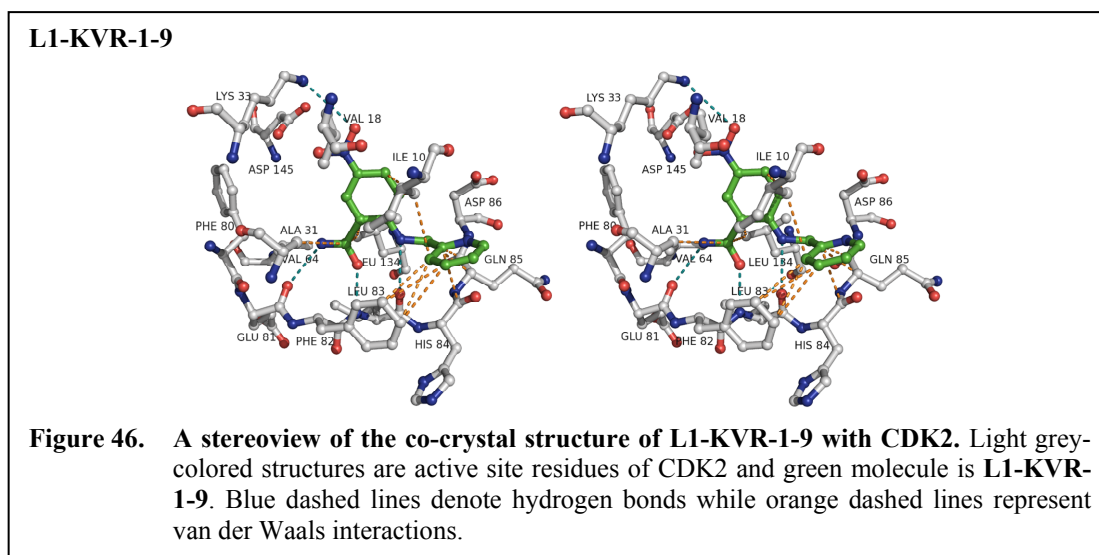
Lead 1 (**L1**, 5-nitro-2-(pyridine-3-ylmethylamino)benzamide), identified by HTS, showed a K_i value of 2.3 μM for CDK2/cyclinA. The crystal structure of **L1** with CDK2 was solved to 1.85 Å (Figure 45A). **L1** was bound in the ATP binding pocket containing three key hydrogen bonds with the backbone carbonyl oxygen atoms of Glu81 and Leu83 and the backbone nitrogen of Leu83: the amide group on C1 forms hydrogen bonds with the backbone carbonyl oxygen atom of Glu81 and the backbone amide nitrogen of Leu83, and the amino group on C2 interacts with the backbone carbonyl of Leu83. The nitro group on C5 forms a salt bridge with the side chain amine of Lys33. The benzene ring of **L1** has hydrophobic interactions with Ile10, Val18, Ala31, and Leu134. Ile10 is also close enough to the pyridine ring of **L1** to make hydrophobic interactions (Figure 45B).



The pharmacophore of **L1** was proposed as the aminobenzamide moiety from structural information obtained from the co-crystal structure of **L1** bound to CDK2. Spaces for elongations from the core structure were available on the 3 and 4 positions of the aminobenzamide ring (Figure 45C), thus the investigations of the derivatives with various groups on those sites were needed. The variation of the pyridine ring to other aromatic ring systems or aliphatic chains and the modification of the nitro group to other hydrogen bond acceptor groups, e.g. carboxylate, were proposed. Several compounds satisfying the above conditions were commercially obtained as well as synthesized, and tested against CDK2/cyclinA (Tables 13 and 14).

The amide group of the **L1** scaffold was confirmed to be critical by kinetic analysis of several **L1** derivatives. Compounds with a carboxylate group instead of an amide on the C1 position of the benzene ring, **L1-KVR-1-38**, **-42**, **-43**, **-46**, and **-52**, lost their inhibitory activity.

The IC₅₀ values of **L1** analogs also indicated that the inhibitory potency of **L1** depended on the presence of a methylene-aromatic ring moiety connected to the amino nitrogen of aminobenzamide (R1 group): all the compounds without the methylene-aromatic ring were inactive against CDK2/cyclinA. Inhibition was not observed for the compounds without the ring system, **L1-3**, **L1-4**, and **L1-13**. The compounds with saturated rings, **L1-9**, **L1-11**, and **L1-KVR-1-25**, did not show inhibitory activity. Although the R1 substituents include aromatic rings, it was observed when the length of the carbon linker between the 2-amino group and the



ring was not one carbon, the inhibitory activities significantly decreased (e.g. **L1-5** (two-carbon linker), **L1-KVR-1-22** (no carbon)).

L1 analogs with variations at the position of the nitrogen atom on the pyridine ring of R1 group, 2-position (**L1-KVR-1-9**), 4-position (**L1-KVR-1-45**), and 2, 5-positions (**L1-KVR-1-67**) have been tested and their activities did not differ from the parent compound, **L1** (3-position). Even the compound without the nitrogen atom on the aromatic ring (**L1-10**) had an IC_{50} that was not much different than the value of the pyridine ring system (**L1**). This result was consistent with the information from structural data, where no specific interaction of the pyridyl nitrogen and CDK2 residues existed. The co-crystal structure of **L1-KVR-1-9** with CDK2 was also solved to 1.95 Å (Figure 46). The interaction of the pharmacophore of the inhibitor with the receptor was the same as **L1**. The orientation of the pyridine ring was rotated a little compared to **L1**. However, the electron density of this part of the molecule was poor, showing high temperature factors (B-factors). This implied that

Table 13. SAR table of the L1 scaffold (1). Blue shaded compounds were co-crystallized with CDK2.

ID	R1	R2	R3	IC ₅₀ (μM)
L1		H	NO ₂	3 (IC ₅₀) 2.3 (K _i)
L1-3		H	NO ₂	> 140
L1-4		H	NO ₂	> 140
L1-5		H	NO ₂	> 140
L1-9		H	NO ₂	> 140
L1-10		H	NO ₂	12
L1-11		H	NO ₂	> 140
L1-13	H	H	NO ₂	> 140
L1-KVR-1-5		H	NO ₂	59
L1-KVR-1-6		H	NO ₂	26
L1-KVR-1-7		H	NO ₂	31
L1-KVR-1-8		H	NO ₂	38
L1-KVR-1-9		H	NO ₂	9.1
L1-KVR-1-12		H	NO ₂	200
L1-KVR-1-13		H	NO ₂	15
L1-KVR-1-15		H	NO ₂	9350
L1-KVR-1-22		H	NO ₂	610
L1-KVR-1-25		H	NO ₂	13800
L1-KVR-1-32		H	NO ₂	440
L1-KVR-1-45		H	NO ₂	7
L1-KVR-1-55		Cl	NO ₂	3.0
L1-KVR-1-55-2			NO ₂	> 1000
L1-KVR-1-56		Cl	NO ₂	1.9

Table 14. SAR tables of the L1 scaffold (2).

The L1 scaffold (2) is a benzamide derivative. It consists of a benzene ring with an amide group (-NH-R₁) at the 1-position, a primary amide group (-NH₂) at the 2-position, and substituents R₂ at the 3-position and R₃ at the 4-position.

ID	R1	R2	R3	IC ₅₀ (μM)
L1-KVR-1-67		H	NO ₂	6.8
L1-KVR-1-74		H	NO ₂	11.7
L1-KVR-1-75		H	NO ₂	14.5
L1-KVR-1-76		H	NO ₂	> 1000
L1-KVR-1-78		Cl	NO ₂	1.0

The L1 scaffold (2) is a benzamide derivative. It consists of a benzene ring with an amide group (-NH-R₁) at the 1-position, a carboxylic acid group (-COOH) at the 2-position, and substituents R₂ at the 3-position and R₃ at the 4-position.

ID	R1	R2	R3	IC ₅₀ (μM)
L1-KVR-1-38		H	NO ₂	> 5000
L1-KVR-1-42		H	NO ₂	36000
L1-KVR-1-43		H	NO ₂	470
L1-KVR-1-46		H	NO ₂	4900
L1-KVR-1-52		H	NO ₂	> 5000

the R1 group of L1 analogs was flexible and did not have critical interactions with CDK2, thus it needs to be modified to have specific binding in the active site. One suggestion is a substitution on the phenyl ring with hydrogen bond acceptors and/or donor groups because Lys, Asp and Glu residues are located near the phenyl group binds. The R1 group is also open to solvent exposed space, thus it possibly stabilizes the binding of the ligand on CDK2.

The attempt to increase inhibitory potency was carried out by varying the electronic character of the aromatic ring of R1. Analogs with the substitutions on the phenyl ring with *p*-methoxy (L1-KVR-1-5), *p*-methyl (L1-KVR-1-6), *p*-chloride (L1-KVR-1-7), *p*-fluoride (L1-KVR-1-8), 2,3-difluoro (L1-KVR-1-12), 3,4-difluoro

(**L1-KVR-1-13**), *p*-trifluoromethyl (**L1-KVR-1-15**), and 3,4-dichloro (**L1-KVR-1-32**) were synthesized and their inhibitory activities were tested. As a result, none of the analog compounds with substituents on the aromatic ring had significantly better potencies. Compounds, **L1-KVR-1-12**, **-15**, and **-32**, showed even considerably less activities than **L1-10** (no substitution on the phenyl ring). Thus, it was assumed that the electronic properties of the aromatic ring did not affect the interaction of the **L1** analogs with CDK2. In addition to the hydrophobic substitutions on the phenyl ring, a couple of hydrophilic derivatives, *p*-carboxylic acid (**L1-KVR-1-74**), *p*-aminomethyl (**L1-KVR-1-75**) were synthesized to enhance solvent contacts as well as possible hydrogen bonds. However, both analogs exhibited similar potency compared to **L1-10**, suggesting that neither *p*-carboxylate nor *p*-aminomethyl groups involve the binding to CDK2. Thus may result because the substitutions are not on the right position or they are too small groups to have interactions with CDK2. Thus, future studies should probably include substitution on different positions of the phenyl ring with large hydrophilic functional groups such as sulfonamides.

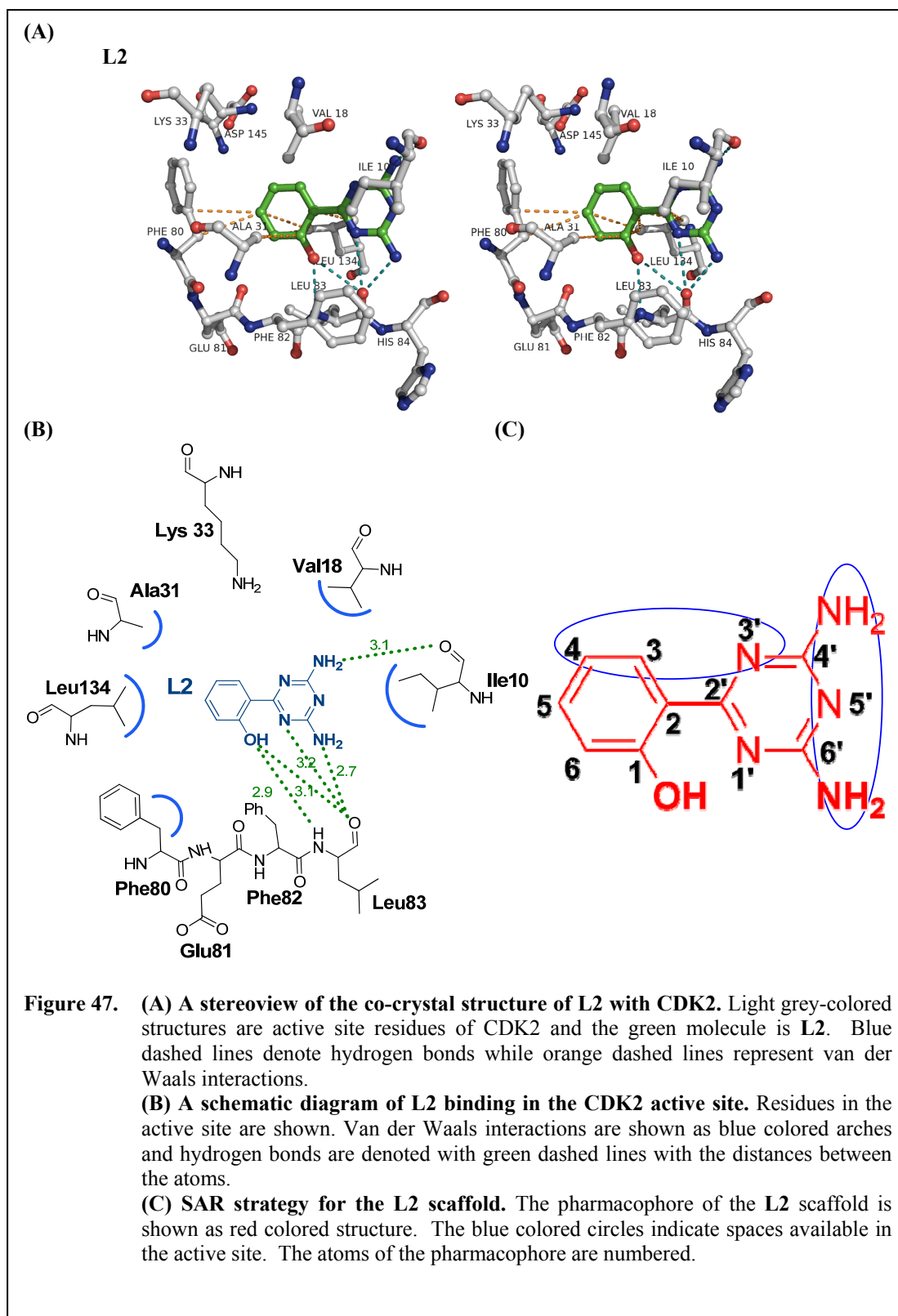
The variation of the R2 group with chloride, **L1-KVR-1-55**, **L1-KVR-1-56**, and **L1-KVR-1-78**, showed 3-fold increased inhibitory potency compared to the analogs without chloride, **L1-KVR-1-9**, **L1-KVR-1-45**, and **L1**. From the structures of **L1** and **L1-KVR-1-9**, it was not possible to explain the increased inhibition because the space for R2 substitution is widely open and the chloride atom does not seem to have interactions with any residues. Thus, the attempt to obtain the structures of the R2-chloride substituted analogs with CDK2 is currently ongoing. **L1-KVR-1-55-2** (R2:

pyridinyl-2-methylamino group) was not active against CDK2/cyclinA, possibly because R2 is too large, thus causing steric clash. Further investigation with various substituents of R2 needs to be performed as well as the modification of the nitro group on R3.

3.3.2. Lead 2 and its analogs

Lead compound 2 (**L2**, 2-(4,6-diamino-1,3,5-triazin-2-yl)phenol) inhibits CDK2 reversibly and competitively with respect to ATP with a K_i value of 7.8 μM . The crystal structure of human CDK2 liganded with **L2** was determined at 2.0 Å resolution (Figure 47A). **L2** has hydrogen bonds with the backbone carbonyl oxygen and the backbone nitrogen of Leu83 in the adenine binding pocket. In addition to the key hydrogen bonds, the amine on C4' of the triazine ring interacts with the backbone carbonyl of Ile10 via a hydrogen bond. The side chain of Ile10 is within a distance of van der Waals interaction ($3.3 \text{ \AA} < d < 3.8 \text{ \AA}$) with the triazine ring of **L2**. The phenol ring is located in the hydrophobic pocket of Ala31, Leu134, and Val18 (Figure 47B).

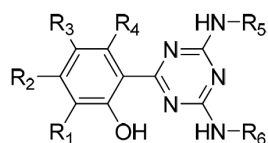
The analysis of the co-crystal structure of **L2** with CDK2 suggested that the pharmacophore of **L2** is **L2** itself (Figure 47C), although the 3'-positioned nitrogen atom of the triazine ring might be replaced by a carbon atom since the nitrogen atom does not have any specific interactions with CDK2. A substitution on C6 of the phenol ring with a functional group containing a hydrogen bond donor is able to increase the inhibitory potency through an additional hydrogen bond with the backbone carbonyl of Glu81. However, modifications on the R1 group are almost not



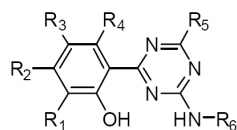
possible due to the limited space: the distance between C6 of the phenol ring and the backbone oxygen atom of Glu81 is 3.3 Å. The space available for substituents on C5 of the phenol ring is not large, thus the variations on the R2 group were proposed with small substituents either to increase hydrophobic forces with neighboring Phe80 and Val64 or to have interactions with π -electrons of the side chain of Phe80. The distances from C4 of the phenol ring to Lys33 and Asp145 are 4.3 and 4.8 Å, respectively. The addition of a functional group for the ionic interaction with either Lys33 or Asp145 was suggested. Substitutions of R4, R5, and R6 with large groups seem to be possible based on the structural information obtained from **L2** bound CDK2.

Commercially available or synthesized derivatives of **L2** were tested for the CDK2/cylinA inhibition using steady-state kinetics (Tables 15 and 16). It was suggested that the 2-OH group of the phenol ring was critical for the inhibitory activity of the **L2** analog by the co-crystal structure of **L2** with CDK2, and this idea was supported by activity tests of **L2** derivatives once again. The elimination of the hydroxyl group of the phenol ring, **L2-JWS-6-1**, **L2-JWS-6-14**, **L2-JWS-6-16**, **L2-JWS-6-22**, **L2-JWS-6-24**, **L2-JWS-6-38**, **L2-JWS-6-44**, and **L2-JWS-6-46**, resulted in significant decreases of the inhibitory activity. The role of the 4' amine group of the triazine ring was confirmed to be essential from the results that the compounds, **L2-10** and **L2-11**, without the amine group on the 4'-position of the triazine ring show no inhibitory potency up to 140 μ M.

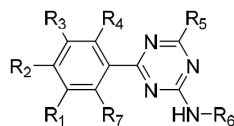
Table 15. SAR tables of the L2 scaffold (1). Blue shaded compounds were co-crystallized with CDK2.



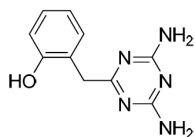
ID	R1	R2	R3	R4	R5	R6	IC ₅₀ (μM)
L2	H	H	H	H	H	H	15 (IC ₅₀) 5.7 (K _i)
L2-2	H	H	Cl	H		H	1.1 (K _i)
L2-3	H	H	Cl	H		H	1.4 (K _i)
L2-4	H	H	Cl	H		H	1.8 (K _i)
L2-5	H	H	Cl	H	H	H	2.2 (K _i)
L2-6	H	H	Cl	H		H	1.3 (K _i)
L2-7	H	H	Cl	H		H	1.0 (K _i)
L2-8	H	H	Cl	H		H	1.7 (K _i)
L2-20	H	H	Cl	H		H	> 140
L2-21	H	H	Cl	H		H	> 140
L2-JWS-6-48	H	H	- OCH ₃	H	H	H	5.6
L2-JWS-6-50	H	- OCH ₃	H	H	H	H	82.5
L2-JWS-6-52	H	H	OH	H	H	H	7.4
L2-JWS-6-76	H	H	F	H	H	H	4.1
L2-JWS-6-78	H	H	- CH ₃	H	H	H	7.4
L2-JWS-6-88		H		H	H	H	181
L2-JWS-6-106	H	Cl	Cl	H	H	H	350



ID	R1	R2	R3	R4	R5	R6	IC ₅₀ (μM)
L2-10	H	H	H	H	- CH ₃	- CH ₃	> 140
L2-11	H	H	H	H		- NH ₂	> 140

Table 16. SAR table of the L2 scaffold (2).

ID	R1	R2	R3	R4	R5	R6	R7	IC ₅₀ (μM)
L2-JWS-6-1	H	Cl	Cl	H	H	H	H	130
L2-JWS-6-14	H	H	Cl	Cl	H	H	H	> 1000
L2-JWS-6-16	H	H	Cl	H	H	H	H	410
L2-JWS-6-22	-CF ₃	H	H	Cl	H	H	H	> 1000
L2-JWS-6-24	H	H	H	H	H	H	H	> 1000
L2-JWS-6-38	H	-CH ₃	-CH ₃	H	H	H	H	> 1000
L2-JWS-6-44	H	H	-OCH ₃	H	H	H	F	1800
L2-JWS-6-46	H	H	-NO ₂	Cl	H	H	H	1900



L2-JWS-6-100

IC₅₀ (μM) : > 1000

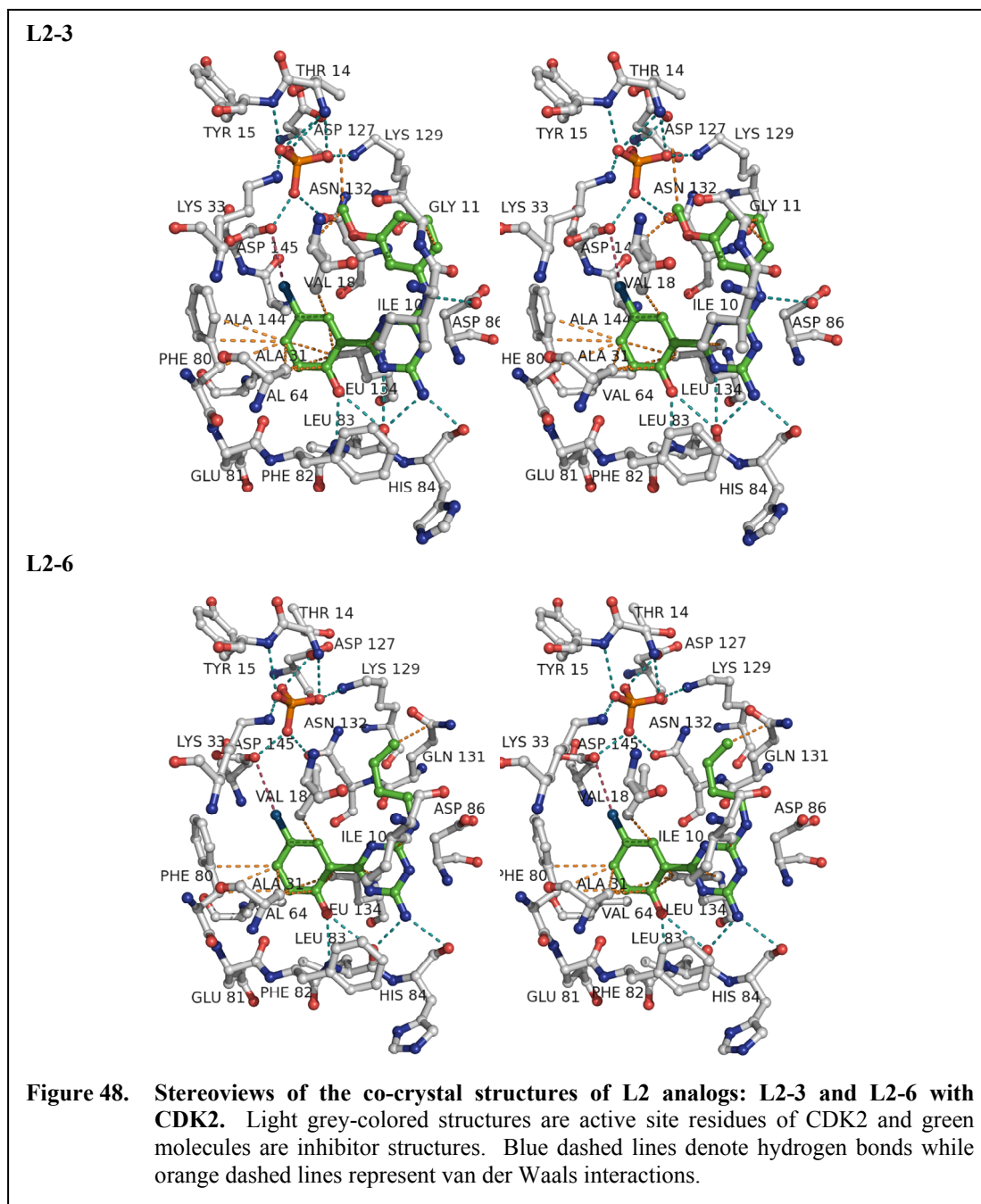
L2 analogs with variations of the R2 group, **L2-JWS-6-50** (methoxy) and **L2-JWS-6-106** (chloride), were tested. The methoxy group on C5 of the phenol ring was still tolerable, but decreased the inhibitory potency by more than 10-fold, implying the methoxy group was too large a substituent on R2. The chloride derivative, **L2-JWS-6-106**, exhibited even lower inhibitory potency (IC₅₀ = 350 μM) than the methoxy derivative (IC₅₀ = 83 μM). The electronic character of methoxy and chloride groups might be the explanation for the difference on their inhibitory potencies despite their similar sizes. The methoxy group, an electron-donating group, is partially positive-charged on the phenol ring, while the chloride group has an electron-withdrawing character, and it is thus partially negative-charged. The side chain of Phe80 is located in the binding pocket of R2 group. Thereafter, the methoxy

group is able to involve a π -cation interaction with Phe80, while the chloride group cannot. A protonated or partially positive-charged small group (e.g. amine or hydroxyl) is expected to participate in a π -cation interaction with the benzene ring of Phe80, and thus enhance the binding affinity of the **L2** analogs to CDK2.

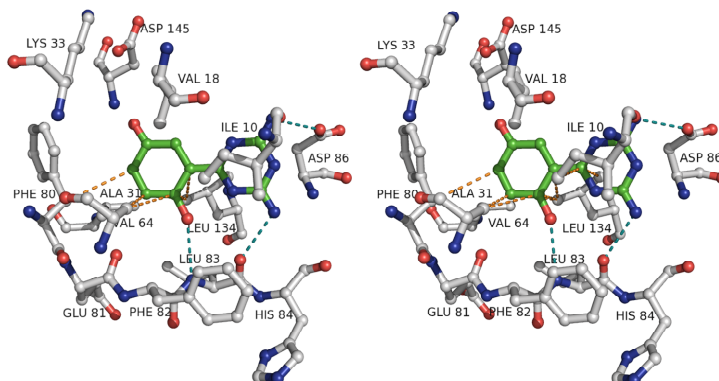
Several different modifications of R3 were made. The substitution of R3 to a chlorine atom, **L2-5**, demonstrated a two to three-fold increase of inhibitory potency, while the modifications with methoxy (**L2-JWS-6-48**), hydroxyl (**L2-JWS-6-52**), fluoride (**L2-JWS-6-76**), and methyl (**L2-JWS-6-78**) did not show a gain in potency. Several variations of the compound **L2-5** were carried out on the 4'-amino group of the triazine ring to various aliphatic and aromatic groups. Most of them showed up to 2-fold increased activity, e.g. **L2-7** with a K_i value of 1.0 μM , than **L2-5**. However, when it was changed to a *p*-halophenyl group, **L2-20** and **L2-21**, the inhibitory activity was considerably decreased. It is considered that the *para*-substituted phenyl ring as the R5 group with an electron-withdrawing group loses the inhibitory potency. The co-crystallization studies of **L2-20** and **L2-21** are ongoing.

The crystal structure of CDK2 liganded with **L2-3** was determined to 2.1 Å resolution (Figure 48). The chlorine atom on C4 of the phenol ring is close to Asp145 ($d = 3.5$ Å) and induces conformational changes of residues “above” the inhibitor binding site, Thr14, Tyr15, Lys129, and Asp127. It appears that these structural changes provide space for the binding of a phosphate ion that is present in the crystallization buffer. The repulsive forces between the chlorine atom of **L2-3** and Asp145 slightly shift the inhibitor molecule towards the backbone of residues

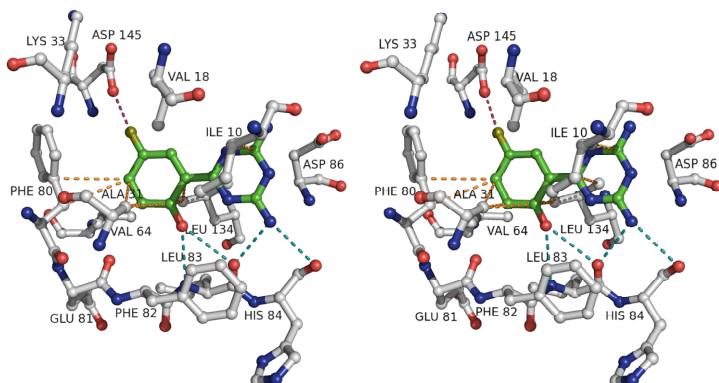
Leu83 and His84, resulting in shorter and presumably stronger hydrogen bonding interactions. The bulky methoxy phenyl group on the C4' position of the triazine ring is relatively loosely bound to the enzyme. The co-crystal structures with L2-6 and



L2-JWS6-52



L2-JWS6-76



L2-JWS6-48

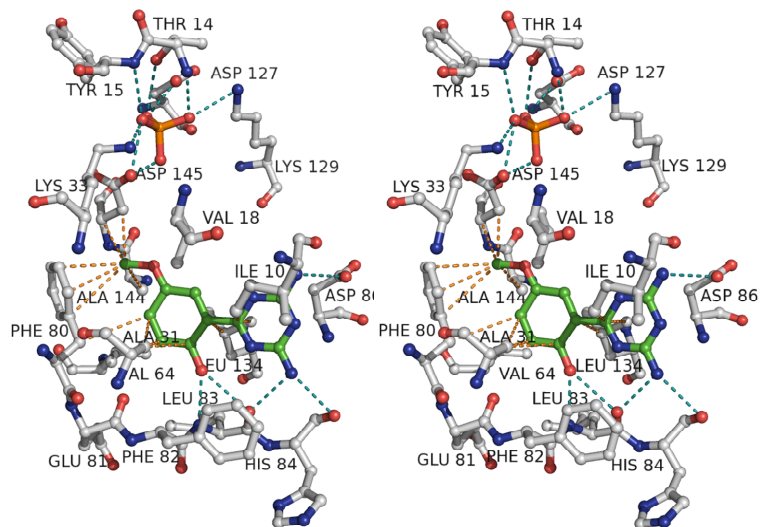
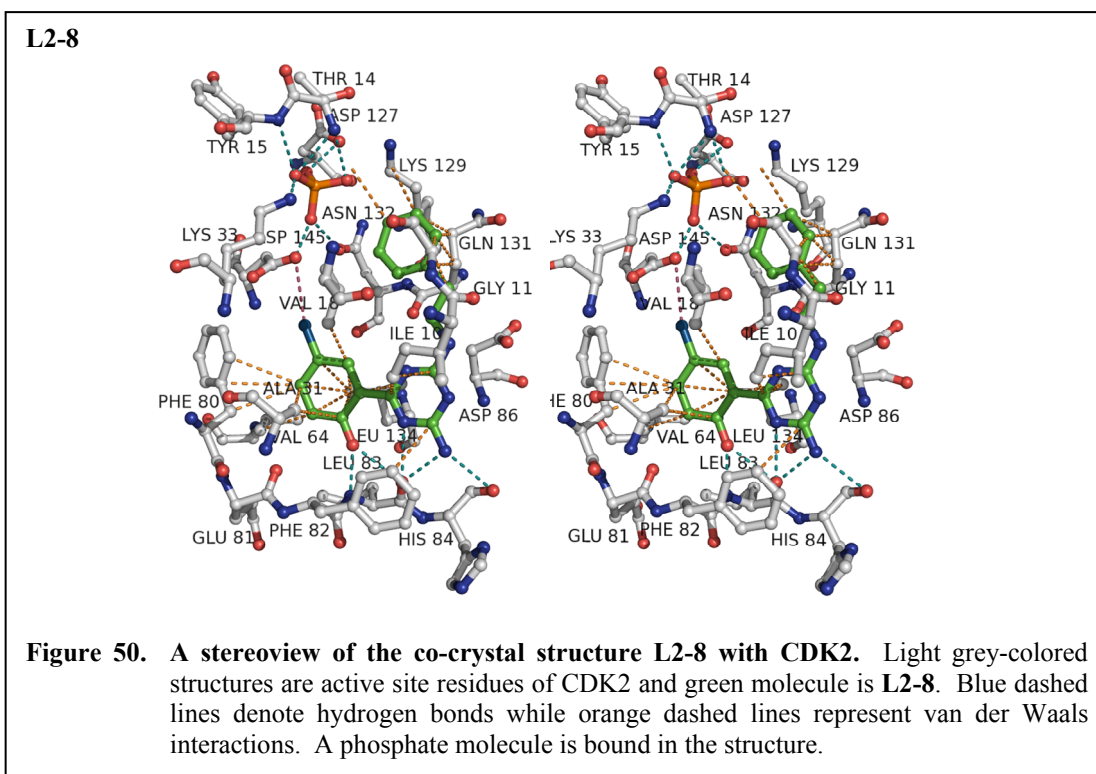


Figure 49. Stereoviews of the co-crystal structures of L2 analogs: L2-JWS6-52, L2-JWS6-76, and L2-JWS6-48 with CDK2. Light grey-colored structures are active site residues of CDK2 and green molecules are inhibitor structures. Blue dashed lines denote hydrogen bonds while orange dashed lines represent van der Waals interactions.



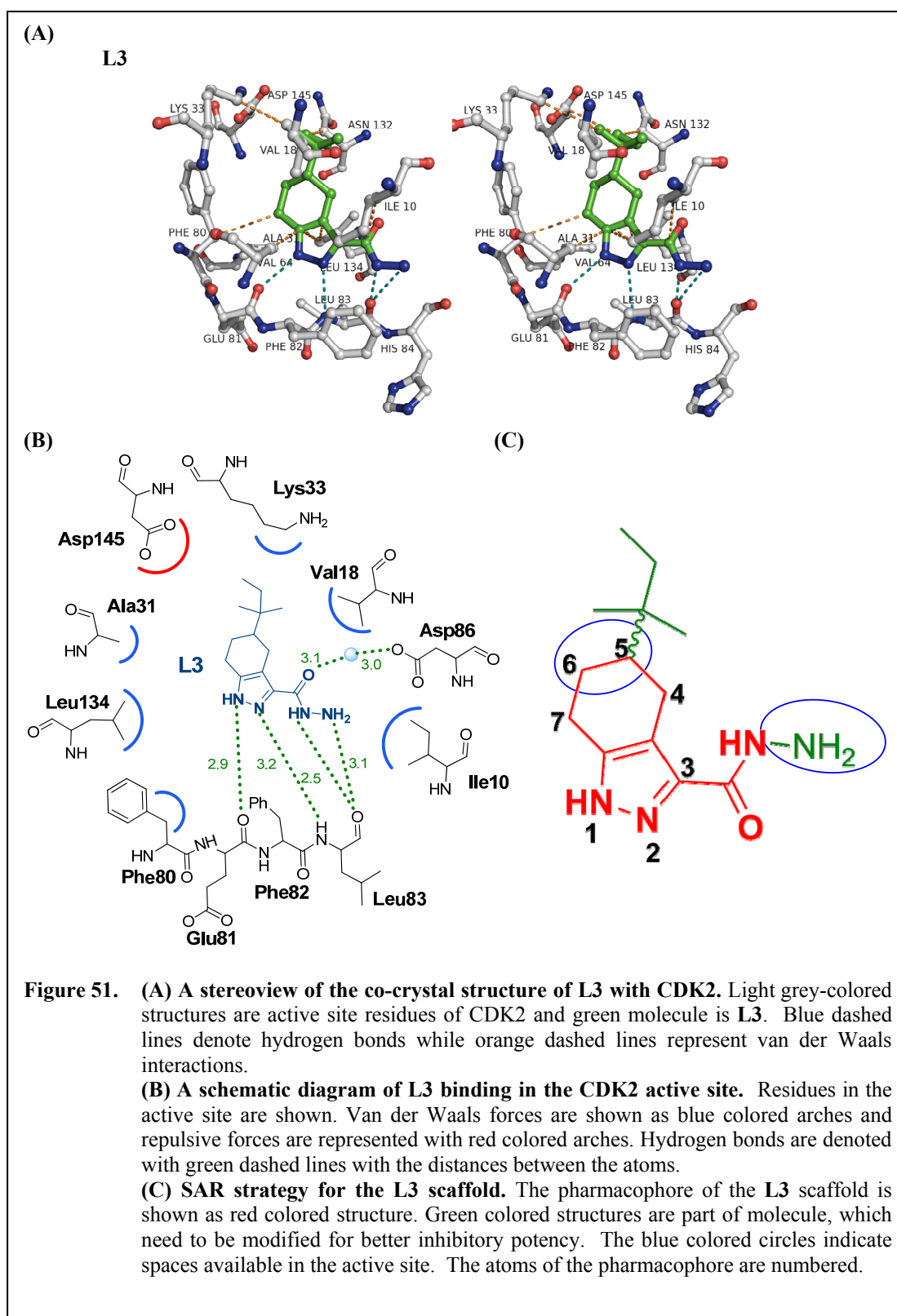
L2-8 with **CDK2** were solved (Figures 48 and 50). The binding modes of **L2-6** and **L2-8** were very similar to **L2-3**. The conformations of the substituents on C4' of the triazine ring could not be well refined because of the poor electron densities. The co-crystal structures of **L2-JWS-6-48** and **L2-JWS-6-52** were determined to 1.80 Å resolutions (Figure 49). The methoxy group of **L2-JWS-6-48** establishes hydrophobic interactions with the C β of Asp145 and the side chain of Phe80, and a phosphate ion is found at the same binding site of **L2-3**, **L2-6**, and **L2-8**. The hydroxyl group of **L2-JWS-6-52** does not establish interactions with the enzyme, and this explains the similar potency. In the co-crystal structure of **L2-JWS-6-76** with **CDK2**, the fluoride group interacts with the side chain of Asp145 in the same way as it does with the chloride group in **L2-3**, **L2-6**, and **L2-8** (Figure 48). This extra

interaction explains the somewhat better activity of **L2-JWS-6-76** than **L2**. However, it is not as active as chloride-substituted **L2** analogs. This is probably due to the smaller atomic size of fluoride than chloride, thus the interaction with Asp145 is not strong with the fluoride as with the chloride.

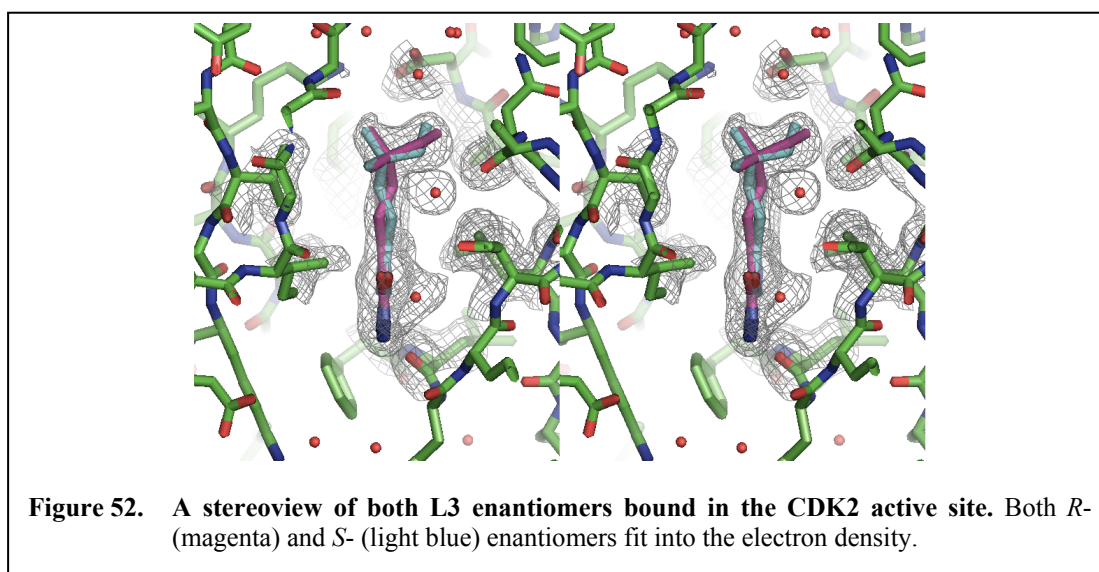
Future studies of **L2** analogs will include variations on the R4 group. The exchanges of the 3'- and 5'-nitrogen atoms on the triazine ring to carbon atoms will also be attempted for a SAR study. The substituents of 4'-amine group tested thus far did not show any specific interactions with CDK2 based on the crystal structures, thus further modifications are ongoing. Along with these variations, substitutions on 6'-amine group will be added to enhance the inhibitory potencies. The 6'-amine group will be elongated with large hydrophilic groups because the direction of the 6'-amine group is toward solvent exposure space. The improved hydrophilicity is expected to increase solvent contacts and to interact with hydrophilic residues, and thereafter enhance the inhibitory potency of the compounds.

3.3.3. Lead 3 and its analogs

The compound, Lead 3 (**L3**, 5-*tert*-pentyl-4,5,6,7-tetrahydro-1H-indazole-3-carbohydrazide), was identified as a reversible competitive inhibitor with respect to ATP, with a K_i value of 8.0 μM . The crystal structure of **L3** bound to human CDK2 was determined at 1.85 Å resolution. As expected from the kinetic data, **L3** bound to the ATP binding site of CDK2 (Figure 51A). **L3** also made three key hydrogen bonds with the Glu81 backbone carbonyl, the Leu83 backbone carbonyl and nitrogen. Due to the large hydrophobic substituent, *tert*-pentyl, on the cyclohexene ring,



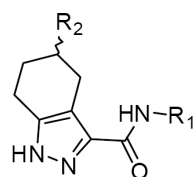
L3 interacted with the side chains of Ile10, Val18, Ala31, Leu134, and Ala144 through hydrophobic forces (Figure 51B). **L3** has a chiral center at C5 of the cyclohexenyl ring. However, both enantiomers could fit the electron density map (Figure 52). Thus, it was not possible to determine which enantiomer was the active isomer in the structure with a 1.85 Å resolution, or whether both stereoisomers possibly inhibited CDK2.



The pharmacophore of **L3** was proposed as a 1H-pyrazole-3-carboxamide moiety from the structural information of **L3** bound CDK2 (Figure 51C). The terminal amine group of the carbohydrazide has been modified to various groups. The cyclohexene ring and *tert*-pentyl group have also been investigated by using other ring systems and various substituents.

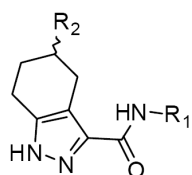
A number of **L3** analogs were obtained and tested for inhibitory activity against CDK2/cyclinA (Tables 17 and 18). Replacing the carbohydrazide moiety of the parent compound with a carboxyl group eliminated inhibitory activity, evident from

Table 17. SAR table of the L3 scaffold (1). Blue shaded compounds were co-crystallized with CDK2.

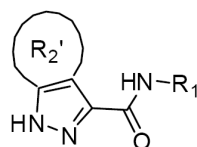


ID	R1	R2	IC ₅₀ (μM)
L3	- NH ₂		20 (IC ₅₀) 8.0 (K _i)
L3-1	- NH ₂	H	> 140
L3-4	- NH ₂		130
L3-5		H	> 140
L3-NSK-MC1-5	- NH ₂		300
L3-NSK-MC1-6	- NH ₂		86
L3-NSK-MC1-9	- NH ₂		2000
L3-NSK-MC1-11	- NH ₂		240
L3-NSK-MC1-12	- CH ₃		4.5
L3-NSK-MC1-13			230000
L3-NSK-MC1-14			193000
L3-NSK-MC1-15	CH ₂ CH ₃		5.4
L3-NSK-MC1-23			> 1000
L3-NSK-MC1-27			> 1000
L3-NSK-MC1-31			38
L3-NSK-MC1-43			25
L3-NSK-MC1-51			> 1000
L3-NSK-MC1-55			3.7
L3-NSK-MC1-63			> 1000

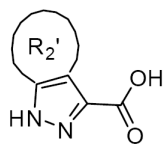
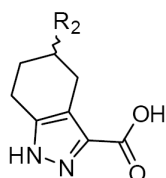
Table 18. SAR tables of the L3 scaffold (2). Blue shaded compounds were co-crystallized with CDK2.



ID	R1	R2	IC ₅₀ (μM)
L3-NSK-MC1-207			> 1000
L3-NSK-MC1-241			53.1
L3-NSK-MC1-253			21.9
L3-NSK-MC1-261			> 1000
L3-NSK-MC1-265			28
L3-NSK-MC1-277			20.6
L3-NSK-MC1-285			> 1000



ID	R1	R2'	IC ₅₀ (μM)
L3-2	-NH ₂		> 140
L3-3	-NH ₂		130
L3-NSK-MC1-1	-NH ₂		750
L3-NSK-MC1-199			678



ID	R2	IC ₅₀ (μM)
L3-NSK-MC1-2		> 1000
L3-NSK-MC1-3		> 1000
L3-NSK-MC1-4		9700
L3-NSK-MC1-7		1960
L3-NSK-MC1-8		> 5000
L3-NSK-MC1-10		18000

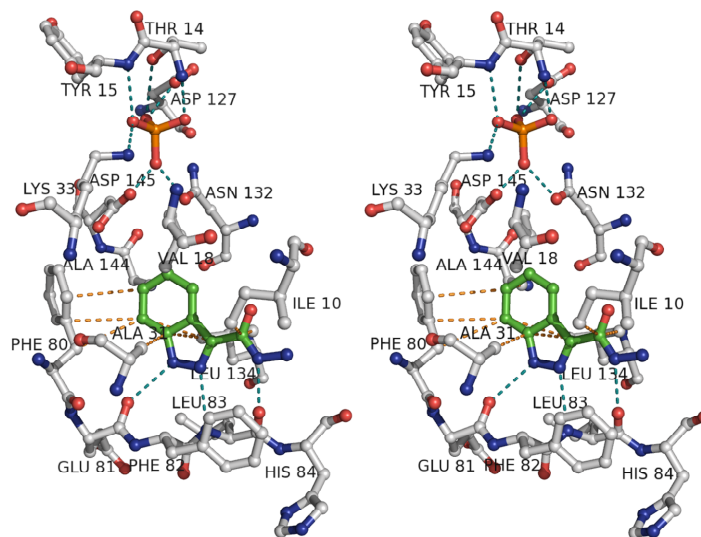
the results for **L3-NSK-MC1-3**. Only **L3-NSK-MC1-7** displayed measurable activity albeit considerably less than the parent compound. Notably, replacement of the carbohydrazide group by amide derivatives influenced the affinity depending on the nature or the size of the R1 group. **L3-NSK-MC1-12** (R1: methyl) and **L3-NSK-MC1-15** (R1: ethyl) were 4-5 times more active than **L3** while **L3-NSK-MC1-277** (R1: *n*-propyl) showed similar activity with **L3**. It was suggested that two carbon chains extended from the amide group had interactions with the enzyme while one additional carbon abolished the positive effect by repulsive forces. In addition to the length of the carbon chains, bulkiness of the aliphatic substituents exhibited a negative effect on the inhibitory potency. Cyclohexyl (**L3-NSK-MC1-14**) and cyclopentyl (**L3-NSK-MC1-13**) substitutions resulted in loss of the activity and **L3-NSK-MC1-241** (R1: *i*-propyl) had 10 times lower activity than **L3-NSK-MC1-15** (R1: ethyl) and 2 times lower than **L3-NSK-MC1-277** (R1: *n*-propyl). Several different *para*-substituted benzyl groups at the R1 position were tested. Interestingly, the sulfonamide group (**L3-NSK-MC1-55**) demonstrated the best inhibitory potency ($IC_{50} = 3.7 \mu\text{M}$) among all **L3** analogs tested so far. However, the other substituents, *p*-chloro (**L3-NSK-MC1-13**), *p*-trifluoromethyl (**L3-NSK-MC1-27**), and *p*-methoxy (**L3-NSK-MC1-285**), did not show any activity against CDK2/cyclinA. The co-crystallization of **L3-NSK-MC1-55** with CDK2 in an attempt to visualize the effect of the sulfonamide on its binding, is currently underway.

Variations on the *tert*-pentyl group did not show better inhibitory potency than **L3**. For example, although **L3-4** differs in only one methyl group from **L3**, it

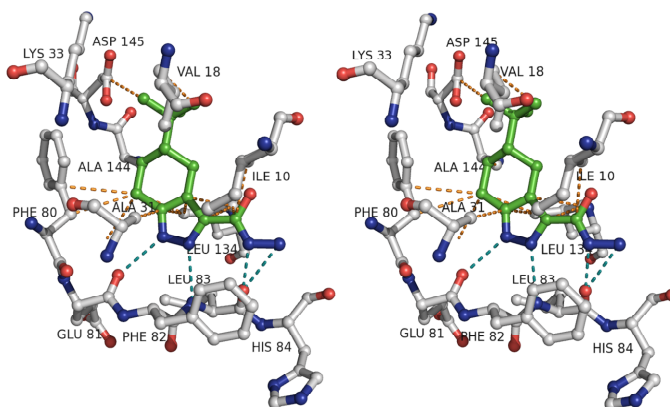
demonstrated 15-fold lower potency, implying that the additional methyl group in **L3** contributes to the proper binding of **L3** to CDK2. In addition to the replacement of the R2 group from *tert*-pentyl to *tert*-butyl, it has been modified to hydrogen (**L3-1**), *n*-propyl (**L3-NSK-MC1-6**), *n*-butyl (**L3-NSK-MC1-11**), phenyl (**L3-NSK-MC1-5**), and cyclohexyl (**L3-NSK-MC1-9**). These analogs showed significantly reduced inhibitory activity against CDK2/cyclinA. The **L3** analogs with different ring systems, cyclopentenyl (**L3-2**), benzene (**L3-3**), and cycloheptenyl (**L3-NSK-MC1-1**) rings, as a replacement of the cyclohexenyl ring (**L3-1**) were evaluated. Although only the benzene ring had a better potency than the compound **L3-1** among these analogs, it exhibited an IC₅₀ value of 130 μM. The low inhibitory activity of the analog **L3-3** is possibly due to its lack of a large hydrophobic group such as *tert*-pentyl in **L3**, resulting in the loss of hydrophobic forces for binding on CDK2.

In the current compound library of **L3** scaffolds, hydrophilic functional groups as the R2 substituents are absent. Since there are several hydrophilic residues, Lys33, Asn132, and Asp134, at the R2 binding site of CDK2, the application of hydrogen bond donors or acceptor groups might improve the binding affinity. For future investigation, it is proposed to eliminate the stereo-center of **L3** by replacing it with nitrogen or amide in the cyclohexenyl ring. This variation would provide better solubility of the compounds as well as possible hydrogen bonds.

L3-3



L3-4



L3-NSK-MC1-6

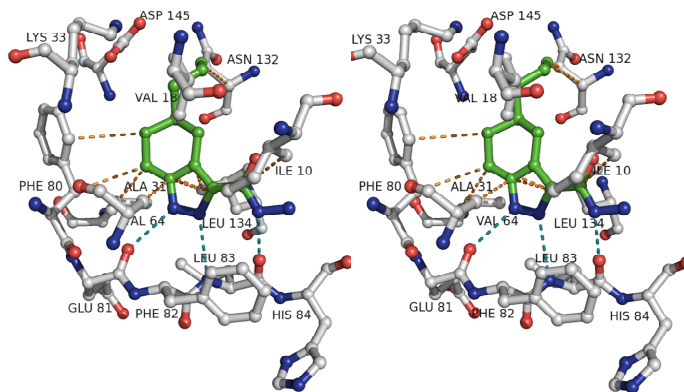
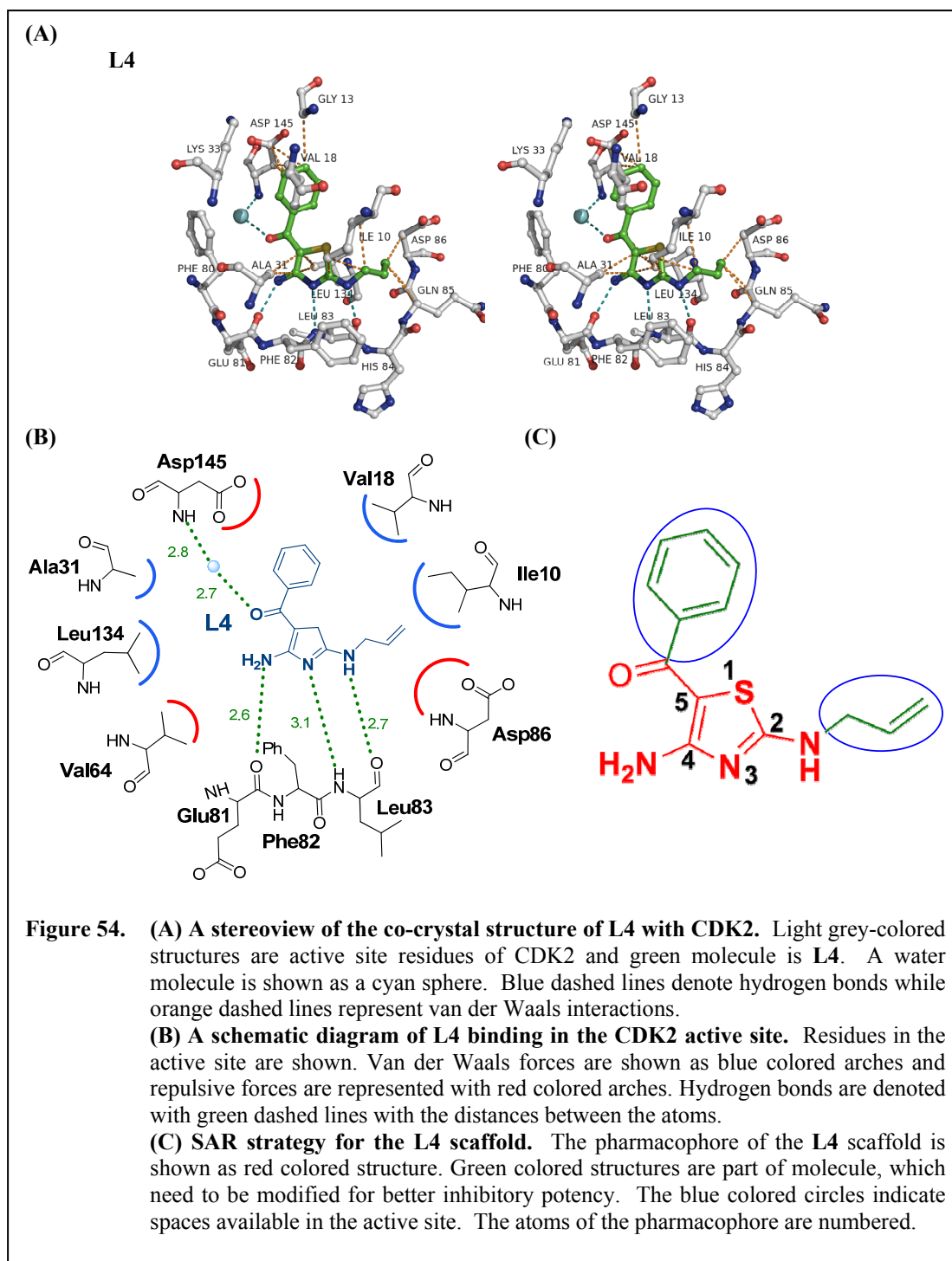


Figure 53. Stereoviews of the co-crystal structures of L3 analogs: L3-3, L3-4, and L3-NSK-MC1-6 with CDK2. Light grey-colored structures are active site residues of CDK2 and green molecules are inhibitor structures. Blue dashed lines denote hydrogen bonds while orange dashed lines represent van der Waals interactions.

In addition to the crystal structure of **L3** on CDK2, the co-crystal structures of **L3-3**, **L3-4**, and **L3-NSK-MC1-6** were obtained (Figure 53). As with the structure of **L3**, the active enantiomers of **L3-4** and **L3-NSK-MC1-6** were not clearly shown on the co-crystal structures. Although the difference in chemical structure between **L3** and **L3-4** or **L3-NSK-MC1-6** is only one or two carbon atoms, the activities of these compounds differ by more than 6-fold. This enormous change of the inhibitory potency could not be explained even with the co-crystal structures. The structure of **L3-3** with CDK2 was solved to 1.80 Å. The benzene (**L3-3**) as a replacement of the cyclohexenyl ring (**L3**) increased the hydrophobic interaction, specifically the π - π interaction with the side chain of Phe80. It was evident that **L3-3** bound in the active site more deeply, i.e. closer to Phe80, than **L3**. Although the hydrophobic forces from the R2 alkyl group do not exist on **L3-3**, the compound maintains its binding affinity to the CDK2 active site due to the extra interactions with Phe80. Thus, it is suggested that the substitution on the benzene ring of **L3-3** would increase the inhibitory potency.

3.3.4. Lead 4 and its analogs

The lead compound 4 (**L4**, (2-(allylamino)-4-aminothiazol-5-yl)(phenyl) methanone) was identified as a competitive CDK2 inhibitor with respect to ATP, exhibiting a K_i value of 7.6 μ M. The co-crystal structure of CDK2 with **L4**, solved to 1.95 Å resolution, confirmed the kinetic data: **L4** was bound in the ATP binding pocket in CDK2 (Figure 54A). The 4-amino group forms a hydrogen bond with the backbone carbonyl of Glu81. The 3-nitrogen atom of the thiazole ring has a



hydrogen bond with the backbone nitrogen of Leu83 and the 2-amino group interacts with backbone carbonyl of Leu83. In addition, the 5-carbonyl group of **L4** interacts with the backbone nitrogen atom of Asp145 through a water molecule. The thiazole ring interacts with the side chain of Ile10, Ala31, and Leu134, the phenyl ring with Gly13, Val18, and Asp145, and the allyl moiety with Ile10 (Figure 54B). However, the electron density of the allyl group, as well as that of the side chain of Ile10, is weak; thus the interaction between those two groups does not seem to be strong.

The pharmacophore of **L4** was recognized as a 2,4-diamino thiazole group, and the 2-amino group can be elongated with hydrocarbon substituents, such as allyl or phenyl groups (Figure 54C). The space that the 4-amino group occupies is not large enough to accept any substitution. This is consistent with the lack of CDK2 inhibition by **L4-RC2-31**. The 5-carbonyl has a hydrogen bond with the backbone nitrogen of Asp145 via a water molecule. However, it is necessary to examine whether this interaction is essential for the binding affinity.

L4 is the most studied scaffold among the four groups to date. Over fifty **L4** analogs with various R1 and R2 groups purchased or synthesized were tested against CDK2/cyclinA (Tables 19-22). It is shown on the SAR tables of the **L4** scaffold that the inhibitory potency of compounds generally depends on the combination of R1 and R2, not on any one single side substitution. For example, **L4-RC1-148** (R1: phenyl, R2: phenyl) showed better activity than **L4** (R1: allyl, R2: phenyl), suggesting phenyl is a better group for the R1 position. However, the opposite result was

Table 19. SAR table of the L4 scaffold (1). Blue shaded compounds were co-crystallized with CDK2.

ID	R1	R2	IC ₅₀ (μM)
L4			10-15 (IC ₅₀) 7.6 (K _i)
L4-4			37
L4-5			35
L4-7		- CH ₃	290
L4-8	- CH ₃	- CH ₃	580
L4-9	- CH ₂ CH ₃		55
L4-10			320
L4-11			70
L4-12			5.7
L4-14			12
L4-17			500
L4-18			130
L4-RC1-132			5
L4-RC1-134			41
L4-RC1-135			2.9
L4-RC1-136			49

Table 20. SAR table of the L4 scaffold (2). Blue shaded compounds were co-crystallized with CDK2.

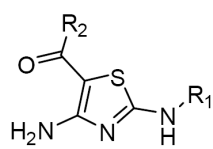
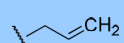
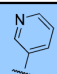
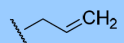
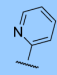
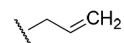
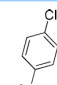
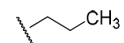
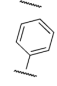
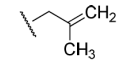
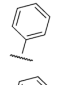
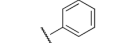
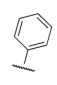
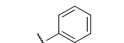
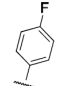
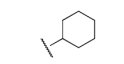
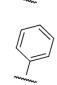
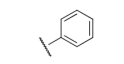
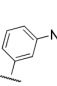
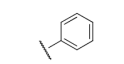
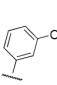
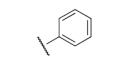
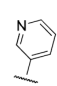
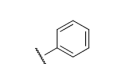
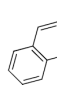
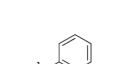
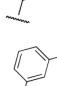
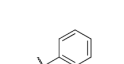
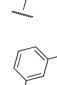
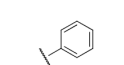
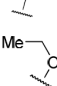
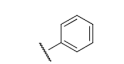
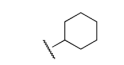
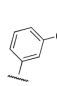
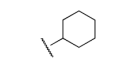
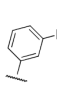
	ID	R1	R2	IC ₅₀ (μM)
	L4-RC1-137			3.1
L4-RC1-138			33	
L4-RC1-145			600	
L4-RC1-146			8.9	
L4-RC1-147			15	
L4-RC1-148			1.3	
L4-RC1-149			1.4	
L4-RC1-151			1.3	
L4-RC2-11			2.2	
L4-RC2-12			3.1	
L4-RC2-13			0.77	
L4-RC2-14			> 1000	
L4-RC2-15			1.6	
L4-RC2-16			99	
L4-RC2-18			865	
L4-RC2-19		- CH ₃	413	
L4-RC2-20			2.4	
L4-RC2-21			1.4	

Table 21. SAR table of the L4 scaffold (3).

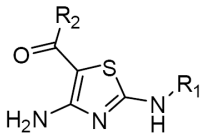
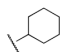
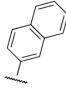
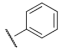
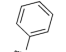
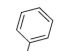
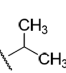
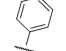

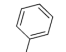
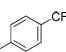
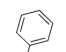
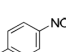
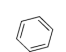
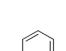
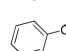
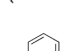
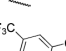
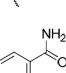
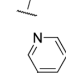
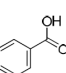
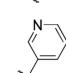
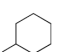
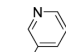
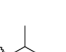
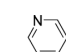
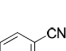
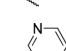
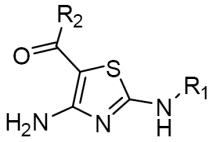
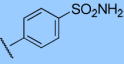
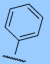
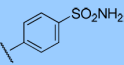
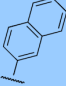
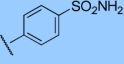
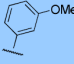
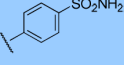
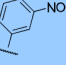
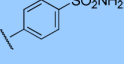
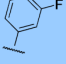
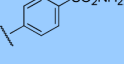
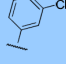
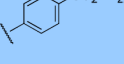
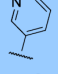
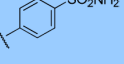
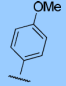
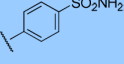
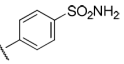
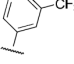
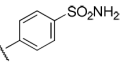
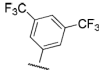
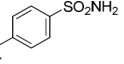

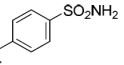
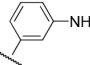
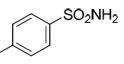
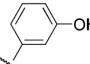
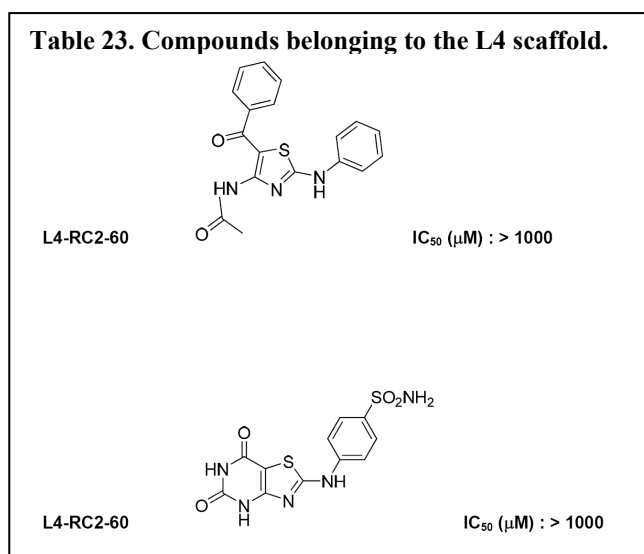
	ID	R1	R2	IC ₅₀ (μM)
	L4-RC2-22			11.6
L4-RC2-23		- NH ₂	> 1000	
L4-RC2-24	- CH ₃		95	
L4-RC2-25	- CH ₂ CH ₃		17	
L4-RC2-26			2.0	
L4-RC2-27			334	
L4-RC2-30			> 1000	
L4-RC2-31			295	
L4-RC2-49			196	
L4-RC2-50			160	
L4-RC2-71			0.3	
L4-RC2-72			4.0	
L4-RC2-73			0.9	
L4-RC2-74			0.8	
L4-RC2-78			2.8	

Table 22. SAR table of the L4 scaffold (4). Blue shaded compounds were co-crystallized with CDK2.



ID	R1	R2	IC ₅₀ (μM)
L4-RC2-32			0.21
L4-RC2-33			81.6
L4-RC2-34			0.64
L4-RC2-35			0.16
L4-RC2-36			0.1
L4-RC2-37			15
L4-RC2-38			0.08
L4-RC2-39			17
L4-RC2-40		- NH ₂	4.8
L4-RC2-51			0.12
L4-RC2-52			24.7
L4-RC2-86			> 1000
L4-RC2-88			0.4
L4-RC2-89			1.5

demonstrated when R2 is naphthyl (**L4-RC1-132** and **L4-RC2-14**): **L4-RC1-132** (R1: allyl, R2: naphthyl) had an IC_{50} value of 5 μ M while **L4-RC2-14** (R1: phenyl, R2: naphthyl) did not show any inhibitory activity up to 1 mM against CDK2/cyclinA. Thus, it is suggested that the flexibility of the R1 substituent allows for a larger group on the R2 position.



Fourteen different R1 groups have been applied when R2 is substituted with a phenyl group. From the activity test of those compounds, phenyl (**L4-RC1-148**), cyclohexyl (**L4-RC1-151**), and *i*-propyl (**L4-RC2-26**) groups at the R1 position increased the

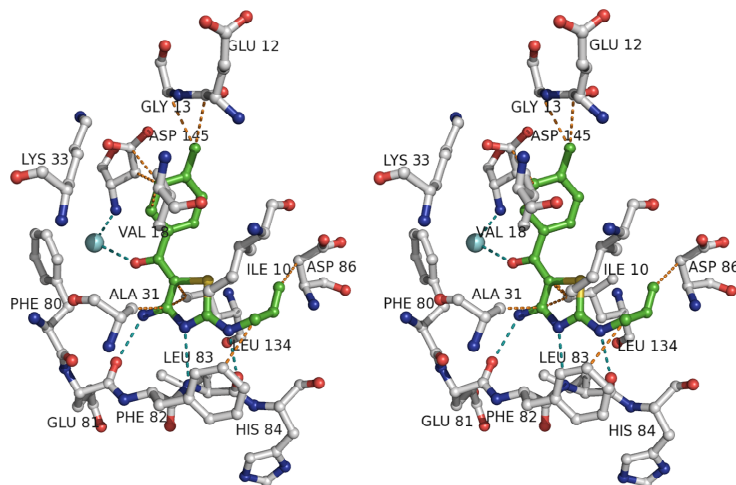
inhibitory potency of the analogs, while *tert*-butyl (**L4-RC2-27**), *p*-trifluoromethyl phenyl (**L4-RC2-30**), and *p*-nitro phenyl (**L4-RC2-31**) groups had adverse effects. Remarkably, **L4-RC2-32** (R1: *p*-sulfonamide phenyl group) exhibited the best inhibition, and the same results were found throughout all different R2 variations. This result is consistent for oxindole with the sulfonamide (compound 7 in Figure 14) which is more potent than the compound without the sulfonamide, reported previously¹¹⁹. It was also found in a SAR study of the **L3** scaffold, in which the sulfonamide derivative at the similar position exhibited the best inhibitory potency. Thus, future attempts to achieve higher inhibitory potency of **L4** analogs would

contain the *p*-sulfonamide or a *p*-N-substituted sulfonamide phenyl group at the R1 position.

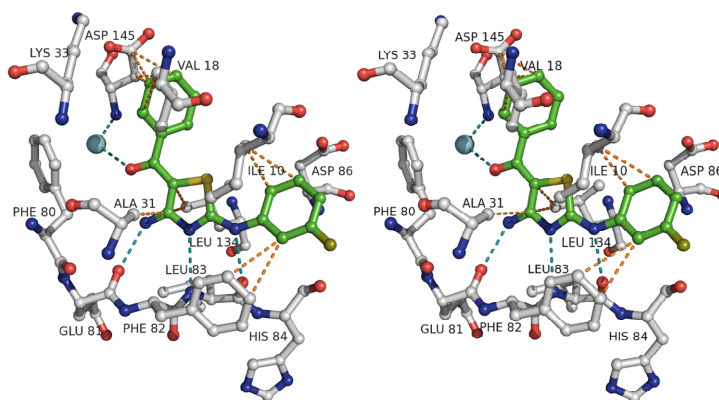
The inhibitions of the **L4** analogs with the allyl group at the R1 position were compared. Among 15 of those compounds, 3-pyridyl (**L4-RC1-137**) and *m*-nitro phenyl (**L4-RC1-135**) substitutions at the R2 position enhanced the activities compared to **L4** (phenyl), while the others had similar or lower potencies. Moreover, those two substitutions had consistently exhibited good inhibitions regardless of the R1 groups.

The efforts to verify SAR of the **L4** analogs were conducted by the co-crystal structures of the compounds with CDK2. More than 10 structures of the **L4** analogs have been solved (Figures 55–59). Three different R1 groups, allyl, *m*-fluoro phenyl, and *p*-sulfonamide phenyl, were included in those structures. The electron densities for the allyl groups were very weak in the structures. Thus it is thought that the allyl group at the R1 position is flexible and does not have specific interactions. In the co-crystal structure of **L4-12**, the electron density of the R1 substituent, *m*-fluoro phenyl, was found to be clearer than the allyl, and had hydrophobic interactions with the side chain of Phe82. The excellent activities of the *p*-sulfonamide phenyl substituted **L4** analogs were explained from the co-crystal structures of those compounds with CDK2. The electron densities of the *p*-sulfonamide phenyl groups were clearly defined. In the structures, the sulfonamide group has extra interactions with CDK2 by forming hydrogen bonds with the backbone nitrogen and the side chain carboxylate of Asp86. In addition to better solubility of the sulfonamide derivatives,

L4-4



L4-12



L4-14

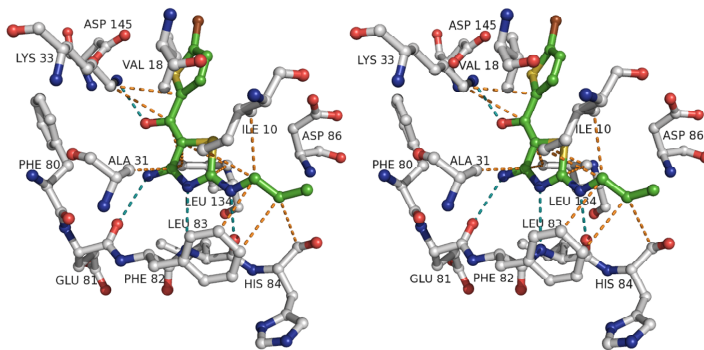
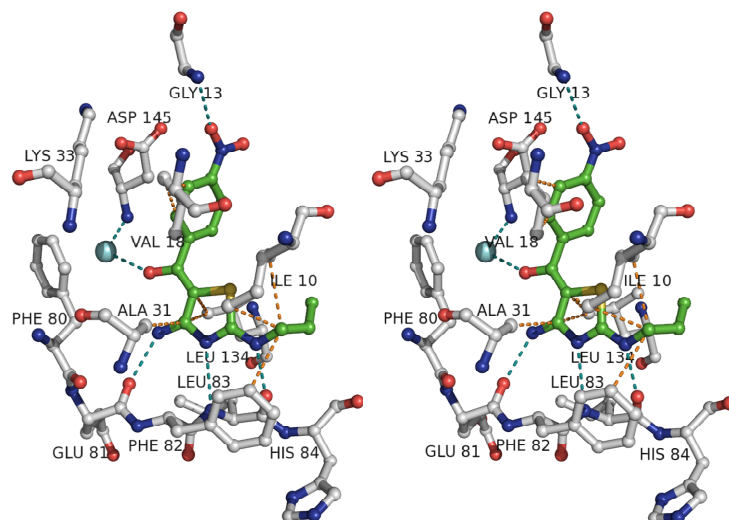


Figure 55. Stereoviews of the co-crystal structures of L4 analogs: L4-4, L4-12, and L4-14 with CDK2. Light grey-colored structures are active site residues of CDK2 and green molecules are inhibitor structures. Water molecules are shown as cyan spheres. Blue dashed lines denote hydrogen bonds while orange dashed lines represent van der Waals interactions.

L4-RC1-34



L4-RC1-35

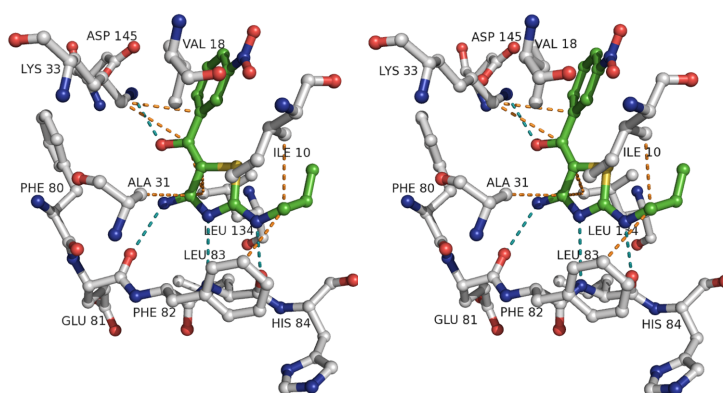
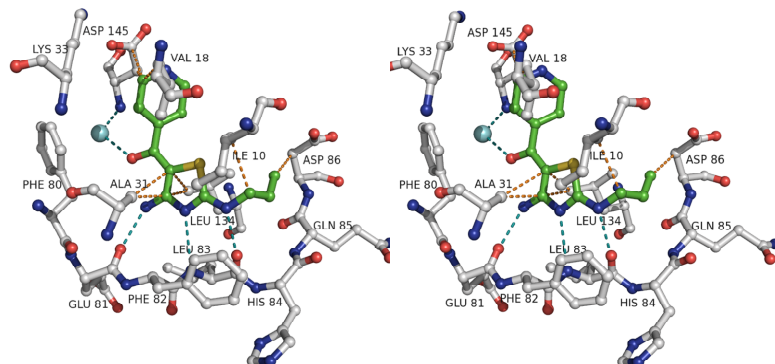
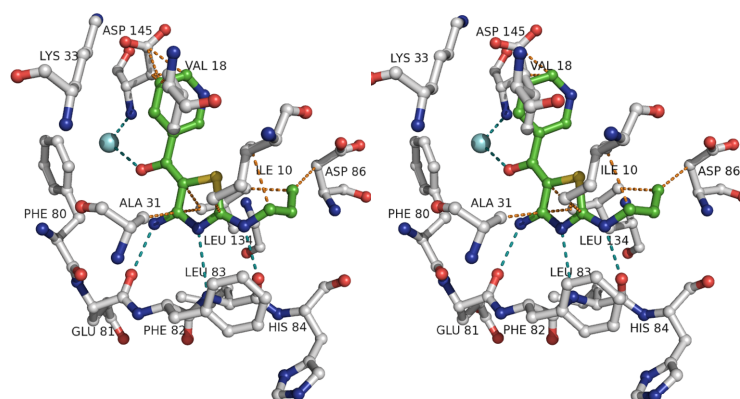


Figure 56. Stereoviews of the co-crystal structures of L4 analogs: L4-RC1-34 and L4-RC1-35 with CDK2. Light grey-colored structures are active site residues of CDK2 and green molecules are inhibitor structures. A water molecule is shown as a cyan sphere. Blue dashed lines denote hydrogen bonds while orange dashed lines represent van der Waals interactions.

L4-RC1-36



L4-RC1-37



L4-RC1-38

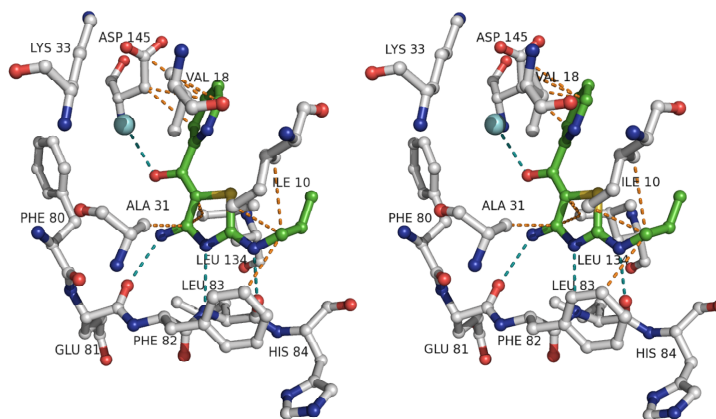
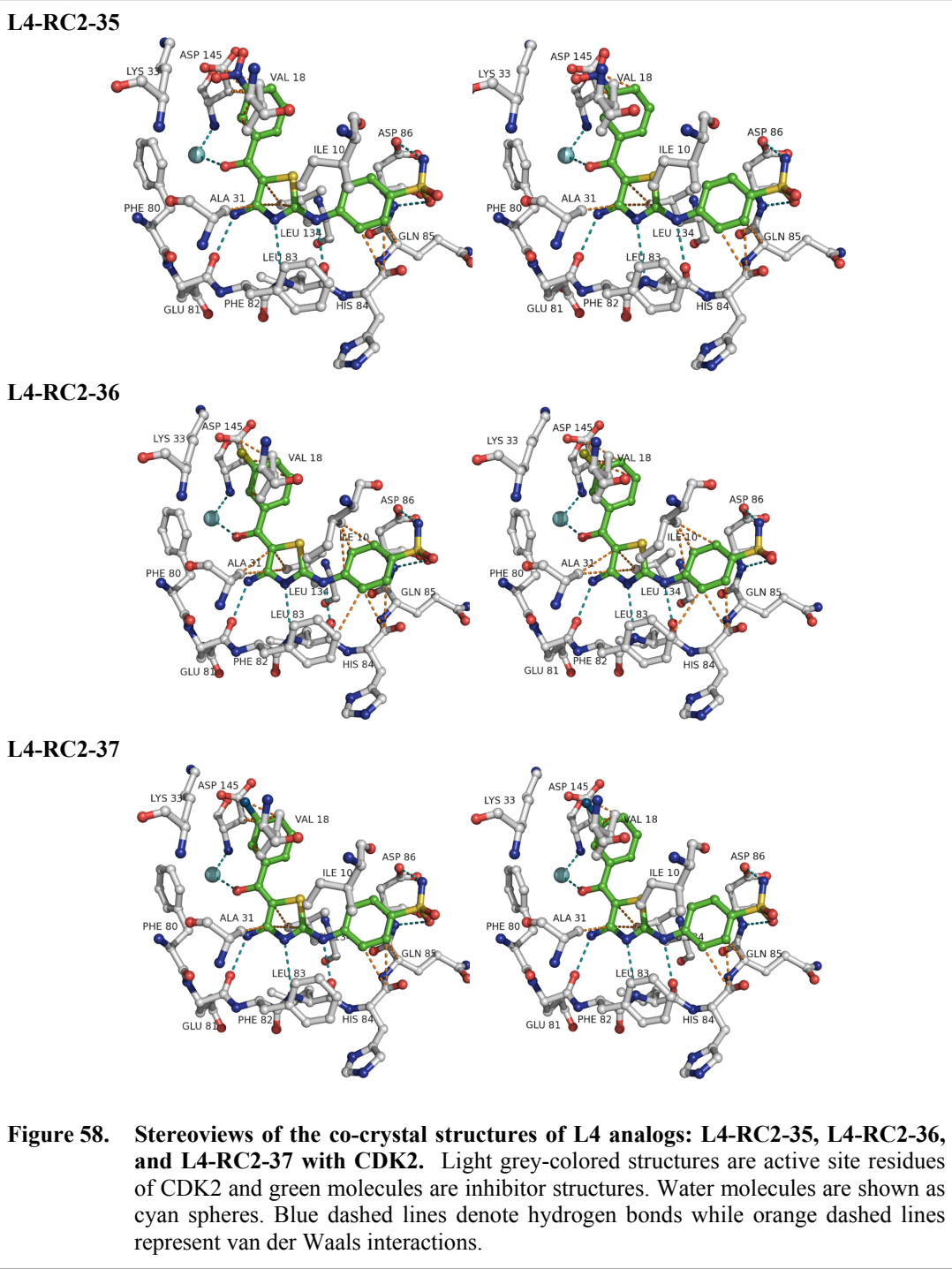


Figure 57. Stereoviews of the co-crystal structures of L4 analogs: L4-RC1-36, L4-RC1-37, and L4-RC1-38 with CDK2. Light grey-colored structures are active site residues of CDK2 and green molecules are inhibitor structures. Water molecules are shown as cyan spheres. Blue dashed lines denote hydrogen bonds while orange dashed lines represent van der Waals interactions.



L4-RC2-38

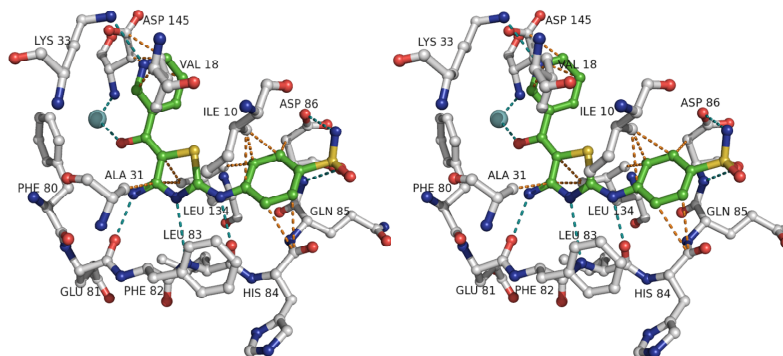


Figure 59. A stereoview of the co-crystal structure of **L4-RC2-38** with CDK2. Light grey-colored structures are active site residues of CDK2 and green molecule is **L4-RC2-38**. A water molecule is shown as a cyan sphere. Blue dashed lines denote hydrogen bonds while orange dashed lines represent van der Waals interactions.

these extra hydrogen bonds found in the crystal structures induce better binding affinity of the molecules to CDK2 thus increase the inhibitory potency. The 5-carbonyl group in all solved structures has a hydrogen bond, although two different ways are shown. One is a direct interaction with the side chain of Lys33, found in the structures of **L4-14** and **L4-RC1-35**, and the other is a hydrogen bond with the backbone nitrogen of Asp145 through a water molecule. From the SAR studies, it was found that small variations of the R2 group, e.g. different positions (2-, 3- or 4-position of nitrogen atom (**L4-RC1-38**, **L4-RC1-37**, and **L4-RC1-36**)) of the same functional groups (pyridine ring), induced large changes in the binding affinities of the **L4** analogs. The co-crystal structures of **L4-RC1-36**, **L4-RC1-37**, and **L4-RC1-38** were solved to identify which structural differences induce the activity changes. Although all three inhibitors were found in the ATP binding site, it was impossible to recognize the factor that determines the inhibitory potency. It is considered that the

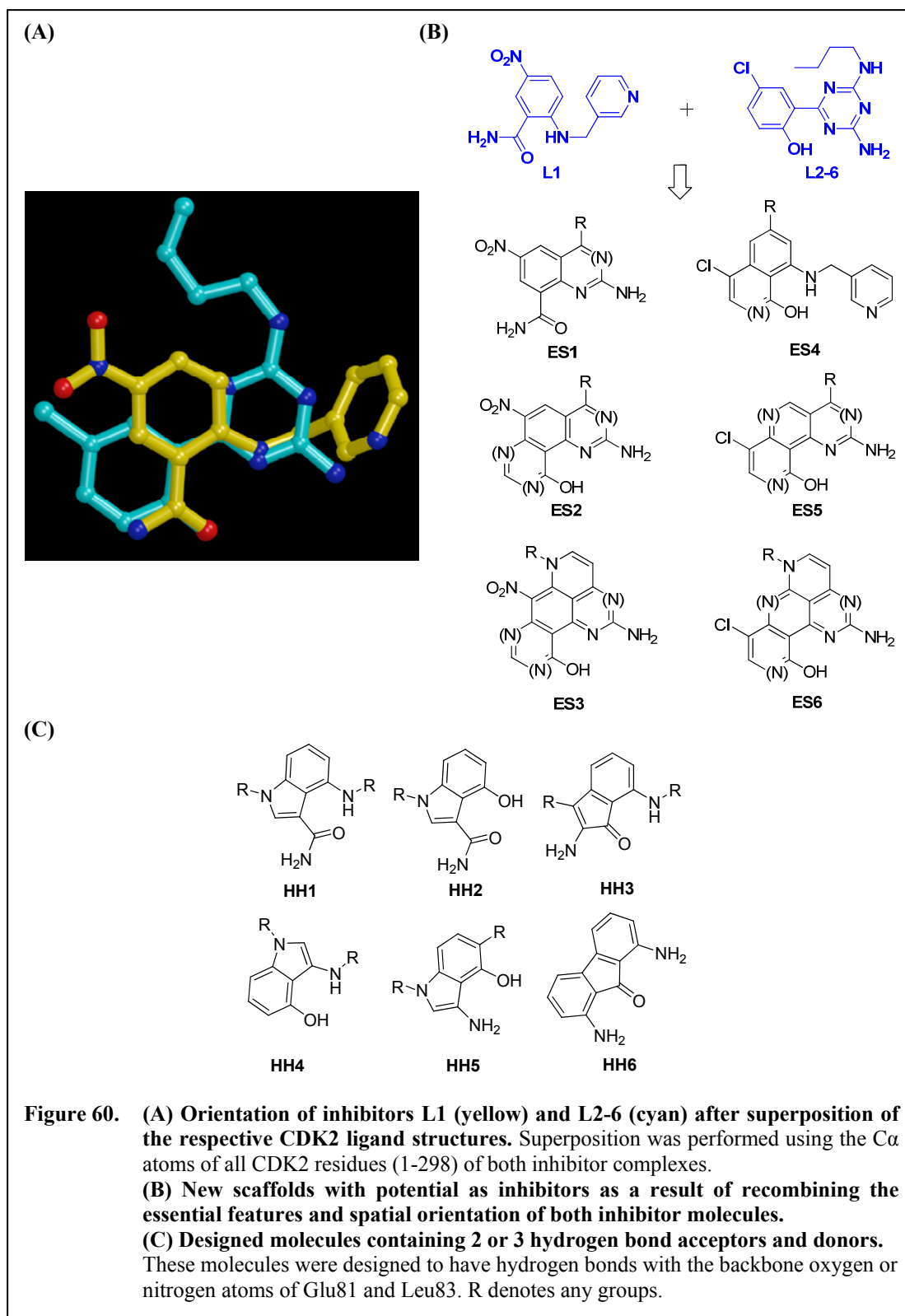
SAR study of the R2 position needs to be performed by the structural study with CDK2/cyclin complex instead of CDK2 only because the residues in the space that R2 group binds undergoes conformational change upon cyclin binding. Thus, the efforts to crystallize the CDK2/cyclinA complex are currently ongoing in Prof. Schönbrunn's laboratory.

The inhibitory activity of the **L4** scaffold has increased 100-fold from the lead compound, **L4**. The sulfonamide group provided the most enhancement of the inhibitory potency. Therefore, future investigation of the **L4** analogs will be conducted where the sulfonamide will be maintained and the elongation from the nitrogen of the sulfonamide will be modified with various substituents.

3.3.5. Design of New Inhibitors and Docking Study

Although the analysis of the kinetic and structural data is an ongoing process and should result in the design of substantially improved analogs of the respective parent compounds, it has been found that the current 4 scaffolds were reported as CDK inhibitors¹⁴⁴⁻¹⁴⁹. Thus, there is a need to discover CDK inhibitors with novel scaffolds.

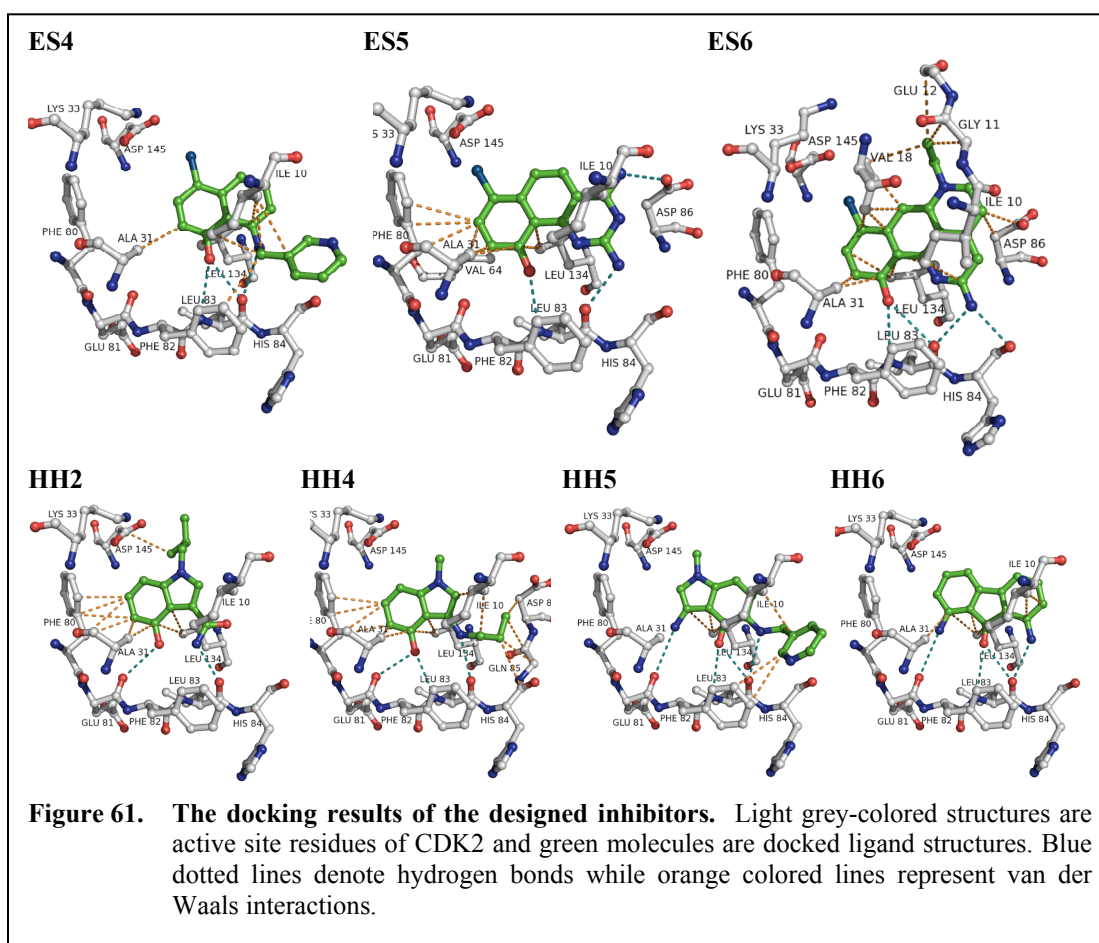
The thorough comparison of the binding patterns of the inhibitors may allow for the design of novel scaffolds with CDK2-inhibitory potential. Superposition of the individual binding sites of the ligands co-crystallized with CDK2 indicates that certain molecule sites may be combined such that new scaffolds emerge: The superposition of structures, CDK2-**L1** and CDK2-**L2-6**, indicates that the free amide group of **L1** may be well confined in a ring system (Figure 60A) and that the phenyl



ring of **L1** may be combined with the triazine ring of **L2**. Even three and four fused ring systems are conceivable as new CDK2 inhibitors resulting from the combination of essential features of **L1** and **L2** (Figure 60B).

More molecules were designed based on the key hydrogen bonds between ligands and CDK2 (Figure 60C). The designed molecules include at least two hydrogen bonding donors or acceptors with similar patterns as known inhibitors, thus they are proposed to bind in the adenine binding site of CDK2.

The molecules of new scaffolds were docked into the ATP binding site of CDK2 using GLIDE¹⁴⁰. Among these compounds, **ES4**, **ES5**, **ES6**, **HH2**, **HH4**, **HH5**, and



HH6 (Figure 61) displayed proper interactions in the ATP binding site of CDK2 by docking. As proposed, the docked molecules maintain at least two hydrogen bonds as well as some hydrophobic interactions. The molecules that docked into CDK2 may represent possible alternatives to current lead structures. Moreover, none of the newly designed molecules have been identified as a CDK inhibitor, thus it is considered that further studies with these compounds would provide a better opportunity to have novel scaffolds of CDK2 inhibitors. Efforts to produce the designed compounds by synthetic methods are currently ongoing at Dr. Georg's laboratory at the University of Minnesota.

3.3.6. Selectivity of CDK2 inhibitors

Selectivity has been a key issue of CDK inhibitors due to the high similarity of the ATP binding sites of all kinases. There is no CDK inhibitor that is selective for a single CDK. Thus, it is expected that the difficulty in selectivity of the CDK2 inhibitors in previous sections would also occur in the near future.

The studies to pre-screen the selectivity of the inhibitors were attempted by docking studies. Prior to the structural studies, the sequences of all CDKs were aligned using ClustalW2¹⁵⁰ (Figure 62 and Table 24). Although they are highly conserved, differences are still found. Thus, it is considered that the selectivity of the inhibitors for a specific CDK can be achieved by changing certain functional groups that respectively interact with different residues from other CDKs. Among these CDKs, 5 different CDK structures are known including the one of CDK2, i.e. CDK2⁸⁶, CDK5 (PDB ID: 1UNL)¹⁵¹, CDK6 (1BLX)¹⁵², CDK7 (1UA2)¹⁵³, and

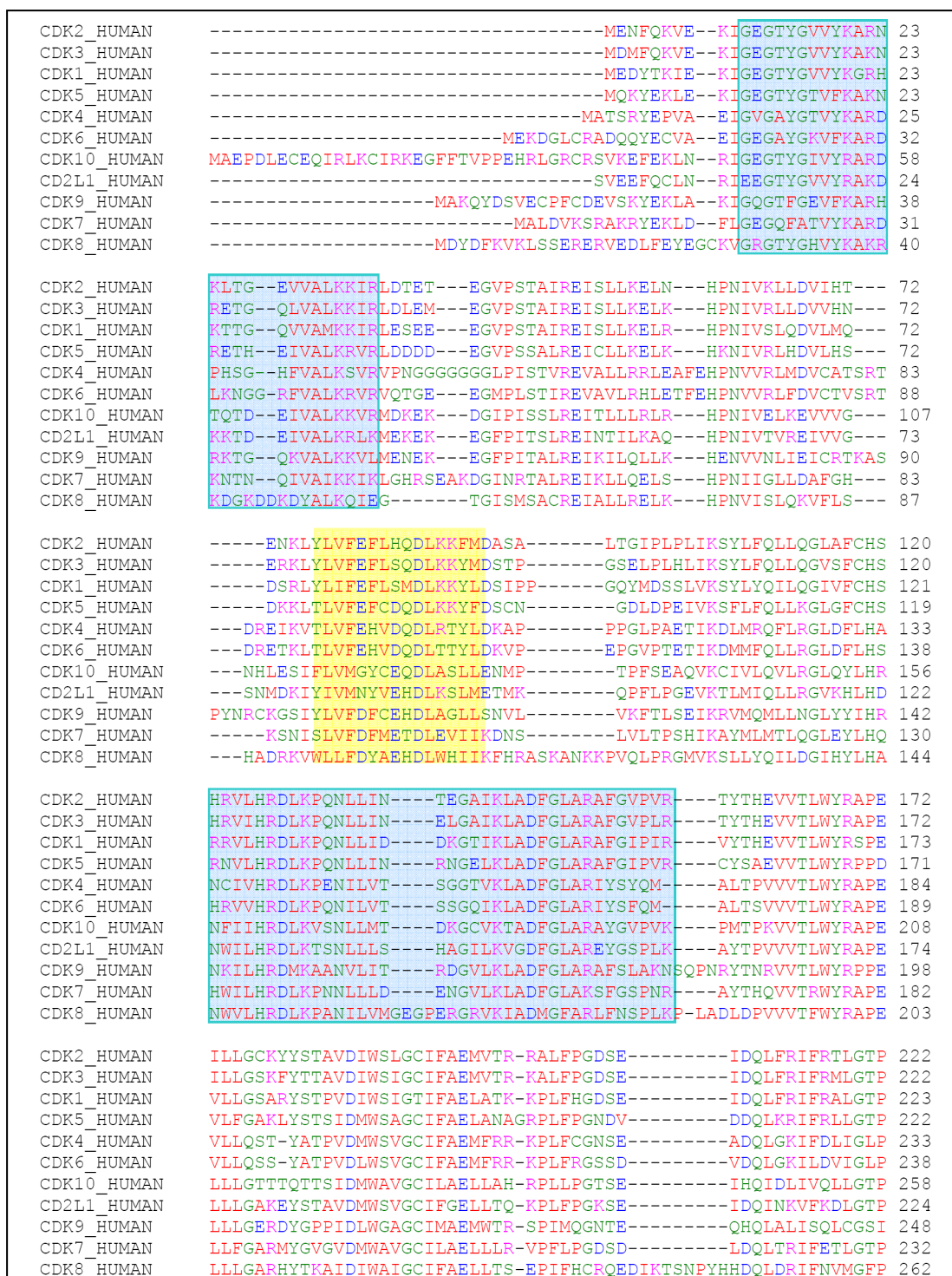


Figure 62. Sequence alignments of all 11 CDKs. The aligned sequences of 1-222 (CDK2 numbering) residues are shown. The yellow box corresponds to the residues involved in the key hydrogen bonds and the blue boxes correspond to the residues in the active site. * CD2L1 is another name of CDK11.

CDK9 (3BLR)¹⁵⁴. The CDK structures were aligned to the CDK2 structure by superimposing secondary structures using the CCP4 program suite¹⁵⁵. The C α -RMSD values of each superimposition were 1.45, 1.83, 1.48 and 2.00 Å, respectively. Four lead compounds, **L1–L4**, docked into the CDK structures. Several inhibitors were found in the ATP binding sites of other CDK structures with the same binding pattern as in the co-crystal structures with CDK2, e.g. **L1** in CDK7 and CDK9, **L2** in CDK5 and CDK9, and **L4** in CDK9 (Figure 64).

Table 24. Sequence alignment scores (in percentage) for CDKs. The sequences of CDK1–CDK11 were aligned with ClustalW2

	CDK2	CDK3	CDK4	CDK5	CDK6	CDK7	CDK8	CDK9	CDK10	CDK11
CDK1	65	64	43	56	46	42	38	40	40	41
CDK2		75	44	59	48	44	37	39	43	44
CDK3			45	61	46	44	39	38	42	44
CDK4				44	68	36	36	34	40	39
CDK5					46	45	36	41	43	41
CDK6						33	30	32	35	36
CDK7							34	35	36	35
CDK8								29	32	33
CDK9									34	32
CDK10										46

In addition, several other kinase structures were investigated in the same way as CDK structures. First, the sequence alignments of AuroraA, mitogen-activated protein kinase (MAPK), glycogen synthase kinase-3 β (GSK3 β), protein kinase A (PKA), and protein kinase C (PKC) were carried out using ClustalW2¹⁵⁰ (Figure 63 and Table 25). The structures of AuroraA (PDB ID: 2NP8)¹⁵⁶, MAPK (1KV1)¹⁵⁷, GSK3 β (1R0E), PKA (2VO3)¹⁵⁸, and PKC (1XJD)¹⁵⁹ were aligned and the C α -RMSD values were 1.97, 2.27, 2.20, 2.00 and 2.01 Å, respectively. The docking studies of these kinase structures were performed with the compounds **L1–L4**.

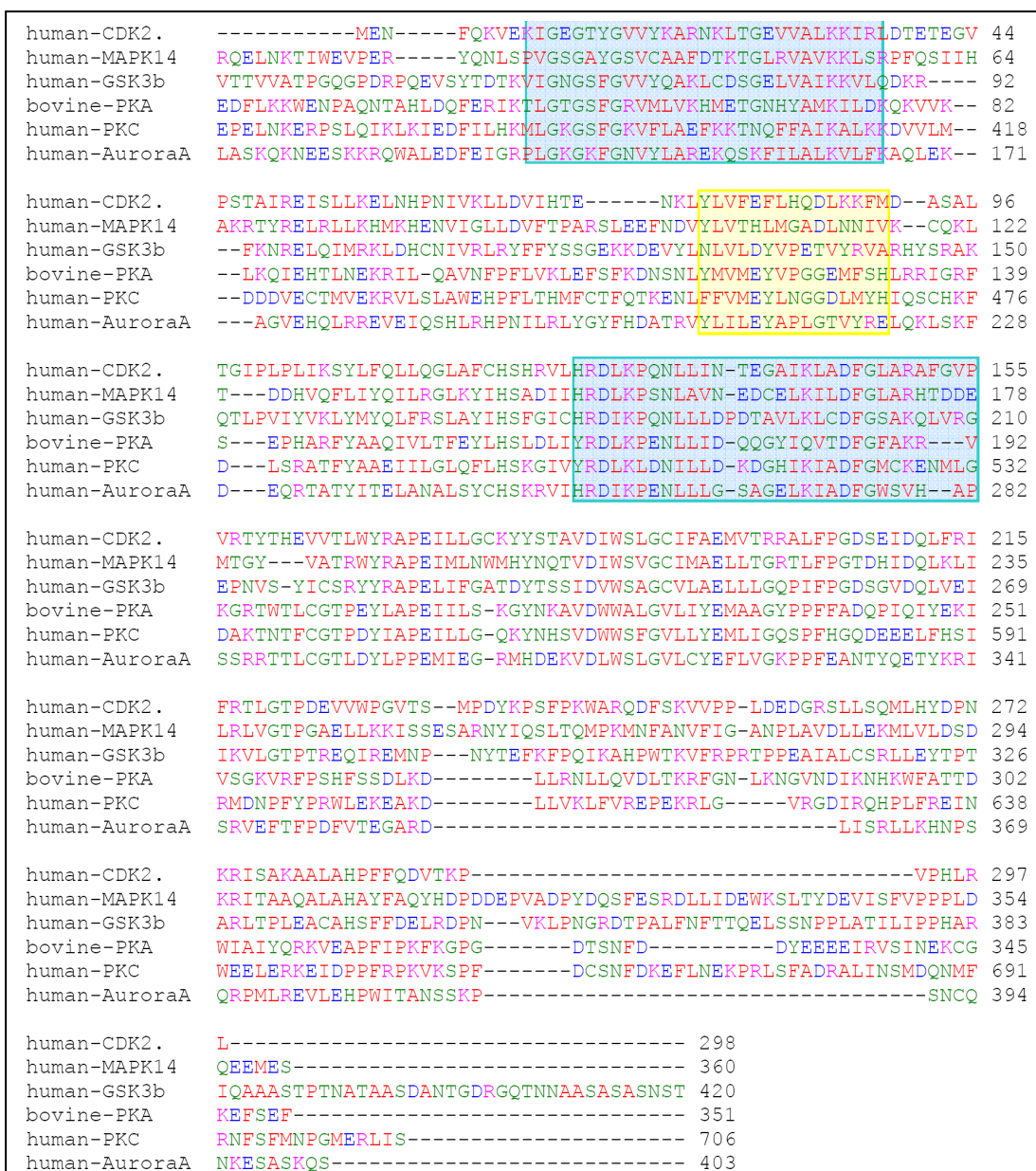
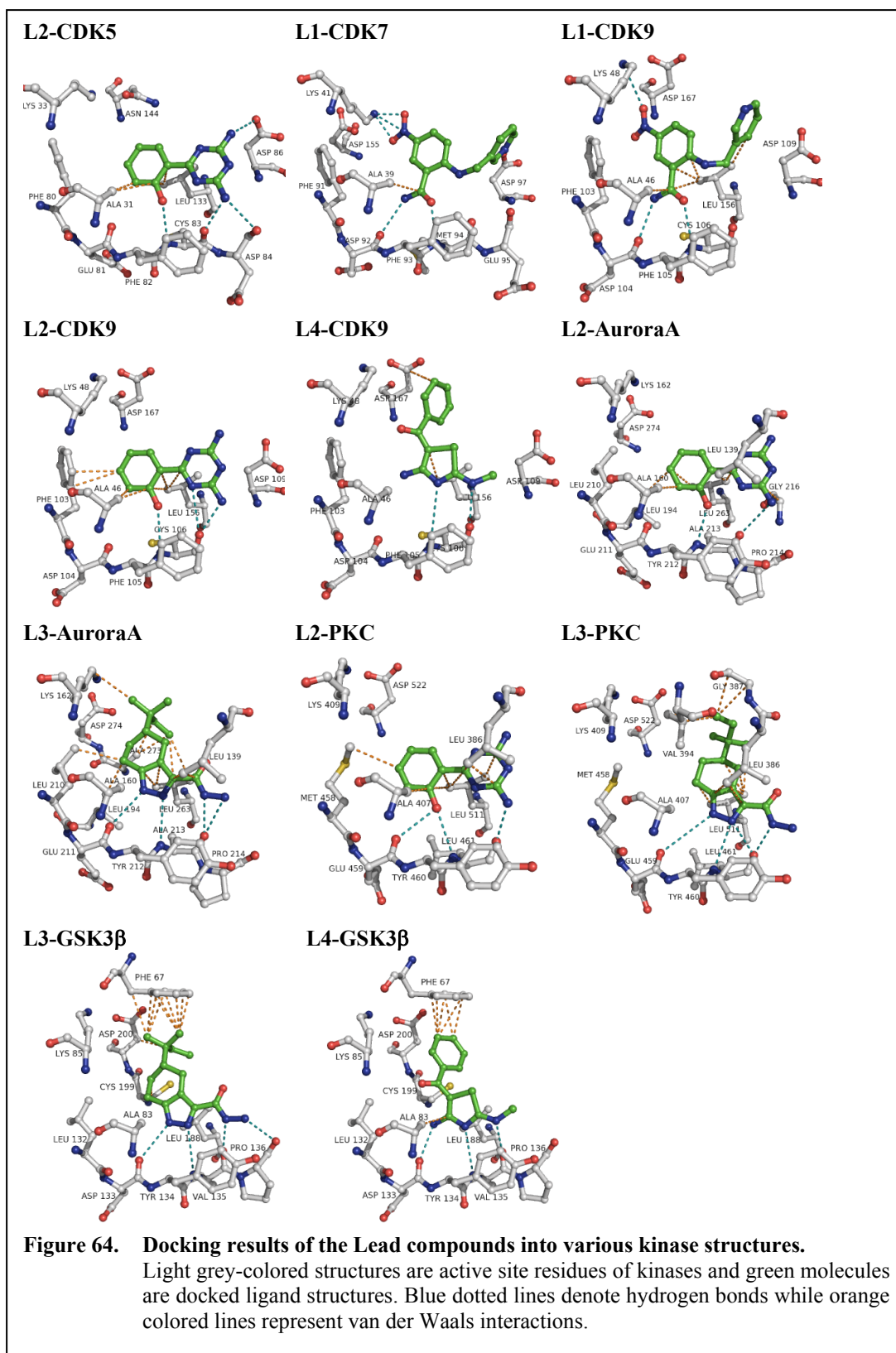


Figure 63. Sequence alignments of several protein kinases (Aurora A, MAPK, GSK3 β , PKA, and PKC) with CDK2. The yellow box corresponds to the residues involved in the key hydrogen bonds and the blue boxes correspond to the residues in the active site. The bovine PKA sequence was used, to be consistent with the structural data.



Inhibitors, **L2** and **L3** were adequately docked into the AuroraA and PKC structures, and **L3** and **L4** were found in the GSK3 β structure (Figure 64).

Table 25. Sequence alignment scores (in percentage) for protein kinases. Sequences of CDK2, Aurora A, MAPK, GSK3b, PKA, and PKC were aligned with ClustalW2.

	Aurora A	MAPK	GSK3b	PKA	PKC
CDK2	27	37	31	23	25
Aurora A		18	19	23	23
MAPK			24	17	18
GSK3b				15	15
PKA					33

The results of the docking studies with other kinase structures imply that the current CDK2 inhibitors might not be selective and they need to be modified to contain specific interactions only with CDK2 to gain the selectivity.

From intensive SAR and structural studies, excellent inhibitory potencies, in the sub-micromolar range were achieved. The selectivities of the current inhibitors are now known yet. Future investigation will include the studies of the selectivity of the inhibitors.

4. Conclusion

The kinetic and structural characterizations of Arg91Lys and Asp123Ala MurA mutants revealed the roles of two residues in the enzymatic mechanism of MurA. Arg91 is a critical residue in the open-closed transition of MurA. Asp123 is involved in the binding of UNAG to MurA.

The crystallographic studies of Arg120Ala MurA provided evidence for the existence of a thio-ketal intermediate between Cys115 and PEP during the reaction. Arg120 presumably functions as a key residue in transferring PEP from Cys115 to the target hydroxyl of UNAG.

The kinetic studies of cnicin, a recently reported MurA inhibitor, indicated slow binding inhibition. In addition, several new inhibitors of MurA were identified by HTS and characterized by enzyme kinetics. It appeared that **HTS2-2** inhibits the enzyme by inducing oligomerization of MurA. From the kinetic and crystallographic studies of the new inhibitors, we conclude that all of these compounds bind in the open form of the enzyme. Future studies will focus on the identification of novel inhibitors, inducing the open-closed conformational changes of MurA, similar to UNAG.

Six different CDK2 inhibitor scaffolds were identified by HTS. The molecular modes of action of four of the representative compounds were revealed by kinetic and crystallographic studies. All inhibitors are competitive with respect to ATP. SAR analysis of each scaffold was conducted with various analogs. Structural information

obtained from crystallographic studies provided the detailed binding modes of the derivatives, and allowed for the design of new analogs with improved binding affinities. Excellent inhibitory potencies to CDK2 in the sub-micromolar ranges of IC_{50} values were achieved. In addition, several new inhibitor scaffolds were designed. The syntheses of the new compounds are currently underway. Selectivities of the inhibitors over other protein kinases are not known yet, and will be a focus in future investigation.

References

1. Stefani, S., Emergence of Multi-Drug Resistance Gram-Positive Bacteria and New Active Antibiotics. *Current Medicinal Chemistry - Anti-Infective Agents* **2005**, *4*, 235–257.
2. Rogers, H. J.; Perkins, H. R.; Ward, J. B., Biosynthesis of Peptidoglycan. In *Microbial cell walls and membranes*. Chapman & Hall: London, 1980; pp 239–297.
3. Van Heijenoort, J., Recent advances in the formation of the bacterial peptidoglycan monomer unit. *Natural Product Reports* **2001**, *18*, 503–519.
4. Bugg, T. D. H.; Walsh, C. T., Intracellular Steps of Bacterial-Cell Wall Peptidoglycan Biosynthesis – Enzymology, Antibiotics, and Antibiotic-Resistance. *Natural Product Reports* **1992**, *9*, 199–215.
5. Bouhss, A.; Crouvoisier, M.; Blanot, D.; Mengin-Lecreulx, D., Purification and characterization of the bacterial MraY translocase catalyzing the first membrane step of peptidoglycan biosynthesis. *Journal of Biological Chemistry* **2004**, *279*, 29974–29980.
6. Taku, A.; Fan, D. P., Identification of an Isolated Protein Essential for Peptidoglycan Synthesis as N-acetylglucosaminyl Transferase. *Journal of Biological Chemistry* **1976**, *251*, 6154–6156.
7. Goffin, C.; Ghuysen, J. M., Multimodular penicillin-binding proteins: An enigmatic family of orthologs and paralogs. *Microbiology and Molecular Biology Reviews* **1998**, *62*, 1079–1093.
8. Van Heijenoort, J., Formation of the glycan chains in the synthesis of bacterial peptidoglycan. *Glycobiology* **2001**, *11*, 25R–36R.
9. Walker, S.; Chen, L.; Hu, Y. N.; Rew, Y.; Shin, D. W.; Boger, D. L., Chemistry and biology of ramoplanin: A lipoglycopeptide with potent antibiotic activity. *Chemical Reviews* **2005**, *105*, 449–475.

10. El Zoeiby, A.; Sanschagrin, F.; Levesque, R. C., Structure and function of the Mur enzymes: development of novel inhibitors. *Molecular Microbiology* **2003**, *47*, 1–12.
11. Koch, A. L., Guest commentary – Autolysis control hypotheses for tolerance to wall antibiotics. *Antimicrobial Agents and Chemotherapy* **2001**, *45*, 2671–2675.
12. Van Heijenoort, J., Biosynthesis of the bacterial peptidoglycan unit. In *Bacterial Cell Wall*, Ghuysen, J. M.; Hackenbeck, R., Eds. Elsevier: Amsterdam, 1994; Vol. 27, pp 39–54.
13. Kahan, F. M.; Kahan, J. S.; Cassidy, P. J.; Kropp, H., The mechanism of action of fosfomycin (phosphonomycin). *Annals of the New York Academy of Sciences* **1974**, *235*, 364–386.
14. Steinrucken, H. C.; Amrhein, N., The herbicide glyphosate is a potent inhibitor of 5-enolpyruvyl-shikimic acid-3-phosphate synthase. *Biochemical and Biophysical Research Communications* **1980**, *94*, 1207–1212.
15. Du, W.; Brown, J. R.; Sylvester, D. R.; Huang, J.; Chalker, A. F.; So, C. Y.; Holmes, D. J.; Payne, D. J.; Wallis, N. G., Two active forms of UDP-N-acetylglucosamine enolpyruvyl transferase in gram-positive bacteria. *Journal of Bacteriology* **2000**, *182*, 4146–4152.
16. Marquardt, J. L.; Brown, E. D.; Walsh, C. T.; Anderson, K. S., Isolation and structural elucidation of a tetrahedral intermediate in the UDP-N-acetylglucosamine enolpyruvyl transferase enzymatic pathway. *Journal of the American Chemical Society* **1993**, *115*, 10398–10399.
17. Cassidy, P. J.; Kahan, F. M., A stable enzyme-phosphoenolpyruvate intermediate in the synthesis of uridine-5'-diphospho-N-acetyl-2-amino-2-deoxyglucose 3-O-enolpyruvyl ether. *Biochemistry* **1973**, *12*, 1364–1374.
18. Brown, E. D.; Marquardt, J. L.; Lee, J. P.; Walsh, C. T.; Anderson, K. S., Detection and characterization of a phospholactoyl-enzyme adduct in the reaction catalyzed by UDP-N-acetylglucosamine enolpyruvyl transferase, MurZ. *Biochemistry* **1994**, *33*, 10638–10645.

19. Skarzynski, T.; Kim, D. H.; Lees, W. J.; Walsh, C. T.; Duncan, K., Stereochemical course of enzymatic enolpyruvyl transfer and catalytic conformation of the active site revealed by the crystal structure of the fluorinated analogue of the reaction tetrahedral intermediate bound to the active site of the C115A mutant of MurA. *Biochemistry* **1998**, *37*, 2572–2577.
20. Eschenburg, S.; Priestman, M. A.; Schönbrunn, E., Evidence that the fosfomycin target Cys115 in UDP-N-acetylglucosamine enolpyruvyl transferase (MurA) is essential for product release. *Journal of Biological Chemistry* **2005**, *280*, 3757–3763.
21. Kim, D. H.; Lees, W. J.; Walsh, C. T., Stereochemical analysis of the tetrahedral adduct formed at the active site of UDP-GlcNAc enolpyruvyl transferase from the pseudosubstrates, (E)- and (Z)-3-fluorophosphoenolpyruvate, in D₂O. *Journal of the American Chemical Society* **1995**, *117*, 6380–6381.
22. Lees, W. J.; Walsh, C. T., Analysis of the enol ether transfer catalyzed by UDP-GlcNAc enolpyruvyl transferase using (E)- and (Z)-isomers of phosphoenolbutyrate: stereochemical, partitioning, and isotope effect studies. *Journal of the American Chemical Society* **1995**, *117*, 7329–7337.
23. Eschenburg, S.; Kabsch, W.; Healy, M. L.; Schönbrunn, E., A new view of the mechanisms of UDP-N-acetylglucosamine enolpyruvyl transferase (MurA) and 5-enolpyruvylshikimate-3-phosphate synthase (AroA) derived from X-ray structures of their tetrahedral reaction intermediate states. *Journal of Biological Chemistry* **2003**, *278*, 49215–49222.
24. Skarzynski, T.; Mistry, A.; Wonacott, A.; Hutchinson, S. E.; Kelly, V. A.; Duncan, K., Structure of UDP-N-acetylglucosamine enolpyruvyl transferase, an enzyme essential for the synthesis of bacterial peptidoglycan, complexed with substrate UDP-N-acetylglucosamine and the drug fosfomycin. *Structure* **1996**, *4*, 1465–1474.
25. Eschenburg, S.; Schönbrunn, E., Comparative X-ray analysis of the unliganded fosfomycin-target murA. *Proteins* **2000**, *40*, 290–298.
26. Schönbrunn, E.; Eschenburg, S.; Krekel, F.; Luger, K.; Amrhein, N., Role of the loop containing residue 115 in the induced-fit mechanism of the bacterial cell wall biosynthetic enzyme MurA. *Biochemistry* **2000**, *39*, 2164–2173.

27. Schönbrunn, E.; Sack, S.; Eschenburg, S.; Perrakis, A.; Krekel, F.; Amrhein, N.; Mandelkow, E., Crystal structure of UDP-N-acetylglucosamine enolpyruvyltransferase, the target of the antibiotic fosfomycin. *Structure* **1996**, *4*, 1065–1075.
28. Eschenburg, S.; Healy, M. L.; Priestman, M. A.; Lushington, G. H.; Schönbrunn, E., How the mutation glycine96 to alanine confers glyphosate insensitivity to 5-enolpyruvyl shikimate-3-phosphate synthase from *Escherichia coli*. *Planta* **2002**, *216*, 129–135.
29. Schönbrunn, E.; Eschenburg, S.; Luger, K.; Kabsch, W.; Amrhein, N., Structural basis for the interaction of the fluorescence probe 8-anilino-1-naphthalene sulfonate (ANS) with the antibiotic target MurA. *Proceedings of the National Academy of Sciences of the United States of America* **2000**, *97*, 6345–6349.
30. Klein, C. D.; Bachelier, A., Molecular modeling and bioinformatical analysis of the antibacterial target enzyme MurA from a drug design perspective. *Journal of Computer-Aided Molecular Design* **2006**, *20*, 621–628.
31. Hendlin, D.; Stapley, E. O.; Jackson, M.; Wallick, H.; Miller, A. K.; Wolf, F.; Miller, T. W.; Chaiet, L.; Kahan, F. M.; Foltz, E. L.; Woodruff, H. B.; Mata, J. M.; Hernandez, S.; Mochales, S., Phosphonomycin, a new antibiotic produced by strains of streptomyces. *Science* **1969**, *166*, 122–123.
32. El Zoeiby, A.; Beaumont, M.; Dubuc, E.; Sanschagrin, F.; Voyer, N.; Levesque, R. C., Combinatorial enzymatic assay for the screening of a new class of bacterial cell wall inhibitors. *Bioorganic & Medicinal Chemistry* **2003**, *11*, 1583–1592.
33. Kahlmeter, G., An international survey of the antimicrobial susceptibility of pathogens from uncomplicated urinary tract infections: the ECOSENS project. *Journal of Antimicrobial Chemotherapy* **2003**, *51*, 69–76.
34. Nilsson, A. I.; Berg, O. G.; Aspevall, O.; Kahlmeter, G.; Andersson, D. I., Biological costs and mechanisms of fosfomycin resistance in *Escherichia coli*. *Antimicrobial Agents and Chemotherapy* **2003**, *47*, 2850–2858.

35. Allerberger, F.; Klare, I., In-vitro activity of fosfomicin against vancomycin-resistant enterococci. *Journal of Antimicrobial Chemotherapy* **1999**, *43*, 211–217.
36. Ungheri, D.; Albini, E.; Belluco, G., In-vitro susceptibility of quinolone-resistant clinical isolates of *Escherichia coli* to fosfomicin trometamol. *Journal of Chemotherapy* **2002**, *14*, 237–240.
37. Marquardt, J. L.; Brown, E. D.; Lane, W. S.; Haley, T. M.; Ichikawa, Y.; Wong, C. H.; Walsh, C. T., Kinetics, stoichiometry, and identification of the reactive thiolate in the inactivation of UDP-GlcNAc enolpyruvyl transferase by the antibiotic fosfomicin. *Biochemistry* **1994**, *33*, 10646–10651.
38. Wanke, C.; Amrhein, N., Evidence that the reaction of the UDP-N-acetylglucosamine 1-carboxyvinyltransferase proceeds through the O-phosphothioketal of pyruvic acid bound to Cys115 of the enzyme. *European Journal of Biochemistry* **1993**, *218*, 861–870.
39. Mendoza, C.; Garcia, J. M.; Llana, J.; Mendez, F. J.; Hardisson, C.; Ortiz, J. M., Plasmid-determined resistance to fosfomicin in *Serratia marcescens*. *Antimicrobial Agents and Chemotherapy* **1980**, *18*, 215–219.
40. Etienne, J.; Gerbaud, G.; Courvalin, P.; Fleurette, J., Plasmid-mediated resistance to fosfomicin in *Staphylococcus epidermidis*. *FEMS Microbiology Letters* **1989**, *52*, 133–137.
41. Suarez, J. E.; Mendoza, M. C., Plasmid-encoded fosfomicin resistance. *Antimicrobial Agents and Chemotherapy* **1991**, *35*, 791–795.
42. O'Hara, K., Two different types of fosfomicin resistance in clinical isolates of *Klebsiella pneumoniae*. *FEMS Microbiology Letters* **1993**, *114*, 9–16.
43. Arca, P.; Reguera, G.; Hardisson, C., Plasmid-encoded fosfomicin resistance in bacteria isolated from the urinary tract in a multicentre survey. *Journal of Antimicrobial Chemotherapy* **1997**, *40*, 393–399.
44. Kadner, R. J.; Winkler, H. H., Isolation and characterization of mutations affecting the transport of hexose phosphates in *Escherichia coli*. *Journal of Bacteriology* **1973**, *113*, 895–900.

45. Tsuruoka, T.; Yamada, Y., Characterization of spontaneous fosfomycin (phosphonomycin)-resistant cells of *Escherichia coli* B *in vitro*. *Journal of Antibiotics* **1975**, *28*, 906–911.
46. Venkateswaran, P. S.; Wu, H. C., Isolation and characterization of a phosphonomycin-resistant mutant of *Escherichia coli* K-12. *Journal of Bacteriology* **1972**, *110*, 935–944.
47. Arca, P.; Hardisson, C.; Suarez, J. E., Purification of a glutathione S-transferase that mediates fosfomycin resistance in bacteria. *Antimicrobial Agents and Chemotherapy* **1990**, *34*, 844–848.
48. Arca, P.; Rico, M.; Brana, A. F.; Villar, C. J.; Hardisson, C.; Suarez, J. E., Formation of an adduct between fosfomycin and glutathione: a new mechanism of antibiotic resistance in bacteria. *Antimicrobial Agents and Chemotherapy* **1988**, *32*, 1552–1556.
49. Garcia-Lobo, J. M.; Ortiz, J. M., Tn2921, a transposon encoding fosfomycin resistance. *Journal of Bacteriology* **1982**, *151*, 477–479.
50. Navas, J.; Garcia-Lobo, J. M.; Leon, J.; Ortiz, J. M., Structural and functional analyses of the fosfomycin resistance transposon Tn2921. *Journal of Bacteriology* **1985**, *162*, 1061–1067.
51. Bernat, B. A.; Laughlin, T.; Armstrong, R. N., Fosfomycin resistance protein (FosA) is a manganese metalloglutathione transferase related to glyoxalase I and the extradiol dioxygenases. *Biochemistry* **1997**, *36*, 3050–3055.
52. Rife, C. L.; Pharris, R. E.; Newcomer, M. E.; Armstrong, R. N., Crystal structure of a genomically encoded fosfomycin resistance protein (FosA) at 1.19 Å resolution by MAD phasing off the L-III edge of Tl^+ . *Journal of the American Chemical Society* **2002**, *124*, 11001–11003.
53. Kim, D. H.; Lees, W. J.; Kempell, K. E.; Lane, W. S.; Duncan, K.; Walsh, C. T., Characterization of a Cys115 to Asp substitution in the *Escherichia coli* cell wall biosynthetic enzyme UDP-GlcNAc enolpyruvyl transferase (MurA) that confers resistance to inactivation by the antibiotic fosfomycin. *Biochemistry* **1996**, *35*, 4923–4928.

54. Llaneza, J.; Villar, C. J.; Salas, J. A.; Suarez, J. E.; Mendoza, M. C.; Hardisson, C., Plasmid-mediated fosfomycin resistance is due to enzymatic modification of the antibiotic. *Antimicrobial Agents and Chemotherapy* **1985**, *28*, 163–164.
55. McCoy, A. J.; Sandlin, R. C.; Maurelli, A. T., In vitro and in vivo functional activity of *Chlamydia* MurA, a UDP-N- acetylglucosamine enolpyruvyl transferase involved in peptidoglycan synthesis and fosfomycin resistance. *Journal of Bacteriology* **2003**, *185*, 1218–1228.
56. Baum, E. Z.; Montenegro, D. A.; Licata, L.; Turchi, I.; Webb, G. C.; Foleno, B. D.; Bush, K., Identification and characterization of new inhibitors of the *Escherichia coli* MurA enzyme. *Antimicrobial Agents and Chemotherapy* **2001**, *45*, 3182–3188.
57. Barbosa, M. D.; Yang, G.; Fang, J.; Kurilla, M. G.; Pompliano, D. L., Development of a whole-cell assay for peptidoglycan biosynthesis inhibitors. *Antimicrobial Agents and Chemotherapy* **2002**, *46*, 943–946.
58. Kutterer, K. M. K.; Davis, J. M.; Singh, G.; Yang, Y.; Hu, W.; Severin, A.; Rasmussen, B. A.; Krishnamurthy, G.; Failli, A.; Katz, A. H., 4-Alkyl- and 4,4-dialkyl-1,2-bis(4-chlorophenyl)pyrazolidine-3,5-dione derivatives as new inhibitors of bacterial cell wall biosynthesis. *Bioorganic & Medicinal Chemistry Letters* **2005**, *15*, 2527–2531.
59. Mansour, T. S.; Caufield, C. E.; Rasmussen, B.; Chopra, R.; Krishnamurthy, G.; Morris, K. M.; Svenson, K.; Bard, J.; Smeltzer, C.; Naughton, S.; Antane, S.; Yang, Y. J.; Severin, A.; Quagliato, D.; Petersen, P. J.; Singh, G., Naphthyl tetronic acids as multi-target inhibitors of bacterial peptidoglycan biosynthesis. *ChemMedChem* **2007**, *2*, 1414–1417.
60. Bachelier, A.; Mayer, R.; Klein, C. D., Sesquiterpene lactones are potent and irreversible inhibitors of the antibacterial target enzyme MurA. *Bioorganic & Medicinal Chemistry Letters* **2006**, *16*, 5605–5609.
61. Dunsmore, C. J.; Miller, K.; Blake, K. L.; Patching, S. G.; Henderson, P. J. F.; Garnett, J. A.; Stubbings, W. J.; Phillips, S. E. V.; Palestrant, D. J.; Angeles J. D. L.; Leeds, J. A.; Chopra, I.; Fishwick, C. W. G., 2-aminotetralones: Novel inhibitors of MurA and MurZ. *Bioorganic & Medicinal Chemistry Letters* **2008**, *18*, 1730–1734.

62. Eschenburg, S.; Priestman, M. A.; Abdul-Latif, F. A.; Delachaume, C.; Fassy, F.; Schönbrunn, E., A novel inhibitor that suspends the induced fit mechanism of UDP-N-acetylglucosamine enolpyruvyl transferase (MurA). *Journal of Biological Chemistry* **2005**, *280*, 14070–14075.
63. Molina-Lopez, J.; Sanschagrin, F.; Levesque, R. C., A peptide inhibitor of MurA UDP-N-acetylglucosamine enolpyruvyl transferase: The first committed step in peptidoglycan biosynthesis. *Peptides* **2006**, *27*, 3115–3121.
64. Bernhardt, T. G.; Wang, I. N.; Struck, D. K.; Young, R., A protein antibiotic in the phage Q β virion: diversity in lysis targets. *Science* **2001**, *292*, 2326–2329.
65. Seet, B. T.; Dikic, I.; Zhou, M. M.; Pawson, T., Reading protein modifications with interaction domains. *Nature Reviews Molecular Cell Biology* **2006**, *7*, 473–483.
66. Yang, X. J., Multisite protein modification and intramolecular signaling. *Oncogene* **2005**, *24*, 1653–1662.
67. Cohen, P., The origins of protein phosphorylation. *Nature Cell Biology* **2002**, *4*, E127–E130.
68. Manning, G.; Whyte, D. B.; Martinez, R.; Hunter, T.; Sudarsanam, S., The protein kinase complement of the human genome. *Science* **2002**, *298*, 1912–1934.
69. Pines, J., Cyclins and cyclin-dependent kinases – theme and variations. *Advances in Cancer Research* **1995**, *66*, 181–212.
70. Morgan, D. O., Cyclin-dependent kinases: Engines, clocks, and microprocessors. *Annual Review of Cell and Developmental Biology* **1997**, *13*, 261–291.
71. Sherr, C. J., Cancer cell cycles. *Science* **1996**, *274*, 1672–1677.
72. Pines, J., Cyclins and cyclin-dependent kinases – a biochemical view. *Biochemical Journal* **1995**, *308*, 697–711.
73. Norbury, C.; Nurse, P., Animal-cell cycles and their control. *Annual Review of Biochemistry* **1992**, *61*, 441–470.

74. Nigg, E. A., Cyclin-dependent protein-kinases – key regulators of the eukaryotic cell-cycle. *Bioessays* **1995**, *17*, 471–480.
75. Edgar, B. A.; Lehner, C. F., Developmental control of cell cycle regulators: A fly's perspective. *Science* **1996**, *274*, 1646–1652.
76. Draetta, G. F., Cell cycle: Will the real CDK-activating kinase please stand up. *Current Biology* **1997**, *7*, R50–R52.
77. Sherr, C. J.; Roberts, J. M., CDK inhibitors: positive and negative regulators of G(1)-phase progression. *Genes & Development* **1999**, *13*, 1501–1512.
78. Lee, M. H.; Yang, H. Y., Negative regulators of cyclin-dependent kinases and their roles in cancers. *Cellular and Molecular Life Sciences* **2001**, *58*, 1907–1922.
79. Polyak, K.; Lee, M. H.; Erdjumentbromage, H.; Koff, A.; Roberts, J. M.; Tempst, P.; Massague, J., Cloning of p27(Kip1), a cyclin-dependent kinase inhibitor and a potential mediator of extracellular antimitogenic signals. *Cell* **1994**, *78*, 59–66.
80. Kamb, A., Cell-cycle regulators and cancer. *Trends in Genetics* **1995**, *11*, 136–140.
81. Sgambato, A.; Flamini, G.; Cittadini, A.; Weinstein, I. B., Abnormalities in cell cycle control in cancer and their clinical implications. *Tumori* **1998**, *84*, 421–433.
82. D'Amico, M.; Wu, K. M.; Fu, M. F.; Rao, M.; Albanese, C.; Russell, R. G.; Lian, H.; Bregman, D.; White, M. A.; Pestell, R. G., The inhibitor of cyclin-dependent kinase 4a/alternative reading frame (INK4a/ARF) locus encoded proteins p16(INK4a) and p19(ARF) repress cyclin D1 transcription through distinct cis elements. *Cancer Research* **2004**, *64*, 4122–4130.
83. De Marval, P. L. M.; Macias, E.; Rounbehler, R.; Sicinski, P.; Kiyokawa, H.; Johnson, D. G.; Conti, C. J.; Rodriguez-Puebla, M. L., Lack of cyclin-dependent kinase 4 inhibits c-myc tumorigenic activities in epithelial tissues. *Molecular and Cellular Biology* **2004**, *24*, 7538–7547.

84. Berman, H. M.; Westbrook, J.; Feng, Z.; Gilliland, G.; Bhat, T. N.; Weissig, H.; Shindyalov, I. N.; Bourne, P. E., The Protein Data Bank. *Nucleic Acids Research* **2000**, *28*, 235–242. [URL] <http://www.pdb.org>
85. Hanks, S. K.; Hunter, T., Protein kinases 6. The eukaryotic protein-kinase superfamily – kinase (catalytic) domain-structure and classification. *Faseb Journal* **1995**, *9*, 576–596.
86. SchulzeGahmen, U.; DeBondt, H. L.; Kim, S. H., High-resolution crystal structures of human cyclin-dependent kinase 2 with and without ATP: Bound waters and natural ligand as guides for inhibitor design. *Journal of Medicinal Chemistry* **1996**, *39*, 4540–4546.
87. Schulzegahmen, U.; Brandsen, J.; Jones, H. D.; Morgan, D. O.; Meijer, L.; Vesely, J.; Kim, S. H., Multiple-modes of ligand recognition - crystal-structures of cyclin-dependent protein-kinase-2 in complex with ATP and 2 inhibitors, olomoucine and isopentenyladenine. *Proteins-Structure Function and Genetics* **1995**, *22*, 378–391.
88. Wu, S. Y.; McNae, I.; Kontopidis, G.; McClue, S. J.; McInnes, C.; Stewart, K. J.; Wang, S. D.; Zheleva, D. I.; Marriage, H.; Lane, D. P.; Taylor, P.; Fischer, P. M.; Walkinshaw, M. D., Discovery of a novel family of CDK inhibitors with the program LIDAEUS: Structural basis for ligand-induced disordering of the activation loop. *Structure* **2003**, *11*, 399–410.
89. Brown, N. R.; Noble, M. E. M.; Lawrie, A. M.; Morris, M. C.; Tunnah, P.; Divita, G.; Johnson, L. N.; Endicott, J. A., Effects of phosphorylation of threonine 160 on cyclin-dependent kinase 2 structure and activity. *Journal of Biological Chemistry* **1999**, *274*, 8746–8756.
90. Russo, A. A.; Jeffrey, P. D.; Pavletich, N. P., Structural basis of cyclin-dependent kinase activation by phosphorylation. *Nature Structural Biology* **1996**, *3*, 696–700.
91. Jeffrey, P. D.; Russo, A. A.; Polyak, K.; Gibbs, E.; Hurwitz, J.; Massague, J.; Paveltich, N. P., Mechanism of CDK activation revealed by the structure of a cyclinA-CDK2 complex. *Nature* **1995**, *376*, 313–320.
92. Davis, S. T.; Benson, B. G.; Bramson, H. N.; Chapman, D. E.; Dickerson, S. H.; Dold, K. M.; Eberwein, D. J.; Edelstein, M.; Frye, S. V.;

- Gampe, R. T.; Griffin, R. J.; Harris, P. A.; Hassell, A. M.; Holmes, W. D.; Hunter, R. N.; Knick, V. B.; Lackey, K.; Lavejoy, B.; Luzzio, M. J.; Murray, D.; Parker, P.; Rocque, W. J.; Shewchuk, L.; Veal, J. M.; Walker, D. H.; Kuyper, L. F., Prevention of chemotherapy-induced alopecia in rats by CDK inhibitors. *Science* **2001**, *291*, 134–137.
93. Lawrie, A. M.; Noble, M. E. M.; Tunnah, P.; Brown, N. R.; Johnson, L. N.; Endicott, J. A., Protein kinase inhibition by staurosporine revealed in details of the molecular interaction with CDK2. *Nature Structural Biology* **1997**, *4*, 796–801.
94. Gray, N. S.; Wodicka, L.; Thunnissen, A.; Norman, T. C.; Kwon, S. J.; Espinoza, F. H.; Morgan, D. O.; Barnes, G.; LeClerc, S.; Meijer, L.; Kim, S. H.; Lockhart, D. J.; Schultz, P. G., Exploiting chemical libraries, structure, and genomics in the search for kinase inhibitors. *Science* **1998**, *281*, 533–538.
95. Shewchuk, L.; Hassell, A.; Wisely, B.; Rocque, W.; Holmes, W.; Veal, J.; Kuyper, L. F., Binding mode of the 4-anilinoquinazoline class of protein kinase inhibitor: X-ray crystallographic studies of 4-anilinoquinazolines bound to cyclin-dependent kinase 2 and p38 kinase. *Journal of Medicinal Chemistry* **2000**, *43*, 133–138.
96. Meijer, L.; Thunnissen, A.; White, A. W.; Garnier, M.; Nikolic, M.; Tsai, L. H.; Walter, J.; Cleverley, K. E.; Salinas, P. C.; Wu, Y. Z.; Biernat, J.; Mandelkow, E. M.; Kim, S. H.; Pettit, G. R., Inhibition of cyclin-dependent kinases, GSK-3 beta and CK1 by hymenialdisine, a marine sponge constituent. *Chemistry & Biology* **2000**, *7*, 51–63.
97. Arris, C. E.; Boyle, F. T.; Calvert, A. H.; Curtin, N. J.; Endicott, J. A.; Garman, E. F.; Gibson, A. E.; Golding, B. T.; Grant, S.; Griffin, R. J.; Jewsbury, P.; Johnson, L. N.; Lawrie, A. M.; Newell, D. R.; Noble, M. E. M.; Sausville, E. A.; Schultz, R.; Yu, W., Identification of Novel Purine and Pyrimidine Cyclin-Dependent Kinase Inhibitors with Distinct Molecular Interactions and Tumor Cell Growth Inhibition Profiles. *Journal of Medicinal Chemistry* **2000**, *43*, 2797–2804.
98. Dreyer, M. K.; Borcharding, D. R.; Dumont, J. A.; Peet, N. P.; Tsay, J. T.; Wright, P. S.; Bitonti, A. J.; Shen, J.; Kim, S. H., Crystal structure of human

cyclin-dependent kinase 2 in complex with the adenine-derived inhibitor H717. *Journal of Medicinal Chemistry* **2001**, *44*, 524–530.

99. Davies, T. G.; Bentley, J.; Arris, C. E.; Boyle, F. T.; Curtin, N. J.; Endicott, J. A.; Gibson, A. E.; Golding, B. T.; Griffin, R. J.; Hardcastle, I. R.; Jewsbury, P.; Johnson, L. N.; Mesguiche, V.; Newell, D. R.; Noble, M. E. M.; Tucker, J. A.; Wang, L.; Whitfield, H. J., Structure-based design of a potent purine-based cyclin-dependent kinase inhibitor. *Nature Structural Biology* **2002**, *9*, 745–749.
100. Bramson, H. N.; Corona, J.; Davis, S. T.; Dickerson, S. H.; Edelstein, M.; Frye, S. V.; Gampe, R. T.; Harris, P. A.; Hassell, A.; Holmes, W. D.; Hunter, R. N.; Lackey, K. E.; Lovejoy, B.; Luzzio, M. J.; Montana, V.; Rocque, W. J.; Rusnak, D.; Shewchuk, L.; Veal, J. M.; Walker, D. H.; Kuyper, L. F., Oxindole-based inhibitors of cyclin-dependent kinase 2 (CDK2): Design, synthesis, enzymatic activities, and X-ray crystallographic analysis. *Journal of Medicinal Chemistry* **2001**, *44*, 4339–4358.
101. Anderson, M.; Beattie, J. F.; Breault, G. A.; Breed, J.; Byth, K. F.; Culshaw, J. D.; Ellston, R. P. A.; Green, S.; Minshull, C. A.; Norman, R. A.; Pauptit, R. A.; Stanway, J.; Thomas, A. P.; Jewsbury, P. J., Imidazo[1,2-a]pyridines: A potent and selective class of cyclin-dependent kinase inhibitors identified through structure-based hybridisation. *Bioorganic & Medicinal Chemistry Letters* **2003**, *13*, 3021–3026.
102. Liu, J. J.; Dermatakis, A.; Lukacs, C.; Konzelmann, F.; Chen, Y.; Kammlott, U.; Depinto, W.; Yang, H.; Yin, X. F.; Chen, Y. S.; Schutt, A.; Simcox, M. E.; Luk, K. C., 3,5,6-trisubstituted naphthostyrils as CDK2 inhibitors. *Bioorganic & Medicinal Chemistry Letters* **2003**, *13*, 2465–2468.
103. Moshinsky, D. J.; Bellamacina, C. R.; Boisvert, D. C.; Huang, P.; Hui, T.; Jancarik, J.; Kim, S. H.; Rice, A. G., SU9516: biochemical analysis of cdk inhibition and crystal structure in complex with CDK2. *Biochemical and Biophysical Research Communications* **2003**, *310*, 1026–1031.
104. Wang, S. D.; Meades, C.; Wood, G.; Osnowski, A.; Anderson, S.; Yuill, R.; Thomas, M.; Mezna, M.; Jackson, W.; Midgley, C.; Griffiths, G.; Fleming, I.; Green, S.; McNae, I.; Wu, S. Y.; McInnes, C.; Zheleva, D.; Walkinshaw, M. D.; Fischer, P. M., 2-anilino-4-(thiazol-5-yl)pyrimidine CDK

- inhibitors: Synthesis, SAR analysis, X-ray crystallography, and biological activity. *Journal of Medicinal Chemistry* **2004**, *47*, 1662–1675.
105. Hamdouchi, C.; Keyser, H.; Collins, E.; Jaramillo, C.; De Diego, J. E.; Spencer, C. D.; Dempsey, J. A.; Anderson, B. D.; Leggett, T.; Stamm, N. B.; Schultz, R. M.; Watkins, S. A.; Cocks, K.; Lemke, S.; Burke, T. F.; Beckmann, R. P.; Dixon, J. T.; Gurganus, T. M.; Rankl, N. B.; Houck, K. A.; Zhang, F. M.; Vieth, M.; Espinosa, J.; Timm, D. E.; Campbell, R. M.; Patel, B. K. R.; Brooks, H. B., The discovery of a new structural class of cyclin-dependent kinase inhibitors, aminoimidazo[1,2-a]pyridines. *Molecular Cancer Therapeutics* **2004**, *3*, 1-9.
 106. Luk, K. C.; Simcox, M. E.; Schutt, A.; Rowan, K.; Thompson, T.; Chen, Y.; Kammlott, U.; DePinto, W.; Dunten, P.; Dermatakis, A., A new series of potent oxindole inhibitors of CDK2. *Bioorganic & Medicinal Chemistry Letters* **2004**, *14*, 913–917.
 107. Byth, K. F.; Cooper, N.; Culshaw, J. D.; Heaton, D. W.; Oakes, S. E.; Minshull, C. A.; Norman, R. A.; Pauptit, R. A.; Tucker, J. A.; Breed, J.; Pannifer, A.; Rowsell, S.; Stanway, J. J.; Valentine, A. L.; Thomas, A. P., Imidazo[1,2-b]pyridazines: a potent and selective class of cyclin-dependent kinase inhibitors. *Bioorganic & Medicinal Chemistry Letters* **2004**, *14*, 2249–2252.
 108. Knockaert, M.; Greengard, P.; Meijer, L., Pharmacological inhibitors of cyclin-dependent kinases. *Trends in Pharmacological Sciences* **2002**, *23*, 417–425.
 109. Malumbres, M.; Pevarello, P.; Barbacid, M.; Bischoff, J. R., CDK inhibitors in cancer therapy: what is next? *Trends in Pharmacological Sciences* **2008**, *29*, 16–21.
 110. Meijer, L., Chemical inhibitors of cyclin-dependent kinases. *Trends in Cell Biology* **1996**, *6*, 393–397.
 111. Gadbois, D. M.; Hamaguchi, J. R.; Swank, R. A.; Bradbury, E. M., Staurosporine is a potent inhibitor of p34CDC2 and p34CDC2-like kinases. *Biochemical and Biophysical Research Communications* **1992**, *184*, 80–85.

112. Pereira, E. R.; Belin, L.; Sancelme, M.; Prudhomme, M.; Ollier, M.; Rapp, M.; Severe, D.; Riou, J. F.; Fabbro, D.; Meyer, T., Structure-activity relationships in a series of substituted indolocarbazoles: Topoisomerase I and protein kinase C inhibition and antitumoral and antimicrobial properties. *Journal of Medicinal Chemistry* **1996**, *39*, 4471–4477.
113. Wood, J. L.; Stoltz, B. M.; Goodman, S. N., Total synthesis of (+)-RK-286c, (+)-MLR-52, (+)-staurosporine, and (+)-K252a. *Journal of the American Chemical Society* **1996**, *118*, 10656–10657.
114. Noble, M. E. M.; Endicott, J. A.; Johnson, L. N., Protein kinase inhibitors: Insights into drug design from structure. *Science* **2004**, *303*, 1800–1805.
115. Sedlacek, H. H.; Czech, J.; Naik, R.; Kaur, G.; Worland, P.; Losiewicz, M.; Parker, B.; Carlson, B.; Smith, A.; Senderowicz, A.; Sausville, E., Flavopiridol (L86 8275; NSC 649890), a new kinase inhibitor for tumor therapy. *International Journal of Oncology* **1996**, *9*, 1143–1168.
116. Carlson, B. A.; Dubay, M. M.; Sausville, E. A.; Brizuela, L.; Worland, P. J., Flavopiridol induces G(1) arrest with inhibition of cyclin-dependent kinase (CDK)2 and CDK4 in human breast carcinoma cells. *Cancer Research* **1996**, *56*, 2973–2978.
117. Carlson, B.; Lahusen, T.; Singh, S.; Loaiza-Perez, A.; Worland, P. J.; Pestell, R.; Albanese, C.; Sausville, E. A.; Senderowicz, A. M., Down-regulation of cyclin D1 by transcriptional repression in MCF-7 human breast carcinoma cells induced by flavopiridol. *Cancer Research* **1999**, *59*, 4634–4641.
118. De Azevedo, Jr., W. F.; Mueller-Dieckmann, H. J.; Schulze-Gahmen, U.; Worland, P. J.; Sausville, E.; Kim, S. H., Structural basis for specificity and potency of a flavonoid inhibitor of human CDK2, a cell cycle kinase. *Proceedings of the National Academy of Sciences of the United States of America* **1996**, *93*, 2735–2740.
119. Hardcastle, I. R.; Golding, B. T.; Griffin, R. J., Designing inhibitors of cyclin-dependent kinases. *Annual Review of Pharmacology and Toxicology* **2002**, *42*, 325–348.

120. Kent, L. L.; Hull-Campbell, N. E.; Lau, T.; Wu, J. C.; Thompson, S. A.; Nori, M., Characterization of novel inhibitors of cyclin-dependent kinases. *Biochemical and Biophysical Research Communications* **1999**, *260*, 768–774.
121. Hoessel, R.; Leclerc, S.; Endicott, J. A.; Nobel, M. E. M.; Lawrie, A.; Tunnah, P.; Leost, M.; Damiens, E.; Marie, D.; Marko, D.; Niederberger, E.; Tang, W. C.; Eisenbrand, G.; Meijer, L., Indirubin, the active constituent of a Chinese antileukaemia medicine, inhibits cyclin-dependent kinases. *Nature Cell Biology* **1999**, *1*, 60–67.
122. Vesely, J.; Havlicek, L.; Strnad, M.; Blow, J. J.; Donelladeana, A.; Pinna, L.; Letham, D. S.; Kato, J.; Detivaud, L.; Leclerc, S.; Meijer, L., Inhibition of cyclin-dependent kinases by purine analogs. *European Journal of Biochemistry* **1994**, *224*, 771–786.
123. Buquet-Fagot, C.; Lallemand, F.; Montagne, M. N.; Mester, J., Effects of olomoucine, a selective inhibitor of cyclin-dependent kinases, on cell cycle progression in human cancer cell lines. *Anti-Cancer Drugs* **1997**, *8*, 623–631.
124. Meijer, L.; Borgne, A.; Mulner, O.; Chong, J. P. J.; Blow, J. J.; Inagaki, N.; Inagaki, M.; Delcros, J. G.; Moulinoux, J. P., Biochemical and cellular effects of roscovitine, a potent and selective inhibitor of the cyclin-dependent kinases CDC2, CDK2 and CDK5. *European Journal of Biochemistry* **1997**, *243*, 527–536.
125. Havlicek, L.; Hanus, J.; Vesely, J.; Leclerc, S.; Meijer, L.; Shaw, G.; Strnad, M., Cytokinin-derived cyclin-dependent kinase inhibitors: Synthesis and cdc2 inhibitory activity of olomoucine and related compounds. *Journal of Medicinal Chemistry* **1997**, *40*, 408–412.
126. DeAzevedo, W. F.; Leclerc, S.; Meijer, L.; Havlicek, L.; Strnad, M.; Kim, S. H., Inhibition of cyclin-dependent kinases by purine analogues - Crystal structure of human cdk2 complexed with roscovitine. *European Journal of Biochemistry* **1997**, *243*, 518–526.
127. Norman, T. C.; Gray, N. S.; Koh, J. T.; Schultz, P. G., A structure-based library approach to kinase inhibitors. *Journal of the American Chemical Society* **1996**, *118*, 7430–7431.

128. Chang, Y. T.; Gray, N. S.; Rosania, G. R.; Sutherlin, D. P.; Kwon, S.; Norman, T. C.; Sarohia, R.; Leost, M.; Meijer, L.; Schultz, P. G., Synthesis and application of functionally diverse 2,6,9-trisubstituted purine libraries as CDK inhibitors. *Chemistry & Biology* **1999**, *6*, 361–375.
129. Arris, C. E.; Boyle, F. T.; Calvert, A. H.; Curtin, N. J.; Endicott, J. A.; Garman, E. F.; Gibson, A. E.; Golding, B. T.; Grant, S.; Griffin, R. J.; Jewsbury, P.; Johnson, L. N.; Lawrie, A. M.; Newell, D. R.; Noble, M. E. M.; Sausville, E. A.; Schultz, R.; Yu, W., Identification of novel purine and pyrimidine cyclin-dependent kinase inhibitors with distinct molecular interactions and tumor cell growth inhibition profiles. *Journal of Medicinal Chemistry* **2000**, *43*, 2797–2804.
130. Mesguiche, V.; Parsons, R. J.; Arris, C. E.; Bentley, J.; Boyle, F. T.; Curtin, N. J.; Davies, T. G.; Endicott, J. A.; Gibson, A. E.; Golding, B. T.; Griffin, R. J.; Jewsbury, P.; Johnson, L. N.; Newell, D. R.; Noble, M. E. M.; Wang, L. Z.; Hardcastle, I. R., 4-alkoxy-2,6-diaminopyrimidine derivatives: Inhibitors of cyclin dependent kinases 1 and 2. *Bioorganic & Medicinal Chemistry Letters* **2003**, *13*, 217–222.
131. Sielecki, T. M.; Johnson, T. L.; Liu, J.; Muckelbauer, J. K.; Grafstrom, R. H.; Cox, S.; Boylan, J.; Burton, C. R.; Chen, H. Y.; Smallwood, A.; Chang, C. H.; Boisclair, M.; Benfield, P. A.; Trainor, G. L.; Seitz, S. P., Quinazolines as cyclin dependent kinase inhibitors. *Bioorganic & Medicinal Chemistry Letters* **2001**, *11*, 1157–1160.
132. Zaharevitz, D. W.; Gussio, R.; Leost, M.; Senderowicz, A. M.; Lahusen, T.; Kunick, C.; Meijer, L.; Sausville, E. A., Discovery and initial characterization of the paullones, a novel class of small-molecule inhibitors of cyclin-dependent kinases. *Cancer Research* **1999**, *59*, 2566–2569.
133. Schultz, C.; Link, A.; Leost, M.; Zaharevitz, D. W.; Gussio, R.; Sausville, E. A.; Meijer, L.; Kunick, C., Paullones, a series of cyclin-dependent kinase inhibitors: Synthesis, evaluation of CDK1/cyclin B inhibition, and in vitro antitumor activity. *Journal of Medicinal Chemistry* **1999**, *42*, 2909–2919.

134. Kabsch, W., XDS. In *International Tables for Crystallography*, Rossmann, M. G.; Arnold, E., Eds.; Kluwer Academic Publishers: Dordrecht, 2001; Vol. F. Crystallography of Biological Macromolecules, pp 730–734.
135. Otwinowski, Z.; Minor, W., Processing of X-ray Diffraction Data Collected in Oscillation Mode. *Methods in Enzymology* **1997**, *276*, 307–326.
136. Brünger, A. T.; Adams, P. D.; Clore, G. M.; DeLano, W. L.; Gros, P.; Grosse-Kunstleve, R. W.; Jiang, J. S.; Kuszewski, J.; Nilges, M.; Pannu, N. S.; Read, R. J.; Rice, L. M.; Simonson, T.; Warren, G. L., Crystallography & NMR system: A new software suite for macromolecular structure determination. *Acta Crystallographica Section D* **1998**, *54*, 905–921.
137. Jones, T. A.; Zou, J. Y.; Cowan, S. W.; Kjeldgaard, M., Improved methods for building protein models in electron density maps and the location of errors in these models. *Acta Crystallographica Section A* **1991**, *47*, 110–119.
138. Kleywegt, G. J.; Zou, J. Y.; Kjeldgaard, M.; Jones, T. A., Around O. In *International Tables for Crystallography*, Rossmann, M. G.; Arnold, E., Eds. Kluwer Academic Publishers: Dordrecht, 2001; Vol. F. Crystallography of Biological Macromolecules, pp 353–356.
139. Kraulis, P. J., MOLSCRIPT: a program to produce both detailed and schematic plots of protein structures. *Journal of Applied Crystallography* **1991**, *24*, 946–950.
140. *Glide*, version 4.5. Schrödinger, LLC.: New York, NY, 2007.
141. Priestman, M. A., Ph.D. thesis, Probing the Antibiotic Targets MurA and EPSPS. University of Kansas, Lawrence, KS, 2005.
142. Morikawa, M.; Izui, K.; Taguchi, M.; Katsuki, H., Regulation of escherichia-coli phosphoenolpyruvate carboxylase by multiple effectors invivo .1. estimation of the activities in the cells grown on various compounds. *Journal of Biochemistry* **1980**, *87*, 441–449.
143. Steinbach, A.; Scheidig, A. J.; Klein, C. D., The Unusual Binding Mode of Cnicin to the Antibacterial Target Enzyme MurA Revealed by X-ray Crystallography. *Journal of Medicinal Chemistry* **2008**, *51*, 5143–5147.

144. Cao, S. X.; Bounaud, P. Y.; Chen, X.; Chung, H. H.; Kumar KC, S.; Min, C.; Yang, J. Y.; Long, M. C., Inhibitors of protein kinase for the treatment of disease. U.S. Patent 2003/0187007 A1, May 28, 2002.
145. Berdini, V.; Carr, M.; Saxty, G.; Woolford, A. J.; Wyatt, P. G., 3-(carbonyl)-1H-indazole compounds as cyclin dependent kinase (CD) inhibitors. U.S. Patent 2006/0135516 A1, Aug 8, 2003.
146. D'Orchymont, H.; Van Hijfte, L.; Zimmermann, A., Indazolecarboxamide derivatives, preparation and use thereof as CDK1, CDK2, and CDK4 inhibitors. U.S. Patent 2006/0004000 A1, Apr 1, 2005.
147. Zhang, C.; Lundgren, K.; Yan, Z.; Arango, M. E.; Price, S.; Huber, A.; Higgins, J.; Troche, G.; Skaptason, J.; Koudriakova, T.; Nonomiya, J.; Yang, M.; O'Connor, P.; Bender, S.; Los, G.; Lewis, C.; Jessen, B., Pharmacologic properties of AG-012986, a pan-cyclin-dependent kinase inhibitor with antitumor efficacy. *Molecular Cancer Therapeutics* **2008**, *7*, 818–828.
148. Chen, L.; Chu, X. J.; Lovey, A. J.; Zhao, C., 4-Aminothiazole derivatives. U.S. Patent 2006/0014958 A1, Jun 29, 2005.
149. Chong, W. K. M.; Chu, S. S.; Duvadie, R. K.; Na, J.; Schaffer, L.; Yang, Y.; Li, L., Antiproliferative 2-(sulfo-phenyl)-aminothiazole derivatives and pharmaceutical compositions, and methods for their use. U.S. Patent 2004/0176431 A1, Feb 11, 2004.
150. Larkin, M. A.; Blackshields, G.; Brown, N. P.; Chenna, R.; McGettigan, P. A.; McWilliam, H.; Valentin, F.; Wallace, I. M.; Wilm, A.; Lopez, R.; Thompson, J. D.; Gibson, T. J.; Higgins, D. G., Clustal W and Clustal X version 2.0. *Bioinformatics* **2007**, *23*, 2947–2948.
151. Mapelli, M.; Massimiliano, L.; Crovace, C.; Seeliger, M. A.; Tsai, L. H.; Meijer, L.; Musacchio, A., Mechanism of CDK5/p25 binding by CDK inhibitors. *Journal of Medicinal Chemistry* **2005**, *48*, 671–679.
152. Brotherton, D. H.; Dhanaraj, V.; Wick, S.; Brizuela, L.; Domaille, P. J.; Volynik, E.; Xu, X.; Parisini, E.; Smith, B. O.; Archer, S. J.; Serrano, M.; Brenner, S. L.; Blundell, T. L.; Laue, E. D., Crystal structure of the complex

- of the cyclin D-dependent kinase CDK6 bound to the cell-cycle inhibitor p19INK4d. *Nature* **1998**, *395*, 244–250.
153. Lolli, G.; Lowe, E. D.; Brown, N. R.; Johnson, L. N., The crystal structure of human CDK7 and its protein recognition properties. *Structure* **2004**, *12*, 2067–2079.
154. Baumli, S.; Lolli, G.; Lowe, E. D.; Troiani, S.; Rusconi, L.; Bullock, A. N.; Debreczeni, J. E.; Knapp, S.; Johnson, L. N., The structure of P-TEFb (CDK9/cyclin T1), its complex with flavopiridol and regulation by phosphorylation. *Embo Journal* **2008**, *27*, 1907–1918.
155. The CCP4 Suite: Programs for Protein Crystallography. *Acta Crystallographica Section D* **1994**, *50*, 760–763.
156. Tari, L. W.; Hoffman, I. D.; Bensen, D. C.; Hunter, M. J.; Nix, J.; Nelson, K. J.; McRee, D. E.; Swanson, R. V., Structural basis for the inhibition of Aurora A kinase by a novel class of high affinity disubstituted pyrimidine inhibitors. *Bioorganic & Medicinal Chemistry Letters* **2007**, *17*, 688–691.
157. Pargellis, C.; Tong, L.; Churchill, L.; Cirillo, P. F.; Gilmore, T.; Graham, A. G.; Grob, P. M.; Hickey, E. R.; Moss, N.; Pav, S.; Regan, J., Inhibition of p38 MAP kinase by utilizing a novel allosteric binding site. *Nature Structural & Molecular Biology* **2002**, *9*, 268–272.
158. Caldwell, J. J.; Davies, T. G.; Donald, A.; McHardy, T.; Rowlands, M. G.; Aherne, G. W.; Hunter, L. K.; Taylor, K.; Ruddle, R.; Raynaud, F. I.; Verdonk, M.; Workman, P.; Garrett, M. D.; Collins, I., Identification of 4-(4-Aminopiperidin-1-Yl)-7H-Pyrrolo[2,3-D]Pyrimidines as Selective Inhibitors of Protein Kinase B Through Fragment Elaboration. *Journal of Medicinal Chemistry* **2008**, *51*, 2147–2157.
159. Xu, Z. B.; Chaudhary, D.; Olland, S.; Wolfrom, S.; Czerwinski, R.; Malakian, K.; Lin, L.; Stahl, M. L.; Joseph-McCarthy, D.; Benander, C.; Fitz, L.; Greco, R.; Somers, W. S.; Mosyak, L., Catalytic domain crystal structure of protein kinase C- θ (PKC θ). *Journal of Biological Chemistry* **2004**, *279*, 50401–50409.